Silk Fibroin and Cellulose Interactions at Different Length-scales

James Andew King

Department of Physics and Astronomy

University of Leeds

Submitted in accordance with the requirements for the degree of

Doctor of Philosophy

November 2025

The candidate confirms that the work submitted is his own, except where work which has formed part of jointly authored publications has been included. The contribution of the candidate and the other authors to this work has been explicitly indicated below. The candidate confirms that appropriate credit has been given within the thesis where reference has been made to the work of others.

The work presented in Chapter 3 is based off the following published work: Understanding the Dissolution of Cellulose and Silk Fibroin in 1-ethyl-3-methylimidazolium Acetate and Dimethyl Sulphoxide for Application in Hybrid Films. *James A. King, Peter J Hine, Daniel L Baker, Michael E Ries* Materials **2024**, 17 (21), 5262

The work presented in Chapter 4 is based off the following published work: Hybrid Biocomposites: From Molecular Behaviour to Material Properties in Silk Fibroin/Cellulose Films. *James A. King, Peter J Hine, Daniel L Baker, Matthew Creswick, Michael E Ries* The International Journal of Biological Macromolecules **2025**, 321 (1), 145931, ISSN 0141-8130

The work presented in Chapter 5 is based off the following work which is under review for publication: Understanding Novel Biocomposites Comprising of Short Cellulose Fibres in a Hybrid Cellulose/Silk Fibroin Matrix. *James A. King, Dr. Peter J. Hine, Dr. Daniel L. Baker, Prof. Yu Shi, Prof. Xiaoling Liu, Jiawen Lu, Saihua Li, Xiaoye Cong, Prof. Michael E. Ries* Composites Part A: Applied Science and Manufacturing

For Natalie, Mum, Dad, Helen, Sandy, and Stuart. Also, for Phil, Jake, and Oscar. I love you all.

Acknowledgements

This work couldn't have been completed without, and isn't finished, without acknowledgement to the great number of people who added to it. Forefront among these are my supervisors: Professor Mike Ries, Dr Peter Hine, and Dr Dan Baker. Throughout my time at Leeds they have been role models and mentors and have helped me navigate the difficulties in studying a PhD. In the last four years I feel I have grown as a person and towards understanding a very small portion of the world. This is largely due to their guidance and patience, driving me to pursue new ideas which I hope can help the contribute to the planet.

I would also like to thank the host of diverse friends and colleagues who I've worked alongside in the Biopolymer Dream Team, Bragg, and SOFI^2. It has been a joy to share all the laughs and inspiration across the years. I can't imagine completing my work without long nights with Daniel, or my training without Libby's dinner parties. Most of all, I've loved every minute spent with Megan, who's kept me sane and laughing. There are too many people to thank here but I am grateful for you all.

Most importantly, I would like to thank my family: Natalie, Mum, Dad, Sandy, Stuart, and Helen. You are, and always will be, my inspiration. You all motivate me to stay hopeful and every tough day has flown by when coming home to Natalie. Though I'm sure you'll be glad to stop hearing about cellulose and silk, I hope I can keep making a greener future for us.

Abstract

Recent developments in biocomposite research are leading towards a more sustainable future with higher performance materials. Silk fibroin (SF) and cellulose are two abundant biopolymers capable of forming composites with biocompatibility, high mechanical performance, and biodegradability. Optimising biodegradable materials offers a replacement to traditional plastics that reduces reliance on recycling for sustainability and minimizes the impact of unavoidable leaching into the environment. This thesis investigates the dissolution, molecular interactions, and macroscopic material properties of SF–cellulose hybrid systems with the ultimate aim of producing self-reinforcing biocomposites from waste textile streams.

Using a solvent system of the ionic liquid 1-ethyl-3-methylimidazolium acetate (EmimAc) and the cosolvent dimethyl sulfoxide (DMSO), optimal conditions for dissolving cellulose and SF were established. Interestingly, these were found to differ. Cellulose was most quickly and efficiently dissolved in a 2:8 EmimAc:DMSO solvent mixture, and SF fibres were most efficiently dissolved in an 8:2 EmimAc:DMSO solvent mixture. The macroscopic and microscopic behaviours were seen to differ with the bulk saturation being below the molecular saturation concentration investigated with nuclear magnetic resonance, as observed by polarized optical microscopy.

Understanding the dissolution of both biopolymers enabled the preparation of homogeneous hybrid solutions and fabrication of coagulated SF and cellulose films with varied compositions. Macroscopic mechanical testing showed that hybrid films exhibited enhanced modulus and strength (2.2 $\pm$ 0.1 GPa and 28 $\pm$ 1 MPa), with properties

maximised at SF contents of 5–15 wt %. Creep and stress relaxation measurements identified strain-dependent viscoelastic relaxations in hybrid samples. This was rationalised with double network theory, and comparisons with relevant biological materials which also exhibit similar relaxation behaviours. Structural analyses by thermogravimetric analysis confirmed the presence of mixed phases and β-sheet crystallinity, underpinning the observed mechanical strength and increased relaxation behaviours.

Building on these findings, isotropic short-fibre reinforced composites were prepared using optimised hybrid matrices reinforced with short-fibre cotton flock. The short fibres used mimicked potential textile waste for future manufacture of these materials. Sample morphology was investigated with X-ray diffraction to characterise the reinforcing fibre volume percentage. Compared with all-cellulose composites, samples with hybrid matrices achieved elevated Young's moduli, strains at failure, and tensile strengths (3.4 ± 0.2 GPa, 1.3 ± 0.2 %, and 72 ± 2 MPa) at 42 - 55 vol % fibre reinforcement. This behaviour was rationalised with theoretical modelling and imaging with optical microscopy and scanning electron microscopy. Optimal composites showed reduced density and increased material performance while retaining full biodegradability and recyclability. Additional acoustic characterisation highlighted the potential for application in insulation materials as hybrid samples achieved an average acoustic transmission loss of 47 ± 7 dB which exceeds the typical standard for internal interior soundproofing between rooms (45 dB).

Overall, this work demonstrates how controlled dissolution and blending of SF and cellulose can yield a new class of tunable, self-reinforcing hybrid biocomposites. By combining molecular-level miscibility with waste-fibre reinforcement, this thesis establishes fundamental understanding and practical strategies for advancing sustainable, circular biological material technologies.

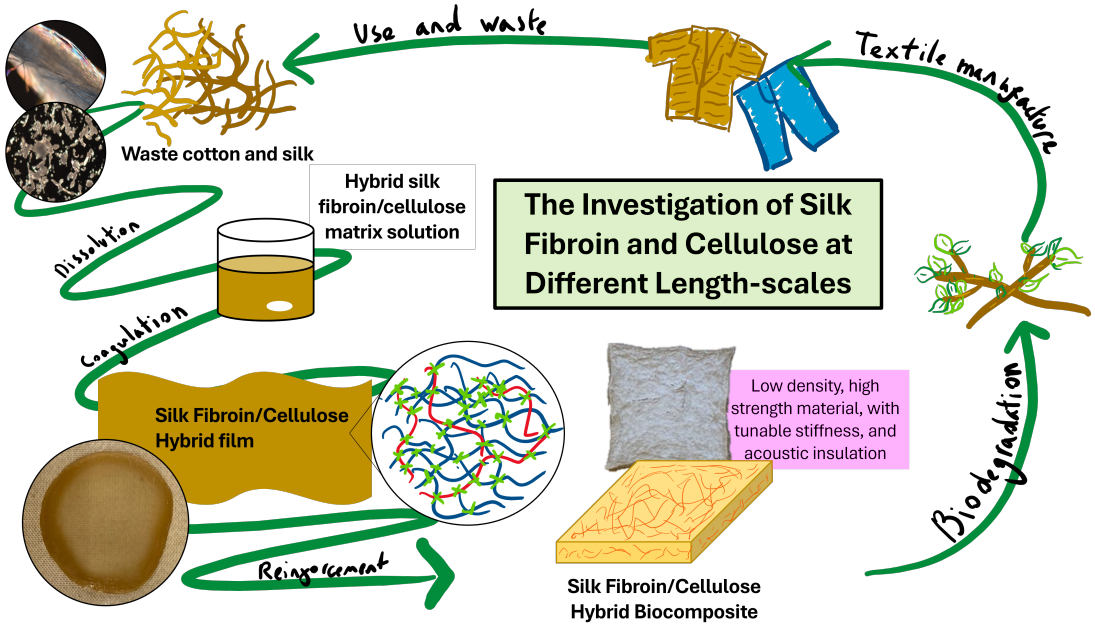

Figure 1: Graphical abstract indicating the circularity and development of materials studied in this thesis.

Publications

The Formation of All-Silk Composites and Time–Temperature Superposition. *James A. King, Xin Zhang, Michael E Ries* Materials **2023**, 16 (10), 3804; https://doi.org/10.3390/ma16103804

Understanding the Dissolution of Cellulose and Silk Fibroin in 1-ethyl-3-methylimidazolium Acetate and Dimethyl Sulphoxide for Application in Hybrid Films. *James A. King, Peter J Hine, Daniel L Baker, Michael E Ries* Materials **2024**, 17 (21), 5262; https://doi.org/10.3390/ma17215262

Hybrid Biocomposites: From Molecular Behaviour to Material Properties in Silk Fibroin/Cellulose Films. *James A. King, Peter J Hine, Daniel L Baker, Matthew Creswick, Michael E Ries* The International Journal of Biological Macromolecules **2025**, 321 (1), 145931, ISSN 0141-8130; https://doi.org/10.1016/j.ijbiomac.2025.145931

Understanding Novel Biocomposites Comprising of Short Cellulose Fibres in a Hybrid Cellulose/Silk Fibroin Matrix. *James A. King, Dr. Peter J. Hine, Dr. Daniel L. Baker, Prof. Yu Shi, Prof. Xiaoling Liu, Jiawen Lu, Saihua Li, Xiaoye Cong, Prof. Michael E. Ries* Composites Part A: Applied Science and Manufacturing **2026**, 202, 109459; https://doi.org/10.1016/j.ijbiomac.2025.145931

Contributions

James A. King: Writing, Review, Editing, Validation, Methodology, Investigation, Formal analysis, Data curation, Conceptualisation.

Prof. Michael E. Ries, Dr. Peter J. Hine, Dr. Daniel L. Baker: Validation, Resources, Review, Conceptualisation, Editing, and Supervision.

In addition to my supervisory team, this work was also supported with data curation, analysis, and review by the following collaborators: Prof. Yu Shi, Prof. Xiaoling Liu, Jiawen Lu, Saihua Li, Xiaoye Cong, Matthew Creswick, and Xin Zhang.

Abbreviations

SF	Silk Fibroin
CNC	Cellulose Nanocrystal
MCC	Microcrystalline Cellulose
IL	Ionic Liquid
DP	Degree of Polymerisation
XRD	X-Ray Diffraction
FTIR	Fourier Transform Infrared Spectroscopy
NMR	Nuclear Magnetic Resonance
DSC	Differential Scanning Calorimetry
SEM	Scanning Electron Microscopy
DMA	Dynamic Mechanical Analysis
ACC	All Cellulose Composites
ASC	All Silk Composite
EMimAc	1-ethyl-3-methylimidazolium acetate
BmimCl	1-butyl-3-methylimidazolium chloride
DMSO	Dimethyl Sulfoxide
rpm	Revolutions per minute
ROM	Rule of mixing
SE	Standard Error
NFRC	Natural Fibre Reinforced Composites

Contents

List of Figures

LIST OF FIGURES

LIST OF FIGURES

Chapter 1

Introduction

Biological materials, and particularly biocomposites, have recently gained attention due to their sustainability, recyclability, and high performance [1]. Synthetic polymers are low cost, and of uniform composition but poor biocompatibility and potentially toxic degradation inhibits their use as a permanent fixture in all functional materials. There is also increasing concern about petroleum based plastics due to their contributions to harmful microplastics [2]. Cellulose and silk fibroin(SF) are both available and abundant enough for application in new materials [1]. Fibres of these are available as a waste resource from the textile chain and, in contrast to fossil fuel plastics or biodegradable polyesters, these biological materials can be considered to be carbon neutral and breakdown more easily [3, 4]. For example, most cellulosic materials will lose 50 % of their mass within 30 days in any natural water [5]. Textile waste is a huge resource of which cellulosic fibres forms the large majority. Textile waste is projected to reach 134 million tons/year by 2030. Of this 75 % is disposed of in landfills and less than 1 % reintegrated into new clothes [6]. Less available but still abundant, the global volume of raw silk averages 80,000 tonnes per year (2023) and across all sectors around 55 % of raw silk mass is wasted during production [7].

Cellulose is an anisotropic, abundant, biocompatible polymer. It is formed of repeat units of anhydroglucose, which form two unit pairs known as anhydrocellobiose. A disaccharide formed by β-1,4-glycosidic bonds between 2 anhydroglucose monomer units, as shown in Figure 1.1 [8]. Anhydroglucose is

present as D-glucopyranose, which corresponds to the lowest energy ring conformation [1, 9, 10]. It is sparingly soluble due to extensive inter- and intramolecular hydrogen bonding and amphiphilic behaviour due to apolar hydrophobic stacking [11]. This unique structure gives rise to Young's moduli of up to 200 GPa, and an ultimate tensile strength of up to 17.8 GPa. This is 7 times stronger than typical steel with a fifth of steel's density [12].

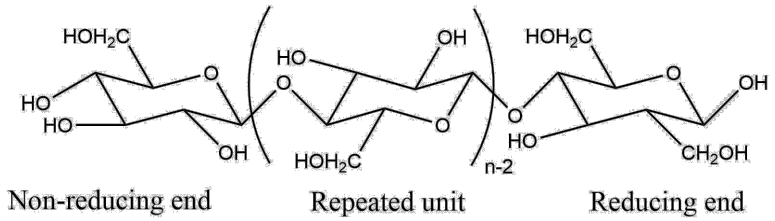

Figure 1.1: Depiction of the chemical structure of cellulose indicating the anhydroglucose monomer unit[8].

Silkworm silk is a fibrous protein pultrusion hierarchically structured of silk sericin and SF proteins. SF provides structural strength and, though the chemical composition varies, typically has a hexapeptide primary sequence of mostly glycine amino acid units as shown in Figure 1.2 [13]. Natural silk fibres are noted for their remarkable properties of toughness, strength, and flexibility. For example, Bonino *et al.* reported spider silk fibres with an elongation of 24 $\pm$ 2 % strain with a tensile strength of 1200 $\pm$ 200 MPa [14]. More remarkable properties have also been reported with bioprospecting by Andersson *et al.* who found *C. darwini* to have the toughest silk in the world [15]. Removal of silk sericin, or degumming, provides silkworm silks with a distinct lustre often seen in commercial silks. Spider silk forms naturally without sericin, which is only present in silks from *Lepidoptera*.

Combining SF and cellulose utilises the benefits of both biopolymers as seen in the natural materials they both form: the strength and stiffness of cellulose, and the elasticity and toughness of silk. Blending and preparation can have unexpected impacts on material properties though. SF films are often seen to be very brittle and weak in contrast to its properties in fibrous form [2]. Introduction of mixed polymers to composites can introduce voids and interfaces which can

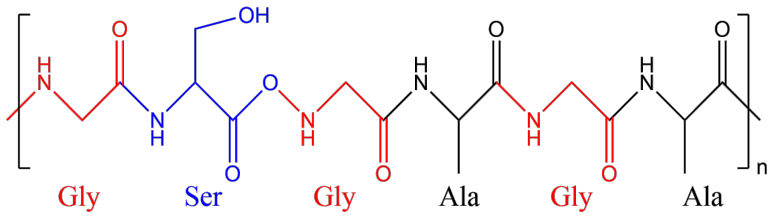

Figure 1.2: Depiction of example typical molecular sequences for silk fibroin repeat units[1]. Amino acid groups are colour coded in the protein.

impact macroscopic properties. This can increase rigidity, while lowering transparency, elasticity, and flexibility if miscibility is low [16]. Thermodynamically, mixing occurs if the free energy of the blend is lower than that of the separate phases. Kinetic reasons can also complicate this case for macromolecules where entanglement, viscosity, association and slowed diffusion can alter the dissolution and blending of polymers [17]. This makes the control of these blends very complex. Tian *et al.* provide some of the most convincing evidence of SF and cellulose molecular miscibility using 2D (^{1}H and ^{13}C) heteronuclear correlation from Nuclear Magnetic Resonance (NMR) experiments [18]. It is noted that dense hydrogen bond assemblies in these materials can supercede hydrogen bonding weakness and confer material strength [18]. Fourier Transform Infrared Spectroscopy (FTIR) and NMR data elucidate specific blend regiochemistries to show homogeneous interdispersion and conformations. These indicate an increase in crystalline structures for certain blend films that improved toughness over pure alternatives [18, 19]

Both silk and cellulose have also been used to produce self-supporting biocomposites in which fibre reinforcement is used with a chemically identical biopolymer matrices [20, 21]. In cellulosic samples these are often labelled all-cellulose composites(ACC), and as all-silk composites (ASC) with silk samples [20, 22, 23]. This powerful concept has been further extended to produce self-supporting hybrid biocomposites at differing length scales, but rarely while preserving entire silk/cellulose fabrics or fibres [24].

Production of varied material types opens opportunities for fine tuning the material properties of composites and altering their application. These could be anything from maintaining historical silk tapestries, to aiding in wound repair

and granulation [24, 25]. This requires an in-depth understanding of the material and molecular behaviours at all length scales to optimise these systems. The behaviours of SF and cellulose hybrid blends in solution, films/gels, and composites are discussed throughout this thesis.

1.1 Cellulose

A Brief Introduction into the Hierarchical Structure of Cellulosic Materials

There are many examples of cellulose based materials, split into woods and non-wood fibres (straws, leaves, grasses, fruits, stems, etc.) [26]. Native cellulose is typically 40-70 % crystalline and bound by lignin and hemicellulose. The degree of polymerisation is typically from 1500-3500 monomer units [9]. In wood, this is commonly organised in complex hierarchical structures to optimise various properties. Cellulose is organised as undulating microfibrils with consistent orientation. In thicker cellulose structures highly oriented lamellae are arranged perpendicular to tangential rings around the stem [26]. These are then supported by lignin and hemicellulose, two polymers also seen in structural plant matter. Hemicellulose is short and branched, and acts as an oriented 'glue' between cellulose and lignin. Lignin is a complex, variable polymer which provides rigidity in plant cells [27, 28]. An example of the hierarchical cellulosic structure of a wood microfibril can be seen in Figure 1.3

Cellulose forms complex and varied hierarchical structures at differing length scales. In nanocellulose (1-1000nm) alone 3 divisions are typically seen: cellulose nanocrystals (CNCs)(up to 90% crystalline particles); cellulose nanofibrils (long entangled fibrils with amorphous and crystalline phases); and bacterial cellulose (high purity ribbon-like fibres in a web) [9]. See Table 1.1 for some other example dimensions of cellulose forms seen in literature, with microcrystalline cellulose (MCC) being the most prevalent.

The differing sizes, lengths, and aspect ratios of cellulose can greatly affect macroscopic material properties. Addition of microfibrils can induce glass tran-

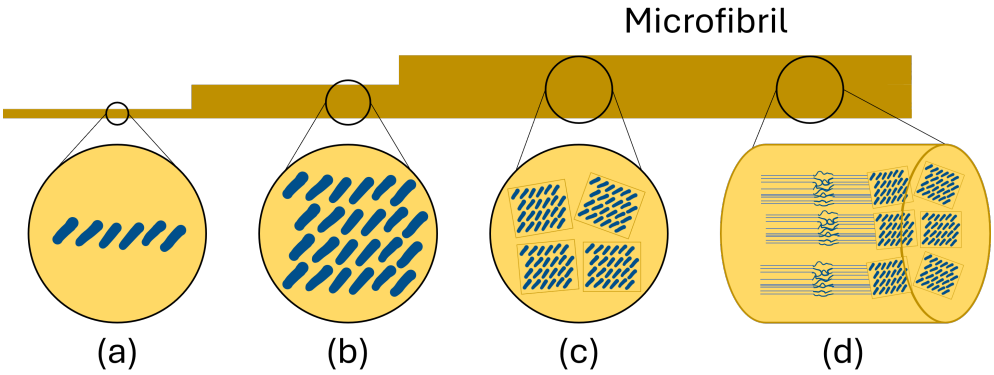

Figure 1.3: Schematic representation of the hierarchical structures of a wood microfibril, showing: (a) cross-section of a single subunit, in which Van der Waal's forces hold the cellulose chains together. Each blue box represents a cellulose chain, looking down the chain-axis; (b) an elementary fibril cross-section. (c) microfibril cross-section composed of 4 elementary fibrils embedded in a matrix composed mostly of hemicellulose and lignin; (d) microfibril lateral section showing both crystalline (linear) and amorphous (nonlinear) regions [1].

sitions to some materials, while hygroscopicity also depends on total interface areas and total available hydrogen bonding sites [29].

Crystalline Cellulose

Cellulose crystalline polymorphs I, II, III, IV exist with differing properties and molecular conformations. Most common are polymorphs I and II, as seen in Figure 1.4. Cellulose I is found in native cellulose materials and provides high strength and crystallinity. This can be in Iα (triclinic) or Iβ (monoclinic) poly-

Table 1.1: Common cellulose dimensions with typical names seen in literature [26]

Structure	**Diameter / nm**	**Length / nm**	**Aspect ratio**
Microfibril	2-10	10,000	1000
Microfibrillated cellulose	10-40	1000	100-150
Cellulose whisker	2-20	100-600	10-100
Microcrystalline cellulose	1000	1000	≈1

morphs. At each sugar unit 2 intramolecular bonds (parallel to the glycosidic bond) and 2 intermolecular hydrogen bonds are seen [30]. Cellulose II is found in regenerated forms of cellulose. After a material has been dissolved and regenerated in an antisolvent, this polymorph formed as the more thermodynamically stable crystalline form [9]. Cellulose II is often seen to have weaker mechanical properties due to a loss of hydrogen bonding order compared to cellulose I. This can be counteracted by an extension of the hydrogen bonding network that may occur during cellulose II formation. Cellulose III is ammonia-mercerised. It is conformationally similar to the center chain of the highly stable cellulose II with parallel orientations like in cellulose I [31]. Glycerol can be used as a protective plasticizing medium to allow sufficient chain mobility to form cellulose IV (or 'high temperature' cellulose) upon heating. This reduces charring. The cellulose source can be varied to alter the glycerol penetration and hence the wt% crystalline change [32]. Reaction pathways between these polymorphs can be seen in Figure 1.5.

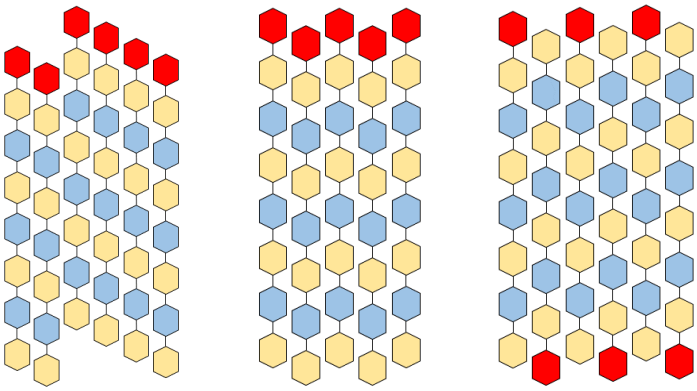

Figure 1.4: Illustration showing common cellulose polymorphs. (**a**) shows the cellulose I-α allotrope with parallel aligned, and mono-oriented polymers It is seen in native cellulose and is of high strength. (**b**) shows the cellulose I-β allotrope with parallel aligned polymers with alternating orientations. It is also seen in native cellulose. (**c**) shows cellulose II with anti-parallel polymer strands. It is thermodynamically stable and is formed in regenerated or mercerized cellulose [9].

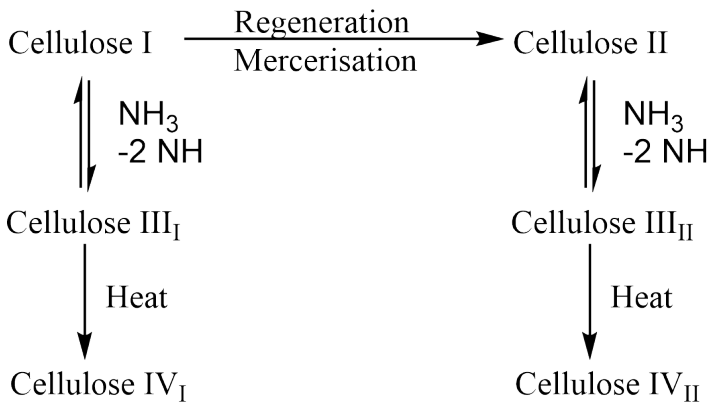

Figure 1.5: Illustration showing the reaction conditions and pathways for conversion between different cellulose polymorphs [9].

Dissolution of Cellulose

Cellulose solubility has been studied more extensively than that of SF and improvements in solvation performance show the importance of researching improved solvation techniques. Historically, due to the insoluble nature of cellulose, harsh and environmentally unfriendly chemical solvents have been used to dissolve cellulose. Most commonly in industry, the viscose or lyocell process is used [11]. The viscose process uses CS_2 to derivatise cellulose going from alkali cellulose to cellulose xanthate. This is essential to improve the molecular rearrangement in the product formation but produces sulphur byproducts: sodium sulphate and hydrogen sulphide. An appropriate level of substitution controls solubility and kinetic hindrance [33]. The entire viscose process is a major environmental concern due to the emission of CS_2 and H_2S [33].

Some aqueous solvents have achieved solubility without harmful emissions or high energy consumption, such as Yue Xi *et al.*, who utilised an aqueous $AlCl_3/ZnCl_2$ solvent system to dissolve cellulose at room temperature. It was proposed that the smaller Al^{3+} ions first penetrated to break hydrogen bonds and provide additional coordination sites. Larger Zn^{2+} ions then break more hydrogen bonds to trigger diffusion and dissolution [34, 35]. These salts, however, can still impact aquatic environments [36]. Hence, it is essential to utilise improved solvent systems where possible. Nemoto and Nakamata used an $\approx$ 80 %

concentration $ZnCl_2$ solution to produce vulcanised (partially dissolved and regenerated) fibres [37] and Sharma *et al.* synthesised a low cost zwitterion capable of dissolving up to 6 wt % cellulose [38]. A timeline of solvent use for cellulose dissolution can be seen in Figure 1.6.

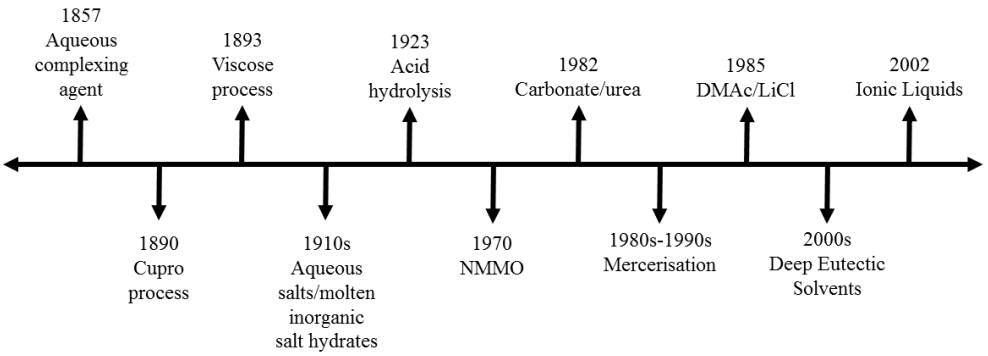

Figure 1.6: Timeline indicating approximate dates at which new solvents for cellulose were proposed and trialled [39].

Cellulose is rarely soluble in most common solvents due to a complex molecular arrangement that is debated in literature. Azimi *et al.* propose extensive intra- and inter-molecular hydrogen bonding is the cause of cellulose's material strength and insolubility [11]. Numerous other articles argue this neglects cellulosic insolubility in polar hydrogen bonding solvent (like water and alcohols), and hence propose that axial non-polar regions cause strong hydrophobic interactions between glucopyranose rings. These cause an amphiphilic crystalline structure with very sparing solubility in polar and apolar solvents as seen in Figure 1.7 [17, 22, 30, 40, 41]. This is contradicted by some older studies which only discuss extensive hydrogen bonding as the cause of cellulosic insolubility [42]. In addition, cellulose is stiffened by chair structures in its back bone which reduces the increase in conformational freedom upon dissolution. This inherently makes it less soluble than SF [17].

Cellulose solubility is dependent on degree of polymerisation (DP), impurities, and temperature. It is proposed there is an upper limit for DP to remain soluble in any solvent system [43]. Decrystallisation (via dissolution and coagulation) of

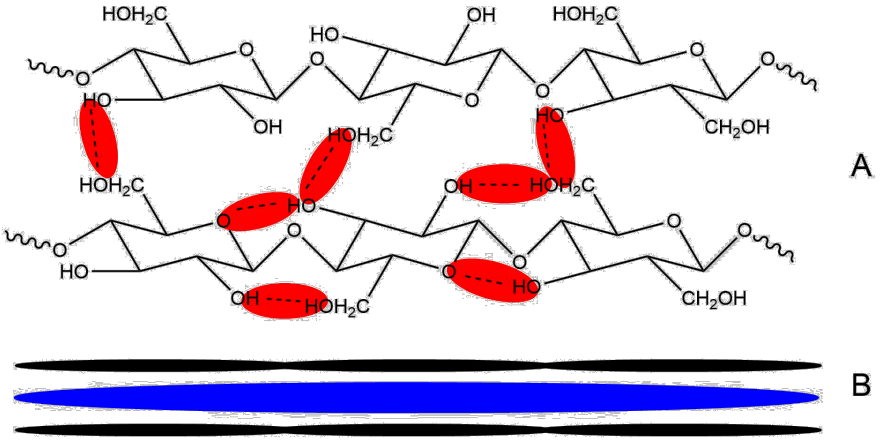

Figure 1.7: Illustration showing hydrophillic and hydrophobic interactions of cellulose molecules. **A** shows the glucopyranose ring plane with inter- and intramolecular hydrogen bonding highlighted. **B** shows hydrophobic attraction between the axial C-H bonds of glucopyranose stacking.

native cellulose is seen to be exothermic due to the increased enthalpic stability of amorphous cellulose and cellulose II over cellulose I [43]. Direct dissolution by solvent disrupts the internal bonding, while derivitizing solvents modify bonding groups of cellulose to avoid formation of strong bonds [44].

Microcrystalline cellulose is seen to dissolve by a 'peeling' mechanism of microfibrils into thinner crystals, prior to full solvation [45]. On a larger length-scale it is seen that fibre exteriors are preferentially dissolved over their cores which often remain in the native state [46]. Other literature has proposed dissolution by formation of 'balloons'. These form by solvent penetration through a primary rigid cellulose membrane. This swells the internal fibres which causes an anurism of the fibre [22, 47].

1.2 Silk and Silk Fibroin

Silk is a natural animal protein. Silk, similarly to cellulose, forms a complex semi-crystalline hierarchical structure in its native state. The most common commercial silk is from the silk worm, *Bombyx Mori*, but silk is also produced by spiders and other species [1].

A Brief Introduction into the Hierarchical Structure of Silk Materials

Natural silk fibres are typically formed of 2 filaments of SF with surrounding matrix of gummy silk sericin to maintain integrity. The continuous phase of silk sericin is removed by degumming using hot water, alkaline or acidic solutions, or other methods. The structure can be seen in Figure 1.8 [1]. In *Bombyx mori* silk fibres content is 66.5 - 73.5 wt% while sericin content makes up 26.5 - 33.5 wt% [48]. SF exists in heavy or light chains, of 390 or 25 kDa respectively, with chaperonin-like P25 proteins in a 6:6:1 ratio [24, 49].

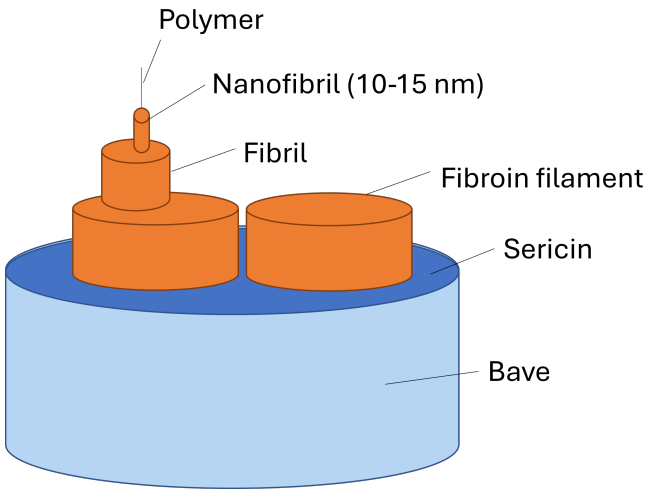

Figure 1.8: Illustration showing hierarchical structure of raw silk fibre with SF core and sericin coating.

The source of this silk can alter it's properties with variations in strength, toughness, and finish. Spiders alone can have 7 different types of silk, controlled by the amino acid content of the protein. Dragline silk, for example, is rich in analine. The effect of glycine and analine amino acid content affects SF crystallinity and resulting properties. Shear and elongation stress also controls conformation, and crystallinity. Silk can reach a strength to weight ratio five times that of steel and three times that of kevlar [50].

Crystalline Silk Fibroin

The high glycine content of SF (see Figure 1.2) allows for tight, and stable packing of antiparallel β-sheet crystallites of SF. These are associated with the mechanical strength of silk [1]. In its native state *Bombyx Mori* SF has a very complex structure with differing amino acid sequences promoting high and low order structures [51]. This typically consists of $56 \pm 5\%$ β-sheet crystallites and $13 \pm 5\%$ α helix conformations with the remaining molecules disordered [52]. SF can form silk I, II, or III. Silk I has an α-helix or zigzag spatial conformation and is metastable. It is relatively soluble and often exists in phases within amorphous or solvated regions [1]. Silk II is the less soluble, stable β-sheet crystal structure, which is a monoclinic system. Silk III is an unstable polymorph only seen at air-water interfaces in regenerated silk [13]. High silk II content is often associated with preferable material properties like strength, and toughness. An example of the complex hierachical structure of a SF microfibril can be seen in Figure 1.9 with the behaviour of the heavy and light chains also indicated.

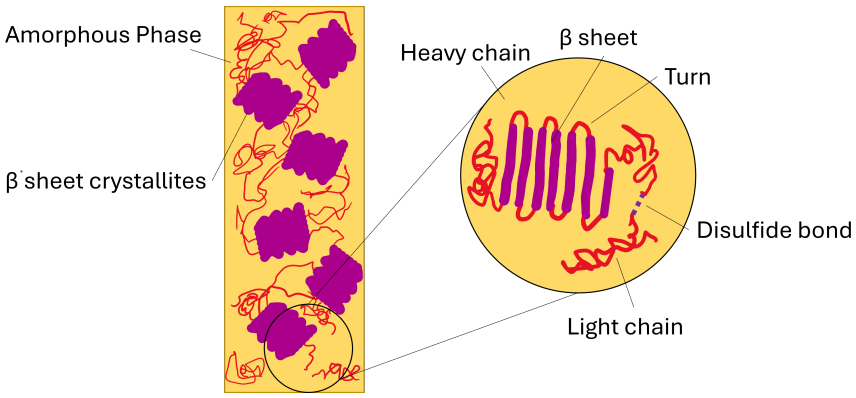

Figure 1.9: Illustration showing hierarchical crystalline structures present in SF microfibrils with the structure of the SF Heavy/Light chain dimer also shown. The cylindric rods represent the highly organized β-sheet crystalline domains of the Heavy chain connected by short linkers.

Dissolution of Silk Fibroin

Silk is seen to have similar dissolution mechanics to cellulose but is often less studied than other equivalent biopolymers [1]. As with cellulose, SF has poor sol-

ubility in many common solvents due to large numbers of inter and intramolecular bonds in the supramolecular structure [52]. The basic requirement of a solvent to solvate SF is to be able to convert the polymer from crystalline form into a fully solvated form surrounded by solvent molecules.

SF is seen to be soluble in some aqueous and organic salt solutions, harsh solvents, and ILs. Despite this the DP can degrade heavily in traditional solvents, while degradation in IL is dependent on temperature and dissolution time [1, 49]. Dissolution of silk fibroin in aqueous solutions of LiBr, $CaCl_2$, and $Ca(NO3)_2$ has been reported to degrade heavy chain fragments from 390-370 to 20-300 kDa. Even in the mildest conditions for dissolution in LiBr intact heavy chain fragments were not detected by electrophoresis [49]. This could also be related to the harsh conditions for removing sericin in many studies, often washing in Na_2CO_3 solutions [49].

The energies of these solvations can be quantitatively estimated using calorimetric parameters and dividing the enthalpy of solution into its components:

$$\Delta H_{\text{dis}} = \Delta H_{\text{s-s}} + \Delta H_{\text{p-p}} + \Delta H_{\text{p-s}} + \Delta H_{\text{dil}} \tag{1.1}$$

where $\Delta H_{\text{s-s}}$ is the endothermic effect of solvent-solvent bond breaking, $\Delta H_{\text{p-p}}$ is the endothermic effect of polymer-polymer bond breaking (associated with crystal structure decomposition), $\Delta H_{\text{p-s}}$ is the exothermic effect of polymer solvation, and ΔH_{dil} is the enthalpy of dilution [52]. Using this, Sashina *et al.* found exothermic dissolution for silk films and fibres in BmimCl and BmimAc. The less ordered film was seen to be more exothermic as expected and BmimAc had more favourable solvent-polymer interactions then other ILs [52].

When in non-solvating liquids silk can swell 30-40 volume % with 2/3 of absorbed solvent retained in the amorphous region [48]. The complex multi-component nature of silk and cellulose fibres can cause variation in dissolution mechanics. Non-uniform diameters and shapes can unevenly disperse the solvent and cause inconsistent dissolution. Variation in composition from sericin to SF or cellulose to lignin and hemicellulose across a sample gives inhomogeneous dissolution behaviours. This causes large void formation that can be resistant

even to compression during formation [53]. Understanding of these macroscopic behaviours is essential to the application of these materials.

After dissolution SF commonly exists as random coils or α-helices which can then coagulate into insoluble aggregates [21]. The conformation of silk is greatly affected by solvent type, due to differing interactions with the amino acid groups. In non-polar solvents hydrophobic fragments are better solvated which encourages the formation of the α-helix structure by hydrogen bonding. In polar solvents hydrogen bonds are instead attacked and transition to β-sheets is promoted [48].

1.3 Solvents

The relationship between solvent system and material components is both complex and key to determining and predicting material properties. Differing solubility of components in the solvent control the length scale of reinforcement and the dispersion of components and the potential degradation of those components [48, 54]. Solvents of SF and cellulose are typically identified with a good hydrogen bond destroying ability, by providing a new hydrogen bonding acceptor [55]. One example is 1-Ethyl-3-methylimidazolium acetate (EmimAc) which can be seen in Figure 1.10.

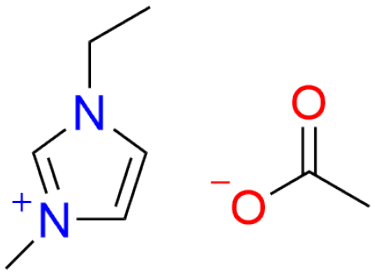

Figure 1.10: Diagram showing the structure of EmimAc, an IL commonly used for dissolution of SF and cellulose.

More volatile traditional solvents can cause protein molecular weight degradation, while ionic liquids are commonly seen to better preserve polymer quality [3, 49, 56]. In general cases, SF is seen to experience degradation above 70

°C in most solvents. In LiBr based solvent systems this can reduce the molecular weight of SF from 390 - 370,000 Da in raw material to 30,000-200,000 Da in dissolved polymer chains [48]. The solvent system will greatly affect the reaction conditions used.

Aqueous Solvents

The most common individual solvent is water. As a poor solvent for both SF and cellulose this is often used with mechanical dispersion techniques and drying to retain fibres and/or fibril structures without complete dissolution [57, 58]. Poor solvent quality for both blends can however reduce miscibility and increase interfacial tension. Zhou *et al.* noted the formation of dendritic cellulose structures above 30 % cellulose content in electrospun fibres from a water solvent. This reduced spinnability and mechanical properties though other similair double network hydrogels have shown high toughness and thermal stability [51]. Despite this, strong composites can be formed using this solvent due to retention of the raw crystal structures [58]. It has been found that crystalline cellulose is impenetrable to water while amorphous regions swell and partially dissolve [10]. Similarly, increased interactions from β-sheet stacking and blending can inhibit water absorption even for typically water soluble SF [19]. Narita *et al.* produced reasonably tough composites with tensile strengths of 249 MPa and 296 MPa for compositions of 8:2 and 1:0 cellulose:SF respectively. They also had a tensile modulus of 9.35 and 10.35 GPa for compositions of 8:2 and 1:0 cellulose:SF respectively [57]. This highlights the potential use of water a green solvent without use of high concentration salt solutions. Despite interpenetration of SF and cellulose polymer matrices being confirmed by Raman spectroscopy and SEM images, the material property increase at 9:1 cellulose:SF that was seen in studies with better solvents was not seen by Narita *et al.* [18, 57]. This may be due to limited solvation occurring and affecting the interfacial behaviour of the blends.

As dissolution mechanisms of aqueous systems often rely upon intrusion of ions into polymer bundles, before dissolution into single chain states, hydrophobicity of crystalline cellulose must be reduced. For this reason, dissolution of cellulose in aqueous systems is often performed at low temperatures when polymer chain

hydrophobicity is minimised [41]. This is because at higher temperatures more intrachain hydrogen bonding is disrupted and instead 3 dimensional hydrogen bonding networks stabilse the structure [41]. The quality of the solvent alters its mode of action. Cuissinat and Navard defined 5 modes where, if 1 is an optimal solvent and 5 is a non solvent, mode 1 is fast dissolution by disintegration into long needles and mode 5 is no dissolution or swelling [47].

Aqueous high concentration neutral salt solutions are highly used in literature [57]. Though some examples, like NaOH/Urea/Water mixtures, do not allow for solvation of cellulose or silk polymers at usefully high concentrations (10 - 15 %) which is reflected in their low usage in literature [59]. This could be the cause of the high use of IL solvents in literature which can dissolve these biopolymers at a higher concentration. Though not yet seen in SF/Cell hybrid composites, aqueous $AlCl_3/ZnCl_2$ has been seen to dissolve cellulose easily at room temperature up to 10 wt%. This can reduce polymer chain breakdown and oligomer concentration in solution, which improves polymer recyclability. Xi *et al.* found the mechanism was non-unique. Small radius, high charge ions (like Al^{3+}) first penetrate and break tight O_3H-O_5 hydrogen bonds. Larger ions (like Zn^{2+}) ions then enter to break more hydrogen bonds and trigger diffusion and dissolution [34]. Binary aqueous solvent systems remain underexplored so could be a future tool for improving non-destructive dissolution of biopolymers.

Ionic Liquids

A potential future sustainable solvent class is thought to be ionic liquids (IL). These are salts that melt below 100 °C. Typically, these have a heterocyclic, non-hydrogen bonding, organic cation with asymmetry and 'awkward' conformations that frustrates crystallisation and reduces the T_m [36, 60, 61]. They are valued due to high dissolving ability, negligible vapour pressure, chemical and thermal stability, non-flammability, and potential recyclability but can be toxic by various mechanisms triggering membrane rupture [11, 38]. ILs allow for customisation of nucleophilicity and ability to break hydrogen bonds via alterations to the anion or cation. EmimAc is the most commonly used cellulose solvent [11, 36]. EmimAc can dissolve up to 27 wt % cellulose at room temperature and low moisture

content [38]. The IL anion is often singly charged and small. Anions can be halogens or small carboxylates (Cl^{-1}, $[Ac]^{-1}$, $[NO_3]^{-1}$) which allows for disruption of hydrogen bonds in crystalline domains [21]. The strong anion cation association of many ILs can cause high viscosity which can negatively affect dissolution performance [35].

Viscosity reducing polymer mobility can be combated with cosolvents or by increasing temperature [62]. Dimethyl sulphoxide (DMSO), see Figure 1.11, acts as an efficient, available, and affordable cosolvent for this purpose [23, 63, 64]. DMSO is a suitable cosolvent, as it is aprotic and highly polar and hence does not impede interactions between IL anions and cellulose [23, 64]. DMSO also offers environmentally friendly sustainability, as it is produced as a by-product from paper production [23]. It can be easily recycled and separated from polymer/solvent/DMSO mixtures by distillation [65]. Computational and experimental studies indicate that DMSO in these systems acts as an 'innocent cosolvent', defined as a cosolvent that does not affect the solvation mechanism [23, 66, 67]. Hawkins et al. showed that DMSO addition affects the rate but not the activation energy (E_a) of dissolution [23]. Similarly, Tomimatsu et al. showed that the solubility of cellulose in binary IL/DMSO mixtures is correlated with the hydrogen bond basicity β, and that β does not change with increasing the DMSO mole fraction (up to 0.9 DMSO mole fraction [64]). Also, the preferential association of DMSO around IL cations makes anions more available for dissolution in binary systems [68, 69]. Lastly, DMSO lowers viscosity and improves mass transport in systems by reducing monomeric friction coefficients in biopolymer/IL/DMSO solutions [23, 70]. Hence, the DMSO addition to IL systems can improve the total biopolymer solubility and dissolution speed. Zhao *et al.* state that similair aprotic solvents encourage IL dissociation without preferential association to cellulose hydrogen bonding sites. This provides additional anions from the IL solvent to better solvate the cellulose [71]. This could provide a good opportunity for further improving future studies by allowing solvation at lower temperatures with less reduction of the DP of the biopolymers.

Lefroy *et al.* highlight a complex relationship between cellulose content and IL type. They found an increase in viscosity and in the number of interactions between the solvent and polymer molecules with increasing concentration. This

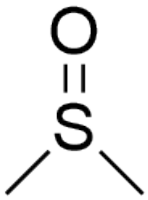

Figure 1.11: Diagram showing the molecular structure of DMSO, a cosolvent commonly used with ILs for the dissolution of biopolymers.

results in a decrease in ion mobility. This affected macroscopic viscosity more than the microscopic viscosity. This is likely due to a larger effect on the energy barrier for flow than the energy barriers for rotation and diffusion [72]. Sescousse *et al.* found Cell-BmimCl solutions have a higher intrinsic viscosity than Cell-EmimAc solutions [59]. Despite this Cl^{-1} anion IL solvents are more prevalent than those with larger anions. This could be due to the the increase in crystalline content and hence material properties as seen by Love *et al.* [13, 59]. The importance of IL cations was confirmed by an increase in $[\eta]$ for large DP cellulose (DP$= 730-830$) dissolved in EmimAc compared to large DP cellulose dissolved in BmimAc. This was not seen with lower DP cellulose (DP$= 180$) which instead indicated that anion effect was more considerable [72]. This agrees with findings by Sescousse *et al.* who state that cellulose in EmimAc had an equivalent $[\eta]$ value to cellulose in BmimAc [59, 72]. This corresponds to equivalent solvent qualities which was seen to decrease with increasing temperature [59]. Both studies utilise Avicel PH-101 MCC (quoted with DP = 180) and Lefroy *et al.* compare this with Vitacel powdered cellulose L00 (quoted with DP = 730-830) [59, 72].

Stanton *et al.* also investigated the effect of IL type on the properties of SF/cellulose composites. They studied coagulated samples and found that thermal properties were independent of cation type, but anion type altered the β-sheet configuration percentage and hence the thermal properties of the sample [73]. An increase in sample crystallinity, material strength, and thermal degradation temperature was correlated with increasing anion size with more hydrogen bonding interaction sites. SF/cellulose composites can form amorphous or semicrystalline structures with miscibility heavily dependent on solvent quality, so the range of 31.0 % to 58.9 % β-sheet crystal fraction seen when using differing IL solvents is

very significant [73]. This study contradicted the conclusions about cation and anion importance made by both Sescousse *et al.*, and Lefroy *et al.* [59, 72, 73]. This could be due to the larger range of IL solvent tested by Stanton *et al.* (six compared to two) or due to them testing during the coagulated rather than the solvated phase. This implies an important effect seen during coagulation. Differences in 'salting-out' could give rise to this effect. 'Salting out' is an effect that encourages coagulation by increasing osmotic pressure experienced by water molecules within the polymer chains. This is due to an enlarging difference in concentration as IL concentration increases in the surrounding antisolvent. This then encourages the formation of stable crystalline cellulose and SF structures [73]. Overall inconsistencies show that further investigation is required to improve the understanding of these complex interactions [13, 59, 72, 73].

1.4 Composites

Throughout history the search for material developments has continued with composite materials often being key to innovation. The term 'composite' was first used to describe the tough and durable bricks made of straw and mud by Egyptian and Mesopotamian builders in 1500 B.C. [74]. Researchers now look for new composite materials for use in everything from biomedical to aerospace industries. Composites are hybrids mixes of two or more components that maximise and combine their individual properties. They are commonly seen in high performance applications like planes, clothes, and packaging [75]. Composites can have reinforcements, binder, and filler components of differing lengthscales, from short unaligned nanofibres to complex 3D aligned fibre networks. Examples of these structures can be seen in Figure 1.12. They are commonly formed of a strengthening reinforcement and a 'gluing' element or matrix.

Natural Fibre Reinforced Composites (NFRC)

Textiles are commonly used as the supporting element of composites, in woven, braided, knitted, or non-woven forms. These reinforcements have many benefits including [75]:

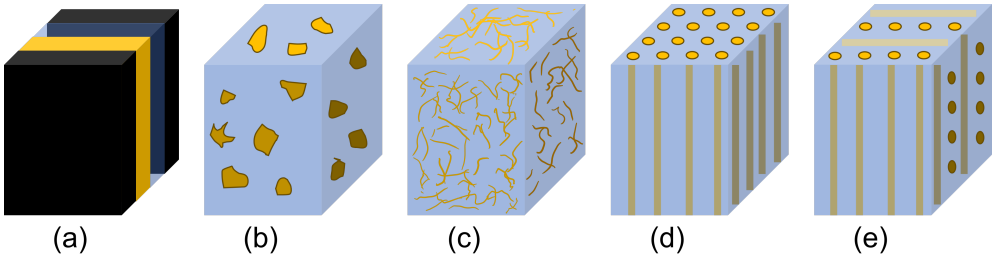

Figure 1.12: Schematic depiction of representative composites showing (a) laminated epoxy composite; (b) particulate reinforced aluminium; and textile based composites with (c) random short-fibre reinforcement; (d) aligned fibre reinforcement; and (e) oriented three dimensional reinforcement made of planar woven sheets [75, 76].

1. Controlled anisotropy with preferential loading directions
2. Good weight/strength ratio compared to other materials
3. Good integrity in extreme conditions
4. Good long term use and resistance to fatigue

Fabric strength comes from conversion of fibre strength to yarn strength to fabric strength. When load is applied friction between fibres occurs then crimp (or fibre curvature) is straightened to take initial load at lower stress [77]. Introduction of a matrix can increase tensile strength, fibre loading and affect other properties like barrier properties. Natural/biological fibres come from animals or plants and include cotton, linen, silk, wool, coir and jute [4].

ASCs and ACCs ensures superior matrix-reinforcement adhesion at interfaces and improved ease of recycling compared to traditional fibre reinforced polymer composites [20, 78, 79]. Fibre reinforced composites can be altered by changing the lengthscale and direction of reinforcement between: discontinuous, randomly oriented short fibres; linear aligned filaments; planar, two-dimensionally aligned, woven fabrics; and three dimensionally aligned, complex, woven, reinforcements [75]. Although higher level reinforcement offers improved strength, short fibre reinforcement reduces anisotropy, can have high mechanical performance, and allows for the use of waste textiles [20, 75, 80]. Hjelm *et al.* demonstrated effective use of post-consumer viscose textile waste with a thermoplastic

binder matrix to create composites with a ultimate strength of 5.4 ± 0.9 MPa and scalable application in packaging [80].

Hybrid Biopolymer Materials

Miscible polymers can also be blended in the matrix of composites [1]. Blending of different polymers allows generation of materials with specific and tunable properties. These blends can aid in material engineering by improving processability, material uniformity, or by tailoring product properties [1].

In SF/cellulose composites properties can depend on dispersion, interfaces, and properties of reinforcements and matrices [81]. Blend composition is vital to indicate matrix strength and viability so underlies most analysis with this complex and nuanced topic [3]. Noishiki *et al.* found a maximum toughness at 80 % cellulose content in solvent cast SF/MCC films [78]. Shang *et al.* coagulated fully dissolved blends of degummed silk and MCC from BmimCl and maximised thermal stability, water stability, and tensile strength at 75 wt % cellulose [19].

Blends

Combining SF and cellulose into hybrid blends offers unique compatibility and useful properties that surpasses other composite examples [2, 78, 82, 83, 84]. Inclusion of SF can improve the biocompatibility of the cellulose bioplastic and aid in biomedical applications [85]. Hybrid materials have also shown improved strain at failure and maximum stress compared to pure cellulose or SF counterparts [18, 86]. This is due to the close molecular associations of SF and cellulose as confirmed by the NMR studies of Tian *et al.* [18]. These show that homogeneous blends of SF and cellulose, as indicated by atomic force microscopy in literature, contain close molecular association between SF and cellulose molecules [18, 82, 87]. An adaptation of the proposed prominent points of hydrogen bonding are shown in Figure 1.13.

As discussed in Chapter 4, the resulting properties of the blend films can be understood with reference to double network theory. Double network materials are formed of interpenetrating polymer networks where the properties of either

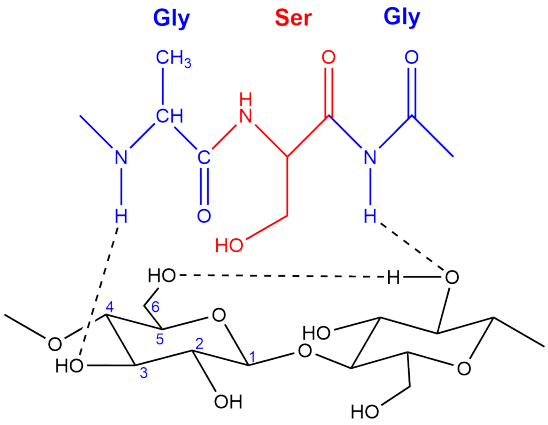

Figure 1.13: The proposed molecular interactions of the SF and cellulose chains with example amino acids adapted from work by Tian *et al.* [18].

pure network is in contrast with the other as network density, rigidity, molecular weight, or cross-linking density [88]. These materials can exhibit surprising toughness based on theorised brittle 'sacrificial bonds' failing at low strains prior to total network failure [89]. Transient networks have even allowed creation of self-healing gels and intriguing creep profiles [89].

Biocomposites

In composite preparation the resulting material properties are dependent on the solvent, polymer concentration, coagulant used, drying method, and conditions (temperature and pressure) at different stages of processing. This can affect material properties like surface roughness, opacity, tensile properties, and more [90]. This can vary even more extremely with changes of the material type produced. Throughout this thesis the term coagulation is used for the formation of solid material from solution by introduction of an antisolvent. The term regenerated is commonly used in literature but strictly refers to coagulation from a derivitizing solvent (i.e. a cellulose composite prepared by regeneration from the Viscose process) [67].

Despite it's importance many studies do not provide exhaustive descriptions of their gelation conditions and causes. Many papers exclude the rpm of stirring during dissolution, which is impactful in dissolution mechanics [19, 41]. Cho Hee

Park show the importance of this by inducing gelation in methylcellulose/SF composites from water by ceasing agitation. The rate of gelation was seen to increase with temperature as polymer mobility increased [91]. This then affected network formation as methylcellulose networks formed more quickly from the solvent due to hydrophobic methyl groups present. A SF gel then formed slowly around the methylcellulose network [91]. This technique results in methyl cellulose networks with phase seperated SF rich matrix surrounding [91]. Control of every aspect of preparation is essential in understanding the material being formed.

Temperature can induce gelation from aqueous solutions, though samples with temperature induced gelation show broader XRD peaks. This indicates less crystalline order than other gelation techniques. This is due to thermal motion increasing random association and entanglement [92]. In aqueous solvent, hydrophobic stacking of cellulose first occurs before hydrogen bond aggregation as shown in Figure 1.14 [92].

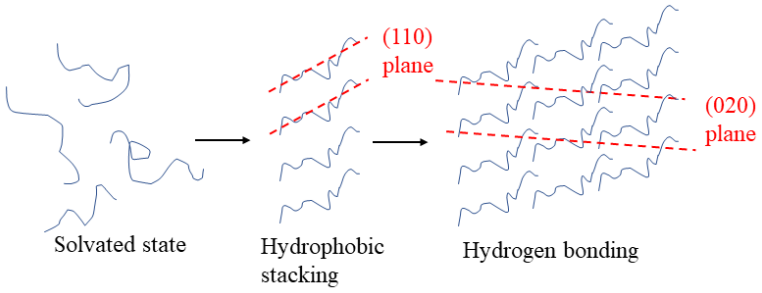

Figure 1.14: Figure indicating the mechanism for temperature induced gelation of cellulose from aqueous solution. Blue coils and lines represent cellulose polymers while red dashed lines indicate planes of crystalline stacking with Millers indices labelled [92].

A common method of composite production is by coagulation of the polymers from solution by submersion in an antisolvent or coagulant [11, 93]. This is also known as solvent exchange [94]. Coagulants halt dissolution by preferentially breaking solvent to cellulose hydrogen bonds in order to form hydrogen bonds between solvent and coagulant molecules [22]. This is prevalent in ASCs and ACCs. These self-supporting biocomposites are typically produced by two methods [53]:

- Complete dissolution of the polymer to form a solution that is applied to undissolved fibres and regenerated.
- Partial dissolution of the surface of fibres followed by regeneration to form the supporting matrix.

Of these methods, known as the one and two step method respectively, the one step method is more common due to issues in using the viscous polymer rich solution [12]. During regeneration of cellulose void formation can occur as a result of differential shrinkage between the water rich non-crystalline gel, or matrix phase, and the crystalline phase. Increased void formation correlates to a reduction in tensile strength, and is pronounced at interfaces (50-100 nm) compared to voids in the polymer matrix [45]. Mechanical strength of these materials can be affected by:

1. Compression of the sample prior to solvent extraction.
2. Differences in precipitation/regeneration/coagulation conditions including temperature, humidity, pressure, and time.
3. Differences in degree of polymerisation, morphology, or chemical composition based on polymer source [26, 45].
4. Difference in drying conditions including rate, temperature, and pressure.
5. Differences in solvation including solution wt %, solvent, aggregate size, dispersion, temperature, and solvation [93].

Huber *et al.* use a solvent infusion process which utilises a vaccum to apply constant pressure [53]. Fluctuations in applied pressure can cause ebbs and flows in solvent capillary action which results in interlaminar void formation. Constant pressure/compression provides more effective distribution and minimises voids, which improves material properties [53, 95]. Even in single component systems differential shrinkage can induce dimensional instability and internal residual stress. This is seen to be reduced by the improved interfacial bonding of the one step method in ACCs [96]. Despite these effects, in high level reinforcement

composites, the quantity of matrix volume fraction is the largest factor in optimising peel strength, and other material properties [20]. This is still very system dependent with values ranging from 20 - 60 % matrix giving optimal values in differing studies [20, 22, 81, 86].

System changes can alter crystal size and morphology which cause macroscopic changes to properties [45]. Some coagulations can occur below the melting point of the pure IL and hence must be supercooled. These must be used quickly to avoid nucleation and crystallisation [97].

Total dissolution induces a random coil/solvated conformation for SF and cellulose molecules [56, 57]. This increases the amorphous content upon coagulation. Instead samples can be prepared by using a poor solvent and mechanical dispersion techniques before drying. This is commonly performed with water as the solvent. Narita *et al.* ground purified SF (1 wt %) and cellulose nanofibers (2 wt%) in water to produce a slurry that was then mixed and dried to form composites [57]. This fibrillates both components without harsh chemicals and preserves SF β-sheet structures. This gives rise to high strength samples. The maximum tensile strength was 230, 249, and 296 MPa for 50, 80, and 100 % cellulose samples respectively. The thermal degradation peak from thermal gravimetric analysis for SF was at 313 °C compared to 270-300 °C for samples produced from concentration salt dissolution. This is due to retained β-sheet structures [57]. It may also be due to a lack of chain degradation lowering the DOP [67, 98]. It is of note that Narita *et al.* found very low strain at failure values in comparison with other studies [57, 99]. This may be due to this method not reducing interfacial tensions. The mechanical properties arise from individual fibril strengths with poor blending of biopolymers at interfaces. Luo *et al.* also note brittleness and reduced strength in fully dissolved composites in which the multiscale fibrillar network is destroyed and cannot be recovered [100]. Numerous degradation pathways also exist that can affect fully dissolved composites. These include hydrolysis or oxidation by environmental factors, or by presence of acids, oxidising agents, metals, or microorganisms. Chemical alterations, chain scissions, and rearrangements can also cause fragility and brittleness [101].

The alignment of fibres can be impactful and can be increased using extrusion or electrospinning to prepare highly oriented composite fibres [86, 102]. Liu *et*

al. used extrusion to create CNC/SF (1:19) fibres with Young's modulus, tensile strength, and breaking strain increased by 195, 160, and 130 % respectively compared to pure SF fibers [102]. Within the dispersion, CNC fibrils bonded with surrounding matrix to mimic and promote β-sheet crystallisation and increase thermal and material properties [102]. Fibres often exhibit superior toughness to films or gels due to polymer alignment [55]. Electrospinning is rarely seen in literature despite its ability to prepare nanofibres with size control from nano- to submicrometer length scales. This enables surface modification, alignment, and drug encapsulation. Electrospinning allows for preparation of materials with more continuous drug release than more conventional methods [103]. It could offer a good future route for small scale applications, but its size limits its use for larger applications.

For samples prepared by coagulation, the coagulant or coagulant composition used has a huge impact on the properties of the composite produced and is often varied in literature. The coagulant affect is dependent on its polarity and specific interactions between the solvent, polymer, and coagulant molecules [48]. In solvent exchange preparation methods methanol is typically used as the preferred coagulant to maximise material properties and SF β-sheet crystalline percentage [1]. Shu *et al.* confirmed methanol's effectiveness in producing β-sheet crystallinity in pure SF samples using molecular simulation [94]. This was in comparison to commonly used acids and water. Despite this, water was often used which shows clear potential alterations for the field. The majority of papers are also seen to use no coagulant due to the prevalence of drying and other methods. This implies the complexity and variation in inducing gelation in natural systems. For example, Lefroy *et al.* and others induce concentration and temperature dependent gelation from solution [72, 104].

Solvent interactions between the coagulant and the polymer control the crystalline polymorph due to the complex amphiphilic nature of the crystal structures in natural polymers [22, 105]. For SF in non-polar solvents hydrophobic fragments are solvated, encouraging the formation of Silk I or α-helix crystallites. Polar solvents will attack hydrogen bonds and hence encourage the formation of apolar stacked Silk II or β-sheet structures [13].

It is noted that SF solubility (in the amorphous or silk I states) in water can lead to its loss when washing or coagulating in aqueous liquids and solutions [56]. Despite this the waters ability as a plasticizer can increase polymer mobility so can increase the total β-sheet content by allowing polymer rearrangement [106]. The effect of this should be investigated further, with regards to water's extensive use.

The coagulation method also affects the material properties greatly. Zhou *et al.* found that coagulating 'gently' from a BmimCl solution in a methanol atmosphere (rather than submersion in a bath) followed by gentle drying at room temperature under vacuum produced strong films. This was due to the avoidance of crystalline 'crusts' on external surfaces and the slow process allowing extensive chain alignment and crystalline formation [99]. This produced pure cellulose, and 1:3 (SF:Cellulose) dry films with breaking stresses of 150 ± 20, and 120 ± 10 MPa respectively. These had Young's moduli of 1.8 ± 0.3, and 1.6 ± 0.4 GPa respectively and breaking strains of 38 ± 9, and 18 ± 3 % respectively [99]. Conversely, Feng *et al.* prepared strong gels via cooling LiBr solutions and argued stronger homogeneous dispersions were encouraged by rapid matrix formation. This inhibits phase separation of hydrophilic cellulose nanofibrils [107]. Feng *et al.* produced pure cellulose, and 1:3 (SF:Cellulose) dry films with breaking stresses of 110 ± 10, and 73 ± 10 MPa respectively. These had Young's moduli of 3.8 ± 0.2, and 1.9 ± 0.2 GPa respectively and breaking strains of 12 ± 2, and 9 ± 1 % respectively [106]. This controversy could arise due to the improved solvent quality of the IL compared to the LiBr solution, the material type being formed, or arise due to differences in film water content. The solvent difference or the void content inherent in gels, compared to films, are the largest probable contribution to this difference which may invalidate the sole claim of these papers of speed of gelation effecting material toughness.

Love *et al.* investigated the effect of a secondary antisolvent by varying the hydrogen peroxide content in aqueous coagulation baths. This showed an increase in crystallinity and crystallite size with increasing hydrogen peroxide content [42, 82]. This is due to alterations in crystal spacing by H_2O_2 hydrogen bonding between polymer chains during IL removal [13, 42]. They favourably hydrate the polymers, and 'salt out' the present IL molecules [13, 42, 73]. This

preferentially bonds to cellulose and SF polymers and stabilises low energy conformations. Upon drying hydrogen peroxide then forms gaseous oxygen and water molecules to collapse polmers in situ into crystalline conformations [13, 42]. As in other papers, cellulose crystallites are seen to act as nucleating or templating agents for other polymers [13, 42, 108]. These papers don't perform mechanical analyses or utilise the more effective alcohol coagulants. This could limit the effectiveness of the coagulant and hydrogen peroxide content in methanol baths should be tested in future. Blessing *et al.* continued this study to test the ionic conductivity of resulting composites and found increased ionic conductivity with more SF content, and with increasing SF β-sheet content. Additionally, in cellulose dominant blends, overall crystallinity correlated with improved ionic conductivity [82]. This could be used to produce medical batteries.

Many papers utilise a secondary washing bath of water to wash composite after coagulation [18]. This is thought to remove both remaining solvent, and antisolvent molecules to allow final drying to occur with minimally toxic chemicals. This is due to competitive interactions. The strong interactions between celllulose-EmimAc solution and water have been tracked by Kim-Anh Lee *et al.* using viscometry [109]. Strong EmimAc-water interactions are implied by an exothermic response upon water addition. With 1 wt % celullose solutions below 15 wt % water content Newtonian flow is observed and above swollen aggregates form a shear thinning suspension. This is temperature dependent due to control of preferential interactions and polymer coil size [109]. Viscosity also has complex behaviour. It decreases up to 15 wt % water due to solvent viscosity reduction and changes to polymer coil size. The intrinsic viscosity of cellulose peaks at 10 % water content due to preferential solvation occurring in local solvent compositions [109]. This correlates with water-EmimAc interactions ($\approx$ 93.64 kJ mol^{-1}) being favoured over water-water hydrogen bonding ($\approx$ 53.99 kJ mol^{-1}) due to EmimAc hygroscopicity [110]. This shows the importance of controlling water content in IL solutions.

Applications of Hybrid Biocomposites

Using blends and composite materials we are better able to produce materials for intended applications. Although fundamental research of cellulose/SF blends is

interesting due to the miscibility and complex blending behaviours [13, 87] they are often researched with intended applications in mind.

Much of the existing literature focuses on applications in biomedical fields [1, 13, 111], as SF can promote cellular adhesion and proliferation of fibroblasts and keratinocytes [101, 112, 113]. SF composites can also be biocompatible, biodegradable and non-toxic, though complex biological responses render biocompatability non-universal [2, 114]. As biological tissues are individual and unique, biomimetic scaffolds or artificial tissues must be engineered to both replicate extensive tissue properties and regulate healing phases. Artificial tissues must then imitate or trigger the correct immunoresponse signals, which has been achieved in hybrid systems [25, 115, 116, 117, 118].

Material tuning can allow for replication of highly variable native or artificial tissue mechanical (shear, tensile, or compressive) moduli [119]:

- Articular cartilage - 0.4-1.6 MPa [119]
- Native femoral artery - $\approx$ 9.0 MPa [119]
- Human medial meniscus - $\approx$ 1.0 MPa [119]
- Fixation plates - $\approx$ 700 MPa [85]
- Cancellous bone - 0.05-5 GPa [118]

SF is confirmed to promote cellular adhesion and proliferation of fibroblasts and keratinocytes [101, 112]. Another benefit for biomedical uses and tissue engineering is that materials can degrade in vivo and trigger minimal inflammatory response, while conventional alternatives require secondary surgeries[107, 120, 121, 122]. Composites have also been prepared with drug retention and release capabilities that show some promise [91].

Min Lee *et al.* tested the composites for use specifically as a fixation plate (typically 60-80 MPa tensile strength) for repositioning and fixation of fractured bones with displacement. Metal plates can cause stress shielding (a reduction in bone density due to the plate stiffness reducing typical stresses), and require post operative removal [85]. Polylactic acid, poly-glycolic acid, poly-L-lactic acid,

poly-D-lactic acid, and poly(lactic-co-glycolic acid) have all been used for resorbable fixation systems with tensile strengths of 60-80 MPa [85]. These don't require removal but have 8.6% rate of complications, including foreign body reactions, wound dehiscence, granulation tissue growth, and device exposure. Min Lee *et al.* produced SF and bacterial cellulose composite films with a tensile strength of 68.28 MPa and high flexibility, which exhibited zero complications in 15 *in vivo* experiments as fixation plates in rats. This gives *in vivo* experimental evidence of cellulose/SF blend films as effective biomedical implants with noted improvements over existing equivalents. Previous data indicates a resorption time of 2-4 years for these and equivalent materials [85].

Scaffolds of biomimetic materials are common forms of biosynergestic composites and function as host environments for cell and tissue growth and proliferation [111]. Eivazzadeh-Keihan *et al.* performed *in vivo* experiments to test $Mg(OH)_2$/SF/Carboxymethyl cellulose hydrogels as scaffolds for wound dressing [101]. Here the composites had a low hemolytic effect of 8.3 % compared to 97.5 and 1.2 % for positive and negative control samples. This indicated good biocompatability. Wounds dressed showed improved healing compared to control subjects over a 12 day test, augmented by the dressing and its high swelling capacity. This allowed absorption of exudates to provide an optimally humid healing environment [101]. This highlights the variability possible for specific medical applications with differing composite material types. Ganguly *et al.* prepared a hybrid composite scaffold of cellulose nanocrystals with an alginate-SF matrix. This was shown to function effectively *in vivo* to improve bioactivity and wound healing[123].

This differs greatly from studies intended for use as artificial cancellous bone (with compressive strength and modulus of 2-12 MPa and 0.05-5 GPa respectively), which instead use gel composites with larger voids [118]. Chen *et al.* reported an ultimate compressed strength of 7.95 $\pm$ 1.22 MPa with a compressed cellulose, n-Hydroxyapatite, and SF (8:1:1) composite aerogel [118, 124]. This compressive strength was larger than that of many other functional examples (1.14-3.57 MPa) but less than that of biodegradable plastics mentioned above (11.76 MPa) [118, 124]. These improvements are due to intercalation of the cellulose scaffold by SF. Of note is a reduced toxicity found in these samples by

biological assays in comparison with other materials, as well as a bone mimicking radial crystal conformation arising from preparation method of freeze-drying [118, 124]. SF/cellulose composites offer a great solution for bone tissue engineering in general. When preparing a composite for bone tissue engineering it must provide [25, 112, 116, 117]:

- Appropriate surface roughness
- Appropriate permeability and absorption
- Correct release behaviour
- Porosity
- Structural stability
- Appropriate mechanical strength
- Thermal stability
- Biocompatability
- Biodegradability

This complexity requires careful preparation of aero- or hydrogels to meet these requirements.

Gong *et al.* investigated phase separation and gelation at differing temperatures. They found an increase of gelation speed and phase separation with increasing temperature, and prepared blend hydrogels that gelated after 1 hr at 37 °C [125]. This was then thermo-irreversible due to high stability. Though only proposed for biomedical purposes this utilisation of thixotropy implies an injectable nature which could be utilised for insertion of the composite gel by non-invasive injection [125].

Supported nanocolloidal arrays can be prepared from hybrid blends but are rarely seen due to material weakness [108, 126]. Despite this, they could offer photonic properties that enable more varied and creative applications. Yan *et al.* produced a photonic crystal array that gives optical changes on response to

small chemical stimuli. With calibration this could easily be used as detector for volatile organic chemicals [126]. SF provided the nanocrystal detective structures while cellulose provided toughness, which was deemed wearable by virtue of being capable of folding or twisting 150 times before cracks appeared [126]. This wasn't investigated with any traditional mechanical testing, so this evidence seems unscientific and unreliable as a descriptor of material properties. These materials were sensitive to humidity, organic compounds, and water content in solvents. This is based on the bright diffractive colour based on the structure and its refractive index. This is seen to follow Bragg's law so that the maximum diffraction wavelength is:

$$\lambda_{max} = 1.633(\frac{d}{m})(\frac{D}{D_0})(n_{\text{eff}}^2 - \sin^2\theta)^{\frac{1}{2}} \tag{1.2}$$

where d is the planar spacing, m is the order of Bragg diffraction, here $m = 1$, n_{eff} is the effective refractive index of the photonic crystal at given conditions, $\frac{D}{D_0} = 1$ is the swelling ratio of the photonic crystal, θ is the angle of the incident light and the normal of the crystal surface. Interactions with SF and the analyte alter the configuration and microstructure of the crystal. This gives colour changes visible to the naked eye for tests with methanol, acetonitrile, acetone, ethanol, isopropanol, n-butanol, carbon tetrachloride, and toluene. These give maximum transmission wavelengths of 470, 595, 600, 608, 612, 618, 623, 645, 646 nm respectively [126]. This creative application shows the potential for these materials for application in numerous fields. Other non-biomedical applications for SF-cellulose hybrid materials exist, including strengthening and restoring tapestries with chemically identical biopolymer solutions[24].

1.5 Project Motivation

Prolific use of plastics is deeply ingrained in modern day culture and is essential to improving modern day life in numerous ways. However, the extensive benefits of using plastics have come at the cost of environmental damage. Plastics are largely non-biodegradable, non-renewable, and contribute to CO_2 emissions driving global warming. Plastic pollution has doubled in the last decade, and

460 million tonnes were produced in 2019 [127]. Reuse and recycling of plastics is only a partial solution to this issue. The UK recycling rate for waste from households was 44.6 % in 2023 [128]. Globally in 2019, only 9 % of plastic waste was recycled while 22 % is mismanaged, so other solutions must be found to combat this issue [129].

Petrochemical polymers in many cases can conceivably be replaced with biopolymers, which can be sourced from a number of renewable resources. In 2020, for example, 109 million tonnes of textile fibres were produced. Textile waste is an abundant waste stream with significant portions of both silk and cellulosic content [130]. As we discuss throughout this work, these materials have great promise for production of green materials.

Unlike petrochemical plastics, materials produced from biopolymers can largely be enzymatically degraded and hence more easily reused within the natural environment [131, 132]. As it is impossible to avoid material entry into the environment by littering, chipping, and other mechanisms, this degradation must be considered in evaluating materials for use. Often, material choice is driven primarily by metrics of performance and cost with sustainability becoming a luxury commodity for consumers who can afford inferior materials or more direct cost increases. It is a societal responsibility to create materials with tunable life spans which can meet consumer needs without contributing to permanent environmental damage. Although the quantity of available textile waste may not address this entire issue specific properties of both hybrid and reinforced materials discussed in this thesis indicate fruitful use in specific applications. For example, significant interest has been show in the automotive industry for interior panelling with these materials.

It is hoped that this work will help contribute to the field of sustainable materials by blending biopolymers to provide biological materials with potential enhancements to material strength, stiffness, hydrophobicity, processabilty, and biocompatibility. Furthermore, we test the opimisation of materials by inclusion of reinforcing fibres with local hierarchical alignment. We hope this will elucidate the first steps to improving self-reinforcing biocomposites with hybrid biopolymer blends, and in turn direct future research and application of these materials in a myriad of uses. In the future we can hope to replicate the quality achieved

by the complex hierarchical structures of natural materials in a sustainable and economic manner.

1.6 Thesis Overview

In this project, we intend to investigate both the matrix behaviour at a molecular level and the material properties at the macroscopic scale. Then by preparing films to characterise and understand the molecular interactions between silk fibroin (SF) and cellulose molecules and crystals in the solid state. Composites will then be prepared to understand the material applications of these matrices in composites. The structure for the experimental portion of this thesis is as follows:

- **Chapter 2** describes the experimental methods used to characterize, analyse, and understand materials in this research.
- **Chapter 3** discusses the dissolution of cellulose and SF in the chosen solvent system of EmimAc and DMSO, to direct understanding of processing of the biopolymers. The solvent composition is first varied to establish an optimum, before the weight percentage is varied to test saturation concentration. Polarized optical microscopy is utilised to establish the presence or lack of undissolved biopolymer contents, and dissolution behaviour is probed with rheology and nuclear magnetic resonance (NMR).
- **Chapter 4** discusses the interactions of SF and cellulose polymers in solid materials. We investigate the behaviours of fully dissolved and coagulated hybrid films at various compositions and characterise the system with X-ray diffraction (XRD), dynamic mechanical thermal, thermogravimetric, and mechanical analyses.
- **Chapter 5** discusses the application of polymer blends as matrices in reinforced biocomposites with short fibre reinforcements. The composites are characterized using XRD, density analysis, tensile testing, optical microscopy, scanning electron microscopy (SEM), and acoustic insulation analysis.

- **Chapter 6** summarises the core findings of each chapter and comments on possible future research and applications of the materials.

Chapter 2

Experimental Methods

The emphasis of this study was to best characterise hybrid biopolymer blend systems and, to that end, numerous characterisation techniques were utilised. This chapter aims to provide the required background to understand the techniques used and evaluate the findings of the project in a suitable context. Generally, and for each technique, we will establish broad principles used and also specific technical details to allow for the reproduction and development of the studies described. Due to the broad nature of characterisation possible, some techniques have been used more sparingly to provide brief insight into certain behaviours or applications dependent on the material in question. Accordingly, the depth of background given for each technique varies with it's importance throughout this project, with mechanical testing ultimately driving the central understanding of material behaviours for the materials.

2.1 Materials

This work studies the behaviours of hybrid blends from dissolution, to non-reinforced films, to isotropically reinforced short-fibre composites and iterates upon each process to further optimize the resulting material. For each chapter, the fabrication method used will be specified but, to maintain comparable results throughout, all sample preparation was performed with the following materials:

- **Silk Fibroin for dissolved content:** Degummed *Bombyx mori* silk thread

was purchased online (mulberry undyed spun silk from Empress Mills, U.K.) After dissolution this silk is referred to as SF, as it comprises of mostly SF.

- **Cellulose for dissolved content:** Microcrystalline cellulose with an approximate 50 μm particle size was purchased online (Avicell PH-101 Microcrystalline cellulose from New York, U.S.A.)

- **The IL for dissolution:** 1-ethyl-3-methylimidazolium acetate (EmimAc), was purchased from Proionic (Raaba-Grambach, Austria), with a purity of 97%.

- **The cosolvent used for dissolution:** Dimethyl Sulfoxide (DMSO) was purchased from Sigma-Aldrich (Devon, U.K.), with a purity of 99.9%.

- **The antisolvent for sample coagulation:** Methanol was purchased from Fisher Scientific (Loughborough, United Kingdom), with purity of 98 %.

- **Cellulosic short fibres for reinforcement in composites:** CD60 milled cotton flock was purchased from Goonvean (Devon, United Kingdom.)

- **Silk short fibres for reinforcement in composites:** CMS60 milled silk fibre was purchased from Goonvean (Devon, United Kingdom.)

All materials were stored under dry conditions. In addition, EmimAc, silk, and cellulose sources were dried overnight at 60 °C under vacuum before use to remove the impacts of water on processing.

2.2 Macroscopic Mechanical Testing

When assessing a material for use, the bulk properties must be a primary consideration of how it will perform. In particular, mechanical performance dictates it's suitability for different applications. We can think of this as the material response to different applied forces. Force can be calculated as:

$$F = m \times a \tag{2.1}$$

where m = mass (g) and a = acceleration (m s^{-2}) . This shows us that "heavier" or more quickly accelerating objects exert more force, but doesn't explain then how a sharp knife can pierce relatively tough materials with little mass and minimal acceleration. This is due to the sharp edge applying the force over a small area, and hence applying a large *stress* where:

$$\text{stress} = \sigma = F/A \tag{2.2}$$

where F is force (N), and A is the area of impact (m^2) [133]. This allows for a better understanding of material affects when applying a force, by capturing geometry as well as force applied. This applied stress can cause deformations in the materials which can be described by the strain Normal strain, when a force acts perpendicular to an object's surface, is often denoted by epsilon, ε:

$$\text{strain} = \varepsilon = \Delta L/L \tag{2.3}$$

where L is the original sample dimension (m), and ΔL is the change in that dimension (m) [133]. This is often given as a percentage, and can be calculated in numerous different ways depending on the sample geometry. Different behaviours can be measured depending also on how stress is applied to a material. The most common example is to measure the stress while deforming the sample at a constant strain or displacement rate = $\dot{\gamma} = \dot{\varepsilon}$ to produce a graph showing stress (y axis) against strain (x axis). Another common example is a creep test, in which a constant stress is applied instantaneously and deformation over time is monitored. Inversely, in stress relaxation tests a constant strain is applied and the stress response over time is measured.

Material Behaviours

Upon application of a given stress many materials display complex material properties with viscous (or Newtonian) and/or elastic (or Hookean) properties. Elastic solids deform depending on the strain:

$$\sigma = E \times \varepsilon \tag{2.4}$$

where E is the spring constant, or elastic modulus. Viscous materials deform with stress dependent on the rate of strain:

$$\sigma = \eta \times \frac{d\gamma}{dt} = \eta \times \dot{\gamma} \tag{2.5}$$

where η is viscosity (Pa s) and t is time (s). The combination of these two behaviours is often modelled as a combination of viscous 'dashpots', and elastic 'springs'. This can give rise to complex behaviours depending on the properties of the material. This gives a measure of time-dependency to all mechanical measurements of real-world materials that demonstrate viscoelasticity.

We can then consider a typical tensile test as performed in our research, at a constant displacement rate. Stress and strain for extensional testing are defined by Eq. 2.2 and Eq. 2.3 respectively, where A is the cross-sectional area of the sample (m^2) and L is the initial length (m). Samples were initially cut into a dumbbell shape then extended uniaxially between two clamps at a constant displacement rate as shown in Figure 2.1. Dumbbell shapes were used to minimise the impact of clamping forces, reduce the possibility of slipping, and ensure sample failure occurred in the tested central region. The force and extension was measured, and converted to stress and strain with initial measurements of sample width, sample depth, and clamp separation.

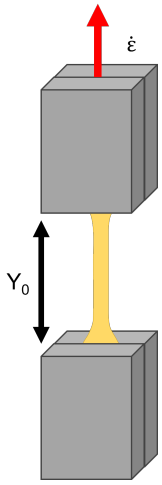

Figure 2.1: Example schematic of a tensile test performed on a given dumbbell sample.

An annotated example of the stress/strain graph produced from this data can be seen in Figure 2.2. As is typical of a polymeric material, both elastic and viscous behaviour can be seen.

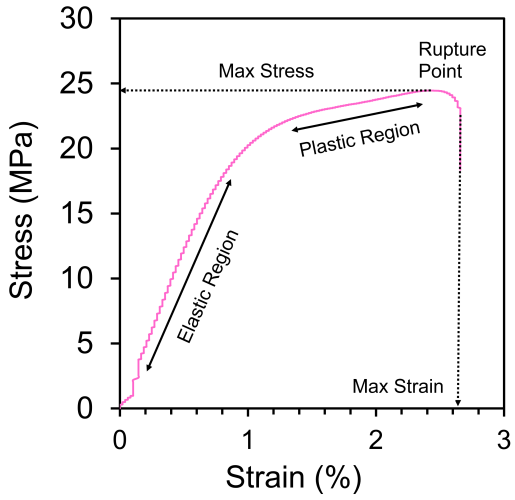

Figure 2.2: Example stress/strain graph for a tensile test of a SF/cellulose film. Annotations indicating elastic and plastic regions, and three key metrics measured have been included. The area under the curve is proportional to the energy needed to break the sample.

Figure 2.2 shows an example of a polymer film tested at a displacement rate of 5 mm/min. Labelled in the diagram are examples of key metrics and regions corresponding to different mechanical behaviours:

- In the **elastic region** the material obeys Hookean laws described in Eq. 2.4 as intermolecular bonds are reversibly stretched. Elastic deformation is characterised by reversibility, as the polymer network can recover to it's original shape if stress is removed. The stress here is proportional to strain in the sample, and the average gradient can be calculated to describe the **Young's Modulus**. This refers specifically to the modulus in extension and is equivalent to Eq. 2.4 rearranged to give:

$$Y = \frac{\sigma}{\epsilon} \tag{2.6}$$

Hence, the Young's modulus can be though of as the stress required to deform a material over a given distance. This modulus will be utilised for all extensional testing in the remainder of the thesis.

- In the **plastic region** intermolecular bond energies are overcome to encourage dislocation and movement in the polymer network. The mesomolecular structure changes as loading continues and the polymer network is rearranged. This viscous behaviour is characterised by a permanent deformation which would not recover if the sample is released, due to the dislocation of constituent polymer chains.

- Finally, samples undergo **failure**, where a maximum stress is achieved and sample components begin to fail, and then **rupture**, where the sample fractures completely and stress drops to zero. The **maximum stress** achieved indicates the sample strength and ability to be loaded before it fails. The **strain at failure** is taken to indicate the materials ductility. The energy needed to achieve this failure is proportional to the area under the curve.

The sample geometry affects stress and strain values as these are extrinsic properties (a property not inherent to the material), unlike moduli at a given temperature which is considered an intrinsic property. This can be considered as the simple relationship that Stiffness = Modulus × Geometric Factor. For example, thicker samples are perceivably 'stiffer' than thin films [134]. Some of these geometric factors are given in Table 2.1 below.

Table 2.1: A list of qualitative sample descriptions with recommended testing fixtures and the relevant geometric factors given. Note: though these rules may be helpful in special circumstances other testing fixtures may be required [133].z_s, x_s, and y_s are the dimensions for rectangular samples, r_s is the radius for samples with a circular cross section, and θ is the cone angle in a cone-plate fixture.

Sample Description	**Testing Fixture**	**Geometric Factor**
Very Hard or Stiff Gel	3-pt Bending	(bar) $4z_s y_s^3/x_s^3$
Pliable or Soft Gel	3-pt Bending	-
	Dual Cantilever	$16z_s y_s^3/x_s^3$
Film or Fiber	Extension	$z_s x_s/y_s$
Fluid or Suspension	Parallel Plates	$2\pi r_s^2/y_s$
(Rheology)	Cone and Plate	$2\pi r_s^3/3\theta$

If a sample is considered to be fully isotropic then small deformations in different testing modes will be comparable, but this is not the case for most samples which exhibit local or macroscopic anisotropy [135]. Hence, in this project we made extensive use of three-point bending flexural testing. This is most useful for samples which are significantly affected by clamping required to test in extension. For example, brittle films may crack from the compressive pressure required to avoid sample slippage. An example diagram of this testing mode can be seen in Figure 2.3.

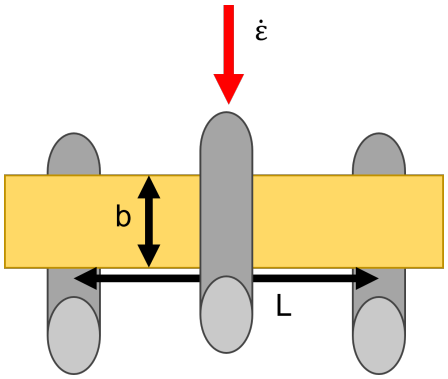

Figure 2.3: Example schematic of a flexural test performed on a given rectangular sample where depth = d, width = b, support span = L and the sample is deformed by D at a given strain rate and the load, F is measured.

The flexural strain was calculated using the equation for rectangular cross section samples in three-point bending [135]:

$$\epsilon_f = \frac{6Dd}{L^2} \tag{2.7}$$

where ϵ_f is the strain in the outer surface (m/m), D is the maximum displacement of the centre (m), d is the thickness of the samples (m), and L is the support span (m). The flexural stress was calculated using the equation [135]:

$$\sigma_f = \frac{3FL}{2bd^2} \tag{2.8}$$

where F is the load (N), and b is the width of the sample (m). Notably, the geometry can affect the stress, strain, and modulus and so the accuracy of these results is also dependent on measurements of the samples themselves. Errors in sample measurements can lead to erroneous results. Also, it should be noted that flexural testing is more dependent on geometry than extensional testing, due to squared terms, so extensional testing is more "error tolerant" [133].

When comparing flexural testing to tensile testing in composite samples it must be considered that the flexural stress and strain equation models deformation only for the maximally deformed outer layer of the sample, compared to extensional testing which models the entire cross-section. As failure occurs at the weakest point in a sample, there is less chance of failure/crack propagation in flexural tests where the surface shows no defects [135]. Compressive resistance of polymeric materials can increase calculated stress values for flexural testing due to contributions from the internal stresses on the internal bending edge [133]. This must be considered when evaluating mechanical performance in different modes. One must also consider behaviours at different rates of applied stress as this can affect the contributions from viscous and elastic behaviours.

Application and Response to Static Stress/Strain

In general, the strength tests described so far only measure short term behaviours. The subjective concept of 'toughness' and other properties are themselves functions of numerous variables related to material and testing conditions [136]. To

probe polymer relaxation and the fundamental material behaviours over a long period a static test is used. Here we can apply a set stress or strain and measure the material response. These not only provide basic information about the polymeric material but indicate the material response under an approximation of real world use. Long-term response can have a huge impact on performance and significant creep is seen in many polymeric materials, like natural actin filaments [137, 138, 139].

As discussed in Section 2.2, springs and dashpots can be used to model and visualise viscoelastic behaviours in creep with some success. Simple models include the Maxwell model (spring and dashpot in series), which models immediate stress reduction when strain is removed, and the Voigt-Kelvin model (spring and dashpot in parallel), which deforms after strain is removed but lacks the instantaneous response from some samples [133]. A four-element model is often seen as an acceptable comprise between accuracy and complexity as visualised in Figure 2.4.

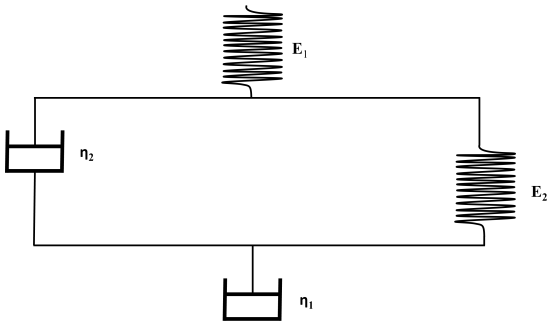

Figure 2.4: Four element model for approximating creep-recovery response with dashpot/spring models [133, 140].

Molecularly, we can consider dashpots as the resistance of the chains to uncoiling. The springs can be considered as a representation of the thermal vibration of chain segments seeking the lowest energy arrangement. The overall deformation can then be modelled as [133]:

$$\epsilon(f) = (\frac{\sigma_0}{E_1}) + (\frac{\sigma_0}{\eta_1}) + (\frac{\sigma_0}{E_2})(e^{(\frac{-tE_2}{\eta_2})}) \tag{2.9}$$

where σ_0 is the applied stress, E is the elastic constant, η is the viscous constant, and $\frac{\eta_2}{E_2}$ is the relaxation time of the polymer. Efforts have been made to tie additional elements in this model to real world components, though the veracity of this has been questioned. It may be of more value to provide this modelling as a complement to bulk measurements [140]. To that effect we performed creep tests and derived the max strain and irrecoverable strain for each cycle as indicated in Figure 2.5.

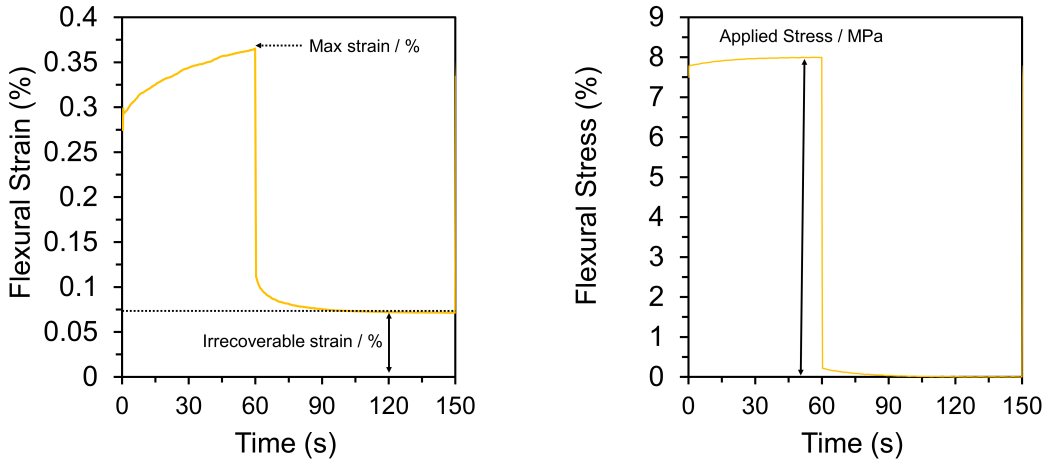

(a) (b)

Figure 2.5: Creep test diagrams indicating example analysed data taken from a measurement cycle of a polymer film for both (a) the flexural strain, and (b) the flexural stress. Indications are included for the irrecoverable strain, and the maximum strain in creep tests for samples held at 8 MPa.

From Figure 2.5, the irrecoverable strain indicates the viscous contribution to polymer behaviour while the maximum strain captures contributions from viscous and elastic deformation during each cycle. Typical creep can be described by three stages: primary creep represents a region of rapid deformation and transient creep contributions; secondary creep has a near constant gradient ; lastly, tertiary creep is also rapid deformation due to necking and reduction of the sample cross section before fracture [141]. Mechanisms of the creep deformation can be extremely varied from translational network relaxation, to elastic responses associated with the entanglement and elongation of molecular chains [137, 142]. Similarly, by

applying static step strain to a sample the stress relaxation behaviours can be probed as shown in Figure 2.6.

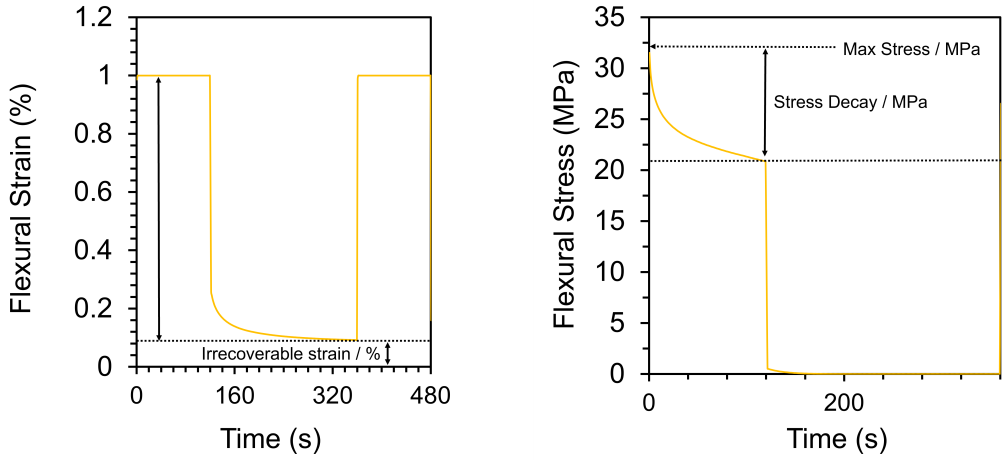

(a) (b)

Figure 2.6: Stress relaxation diagrams indicating the analysed data taken from a measurement cycle of a polymer film for both (a) the flexural strain, and (b) the flexural stress. To note, the irrecoverable strain is taken as a percentage of the total flexural strain of each cycle, at approximately 1 %.

Figure 2.6, indicates bulk measurements indicating key behaviours arising from this testing. Irrecoverable strain again indicates viscous behaviour while max stress is a measure of the materials initial resistance to deformation, or stiffness. In response to a step strain in the linear regime stress relaxations can be fit with a stretched exponential to gather data on relaxation lifetimes [139]:

$$G(t) = G_0 \exp\left(-\left(\frac{t}{\tau_M}\right)^{\beta}\right) \tag{2.10}$$

where G_0 is the plateau modulus, τ_M is the macroscopic relaxation time, and β is the stretching exponent. These values give insight into the mean relaxation time of the system and the distribution. It is still important to note that these complex systems are difficult to model with individual parameters, so could be aided in future with complementary tasts like X-ray photon correlation spectroscopy [139]. Though outside of the scope of this project, time and age dependence could be further probed by looking further into relaxation dynamics [137, 138, 143].

Application and Response to Dynamic Stress/Strain

Using Dynamic Mechanical Analysis (DMA) we can investigate major transitions as well as secondary and tertiary transitions often unidentifiable with other methods. We can also characterise bulk properties that directly affect material performance [133]. In DMA we apply a dynamic oscillatory stress and measure the material response, which allows us to alter the frequency or temperature to investigate different internal structures or polymer behaviours. The DMA can be either stress or strain controlled so can be used for both stress relaxation and creep measurements as described above. An example of a typical equipment setup is shown in Figure 2.7.

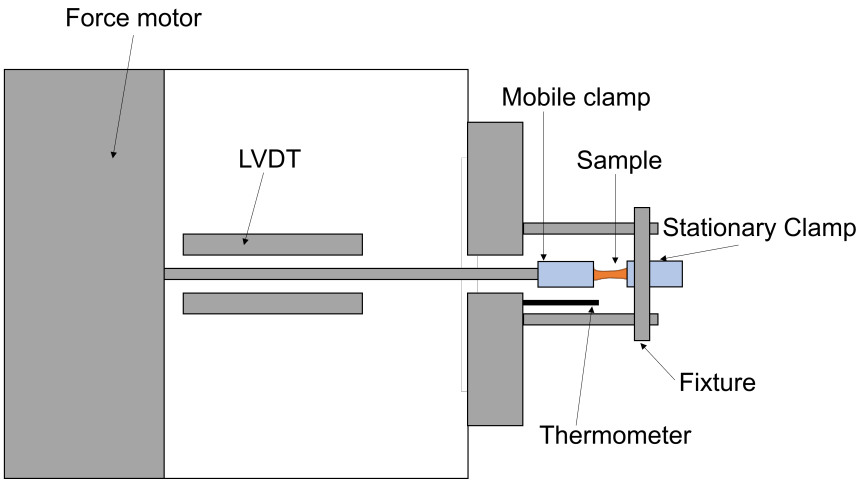

Figure 2.7: Illustration showing equipment set-up for a typical DMA machine. The Linear Variable Differential Transformer converts linear motion into an electrical signal.

Common DMA apparatus allows for different testing procedures including flexural, tensile, and compressive tests. The choice of testing geometry is affected by numerous factors but can selected based broadly on qualitative observations, given with the required geometric factor, shown in Table 2.1.

By application of sinusoidal force to deform a sample, understanding can be gleaned about the behaviour of polymeric materials. This is often applied in a sinusoidal fashion as:

$$\sigma(t) = \sigma_0 \sin \omega t \tag{2.11}$$

where σ is stress at time t, σ_0 is maximum stress, ω is the speed of oscillation, and t is the time. This results in a sinusoidal deformation if performed in the linear regime. The response can be dominated by an elastic response (like a model spring) at the Hookean limit:

$$\varepsilon(t) = \frac{\sigma_0}{E} \sin \omega t = \varepsilon_0 \sin \omega t \tag{2.12}$$

where ε is strain, ε_0 is the maximum strain, and E is the modulus. The deformation can also be dominated by viscous behaviour (like a dashpot) at the Newtonian limit:

$$\varepsilon(t) = \omega \frac{\sigma_0}{\eta} \sin(\omega t + \pi/2) = \omega \varepsilon_0 \cos(\omega t) \tag{2.13}$$

where η is the viscosity. As seen with our other testing, the actual deformation is a combination of these two responses. The difference between the applied stress and the resulting displacement can be quantified as a phase lag, β, as seen in Figure 2.8.

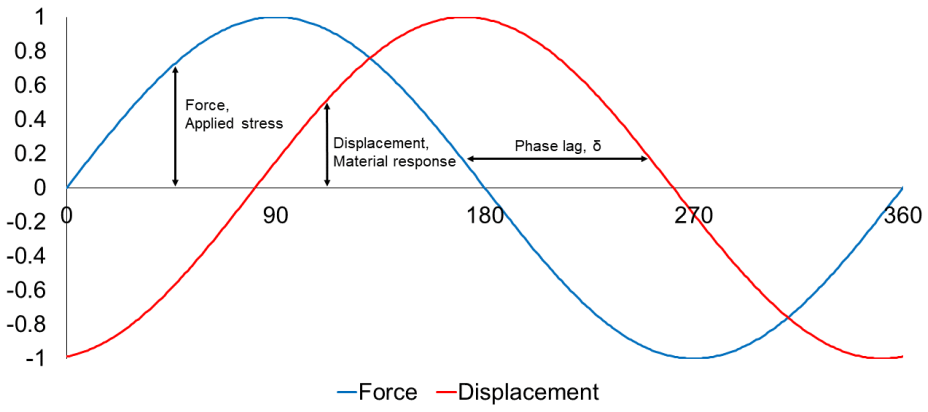

Figure 2.8: Diagram showing applied sinusoidal force and resulting sinusoidal deformation.

After applying trigonometric calculations the vector sum of the two contributions can give the overall or complex strain of the sample:

$$\varepsilon^* = \varepsilon' + i\varepsilon" \tag{2.14}$$

where ε^* is the complex strain, ε' is the elastic strain related to storage of energy, and $\varepsilon"$ is the viscous strain related to the loss of energy. Using this one measurement can be used to calculate both the elastic/Young's modulus (E') and the viscous/loss modulus ($E"$). The tangent of the phase angle is a common measure used, known as damping, which indicates how efficiently a material loses energy to molecular rearrangements and internal friction.

$$\tan\delta = E"/E' = \eta'/\eta" = \varepsilon"/\varepsilon' \tag{2.15}$$

where δ is the phase angle, η' is the energy loss contribution to viscosity, and $\eta"$ is the elastic contribution to viscosity. As $\tan\delta$ is proportional to the ratio between moduli, geometric factors cancel out, and the value is independent of geometry. This can be beneficial to provide consistent measurements between samples where geometry or force applied may vary. Variation in $\tan\delta$ with temperature can be used to glean insight into polymeric relaxations and will be the focus of our studies.

When cooling a polymeric system from melt, if complete crystallisation does not occur, an arrested amorphous solid forms known as a glass. This corresponds to the reduction in larger-scale cooperative α relaxation associated with a glass transition temperature [143]. Shorter length relaxations are labelled hierarchically as β then γ relaxations. Due to complexities in identifying relaxations in large biomolecules these will be referred to broadly as local or secondary relaxations. It is also noted that local fundamental relaxations lead hierarchically to larger α relaxations and even macroscopic material properties [134, 143]. The Crankshaft model can be used to visualise some of the motions in a model polymer chain as seen in Figure 2.9 [133]. Although the local (β and γ) relaxations show local motion it is impossible to identify specific group motions due to correlated motion [143, 144, 145, 146]. Some insight can be found for specific components

and it is shown that secondary relaxations in both silk and cellulose are associated with sorbed water molecules [146, 147, 148]. This will be discussed more in experimental chapters.

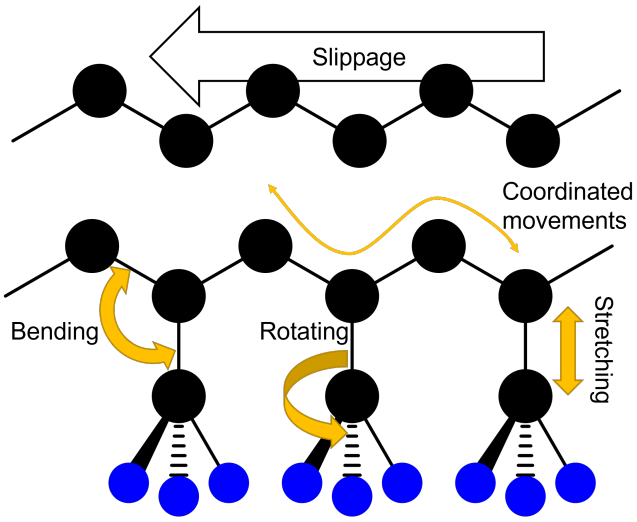

Figure 2.9: Diagram showing the Crankshaft model which highlights motions of a polymer chain associated with certain relaxations. These motions only occur when sufficient free volume or energy is provided [133].

The strength of the β transition (indicated by the amplitude of $\tan(\delta)$) can correlate well with material toughness as the molecular mobility improves energy absorption [133, 134, 149]. This was termed the "activation barrier" for deformation by Bershtein *et al.* [150]. This has been shown to be misleading if the transition does not sufficiently disperse energy or correspond to a larger scale correlate chain motion that does [133]. In this thesis, transitions and relaxations are investigated with temperature ramps at a given frequency. A visual depiction of some typical behaviours can be seen in Figure 2.10.

Challenges exist with the use of DMA to understand modified polymeric materials with fillers, modifiers, or blends. These must be understood in terms of their bulk effects, and hence any molecular insights must be taken with this in mind [134]. Polymer blends, often used to toughen otherwise brittle materials, can have interesting morphological results depending on the polymer blends molecular interactions [3, 18, 73]. Bulk behaviours are also controlled by blend behaviour. For example, a blend of two miscible homopolymers or a random

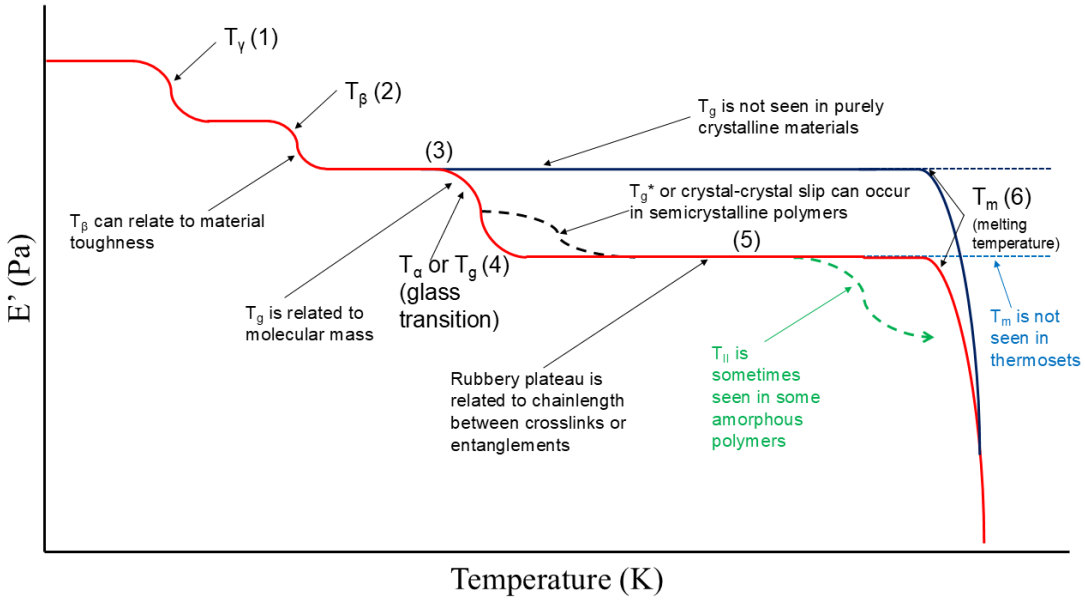

Figure 2.10: An idealized temperature ramp scan showing various labelled molecular relaxations for a polymeric material [133].

copolymer often has a single intermediate T_g. Block copolymers, graft copolymers, and immiscible blends often display the T_g of both constituents [133]. This will be of consideration in our analysis of blend materials.

Many attempts have been made to model the average T_g of binary polymer blends including the Gordon-Taylor and Couchman–Karasz equations [151]. If a mixture is assumed to be entirely homogeneous, miscible, and monodisperse it can be modelled with the widely applied Fox model:

$$\frac{1}{T_g} = \frac{x_1}{T_{g_1}} + \frac{x_2}{T_{g_2}} \tag{2.16}$$

where x_i and T_{g_i} are the molar fraction and glass transition temperature of components 1 and 2 respectively [151]. This model assumes full compatibility so fails in biopolymer blends which can show phase separation, molecular complexity, and polydispersity [1, 151]. Deviation from the modeling can instead be used to indicate the presence of these behaviours.

Cellulose and SF gels can be thought of as similar to a thermoset plastic, due to extensive hydrogen bonding and amphiphilic stacking. This inhibits molecular

Table 2.2: A list of average bond strengths and lengths for some generic intermolecular interactions. [153]

Force	**Strength / kJ mol^{-1}**	**Length / nm**
Van der Waals	0.4 - 4.0	0.3 - 0.6
Hydrogen bonding	12 - 30	0.2 - 0.3
Ionic interactions	20	0.25
Hydrophobic interactions	< 40	Varied

motion. Due to this, an estimated Tm occurs above the temperature of degradation for either polymer chain and only 'secondary' transitions can be easily accessed with DMA [1, 113]. These transitions can be considered as changes in free volume for the polymer. As the space available for the chains increases with thermal expansion larger and larger segments begin to move and give rise to thermal transitions.

When studying a polymeric material with temperature ramps or scans the temperature of a transition will be frequency dependent [133]. This can be utilised with the Arrhenius Equation to derive the activation energy of a transition, which can alternately be used to understand the scale of motion [152]. As a rule of thumb, activations for typical transitions are approximately [133]:

- $E_a(T_g) \approx 300$ - 400 kJ g^{-1}
- $E_a(\beta) \approx 20$ - 30 kJ g^{-1}
- $E_a(\gamma) \approx 3$ - 4 kJ g^{-1}

This can offer an understanding of energy barriers restricting different length-scales of motion within a material [152]. Though related, direct comparison of these values is not possible with typical bonding energies shown in Table 2.2. They can, however, be considered when visualising contributing forces to each transition.

Testing procedures

Tensile tests of the samples were carried out on an Instron 5564 universal test machine equipped with a 2 kN calibrated load cell at room temperature. Tests were performed on laser cut dumbbell shapes of type V according to ASTM D638 (or on rectangular strips of 5 mm width and of 30 mm length if films were unable to be laser cut). Samples were gripped with sandpaper at clamping points to minimise slippage. The gauge length was 25-30 mm. The cross-head speed in the direction parallel to the film is indicated in the appropriate section as this was varied to identify different behaviours. The tensile Young's modulus (in the initial linear strain range of 0.0-0.5%) was measured from the resulting stress strain curves. Flexural tests were performed on samples using the same machine equipped with a bending fixture and a 2 kN calibrated load cell. The flexural modulus at the maximum stress was calculated from the stress strain curves and was calculated at the outer surface of the test specimen at mid-span. The flexural strain was calculated using the equation for rectangular cross section samples in three-point bending [135].

Quasi-static testing (creep, and stress relaxation tests) was performed in three-point bending fixtures. These were performed on a dynamic mechanical analyser (TA Instruments DMA850.) For creep tests, 8 MPa of stress was applied as this was within the elastic region found from flexural testing for all samples in preliminary flexural tests. For stress relaxation tests 1 % flexural strain was used as the displacement held, as this was within the elastic region of all samples in flexural testing. The flexural modulus at the maximum stress was calculated from the stress strain curves and was calculated at the outer surface of the test specimen at mid-span.

All the DMTA tests were performed on a TA Instruments DMA850 under DMTA strain mode. A temperature ramp test was performed with a temperature range of -110 to 0 °C; a temperature ramp rate of 3 °C min^{-1}; the frequency was 1 Hz; and the dynamic strain kept between 0.05-0.1% depending on the optimal signal quality [144]. A preload force of 0.1 N was applied to maintain sample tension throughout oscillation. Data is reported as a function of increasing temperature due to reduced system control in descending ramp tests [144]. After

testing, peaks were analysed by least squares fitting to gaussian peaks and removal of background noise. When deforming samples, 0.5-20 microns amplitude is optimal, and this should remain in the linear regime at all test conditions for the test sample.

2.3 Rheology

Rheology is the study of the deformation and flow of materials in response to applied forces or stresses [154]. We can consider materials as defined by Eq. 2.4 and 2.5 but characterise the solution or suspension of polymers in solution as opposed to a solid material. This gives rise to technical testing differences. The liquid samples are hence characterised by shear stress using rheological parameters as defined by the two-plates model. A sample is placed between two plates separated by a gap, h. The bottom plate is stationary and across the top plate a force, F, is applied over the surface area, A. The shear stress, τ, is defined as [154]:

$$\tau = \frac{F}{A} \tag{2.17}$$

The viscosity can then be defined by rearranging Eq. 2.5 when the stress applied (σ) is the shear stress (τ). The resulting velocity, ν, of the upper plate is measured and a shear rate is defined as:

$$\dot{\gamma} = \frac{\nu}{h} \tag{2.18}$$

The flow properties of a sample can hence be characterised with rheological testing. This shear model can be seen visualised in Figure 2.11.

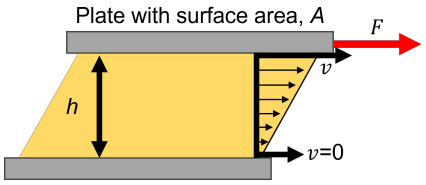

Figure 2.11: Diagram of the two plates model [154].

In this thesis rheology is used to characterise the shear rate dependent viscosity of polymer solutions to understand macromolecular solution behaviours under appropriate dissolution conditions. This can be used to highlight thixotropic and shear-rate dependent behaviours. Some examples of different flow behaviours can be seen in Figure 2.12, though further discussion can be seen in Chapter 3.

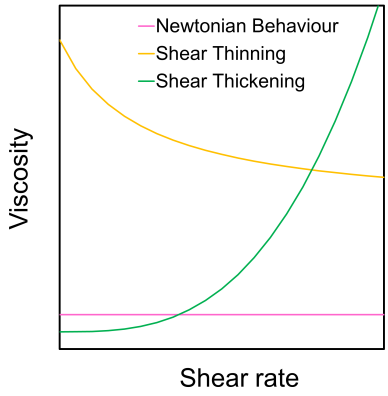

Figure 2.12: Viscosity functions indicating example behaviours of model solutions. Curves for shear thinning (where viscosity reduces during shear) and shear thickening (where viscosity increases during shear) solutions are also shown.

Testing Procedures

Rheological measurements were performed using an Anton Paar MCR302 stress-controlled rotational rheometer (Luton, United Kingdom) with 25 mm parallel plate geometry. The temperature was controlled with a P-PTD200/62/TG Peltier system (Luton, United Kingdom) and a circulating bath. Steady shear experiments were examined at a shear-rate range from 1 to 100 s^{-1} at 100 °C. This range was chosen to minimise the effects of DMSO evaporation, by reducing the run time of individual experiments. To minimise water uptake and DMSO evaporation during experiments, the edges of the sample were coated in a low-viscosity silicone oil, and a solvent trap loaded with DMSO was prepared around the sample. This minimised the effects of solvent evaporation and water evaporation on solution viscosity [109, 132]. Each sample was heated to the desired measure-

ment temperature for 1 min and then pre-sheared for 1 min at 1 s^{-1}, to ensure adequate heating throughout.

In samples with Newtonian behaviours, viscosities at 1 s^{-1} before and after testing were taken to check the effects of water uptake and evaporation. Values within the bounds of uncertainty indicated that the effect of solvent evaporation was negligible during these tests. Due to the small shear rate range tested, and Newtonian behaviours seen in the range, zero shear rate viscosities derived from a Cross equation fitting were deemed inappropriate. Instead, viscosity values were taken from an average over plateaued regions.

2.4 Nuclear Magnetic Resonance (NMR)

Nuclear Magnetic Resonance (NMR) spectroscopy is a sensitive and versatile tool capable of elucidating molecular structure, order, and dynamics. NMR is generated by the quantum spin states of the nuclei comprising the studied material and can be understood to varying levels of complexity and depth. We will briefly outline the theory required to understand typical NMR as follows.

In nuclei possessing an *odd*, mass or *odd* atomic number a quantized spin angular momentum and resulting magnetic moment can be seen. The most common examples are protons, ^{1}H, and carbon-13, ^{13}C. Though normally isotropic, these can be aligned by application of an applied magnetic field, B_0, which results in an energy difference between aligned and unaligned spins as shown in Figure 2.13a. This difference depends on the strength of the applied field which also controls the population of each state as described by a Boltzmann distribution. Once aligned, as shown in Figure 2.13b, the nuclei precess around their axis with an angular frequency, ω, proportional to the applied field [155].

After macroscopic magnetization, the vector is rotated by a radio frequency (RF) pulse through 90° into the perpendicular plane. This process can be seen in Figure 2.14a. The precession then induces a voltage in the pick-up coils which is measured as the free induction decay. This is subsequently Fourier transformed to provide a typical NMR spectrum, as shown in Figure 2.14b [158]. In practice, each nucleus does not experience the same magnetic field but a small locally induced magnetic field. This is because of electron motion inducing an opposing

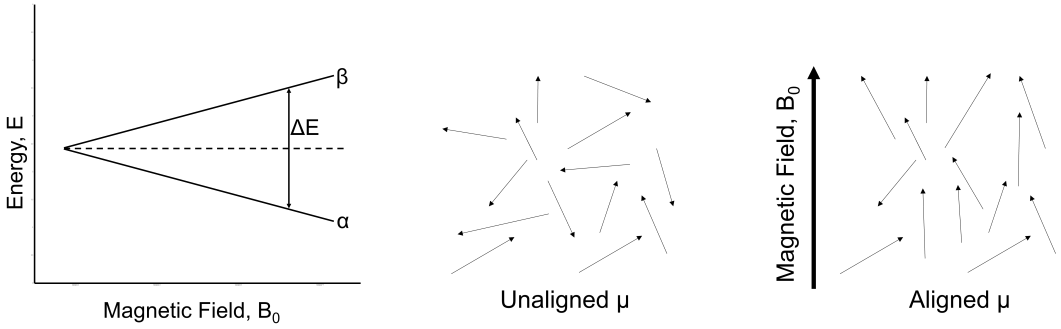

(a) (b)

Figure 2.13: Diagrams showing (a) the spin-state energy separation between the α and β spin states as a function of the strength of the applied magnetic field (B_0), and (b) net magnetisation and alignment of the magnetic moments [155, 156, 157].

magnetic field and *shielding* the nucleus. Hence, it is possible to understand the local chemical environment of a nucleus by the chemical shift relative to a reference compound. As this chemical shift is dependent on the applied field it is typical to divide it by B_0 to make it independent. Chemical shift, δ, is typically given in parts per million or ppm.

Solid state NMR can be used to investigate structure and dynamics in macromolecules in the solid form[156, 158]. However, in cellulose the featureless and broad proton signal can obscure ^{1}H spectra and increase the complexity of investigations [18]. For this reason, and due to the availability of proton signals in considered ranges, analysis of solutions can be more easily performed by investigating the solvent molecules [159, 160]. We use this well established technique to understand the dissolution process in our system as discussed by Zhang *et al.* [160, 161]. More detailed investigation can also be performed with more advanced techniques like fast-field cycling NMR or multi-dimensional NMR [72, 158]. Though not within the scope of this investigation, these could be used in future to better understand entanglement states and diffusion mechanics in hybrid solutions.

Testing Procedures

^{1}H NMR proton spectra were acquired using a Magritek Spinsolve desktop NMR spectrometer at 25 °C. Sixteen scans were taken with a 3.2 s acquisition time,

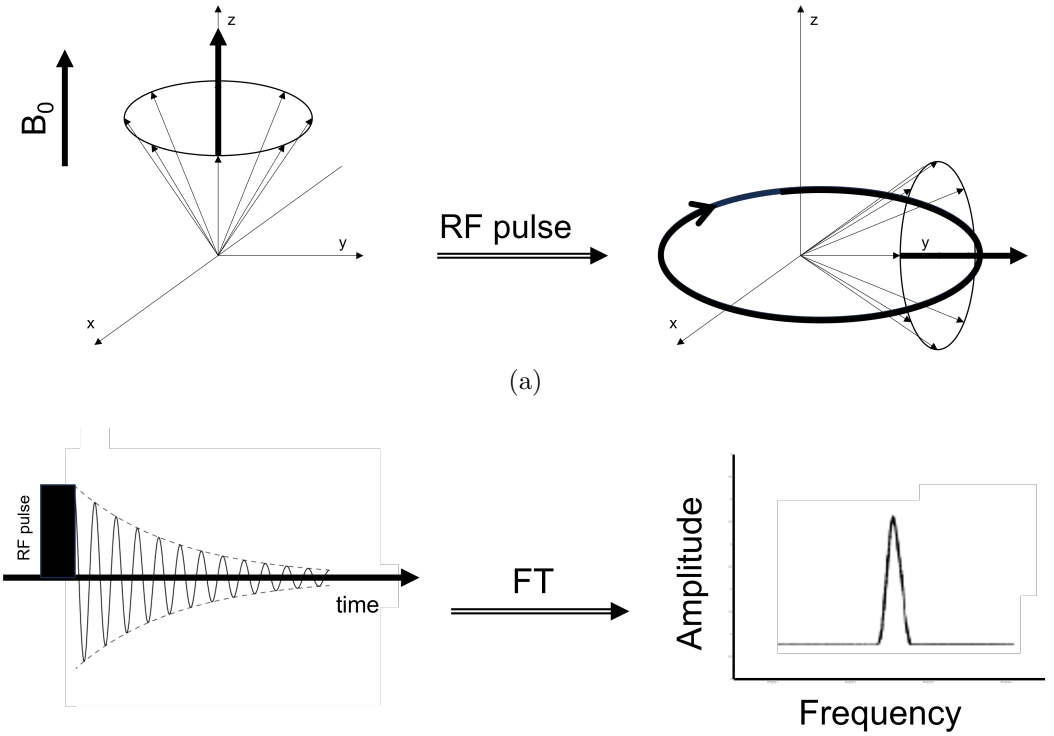

Figure 2.14: Diagrams showing (a) the principles of operating pulsed NMR with initial build-up of magnetisation and rotation through 90° by the RF pulse, and (b) the measured free induction decay NMR signal and the resulting NMR spectrum after Fourier transform [158].

a 4 s repetition time, and 90° pulse angle. In our analysis, spectral band 'e', as defined in Section 3.3 and corresponding to the EmimAc cation methyl group, was used as an internal reference signal and assumed to have a fixed chemical shift independent of the biopolymer concentration. Other ^{1}H NMR studies on imidazolium-based ILs indicate that the chemical shift of this spectral band is largely independent of extrinsic variables, such as IL concentration in water/IL solutions and cellobiose concentration when solvated in EmimAc [160, 161, 162].

2.5 Thermogravimetric analysis (TGA)

Thermogravimetric analysis (TGA) is a technique where a sample is continually weighed while heating under an inert gas atmosphere. In TGA the change in the

mass of a sample is measured as a function of time which can be used to determine the thermal stability, composition, purity, decomposition reactions, decomposition temperatures, and absorbed moisture content of the sample [163]. We will discuss dynamic TGA where the temperature increases over time as mass is recorded. This allows simultaneous analysis of volatile products and the temperature at which a change occurs. The phenomenon causing each mass change can be physical effects(gas adsorption, gas desorption, phase transitions, vaporization, sublimation), or chemical effects (decomposition, gas reactions, chemisorption). The measurement taken generates a thermogram. This gives information about sample composition distinguished by relative thermal stability. This can be seen in Figure 2.15a. A derivative weight loss curve can be used to highlight the most apparent weight loss as seen in Figure 2.15b.

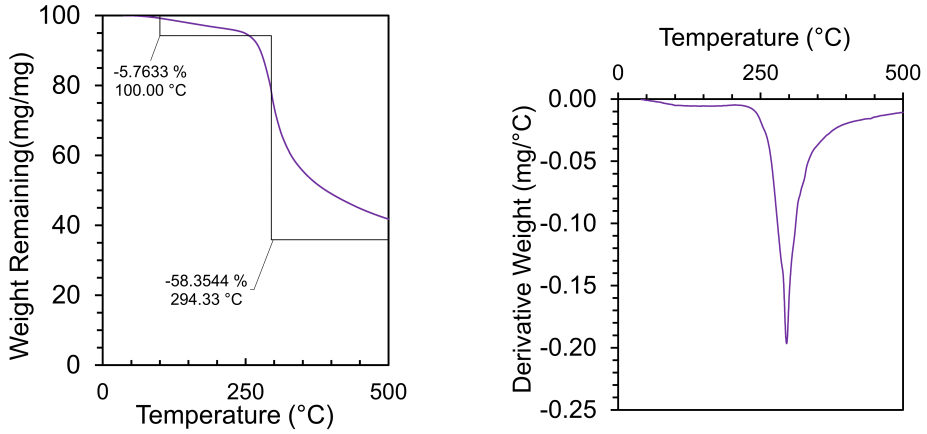

(a) (b)

Figure 2.15: Thermograms showing (a) the decay and analysis of a pure silk film indicating mass losses resulting from water desorption and decomposition of silk, and (b) the first derivative of the thermogram indicating clearly the temperature of each mass loss.

Using the model proposed by Hadadi *et al.* one can also understand the morphology of blend polymer samples studied with TGA [164]. It is proposed that interfaces decompose at lower temperatures than pure crystals based on the different energies required to overcome the adhesive forces between chains [13,

164]. This can be seen visualised in Figure 2.16, and has been noted in studies of SF/cellulose blends to occur due to partial phase separation [13, 164, 165].

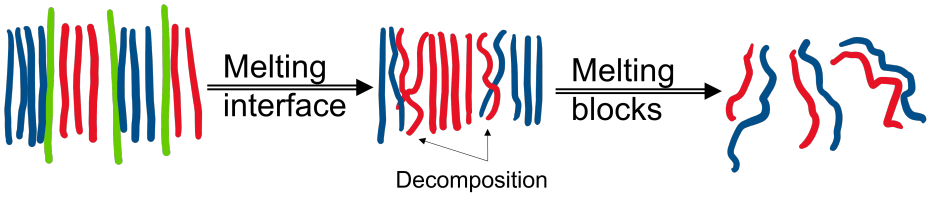

Figure 2.16: Diagram indicating the model for blend polymer materials proposed by Hadadi *et al.* In the blend, interfaces decompose first at a lower temperature and release single component crystals. After melting, the pure crystals decay at a higher temperature [164].

Testing Procedures

All TGA tests were performed on a Shimadzu TGA50. Alumina cells with 20 mg samples were used with a nitrogen purge with a flow rate of 50 ml min^{-1}. The temperature ramp rate was 10 K min^{-1} from 30.0 - 500.0 °C. Weight percentages of each film component were calculated as a percentage of the total weight tested.

2.6 X-Ray Diffraction (XRD)

X-ray diffraction (XRD) is a common technique used to track sample morphology, that can determine a sample's composition or crystalline structure. Broadly, it uses constructive and destructive interference of diffracted X-rays to ascertain distances between atomic planes. Firstly, X-ray radiation is emitted by electron bombardment of copper by thermionic emission in a vacuum. We filtered the source to only consider the Cu Kα emission. The incident beam then is scattered by present atoms and scattered from successive planes in the crystal will travel distances differing by exactly one wavelength. This constructive intereference gives rise to clear signals corresponding to plane seperations when the Bragg's law is satisfied:

$$n\lambda = 2d\sin\theta \tag{2.19}$$

where λ is the wavelength of the X-ray, d is the spacing of the crystal layers, θ is the incident angle between the ray and the scattering plane, and n is an integer. This can be seen schematically in Figure 2.17.

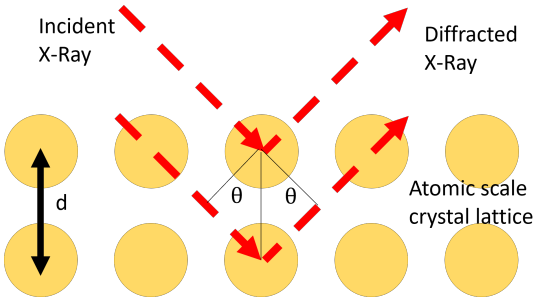

Figure 2.17: Diagram showing the concept of Bragg's law. Two X-rays with equivalent wavelengths are scattered by atoms in a crystalline solid and the second beam travels a further length of $2d\sin\theta$. Constructive interference occurs when this length is equal to an integer multiple of the wavelength of the radiation which gives rise to distinct spectra [166].

In a two dimensional scan this scatter appears as a circle which is scanned by 2θ and β angle changes as described in Figure 2.18. We can measure this in one dimensional scans across the 2θ angle, while crystalline orientation can be interpreted from the α (or azimuthal) angle also shown in Figure 2.18.

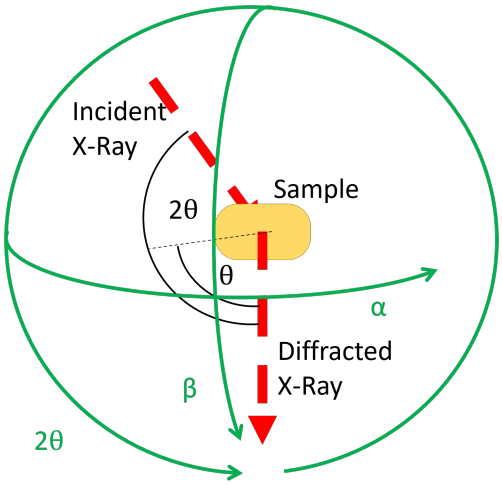

Figure 2.18: Diagram showing the angles of rotation (2θ, β, α) around a sample being scanned with XRD.

XRD was first used by Segal *et al.* to estimate total crystallinity in native cellulose. This was done empirically using the equation:

$$I_{\mathrm{cr}} = 1 - \frac{I_{\mathrm{min}}}{I_{\mathrm{max}}} \tag{2.20}$$

where I_{c} is the crystallinity of cellulose I, I_{max} is the minimum intensity at Bragg angle 18.0 °, and I_{max} at Bragg angle 22.7 ° which corresponds to the characteristic peak of cellulose I [167]. This is useful for high crystallinity samples but can be affected by contributions from other scattering peaks so is often innaccurate. A similar method can be performed at different Bragg angles to find other polymorph % crystallinities. We opted to fit sample spectra with gaussian peaks as shown to be more effective in literature [168, 169]. For all spectra, after correcting for geometric projection, the background signal was removed and gaussian peaks were fitted to the signal with a least squares method to estimate contributions from different polymorphs [168, 169]. To derive the peak position and intensity ratio of different cellulose II indices they were fit within ±2° of reference literature peaks and intensity ratios were calculated by the area of gaussian peaks [170, 171]. An amorphous peak was also included. With cellulose II peak ratios fixed, the cellulose I peaks were fit with a cotton fibre sample known to include undissolved cellulose I content to ascertain peak positions and ratios [67, 79]. With the positions and ratios fixed between all cellulose I and all cellulose II peaks, composite samples were then fit by varying the intensity of the amorphous, cellulose I, cellulose II peak sets. The areas were then compared to calculate crystallinity index of each polymorph, where the crystallinity index is calculated as the ratio between the area of the crystalline contribution and the total area of all peaks. This process can be seen in Figure 2.19.

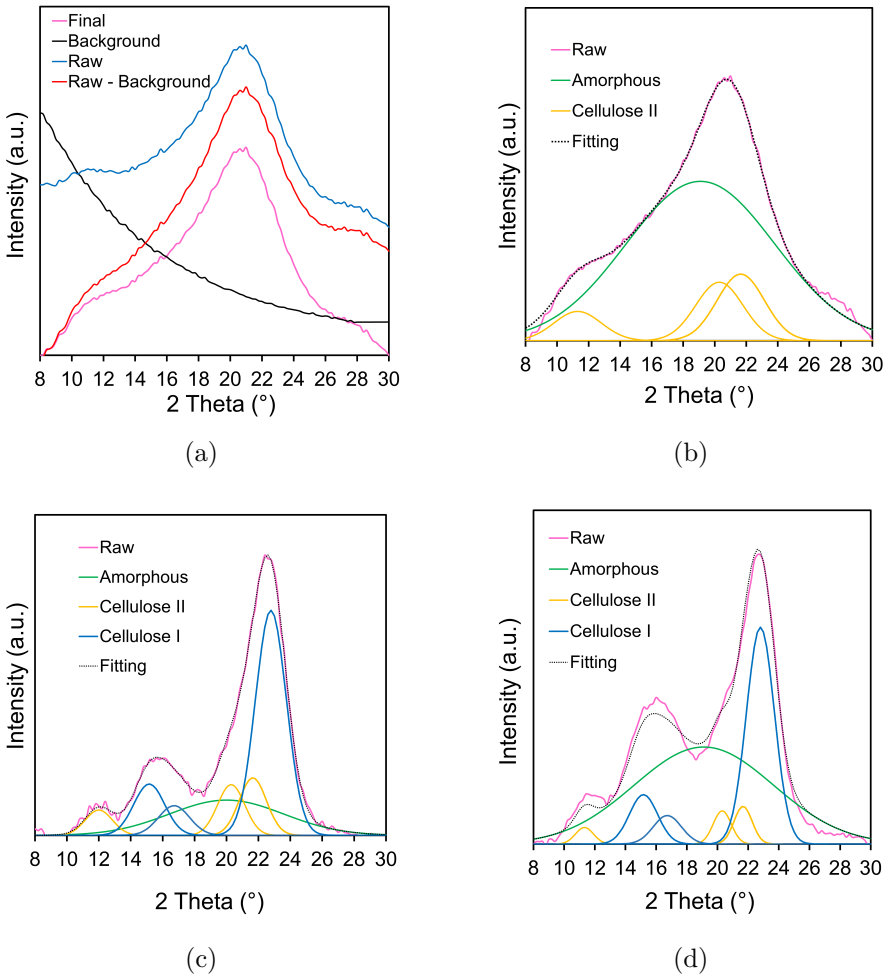

Figure 2.19: Spectra of (a) an example showing procedure for removal of both background signal and signal baseline, (b) a fully dissolved and coagulated cellulose film showing gaussian fittings of amorphous and cellulose II peaks present in signal, (c) a cotton fibre showing the gaussian fittings for amorphous, cellulose II, and cellulose I peaks, and (d) an example composite sample with fitting based on peak positions and intensity ratios derived from cellulose film and cotton fibres.

This process was also repeated with SF with the derived polymorph peaks then being used to fit an XRD spectra for a hybrid sample. This method of data acquisition was deemed unreliable as, due to signal overlap between the Cellulose II peaks, the broad amorphous peak, and the Silk I and II peaks the assignment of peaks may be misleading. This contributes to existing issues with direct eval-

uation of crystallinity from XRD intensities [166, 169]. Additionally, changes in peak broadness could result in different non-unique analysis results and hence misleading results. Different diffraction profiles may also affect peak intensities for each polymer and further mislead XRD analysis [168]. This could further contradict direct comparison of crystalline percentages from XRD intensity analysis. Fourier-transform infrared spectroscopy may offer a more reliable crystalline morphology analysis tool. This has been used in numerous examples to ascertain the ratio of Silk I to Silk II crystallinity [1, 3, 13, 169]. In this manuscript, XRD was used to establish the presence of undissolved cotton fibres in ACCs.

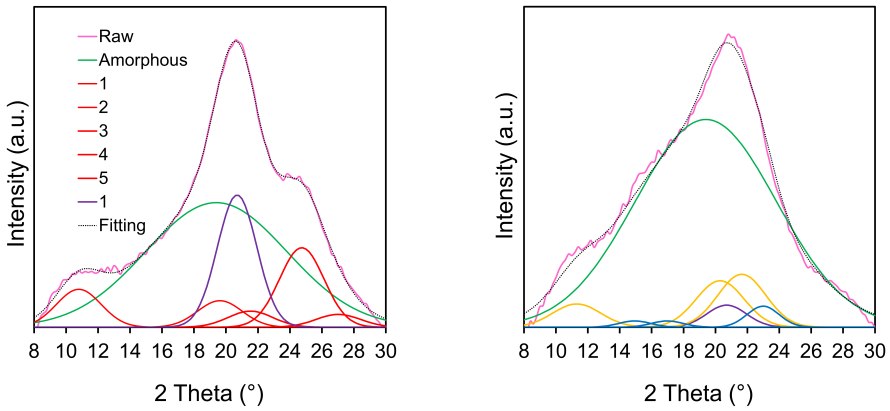

(a) (b)

Figure 2.20: Spectra of (a) a fully dissolved and coagulated SF film showing gaussian fittings of amorphous, SF I, and SF II peaks present in signal, (b) a fully dissolved and coagulated hybrid film showing gaussian fittings of amorphous, SF I, SF II, cellulose I, and cellulose II peaks present in signal. Notable overlap is noted causing this fitting to be unreliable.

Regeneration of cellulose after dissolution can be measured by monitoring transformation of cellulose I to cellulose II. This is commonly seen throughout literature. This phenomenon links decrystallisation to dissolution and crystallisation to regeneration [43]. This can be modelled as a pseudo 1^{st} order reaction where:

$$\frac{\mathrm{d}I_c}{\mathrm{d}t} = \mathrm{k}_{\mathrm{obs}} I_c \tag{2.21}$$

where I_c is the crystallinity, k_{obs} is the observed decrystallisation rate constant, and t is time. Both k_{obs} and I_c can become time-dependent if the study is non-isothermal. This can then be used with the Eyring equation to derive the Gibbs free energy, enthalpy, and entropy of decrystallisation (ΔG, ΔH, ΔS.) Wang and Deng found that ΔH and ΔS were -61.82 kJ mol^{-1} and -0.56 kJ K^{-1} mol^{-1} respectively for dissolution in an alkaline urea solution [43]. The exothermic reaction indicates the increased stability of cellulose II. The negative entropy can contribute to a positive ΔG which indicates an unfavourable reaction process. Notably, this negative entropy is likely caused by the stiff cellulose chain reducing conformational freedoms upon dissolution. The negative entropy shows why this specific solvent system is more effective at low temperatures, which reduces T in the Gibbs Free energy equation:

$$\Delta G = \Delta H - T\Delta S \tag{2.22}$$

Where T is temperature. Stanton *et al.* contradict this by reporting regeneration of cellulose I crystalline morphology in low SF content hybrid composites. They also state cellulose microfibril diameter decreases with increase of SF content [73]. Despite this, it is generally accepted that the more stable cellulose II is always formed upon regeneration, with Kroon-Batenburg *et al.* even labelling the two polymorphs native and regenerated cellulose respectively and stating the change is invariable upon regeneration [30].

XRD was also used to track the total dissolution by loss of fibre orientation as measured by an azimuthal scan. By tracking a percentage loss of peak intensity as the fibre goes from aligned to isotropic this indicates the dissolution process of an orientated fibre. This is similar to Equation 2.21 but utilising crystal orientation rather than polymorph content change.

Testing Procedures

X-ray studies of the films were performed at room temperature, using Cu Kα radiation ($\lambda = 1.54$ Å) at 40 kV and 30 mA (DRONEK 4-AXES Huber Diffractionstechnik GmbH & Co. KG, Germany). The films were mounted on a goniometer. The diffraction intensity data was collected in transmission mode. XRD data was

primarily collected with an equatorial (2θ) scan from $2\theta = 8$ to 30°, at a scanning rate of 0.02° min^{-1} and a 2θ step of 0.2°. For some samples an azimuthal (α) scan was also performed from 0 to 180° at a scanning rate of 0.02° min^{-1} and a 2θ step of 0.2°. XRD results indicated complete dissolution of cellulose was achieved in films by conversion from Cellulose I to II [67, 79].

2.7 Imaging

For qualitative understanding and visual characterization, samples were imaged both optically and with scanning electron microscopy (SEM).

Optical Microscopy (OM)

Optical microscopy is used for imaging of samples and particles above the micron scale as limited by a resolution of approximately 0.2 – 1.0 micron due to the wavelength of the illumination. In addition, imaging of particles is typically performed at low magnifications ($\leq 100\times$) to maintain a sufficient depth of focus [172]. Of particular interest in our samples was the characteristic birefringence of the material. Because of the anisotropic crystalline structure of cellulose and SF polymers, the refractive index in our samples is a direction dependent quality. This is particularly true of hierarchically aligned structures, like fibres, in which the fibre aligned refractive index is lower than that in the perpendicular direction [173]. The magnitude of the birefringence can be described by the following equation:

$$\Delta n = n \parallel - n \perp \tag{2.23}$$

where $n \parallel$ and $n \perp$ are the refractive indices in parallel and perpendicular directions to the anisotropic structures, respectively [173]. It should be noted that birefringence in these materials is the sum of contributions from orientation birefringence from chain anisotropy; glassy birefringence from deformation strain of glassy regions; and form birefringence from micro- or nanoscale patterns of the material. Overall optical birefringence is then related to retardance by the following equation [173]:

$$R = \frac{2\pi d}{\lambda}\Delta n \tag{2.24}$$

where R is retardance, d is the thickness (nm), and λ is the wavelength of light (nm). Though this can be used to find many properties, we have used it with polarizers to provide insights and identify aligned polymers. The presence of birefringence samples can be seen clearly through cross-polarized transmission microscopy and identifies undissolved content. Birefringence of a sample can depend on differences in purity, wavelength, type of processing, source, and measuring temperature [173]. Some example images of these effects can be seen in Figure 2.21. In thicker samples where transmission imaging was unclear, reflection imaging was performed.

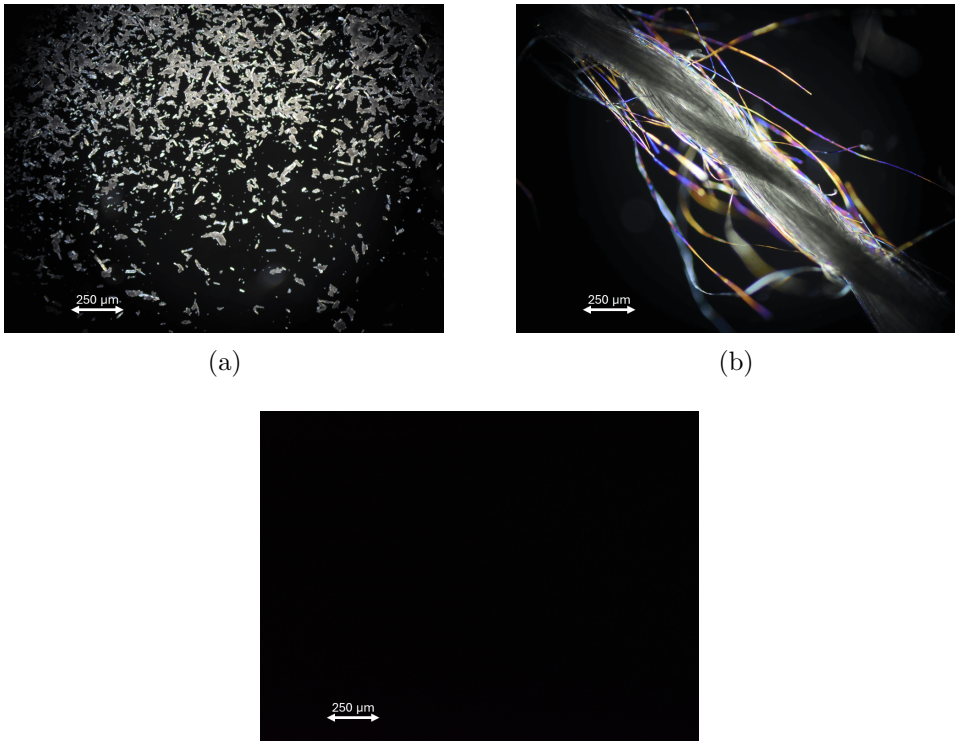

(a) (b)

(c)

Figure 2.21: Images of (a) Microcrystalline Cellulose (MCC), (b) raw silk fibres, and (c) a solution with fully dissolved polymer content after dissolution. Examples of samples with partial dissolution can be seen in Section 3.All images are taken at ×20 magnification using transmission cross-polarised light microscopy. Scale bars shown are equivalent to 250 microns.

Representative samples were taken and imaged on glass slides. Images were taken at 5-20× magnification using a Leica cross-polarised light microscope (London, United Kingdom) with a Nikon D7200 digital camera (Tokyo, Japan). Multiple images were always taken across the whole sample to ensure that the results were fully representative of bulk sample behaviour, though they show an example of a local region.

Scanning Electron Microscopy (SEM)

Insights into material behaviour can also be garnered from higher resolution imaging with SEM. This is a widely used technique to directly ascertain the mor-

phology of material samples due to it's high magnifications and large depth of field [174, 175, 176, 177]. SEM's depth of field arises from the narrow electron beam used for imaging [178]. As the technique uses an electron beam samples must be coated in a conductive material to avoid the build up of static charge, which could otherwise cause artifacts in imaging [178]. Samples must also be dried as imaging is performed under a vacuum [178]. We used this technique to better analyse the morphology of composite samples.

For SEM, cross-sectional samples taken from tensile testing were first coated with a 20nm carbon layer using Leica ACE 600 evaporative coater (Deerfield, US). Samples were then imaged using an Hitachi SU3900 SEM (Chiyoda, Japan) at 15kV accelerating voltage and under a vacuum of 50Pa. Images shown are from the ultra vacuum detector collecting secondary electrons and scale bars can be seen included in all images.

2.8 Complementary techniques

A host of techniques were used for indicative measures of performance and application of the materials discussed in this thesis. These provide valuable insight into applications and future research but are not central to the analyses discussed.

Density Analysis

In our testing we consider both the bulk density and the true density of the samples. These are distinguished as the density of the entire object, including any macroscopic pores, and the density of the material excluding any structural cavities. As the true density is measured using intrusion of nitrogen gas it can be assumed voids below the size of a single molecule are not considered (3-4 Å). By measuring both of these values we can compare molecular and structural impacts on sample density, though it is widely seen that the largest cause of density reduction is internal voiding, as evidenced by Yong *et al.* [179]. In literature, the density of silk fibroin and cellulose fibres or films is (1.3 - 1.5 g cm^{-3}) [21, 180, 181].

The bulk density of samples was calculated as the mass divided by the total volume. RS PRO digital calipers (Corby, UK) were used to measure thicknesses.

Five measurements were taken and a mean average was obtained. The cross-sectional area was obtained with ImageJ for each sample as seen in Figure 2.22. The density was then calculated by dividing the mass of each sample by its volume.

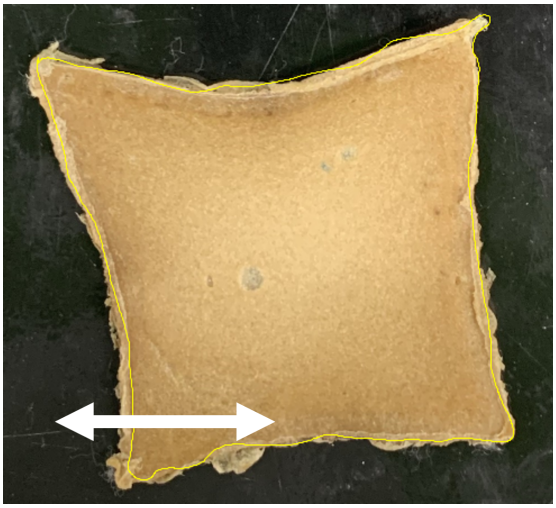

Figure 2.22: Image of example composite with yellow outline drawn during surface area calculation in ImageJ. Calibration of image for accurate sizing was performed using a rule of known length not shown in the image. Scale bar shown is equivalent to 5 cm.

Gas pycnometry was used to determine the true density of the samples. Measurements were taken with an Ultrapyc 5000 from Anton Paar (Luton, United Kingdom). Samples were pelletized into 5 mm^2 sizes before purging and equilibrating to 20 °C for 1 minutes. A flow of nitrogen at 18 psi was used on samples of approximately 10 cm^3 volume. Values were taken as an average over 5 runs in which variation percentage was lower than 0.1 %.

Water Contact Angles

Wettability of samples was measured using contact angle testing, as wetting can play an important role in biological, chemical, and physical processes. These include controlling antimicrobial properties, liquid adhesion, and interfacial attachments [182, 183, 184, 185]. The contact angle can depend on the size, pore size and roughness of the surface of the prepared material [182, 184]. It is also

noted that, though water insoluble, cellulose and silk fibroin interact with water molecules via hydrogen bonds [184, 186]. Hence, these materials absorb or desorb water from the environment to reach an equilibrium moisture content, dictated by the hydrogen bonding site accessibility within the network [147, 184]. These intermolecular interactions can dictate the wettability, and permeability of these materials. The contact angle of these materials can therefore be taken as a representation of the hydrophobicity of these samples [182, 183, 184, 187]. We will use this to rationalise some behaviours observed in our testing and the literature for different SF and cellulose materials.

Contact angles were measured by an Attension Theta Optical Tensiometer using the sessile drop method. 5 μl of deionised water was placed on the surface of the film and the mean contact angle determined by fitting the Young-Laplace model to each side-profile image of the deposited droplet using automatic baseline detection. To minimize the impact of air-gaps, a drop of water was suspended from a needle, and then the film surface was carefully brought into contact with this hanging droplet. Values reported in Section 4.3 represents the mean result derived from a minimum of five tests averaged between 30 and 60 s after droplet deposition, obtained from various locations on the film surface. Images from an example test can be seen in Figure 2.23.

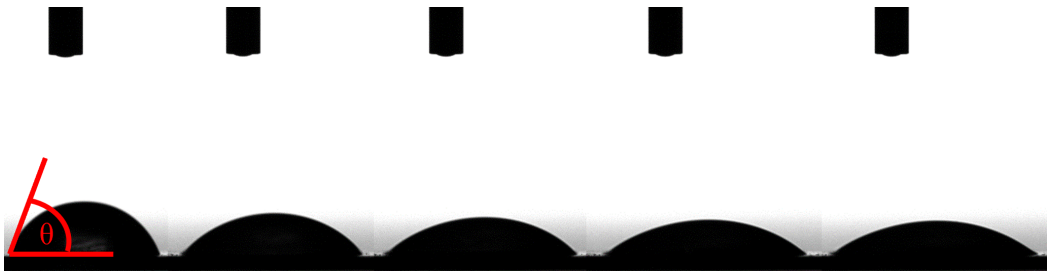

Figure 2.23: Images of the first five frames taken of contact angle testing of an example hybrid film sample. On the first frame a diagrammatic label shows the definition of contact angle used, θ. The spreading mechanism over time can be clearly seen for the water droplet on the micrometer.

Acoustic Insulation Analysis

When a sound wave impacts upon a barrier the sound energy is either reflected, transmitted, or absorbed and dissipated as other energy forms. A visualisation of this can be seen in Figure 2.24.

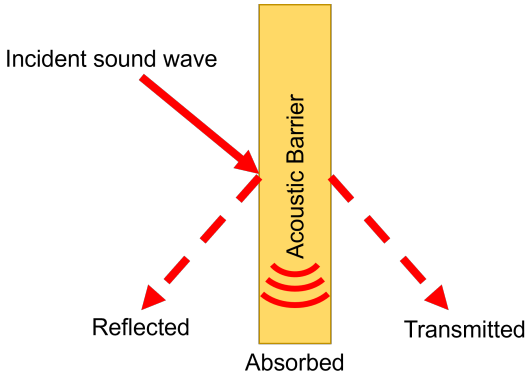

Figure 2.24: Schematic demonstrating different sound wave behaviours after impacting upon an acoustic barrier.

The acoustic performance of a material is quantified in one of two ways:

- **Sound absorption** is a measure of absorbed energy against reflected energy. It indicates how well a material stops noise reverberating within a room and can be measured as the noise reduction coefficient. This quantifies the ability of the partition, at specific mid-range frequencies (250 Hz, 500 Hz, 1000 Hz, and 2000 Hz), to reflect noise. It ranges from 0 (complete reflection) to 1 (no reflection).
- **Sound insulation** is a measure of how well sound is restricted from transmitting between two locations. It is often expressed in acoustic transmission loss.

Acoustic transmission loss (TL) in decibels (dB) can be defined as a ratio of the sound energy transmitted through a treatment versus the amount of sound energy on the incident side of the material where:

$$TL = 10 \log_{10} \frac{W_i}{W_t} \tag{2.25}$$

where W_i and W_t are the sound energy in watts of incident and and transmitted waves respectively [188].

For limp, non-rigid partitions the more mass of the wall the more sound energy required to set it in motion. Hence, the TL increases with mass increase. The mass law states that the TL increases by 6 dB when mass is doubled [189]. In a generic material with some stiffness one must consider the impacts of mass, stiffness, damping, resonance and coincidence [188]. An example of these behaviours at different frequencies can be seen in Figure 2.25.

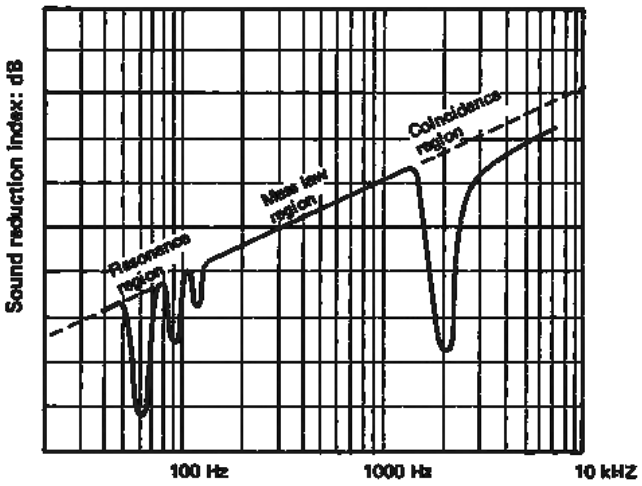

Figure 2.25: A diagram showing model acoustic transmission loss behaviours at different frequencies when impacted by resonance, coincidence, and the mass law [188].

At low frequencies, fundamental resonance impacts transmission behaviours. When the driving (incident) frequency matches the natural frequencies of the sample the system oscillates and transmits sound effectively [190]. This can be reduced with damping. Above this mass law dictates behaviour and it is said to be mass controlled [188]. Coincidence occurs when the frequency of the incident sound matches the bending wavelength of the wall. The bending wavelength refers to the wavelength of acoustic propogation through the material. When these correspond the sound energy can be efficiently transferred through the material so the TL presents a large dip at these frequencies [189].

Acoustic metamaterials are materials that offer improved performance outside the expected behaviours shown in Figure 2.25. This could include increased TL or sound absorption at low frequencies. These behaviours are dictated by geometric, structural or stiffness architectural choices and can allow targeted sound absorption and TL [191]. Some examples include cavity based, membrane-type, gradient-indexed, impedance-matched, scatterer-based, and ventilated metamaterials [191]. Dynamic microstructures, where internal variations may allow changes in response to external stimuli, can control sound wave propogation. Internal resonance can even allow an effective negative mass density and impact greatly the refraction, or reflection of incident sound waves [191, 192]. Natural fibres have been shown to contribute to these behaviours in building insulation applications [193, 194].

The sound transmission loss of normal incidence was measured using a BSWA impedance tube (Beijing, China) according to ASTM E2611-17. Tests were conducted from 1000 - 6300 Hz in a 30 mm tube (SW477). The test frequency span was 2 Hz and testing was performed at room temperature. Samples were prepared with a 30 mm diameter and care was taken to ensure the samples were snug with the interior tube surface [195].

Dealing with Uncertainties

Throughout this project standard error (SE) was used to calculate the uncertainty for each set of measurements where:

$$SE = \frac{\sigma}{\sqrt{N}} \tag{2.26}$$

where σ is the standard deviation of the sample, and N is the number of samples in the set. Unless otherwise stated, $N > 3$ for uncertainties provided. In cases where multiple samples were not possible to test instrumental uncertainties were propagated as noted in the text.

Chapter 3

Dissolution of Silk Fibroin and Cellulose in 1-ethyl-3-methylimadizolium Acetate and Dimethyl Sulphoxide

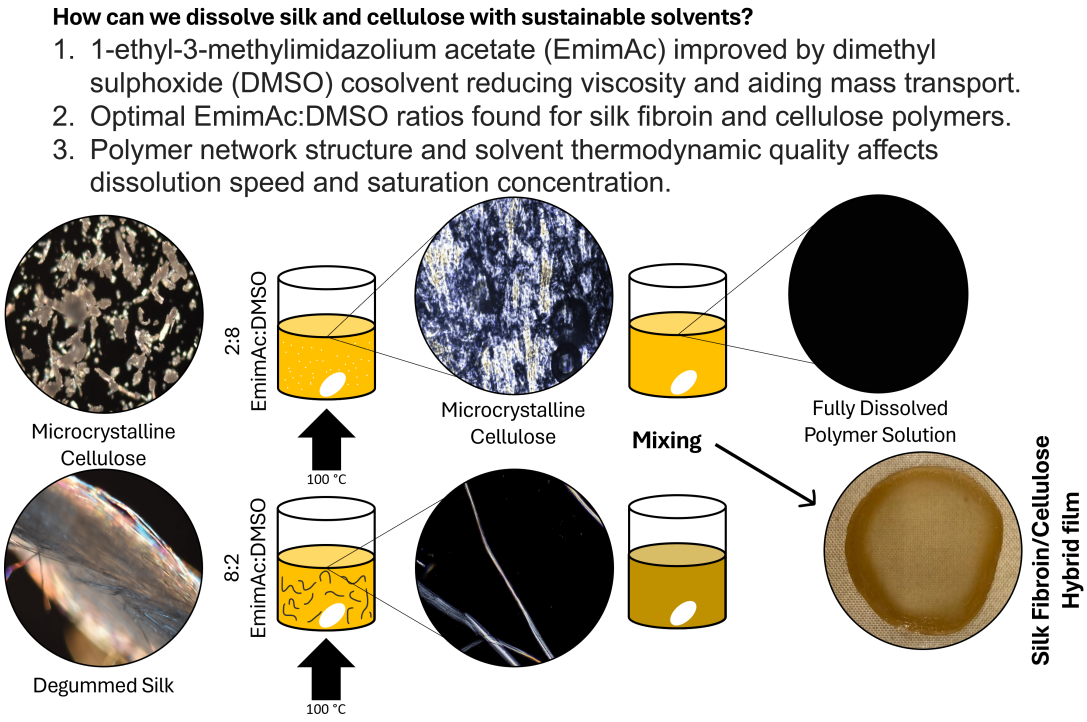

Figure 3.1: Graphical abstract indicating the study performed to understand dissolution behaviour of SF and cellulose in solvent mixtures of EmimAc and DMSO.

3.1 Introduction

Though the potential for biopolymer materials is extremely high, their widespread use is curtailed by challenges in processing them due to inherent insolubility and low degradation temperature [1]. Therefore, when considering the challenge of implementing these materials, one must first aim to understand the processing variables involved in their manufacture. This can offer energy saving, processing, and economic benefits. For example, the paper industry requires an operating temperature of around 170 °C for conversion of wood shavings to pulp [196]. Catalysing this process or improving the solvent system could reduce this required temperature. In Germany, up 75 % of industrial energy demand is from heating [197]. Also, due to the inherent impact of biopolymer source, one must optimise the dissolution procedure for any new material to maximise production and reduce degradation [64].

Despite the evidence of it's effective application, investigations into the EmimAc:DMSO solvent system in dissolution conditions for application in composites are rare [20, 23, 67]. SF and hybrid systems also remain poorly understood despite their intriguing applications [104, 198, 199]. Using solvent systems that are not optimised for a specific process can impact material results. For example, longer dissolution times at higher temperatures can incur biopolymer degradation [72]. Hence, optimising the speed and effectiveness of the dissolution process offers both greater efficiency and retained material quality.

In this chapter, the EmimAc:DMSO solvent system is tested and optimised for the dissolution of SF fibres and MCC in conditions similar to those utilised in composite preparation studies [87, 96, 99] but not yet investigated with respect to their solution behaviours. The EmimAc:DMSO ratio is systematically varied for the dissolution of SF fibres and MCC to establish an optimal solvent composition for both biopolymers. Interestingly, the optimal solvent ratio was found to differ for dissolution of MCC and SF fibres. The established optimal solutions were then tested at a range of weight percentages of the biopolymer. Polarised optical microscopy is utilised to establish the presence or lack of undissolved biopolymer contents, and the dissolution behaviour is probed with rheology and nuclear magnetic resonance (NMR). Characterisation at multiple length scales allows for the

understanding of macroscopic and molecular dissolution behaviours. Ultimately, the proposed systems are demonstrated to produce homogeneous solutions, which we apply in the later production of hybrid biopolymer films and composites.

3.2 Materials and Methods

Due to potentially complex aggregation behaviours of undissolved raw fibres, a brief preliminary investigation was performed to test dissolution behaviours of silk and cellulose sources in an example of the chosen solvent system (8:2 EmimAc:DMSO). This ratio was selected as an example of used for effective dissolution in other studies [20]. This was done with the aim of achieving dissolution to the μm lengthscale to investigate phase behaviour of the system without complex hierarchical fibre structures impacting the study.

After 48 hours it can be seen that dissolution of all flock was still not achieved for both raw silk and cotton flocks. Aggregates could be seen in solution, and no change was noted form 12 to 48 hours. Hence, images taken at 48 hr were taken to represent maximum dissolution under these conditions with these samples. This may be due to gelation occurring around fibre aggregates due to large DOP polymers present in these raw flocks. Without bleaching, mercerization, or degumming no DOP degradation had previously occurred. This causes a reduction in the entanglement concentration and increases solution viscosity at given concentrations compared to more processed fibres. Hence, for investigations into shorter lengthscales, processed cellulose sources and degummed silk fibres were prioritised.

Although comparative measurements to evaluate DOP were not taken, DOP degradation is known to occur during processing allowing easier dissolution, and reducing solution viscosity [52, 114]. Though not within the scope of this project, gel electrophoresis could be used to further characterise DOP and hence a more quantitative measure of its effects in composite behaviours in future studies [200].

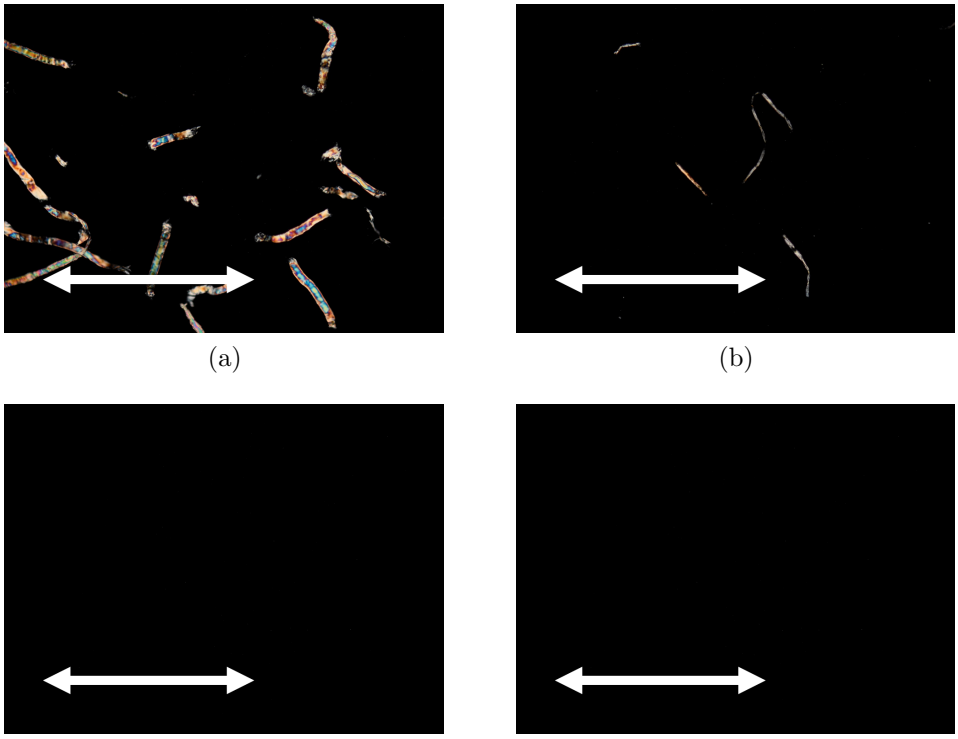

Figure 3.2: Images of (a) raw cotton fibres, (b) raw silk fibres, (c) MCC, and (d) degummed silk fibres dissolved at 100 °C for 48 hr at 200 rpm. All samples are 5 wt% of the mentioned solvate in a 8:2 EmimAc:DMSO solvent mixture. All images are taken at ×20 magnification using transmission cross-polarised light microscopy. Scale bars shown are equivalent to 1 mm.

Sample Preparation

Materials used are described in Section 2.1. Images of the degummed silk fibres and Avicell MCC can be seen in Figure 3.3.

MCC or silk fibres were weighed according to the biopolymer weight percentage of the sample, and solvents were weighed according to the target solvent composition. Polymeric solids were firstly dispersed in the relevant weight of DMSO, then stirred and preheated to 100 °C for 30 min. The relevant weight of EmimAc was preheated at 100 °C for 30 min then mixed with the dispersed solids in DMSO. Solutions were then stirred for 48 h, at 100 °C, at 200 rpm to produce pale yellow to dark amber transparent solutions. SF solutions showed a darker

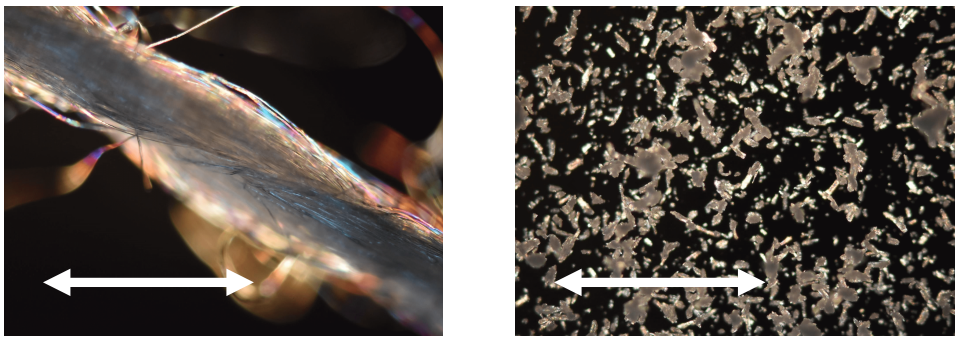

(a) (b)

Figure 3.3: Images of the (a) degummed silk fibres and (b) Avicell MCC. All images are taken at ×20 magnification using transmission cross-polarised light microscopy. Scale bars shown are equivalent to 1 mm.

colour than cellulose solutions. All dissolution was performed in a sealed atmosphere to minimise water uptake. Throughout this study, the solvent composition is referred to as the ratio of EmimAc to DMSO in the form EmimAc:DMSO. The biopolymer content is stated as a weight percentage of the total solution, for example, "10 wt% SF".

After preparation, all samples were stored in sealed vials at room temperature to prevent moisture uptake. The results of subsequent analyses were averaged over at least three measurements unless otherwise mentioned.

Sample Testing

Samples were imaged according to Section 2.7. 1 ml samples were taken during dissolution and imaged at 20 times magnification with cross-polarised microscopy. Steady shear rheological measurements were performed, as described in Section 2.3, over a shear-rate range from 1 to 100 s^{-1} at 100 °C. ^{1}H NMR proton spectra were collected as described in Section 2.4.

3.3 Results and Discussion

Effects of Binary Solvent Composition

The initial solvent composition was investigated at 10 wt% biopolymer content, as this is well below the quoted saturation values of both cellulose and SF in EmimAc at 25 wt% and 20 wt%, respectively [160, 201]. A concentration of 10 wt% was commonly used in studies and seen to produce the resulting materials of high strength [19]. It is of importance to note that achieving a maximal polymer concentration in solution was a priority due to the associated material property improvements [1]. This is due to the highly associated polymer chains promoting crystallite formation and increasing interaction density improving network strength [1].

Optical Microscopy

The birefringence of silk and cellulose biopolymers (see Figure 3.3 was used to ascertain the total dissolution of solutions by polarised light microscopy of the sample [19, 199, 202]. Polarised optical microscopy of 10 wt% solutions of cellulose in various EmimAc:DMSO ratios can be seen in Table 3.1, sampled at various times up to a maximum of 48 h.

Table 3.1: Table showing the dissolution behaviour of Avicell MCC over time (up to 48 h) at different EmimAc:DMSO solvent ratios. All images are taken at ×20 magnification using transmission cross-polarised light microscopy. Scale bars shown are equivalent to 1 mm. Table heading E:D refers to the solvent ratio between EmimAc and DMSO.

E:D	1 h	2 h	4 h	24 h	48 h
1:0	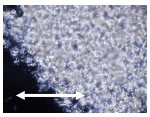	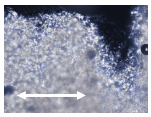	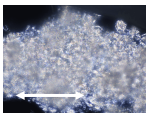	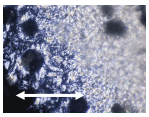	
8:2	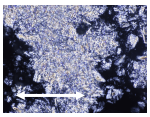	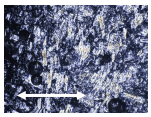	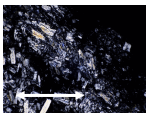		
6:4	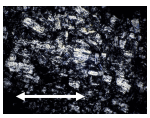	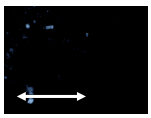	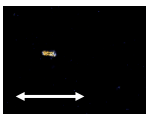		
4:6	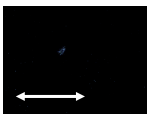	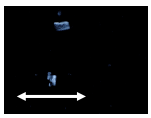			
2:8	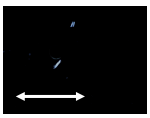				
0:1	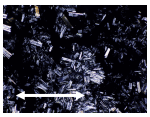	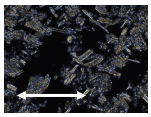	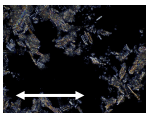	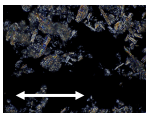	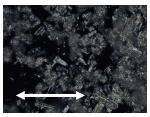

Table 3.1 indicates that the system with a 2:8 EmimAc:DMSO solvent ratio dissolved most quickly, as shown by the lack of birefringent content after two hours. This shows agreement with the studies by Ren *et al.* and Tomimatsu *et al.*, who found system optima at 0.09–0.5 and 0.2 IL mole fraction for the dissolution of MCC in EmimAc:DMSO solvent systems [63, 64]. As a control, no dissolution was seen in a 100% solution of DMSO (0:1) in Table 3.1. Next, a similar set of experiments was conducted with silk fibres. Optical microscopy of 10 wt% solutions of SF in various EmimAc:DMSO ratios can be seen in Table 3.2, sampled at various times up to a maximum of 48 hr.

Table 3.2: Table showing the dissolution behaviour of SF over time (up to 48 h) at different EmimAc:DMSO solvent ratios. All images are taken at ×20 magnification using transmission cross-polarised light microscopy. Scale bars shown are equivalent to 1 mm. Note the presence of undissolved solid after 48 h at 2:8 EmimAc:DMSO solvent composition. Table heading E:D refers to the solvent ratio between EmimAc and DMSO.

E:D	1 h	2 h	4 h	24 h	48 h
1:0	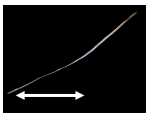	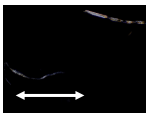	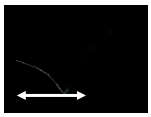	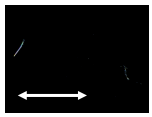	
8:2	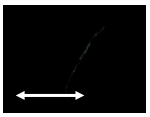	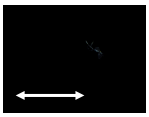	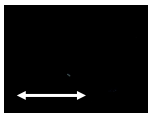	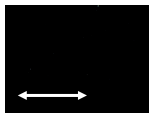	
6:4	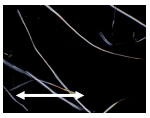	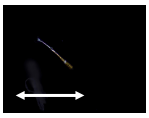	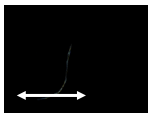	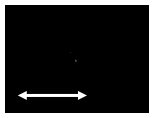	
4:6	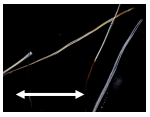	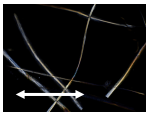	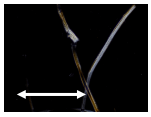	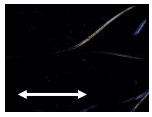	
2:8	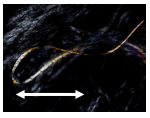	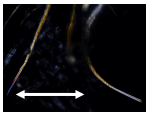	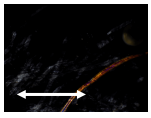	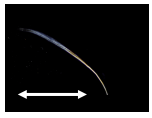	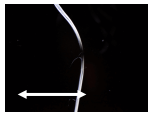
0:1	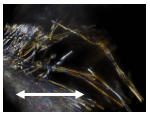	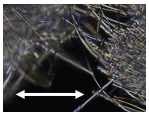	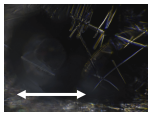	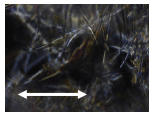	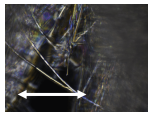

Table 3.2 shows that the system with 8:2 EmimAc:DMSO solvent ratio dissolved most quickly. Very interestingly, this shows a large difference from the optimal EmimAc:DMSO ratio found for MCC, which was 2:8 EmimAc:DMSO as described above. This deviation in optimal solvent composition is impacted by biopolymer choice and physical form. The hierarchical structure impacts the dissolution speed at the macroscopic level by changing bulk viscosity and aggregation behaviour [22, 62, 72]. At the molecular level, biopolymer chemistry can impact monomeric friction coefficients, solvent thermodynamic quality, and IL dissociation [23, 59, 63, 64, 66, 67, 68, 69, 70, 79, 160].

Rheology of Samples

Rheology was performed to investigate the viscosity of solutions after 48 h, at which time the cellulose and SF was completely dissolved in most samples. These tests were performed between 1 and 100 s^{-1} at 100 °C. The same temperature was used in dissolution during similar composite preparation studies of SF and cellulose biopolymer materials [20, 21, 99, 201]. Though total dissolution was the primary concern of this study, a secondary priority was to reduce solution viscosity to ease sample preparation for the manufacture of hybrid biocomposites in later chapters. Reduced viscosity increases matrix penetration into supporting fibres for use in reinforced composites, though it must also be considered that too low a viscosity can cause excess material loss during preparation [20]. Changes to viscosity had large impacts on processing of fibre reinforced samples, so it may be of future benefit to vary the solution viscosity in experimental design. The effects of solution viscosity and penetration into fibres can be seen discussed in Chapter 5. The shear rate sweeps of cellulose, SF, and pure solvent at different solvent compositions can be seen in Figure 3.4.

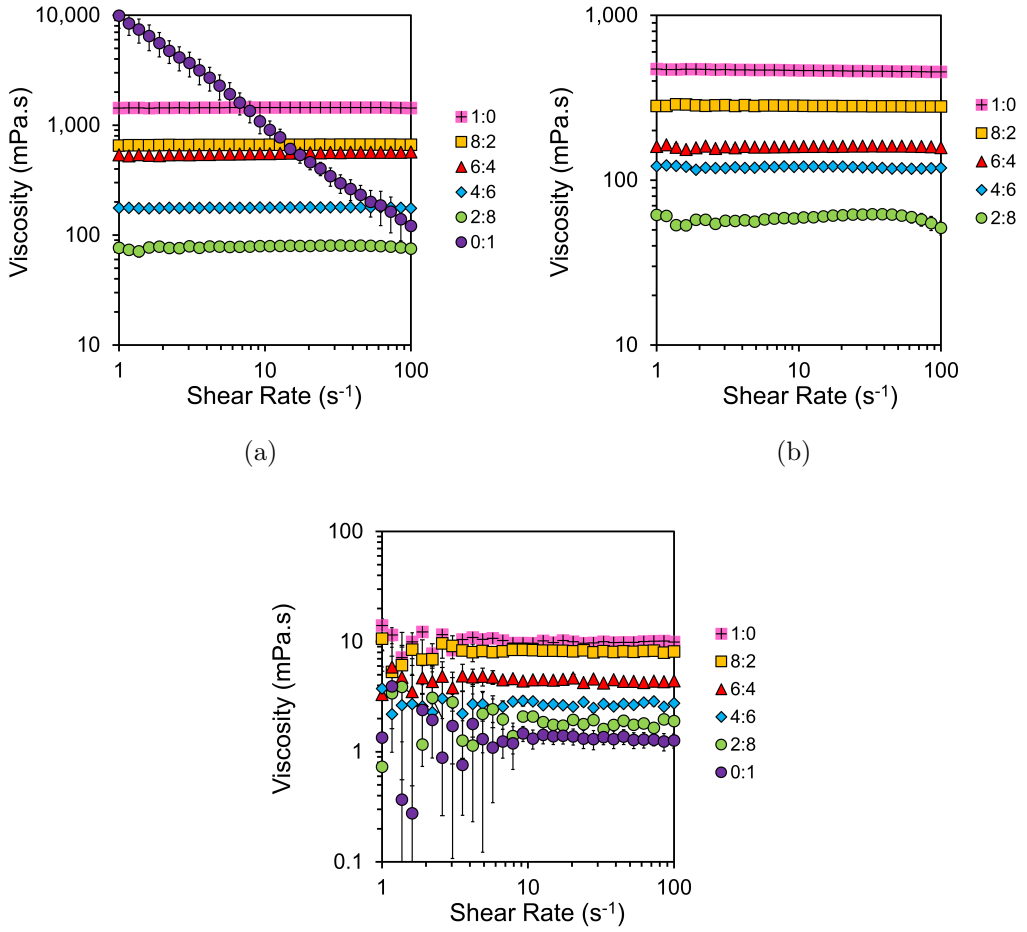

Figure 3.4: Logarithmic plots of shear rate dependence of the steady shear viscosity of (a) 10 wt% cellulose, (b) 10 wt% SF, and (c) pure solvent solutions at various EmimAc:DMSO ratios after dissolution for 48 h. All data points given are mean averages with SE given as uncertainty ($N > 3$).

At the chosen temperature of 100 °C, Newtonian behaviour is noted across most of the shear rate sweeps shown in Figure 3.4 (a), and (b). Deviations from Newtonian behaviour are seen at 0:1 EmimAc:DMSO for 10 wt% cellulose solutions and at 2:8 EmimAc:DMSO for 10 wt% SF solutions. This is supporting evidence for the optical micrographs shown in Figures 3.4 and 3.5, where these were the only two sampled solutions at 48 h that showed remaining undissolved content. SF fibres in a 0:1 EmimAc:DMSO could not be rheologically tested due

to significant jamming from undissolved fibres. In Figure 3.4 (c) it can be seen that a low shear regime of increased variation is seen in samples without dissolved polymers. This behaviour is likely initiated by transient hydrogen bonding occurring between solvent molecules and creating weak clusters [72]. This is discussed in further detail in Section 3.7.

Similarly to Figure 3.4, Owens *et al.* found that increasing the solution temperature of cellulose in EmimAc reduces viscosity and increases the shear rate at which shear thinning behaviour is noted [62]. The intrinsic viscosity was also reported to decrease with elevated temperature due to a decrease in solvent quality and polymer chain size [72]. Vice versa, in studies at lower temperatures or without a DMSO cosolvent, shear thinning was commonly observed [62, 70, 72, 104, 198, 203].

Average solution viscosities in terms of EmimAc:DMSO ratios and the biopolymer type can be seen in Figure 3.5, highlighting the exponential decrease in viscosity seen with the addition of DMSO.

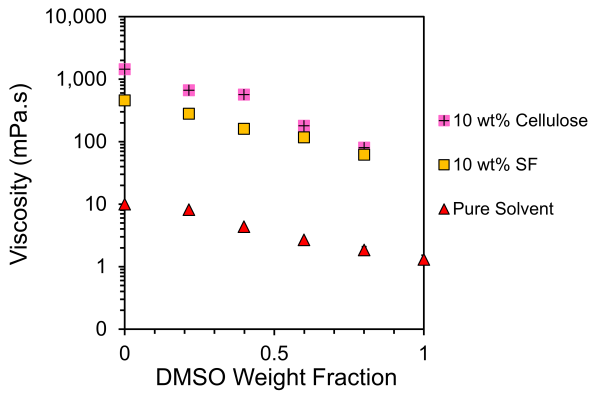

Figure 3.5: Plot of logarithmic viscosities against the weight fraction of DMSO in solvent. The DMSO/SF solution was unable to be tested, and the DMSO/MCC solution showed significant deviation from Newtonian behaviour, so both were excluded. All data points given are mean averages with SE given as uncertainty ($N > 3$).

Figure 3.5 indicates three main aspects. First, the average viscosities of the 10% weight solutions for both cellulose and silk are two orders of magnitude higher than the equivalent pure solvents at the same EmimAc:DMSO ratio. Second, as

expected, the average viscosity of the solutions falls as the DMSO content is increased. And thirdly, the average viscosities of the two biopolymer solutions are comparable for all EmimAc:DMSO ratios though cellulose solutions have a higher viscosity.

The effect of organic cosolvents on the viscosity of ILs has previously been expressed by an exponential equation [68, 70]. This relationship between the viscosity of the IL/cosolvent mixture and the concentration of the cosolvent can be described by the following equation [68, 70]:

$$\ln \eta = \ln \eta_{IL} - \frac{x_{DMSO}}{\alpha} \tag{3.1}$$

where η and η_{IL} are the viscosities of a given solution and the solution with a pure EmimAc solvent; x_{DMSO} is the mole fraction of DMSO in the solvent mixture; and α is a constant. When $x_{DMSO} = 1$, Eq. (3.1) can be rewritten as the ratio of viscosities of solutions of pure EmimAc and pure DMSO solutions. Therefore, this fitting tells us about the ratio of solution viscosities in the conditions shown. To best represent the logarithmic fitting behaviour modelled, the fit was performed between zero and the data point with the highest DMSO content. The fittings for solvent mixture, 10 wt% SF, and 10 wt% cellulose solutions at 100 °C are shown in Figure 3.6.

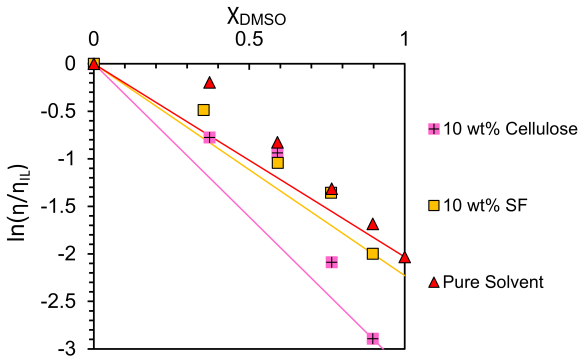

Figure 3.6: Logarithmic plot of viscosities against the DMSO mole fraction with linear fittings calculated according to Equation (3.1). The DMSO/SF solution was unable to be tested, and the DMSO/MCC solution showed significant deviation from Newtonian behaviour due to macroscopic jamming, so both were excluded from the fittings. All data points given are mean averages with SE given as uncertainty ($N > 3$).

The logarithmic fitting in Figure 3.6 shows that pure solvent solutions at this temperature vary less with DMSO than solutions with biopolymer content. All fitting values can be seen in Table 3.3 below.

Table 3.3: Table of α and $\mathbf{R}^2$ values for log fitting of IL/DMSO solutions with Equation (3.1). Values for 25 °C pure solvent fitting are taken from the literature [70]. Errors in α values are estimated from the least-squares fitting using the 'jack-knife' or numerical substitution method [204].

Solute	**Temperature/°C**	α	$\mathbf{R^2}$
10 wt% Cellulose	100	0.31 ± 0.01	0.88
10 wt% SF	100	0.44 ± 0.01	0.95
None	100	0.49 ± 0.01	0.91
None	25	0.15	0.99

Both Figure 3.6, and the $\mathbf{R}^2$ values in Table 3.3 show deviation from the logarithmic fitting. It is reported that DMSO disrupts the dynamic ion clusters within ILs [68, 72], and the small increase in experimental viscosity above the theoretical mixing law indicates weak interactions between the DMSO and IL system

components [68]. The larger deviation shown in 10 wt% cellulose samples could indicate a larger effect on viscosity from DMSO/IL interactions in these solutions. Interestingly, it has also been shown that cellulose dissolution is dependent on ion mobility and IL hydrogen bond basicity β, conferring the importance of IL and DMSO interactions [64].

Based on the speed of dissolution shown in Table 3.1, and the Newtonian behaviours shown in Figure 3.4a, a solvent composition of 2:8 EmimAc:DMSO will be further investigated for the effective dissolution of cellulose. This is a similar composition to the optima proposed by Ren *et al.* and Tomimatsu *et al.* for the rapid dissolution of MCC but differs from studies on the dissolution of cellulose fibres [20, 23, 63, 64].

Based on Table 3.2 and Figure 3.4b, a solvent composition of 8:2 EmimAc:DMSO will be further investigated for the dissolution of SF. Though this composition choice may be influenced by the biopolymer type, Seoud *et al.* found system optima between 0.5 and 0.9 DMSO mole fraction in similar IL/DMSO binary solvent mixtures [199]. This implies the largest effect dictating optimal IL/DMSO compositions may be of a biopolymer form or macroscopic hierarchical structure.

While studying flax fibre dissolution, Hawkins *et al.* reported a reduction in the dissolution rate above 50 wt% DMSO [23]. This was attributed to a change in DMSO preferential association from cation to anion above 0.6 mole fraction DMSO [68, 69, 71], despite an activation energy of dissolution of 100 $\pm$ 10 kJ mol^{-1} independent of the DMSO concentration [23]. Conversely, lower DP cellulose forms have shown effective dissolution at higher DMSO concentrations [63, 64]. This contradiction implies that IL/DMSO systems are effective solvents at high DMSO concentrations but are unable to disrupt larger, more entangled biopolymer networks. This could indicate that longer chain biopolymers (like MCC compared to fibres [1, 72]) are governed primarily by macroscopic viscosity and diffusive effects in these systems [1, 34, 64, 205]. This supports Liang *et al.*, who found a difference in dissolution speed across three different arrangements of cotton fibre bundles, despite a consistent activation energy of dissolution [22]. Most studies have focused on dissolution mechanisms at the mesomolecular level as dictated by cellulose's largely insoluble amphiphilic structure [206], but the

work by Cuissinat and Navard highlights five modes of interaction for the dissolution of cellulose fibres observable by optical microscopy [22, 47]. We could therefore rationalise the different dissolution speeds by investigating their impact on the following modes [47]: (1) fast dissolution by disintegration into fragments; (2) large swelling by disintegration and complete dissolution; (3) large swelling by ballooning and no complete dissolution; (4) homogeneous swelling and no dissolution; and (5) no swelling and no dissolution. This is notably dependent on both the fibre source and solvent, which can both impact macroscopic dissolution behaviours [22, 47].

Interestingly, discrepancies seen may be exacerbated by differences in the definition of dissolution across the literature. In some studies, dissolved sections are measured by total coagulated content around a partially dissolved fibre after partial solvation in an IL and coagulation in an antisolvent [20, 22, 23, 207]. This implies that the coagulated content does not disperse fully into the solution to achieve a full solvation cage. The term 'dissolution' in this case may more accurately refer to the entry of solvent ions into the polymer network and the disruption of the crystalline content. Other techniques, such as small-angle X-ray scattering and NMR, can indicate dissolution to the molecular level up to high biopolymer concentrations [160, 208, 209, 210]. In other studies, the saturation concentration is tested by the timed addition of undissolved content [63]. This could impart a greater impact from dissolution speed as opposed to truly finding a system's saturation concentration.

Lastly, in consideration of the solvent mixtures impact on dissolution behaviour we should indicate if the pretreatment of samples with DMSO affected the solvation properties. It has been noted that efficient pretreatment can aid in dispersal of polymer sources in the given solvent [93]. Cellulose samples were prepared without pretreatment and dispersal in DMSO, but otherwise as described in Section 3.2. This was performed in the optimal solvent composition of 2:8 EmimAc:DMSO for cellulose as described in Section 3.3.

Table 3.4: Table showing the dissolution behaviour of Avicell MCC solution in 2:8 EmimAc:DMSO solvent composition without initial dispersion, at 100 °C. All images were taken at ×20 magnification using transmission polarised light microscopy. Scale bars shown are equivalent to 1 mm.

Time Elapsed			
1 hr	3 hr	4 hr	24 hr
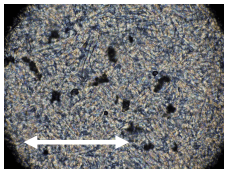	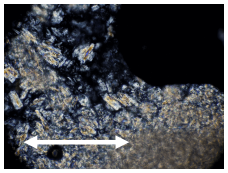	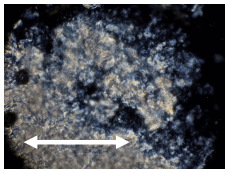	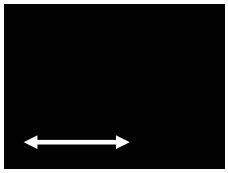

Imaging of these samples (see Table 3.4) showed slower dissolution but no difference in the ultimate solution behaviour. For our purposes, this indicates pretreatment aids dispersal and increases dissolution speed in this system [93]. It is unclear if this is due to DMSO effecting bulk behaviours and avoiding macroscopic aggregates or if DMSO enters the polymer network and facilitates cellulose swelling. Aprotic DMSO is noted to improve biopolymer dissolution in ILs in a number of ways [211]:

- Swelling the cellulose network
- Reducing IL viscosity
- Increasing dissociation of and solvating IL cation and anions
- Improving IL mass transport

Weight Percentage of Biopolymers in Optimal Solvent Systems

After establishing optimal EmimAc:DMSO solvent ratios for both biopolymers in a 10 wt% composition, we then investigated the total solubility of the given biopolymers in these solutions between 0 and 20 wt% biopolymer. This was to confirm the solvation behaviour over the concentration range chosen, and to

establish the saturation concentration of the solvent systems used. Again, all solutions were stirred at 200 rpm, and 100 °C for 48 h to dissolve prior to testing.

Optical Microscopy

The optical microscopy of different weight percentage solutions of MCC in a solvent composition of 2:8 EmimAc:DMSO can be seen in Table 3.5.

Table 3.5: Table showing the dissolution behaviour of MCC at various weight percentages after 48 h of dissolution with stirring at 100 °C. All images were taken at ×20 magnification using transmission polarised light microscopy. Scale bars shown are equivalent to 1 mm. Note: at 11 weight percent of cellulose in solution, undissolved crystalline content can be seen on the µm length scale as highlighted.

Weight Percentage of Cellulose in Solution			
0 wt%	5 wt%	9 wt%	10 wt%
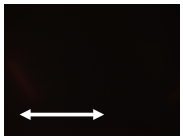	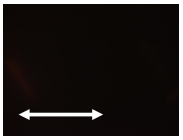	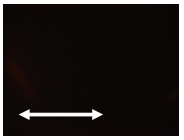	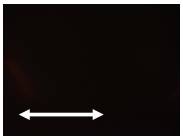
11 wt%	15 wt%	20 wt%	
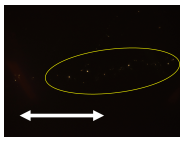	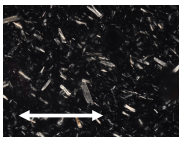	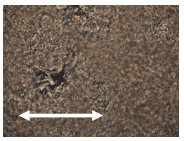	

Table 3.5 shows that above 10 wt% cellulose for our dissolution conditions undissolved particles at a µm length scale remain in solution. This value indicates a saturation concentration below some literature examples with lower DMSO concentrations [63, 160, 203]. This could be linked to the lower total quantity of IL ions stabilising the solvation shell in solution but only confirms the macroscopic behaviours [62]. Molecular behaviours with changes in weight percentage are discussed in Section 3.3. The optical microscopy of different weight percentage solutions of SF in a solvent composition of 8:2 EmimAc:DMSO can be seen in Table 3.6.

Table 3.6: Table showing the dissolution behaviour of SF fibres at various weight percentages after 48 h of dissolution with agitation at 100 °C. All images were taken at ×20 magnification using transmission polarised light microscopy. The scale bars shown are equivalent to 1 mm.

Weight Percentage of Silk Fibroin in Solution			
0 wt%	5 wt%	9 wt%	10 wt%
			
11 wt%	15 wt%	20 wt%	
	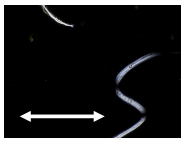	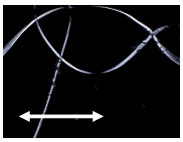	

Table 3.6 shows SF solutions with undissolved fibres above 11 wt%. This implies a saturation concentration between 11 and 15 wt% in this solvent system. This is above the concentrations used in many literature examples [104, 198, 199], but lower than the maximum of 20 wt% SF achieved by Zhang et al. in pure EmimAc [201]. This reduced saturation concentration could indicate that the total solubility in this solvent composition is reduced by the introduction of DMSO into the solvent composition.

Rheology

Shear rate sweeps were taken at various weight percentages of MCC in a solvent composition of 2:8 EmimAc:DMSO; see Figure 3.7a. Viscosities were then plotted against cellulose weight percentage; see Figure 3.7b. Equivalent plots for SF fibres dissolved in 8:2 EmimAc:DMSO solutions can be seen in Figure 3.7c,d. The viscosity values in the semi-dilute entangled regime were fitted with a power law dependency as described by Lefroy et al. [72]:

$$\eta = kc^n \tag{3.2}$$

where η is the sample viscosity, k is a constant, c is the biopolymer weight percentage, and n is the power law exponent.

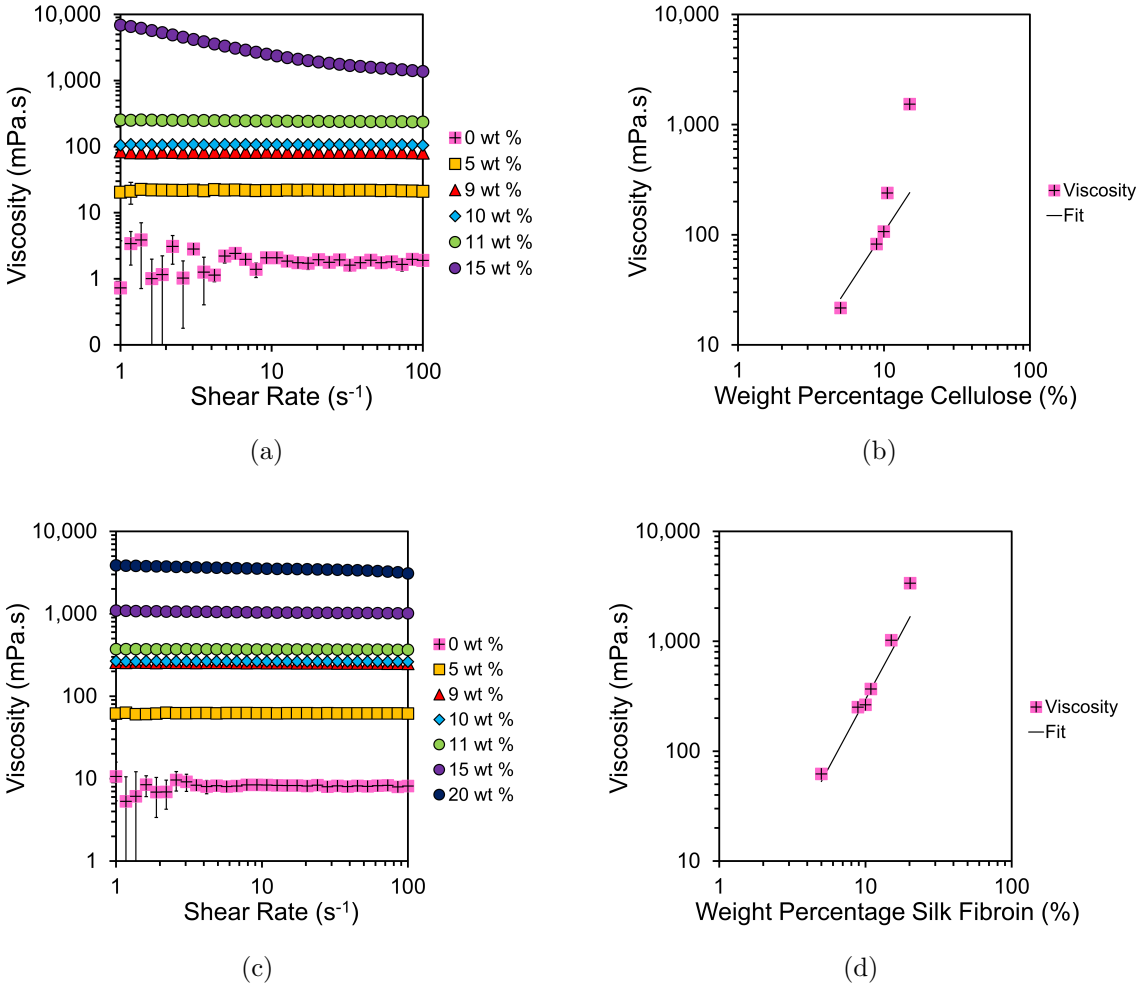

Figure 3.7: Logarithmic plots of viscosity as a function of (a, c) shear rate at each given weight percentage of cellulose and SF; and (b, d) the weight percentage of cellulose or SF with fits extrapolated according to Equation (3.2). All data points given are mean averages with SE given as uncertainty ($N > 3$).

Figures 3.7 (a), (c) and 3.4 (c) highlight the low shear regime (of increased variation) shown in EmimAc:DMSO solutions at 0 wt% cellulose or SF. This is likely caused by the hydrogen bonding of EmimAc ions causing weak cluster networks [72]. The presence of this behaviour despite preshear indicates dynamic

networks with rapid formation at low shear rates. Lefroy et al. found that this behaviour disappears with cellulose introduction due to the disruption of IL clusters by fully dissolved polymer chains [72]. We confirm this finding for both biopolymer examples.

Figures 3.7a,c show predominantly Newtonian behaviours below the saturation concentrations proposed in Section 3.3. The lack of shear thinning differs from similar weight percentage cellulose solutions in the literature at lower DMSO solvent contents and lower temperatures [70, 203]. This shows an increase in the onset value of shear thinning in the samples tested at higher temperatures [62, 70, 72, 104]. Viscosity is also reduced by the introduction of DMSO and increased temperature [62, 70, 72, 104, 203].

Viscosities seen for SF solutions with 8:2 EmimAc:DMSO solvent ratios, in Figure 3.7c, are higher than the equivalent weight percentages in cellulose solutions with 2:8 EmimAc:DMSO solvent composition. This shows the DMSO content of the solvent system to be more impactful than the biopolymer in controlling solution viscosity in this case. Despite this, SF solutions are noted to be less viscous than equivalent cellulose solutions due to greater chain flexibility and/or lower molecular weights [1, 21, 113].

By fitting with Equation (3.2) for values up to 10 wt% cellulose in Figure 3.7b, and up to 11 wt% SF in Figure 3.7d, a transition from the semi-dilute entangled regime to incomplete dissolution is shown. This deviation supports the optical micrographs in Tables 3.5 and 3.6 in showing showing a saturation concentration at 10 wt% and 11 wt% for cellulose and SF respectively. All values tested are above the literature entanglement concentrations for MCC $C_e = 1.3 \pm 0.1$ [70, 212], so they show only the semi-dilute entangled regime. Our fittings show an exponent of $n = 2.3 \pm 0.1$ for cellulose solutions and $n = 2.2 \pm 0.1$ for SF solutions, which match the results by Gericke *et al.* for the equivalent region of pure EmimAc/MCC solutions at 100 °C [203].

Predictions for neutral polymers give a power law index, n, of 1, 2 and 14/3 in a θ solvent, and 1, 1.3 and 3.9 in a good solvent for neutral polymer solutions in dilute, semi-dilute unentangled, and semi-dilute entangled regimes, respectively [212]. n values for both SF and cellulose solutions are less than

the theoretical predictions for θ solvents. This indicates a deviation from θ-solvent behaviour with increased temperature, as previously shown with similar IL-biopolymer solutions, but that the solvent composition tested does not effect the solvent quality [59, 70, 203, 212].

Despite variations in the DMSO concentration, the entanglement state of the SF or cellulose biopolymer in EmimAc:DMSO solutions tested is relatively unchanged. This finding extends from the work by Lv *et al.*, who showed that an increased DMSO concentration (50 wt%) does not affect the entanglement state but reduces the monomeric friction coefficient and hence the viscosity and relaxation times [70]. Tomimatsu *et al.* also confirmed a maximum cellulose solubility at approximately 0.8 DMSO mole fraction due to an increase in ion mobility [64]. They showed that the IL solvation ability correlates with hydrogen bond basicity, β, and that the β of EmimAc is largely constant up 0.9 DMSO mole fraction [64]. This supports our conclusion that the solvent quality is maintained from 1:0 to 2:8 EmimAc:DMSO solvent compositions.

NMR

To investigate the molecular behaviour of solutions, NMR was performed. Cellulose peaks cannot be clearly defined due to the relatively low population of protons in the studied ranges [160], and hence the local interactions and molecular behaviours are studied by the chemical shift dependence of EmimAc peaks on the biopolymer concentration as shown in Figure 3.8.

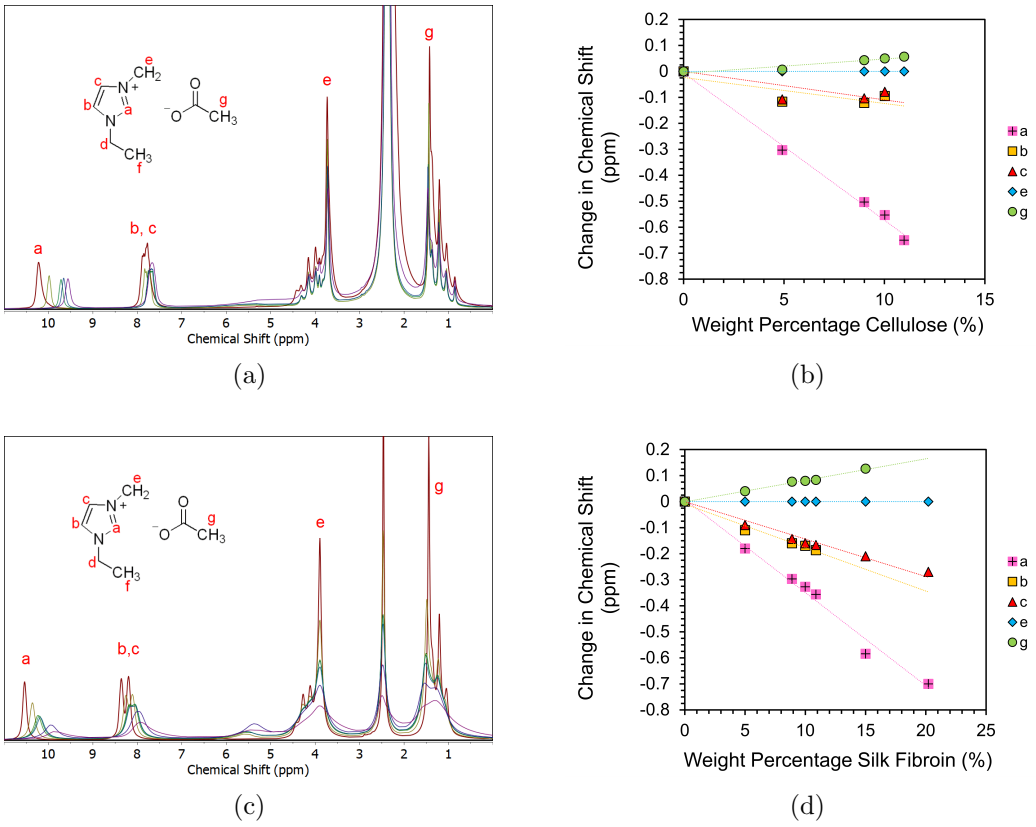

Figure 3.8: (a,c) ^{1}H NMR spectra of 2:8 EmimAc:DMSO solutions at various cellulose concentrations and 8:2 EmimAc:DMSO solutions at various SF concentrations, respectively. The inset shows the chemical structure of the $[Emim]^{+}$ and $[Ac]^{-}$ ions of EmimAc. Peaks signals labeled a-g are attributed to equivalent proton environments seen on the EmimAc diagrams. (b,d) show the concentration dependence of the change in ^{1}H NMR chemical shifts for the proton environments labelled in the inset molecular diagram. Linear fits are included as a guide to the eye. The error bars are approximately equal to the size of the data points used. Samples above 11 wt% MCC are too viscous to be prepared in the given NMR tubes. In SF fibre solutions with undissolved content, the solution is pipetted away from the undissolved content for NMR analysis. All peak integrals and tabulated raw data can be seen in Tables 3.7 and 3.8.

Figure 3.8 (a), (b) show a shift in the EmimAc chemical environment up to 11 wt% MCC, indicating that the local environment for EmimAc cations is changing [160]. This is consistent with the coordination of IL ions with cellulose hydroxyl groups as proposed by Zhang *et al.* for the dissolution and solvation

mechanism of cellobiose in EmimAc [160, 161]. The change in chemical shift seen implies an increase in the cellulose content in solution and hence confirms alterations in the molecular level behaviour of these samples.

A shift in spectral bands is also seen with increasing the SF content in Figure 3.8 (c), and (d) indicating the association of IL cations with SF hydroxyl groups equivalent to that seen in cellulose and cellulose-derived biopolymers [160, 161, 207]. This confirms the SF dissolution mechanism theorised by Phillips *et al.* that IL ions disrupt the hydrogen bonding domains in β-sheet/crystalline regions of SF, incurring solvation [1, 207].

Figure 3.8 (d) shows the continued chemical shift at concentrations in which fibres were seen to be undissolved (15-20 wt% SF). This highlights the distinction between macroscopic and microscopic dissolution behaviours [22, 41, 72]. Though the solution increased in concentration of SF molecules, the solvent system was not capable of dissolving the fibres as seen in Section 3.3. The difference between local molecular (NMR) and bulk (rheology and optical microscopy) saturation concentrations indicates a distinction between the solvent thermodynamic quality at the molecular level, and the ability of a solvent system to disrupt and disperse polymer networks.

Notably, peaks in Figure 3.8 (c) are more clearly distinguished than those in Figure 3.8 (a) due to the larger relative population of EmimAc protons in the solvent composition. Samples with higher weight percentages of biopolymers are also higher in viscosity, which reduce the sample isotropy and hence signal quality [160]. Any data points omitted in Figure 3.8b,d are excluded due to the peaks being poorly distinguished at higher biopolymer concentrations.

Table 3.7: Raw data from ^{1}H NMR spectra of 2:8 EimAc:DMSO solutions at various cellulose concentrations. Samples above 11 wt % MCC were too viscous to be prepared in the given NMR tubes. All data shown is prior to normalisation and correction for drift by use of peak e as a stationary reference signal. To increase legibility in the table the following abbreviations have been made: "Weight Percentage of Cellulose / %" has been shortened to "wt %"; "Average Peak Position / ppm" has been shortened to "Pos."; and "Average Peak Integral" has been shortened to "Int."

	Peak Labels									
wt %	a		b		c		e		g	
	Pos. / ppm	Int.	Pos. / ppm	Int.	Pos. / ppm	Int.	Pos. / ppm	Int.	Pos. / ppm	Int.
0.00	10.23	287.67	7.86	96.04	7.78	170.82	3.73	1124.78	1.43	573.99
4.91	10.05	292.19	7.87	66.74	7.80	184.61	3.86	834.46	1.56	871.11
8.99	9.78	259.79	7.79	91.62	7.73	211.49	3.78	761.96	1.52	777.95
10.02	9.78	273.24	7.87	129.46	7.81	129.36	3.84	705.17	1.58	784.23
10.98	9.67	254.53					3.82	683.51	1.57	692.92

Table 3.8: Raw data from ^{1}H NMR spectra of 8:2 EmimAc:DMSO solutions at various SF concentrations. All data shown is prior to normalisation and correction for drift by use of peak e as a stationary reference signal. To increase legibility in the table the following abbreviations have been made: "Weight Percentage of SF / %" has been shortened to "wt %"; "Average Peak Position / ppm" has been shortened to "Pos."; and "Average Peak Integral" has been shortened to "Int."

	Peak Labels									
wt %	a		b		c		e		g	
	Pos. / ppm	Int.	Pos. / ppm	Int.	Pos. / ppm	Int.	Pos. / ppm	Int.	Pos. / ppm	Int.
0.00	10.53	1172.97	8.36	682.22	8.19	823.18	3.89	3584.61	1.44	3451.77
4.99	10.19	1077.21	8.09	1131.77	7.94	1047.52	3.73	3087.11	1.32	3309.24
8.89	10.09	1135.95	8.05	1121.26	7.90	951.6	3.74	3167.98	1.37	3319.18
9.99	10.07	1125.56	8.05	1110.25	7.89	991.31	3.75	3179.3	1.38	3295.93
10.88	10.05	1087.48	8.05	1127.87	7.90	992.97	3.77	3205.94	1.40	3304.19
15.00	9.76	1154.31			7.79	1471.21	3.70	3591.78	1.38	3113.76
20.21	9.50	735.58			7.59	1697.97	3.56	5351.98	0.98	7310.55

Demonstration of Hybrid Solutions

Having achieved the dissolution of both SF and cellulose biopolymers and created solutions of minimal viscosities, solutions of 10 wt% cellulose in 2:8 EmimAc:DMSO solvent ratio and 10 wt% SF in 8:2 EmimAc:DMSO solvent ratio are prepared by with the method described in Section 3.2. Equal masses of these solutions are mixed at 200 rpm for 30 min at 100 °C to indicate the effectiveness in producing hybrid solutions for composite preparation. This causes no coagulation or aggregation out of solution as indicated by the optical microscopy in Figure 3.9 (a) and the Newtonian behaviour with a viscosity of 142 ± 2 mPa.s as seen in Figure 3.9 (b). This implies the homogeneity and stability of the biopolymers in solution and indicates the effectiveness of the dissolution method for future hybrid biocomposite preparation.

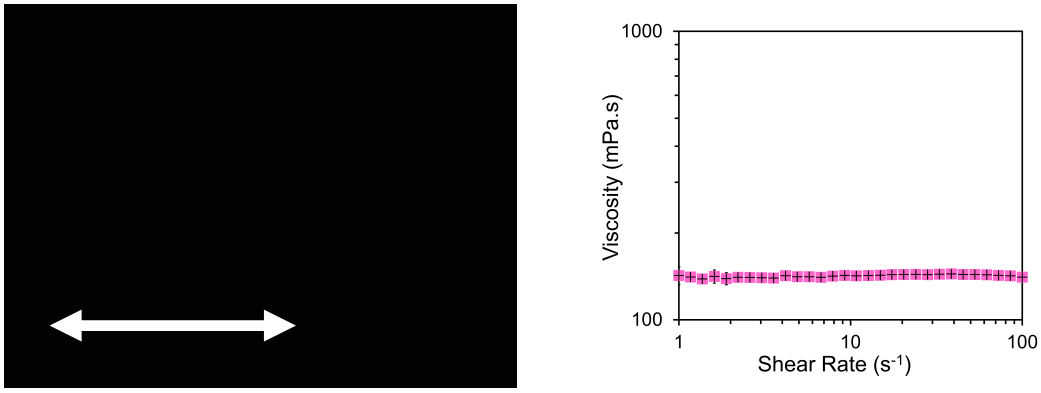

(a) (b)

Figure 3.9: (a) Polarised optical microscopy images at x20 magnification of 10 wt % hybrid biopolymer solution. This is in a 1:1 silk fibroin:cellulose weight ratio. All images are taken at x20 magnification using transmission cross-polarised light microscopy. Scale bars shown are equivalent to 1 mm. (b) Logarithmic plot of the shear rate dependence of the steady shear viscosity of 10 wt % hybrid biopolymer solution. This is in a 1:1 silk fibroin:cellulose weight ratio. All data points given are mean averages with SE given as uncertainty ($N > 3$).

3.4 Conclusions

In this chapter, the effect of the EmimAc:DMSO solvent ratio was first investigated for the dissolution of a 10 wt% fraction of SF and MCC at 100 °C. MCC was most quickly and efficiently dissolved in a 2:8 EmimAc:DMSO solvent mixture, and SF fibres were most efficiently dissolved in an 8:2 EmimAc:DMSO solvent mixture. The steady-shear rheology of solutions at various solvent compositions with 10 wt% biopolymer content (for samples dissolved for 48 h) was measured and showed mostly Newtonian behaviours. Deviation from Newtonian behaviour was only found for samples that showed undissolved material in optical microscopy, offering an additional method to establish when full dissolution had occurred. The steady shear viscosities were then plotted as function of the DMSO mole fraction, and deviation from the exponential mixing rules of solvents indicated that EmimAc:DMSO interactions affected the viscosity significantly in all solvent systems studied. This showed the impact of solvent–cosolvent interactions on bulk viscosity. Comparison with trends in the literature indicated that

the dissolution behaviour of different solvent compositions was greatly affected by the biopolymer form [22, 23, 63, 64]. Larger hierarchical structures or longer-chain biopolymer networks required solutions with a higher IL concentration to effectively disrupt the polymer network.

The total solvation ability of the selected optimal solvent mixtures was then tested at different biopolymer weight percentages. The macroscopic dissolution behaviours to the μm length scale were investigated with optical microscopy and rheology. Imaging showed undissolved content at 11 wt% cellulose upwards and from 15 wt% SF upwards. This implied a saturation concentration between 10–11 wt% and 11–15 wt% for cellulose and SF respectively. This was confirmed by deviation from a power law dependency in viscosity against sample concentration at these values. This fitting in the semi-dilute entangled region showed agreement with similar studies at lower DMSO contents, with power law exponents, n, of 2.2 and 2.3 $\pm$ 0.1 for SF and cellulose solutions, respectively [203]. This confirmed that the solvent systems thermodynamic quality and biopolymer conformations remained relatively constant from 1:0 to 2:8 EmimAc:DMSO solvent compositions.

Lastly, a discrepancy between the molecular and macroscopic behaviours is evidenced by the difference in the apparent saturation content in the SF fibres in this study. NMR evidence shows continued solvation up to 20 wt% SF as expected from the literature [201], beyond the optically observed saturation point between 11 and 15 wt% SF. Hence, the thermodynamic quality of the solvent at the molecular level is shown to be beyond the macroscopic dissolution achievable with this procedure. This highlights the necessity of investigating multiple length scales in evaluating solvation behaviour.

This research improves the understanding of biopolymer dissolution in EmimAc:DMSO systems and shows how this could be applied to produce hybrid biopolymer solutions. It provides further insights into the dissolution behaviours occurring on a macroscopic and local level, which is crucial to understand the properties of materials coagulated from IL solutions. Having developed the optimal EmimAc:DMSO ratios for dissolving the two biopolymers, and blended them, the subsequent chapters will examine the mechanical properties of a range of hy-

brid biopolymer films with differing cellulose/silk ratios and hybrid biopolymer composites with reinforcing fibres.

3. DISSOLUTION OF SILK FIBROIN AND CELLULOSE IN 1-ETHYL-3-METHYLIMADIZOLIUM ACETATE AND DIMETHYL SULPHOXIDE

Chapter 4

Properties of Hybrid Silk Fibroin/Cellulose Films

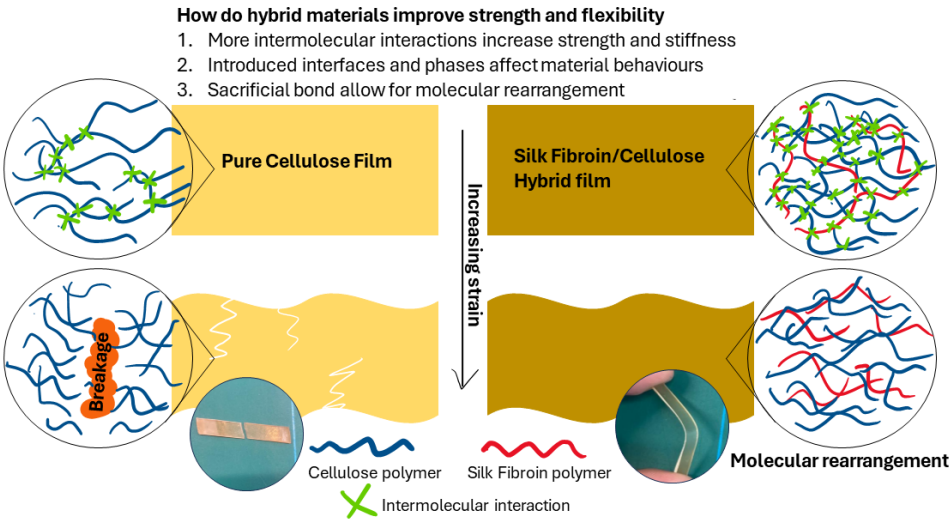

Figure 4.1: Graphical abstract indicating the study performed on fully dissolved and coagulated films of cellulose and SF blends to understand their behaviours from the molecular to bulk levels.

4.1 Introduction

The negative impact of petrochemical plastic use on the climate necessitates sustainable alternatives to conventional plastics, such as biologically derived materials [6, 58, 213, 214]. These can take the form of natural-fibre reinforced materials, self supporting biopolymer composites or bioplastics formed of biopolymer networks [24, 75, 96]. Taking advantage of the high performance and sustainability of these may offer beneficial results with applications in the biomedical, structural, or aerospace fields [1, 20, 113, 215]. As discussed in Chapter 1, a promising route to optimisation of these materials is by the hybridisation of biopolymer materials.

Despite promise shown in the behaviours of hybrid biopolymer composites, the nature of the sample behaviour remains a contentious issue. Many studies indicate a performance increase with a small addition of 5-30 % SF content to a cellulose network [18, 19, 78, 86, 164]. Other studies indicate a negative trend in maximum strength or strain at failure with addition of SF [86, 99]. Other variations include quoted strains of failure in ranges from 40-60 % by Shang *et al.* or 8-10 % by Tian *et al.* [18, 19]. These differences are not explained by variations in sample water content between studies, which could induce softening due to disruption of inter- and intramolecular hydrogen bonds [53]. These variations also occur in studies with comparable component sources and preparation techniques. Inconsistencies in reported behaviours may be due to compositional effects and relaxation behaviours not previously considered, so establishing an understanding of these behaviours is of central importance before manufacture, testing, and application of hybrid materials.

This chapter investigates relaxation behaviours and molecular/mesomolecular length scale behaviours alongside bulk mechanical measurements to elucidate the contradictory behaviour of these materials beyond previous studies. This could enable improved application beyond already promising investigations into biomedical uses. We prepare fully dissolved and regenerated films of SF and cellulose using ionic liquids as a sustainable solvent with effective dissolution, recyclability, and minimal environmental impact [11, 34, 35]. Complete dissolution and homogenous dispersal of polymers avoids retention of undissolved fibres which

impacts behaviours based on level of dissolution, level of fibre entanglement, orientation, and fibre-matrix interfaces [20, 96, 181, 216]. This enables us to draw conclusions about fundamental behaviours affecting molecular interactions in all examples of these hybrid materials. We utilise double network theory, and comparisons with relevant biological materials to rationalise contradictions and trends seen within literature. We then establish the presence of a slow stress relaxation and viscoelastic behaviour similar to complex biological systems [138, 217, 218]. Notably, we discuss the variability in strength and flexibility with addition of SF to cellulose materials beyond effects of solvent choice, polymer source, purity, alignment, and level of reinforcement [75, 85, 86, 117]. In this case, films will be studied due to the benefits inherent over more porous samples. These can exhibit reduced bending, tensile, and compressive strength, which must be alleviated by compression [124]. These also show added variation due to porosity, which can affect mechanical properties [124].

4.2 Materials and Methods

Sample Preparation

The dissolution conditions were selected based on Chapter 3 findings probing effective dissolution of SF and cellulose with EmimAc and DMSO solvent mixtures [159]. Cellulose was dissolved at 10 wt% in an 20:80, EmimAc:DMSO mixture of solvents. Silk fibres were dissolved at 10 wt % in a 80:20, EmimAc:DMSO mixture of solvents. Polymeric solids were firstly dispersed in the relevant weight of DMSO, then stirred and preheated to 100 °C for 30 mins. The relevant weight of EmimAc was preheated at 100 °C for 30 mins then mixed with the dispersed solids in DMSO. Solutions were then stirred for 16 hr, at 100 °C, at 200 rpm to produce pale yellow to dark amber transparent solutions. SF solutions showed darker colour than cellulose solutions. After dissolution a hybrid solution was prepared by mixing the solution for 30 minutes, at 100 °C, at 200 rpm. All dissolution was performed in sealed vessels to minimise the effects of humidity. Optical microscopy confirms complete dissolution within our solutions as shown in Chapter 3 [159].

Film composition was altered by changing the cellulose:SF weight ratio with the total mass of polymeric solid remaining the same. The polymer solution was poured into a circular petri dish (10 cm diameter) and left to deaerate for 2 hr at 70 °C under vacuum. The cast film was then coagulated in a methanol atmosphere statically for 24 hours, by placing under a vacuum environment with 200 ml of methanol. The film was then washed in deionised water (5 l) for 48 hr. The water was replaced twice in that period. The film was then dried at room temperature and humidity for 6 hr. Films were then pinched between flat metal sheets ($\approx$ 10 KPa using bulldog clips), to alleviate deformation due to differential shrinkage during drying and cooling, then dried for 24 hr at 60 °C. Examples can be seen in Figure 4.2.

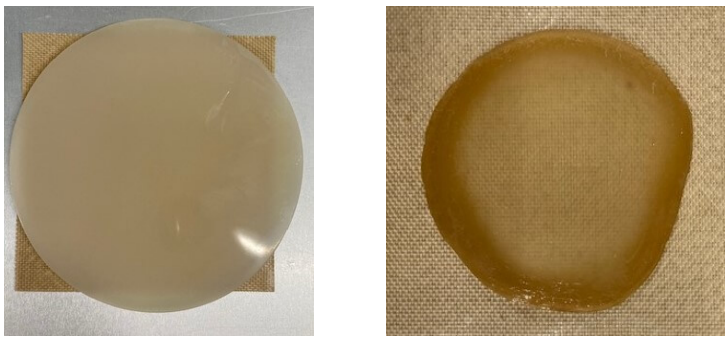

(a) (b)

Figure 4.2: Images of (a) an example wet gel formed during fabrication and (b) an example dried film showing edge effects. The size of the film is approximately 5 cm in diameter.

Approximately 65 - 80 % of the original polymeric mass was left after drying the films and higher SF compositions showed higher mass loss during washing. A schematic of the production methodology can be seen in Figure 4.3.

Before any characterisation, samples were equilibrated under ambient conditions for at least 24 hours. The average room humidity was 50 $\pm$1 % and the average temperature was 20.6 $\pm$0.2 °C. Analysis results were averaged over at least three measurements unless otherwise mentioned. Most analyses in Section 4.3 discuss properties as a function of SF content with a focus on 0-50% SF. Qualitatively, it has been found that in fully dissolved blends SF contents over 50

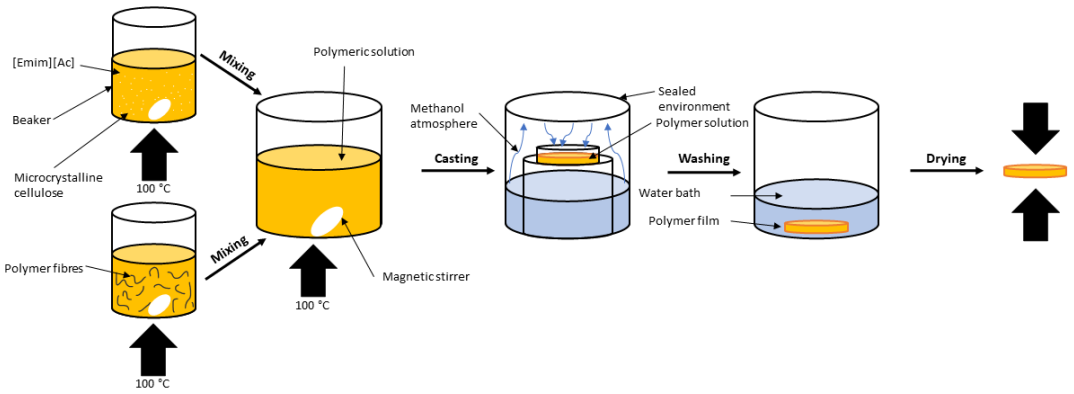

Figure 4.3: Schematic showing the preparation procedure for hybrid cellulose and silk fibroin films.

% caused mechanically unstable composites [3]. It is widely recorded that pure SF films are brittle and weak [54, 56, 99].

Sample Testing

The bulk mechanical behaviour of samples was testing in flexural and extensional regimes according to Section 2.2. Quasi-static stress relaxation and creep tests were performed as described in Section 2.2. 2θ XRD diffractograms were gathered as described in Section 2.6. Thermal behaviours were investigated with TGA experiments according to Section 2.5. DMTA was performed as indicated in Section 2.2. Lastly, additional testing on the water contact angle was performed according to Section 2.8.

4.3 Results and Discussion

Sample Morphology - XRD

To ascertain the the morphology of samples 2θ scans were performed for each sample. The resulting diffractograms can be seen in Figure 4.4. Also shown is a diagram indicating the templating mechanism shown in literature to encourage the formation of Silk II structures in hybrid cellulose/SF materials [18, 99].

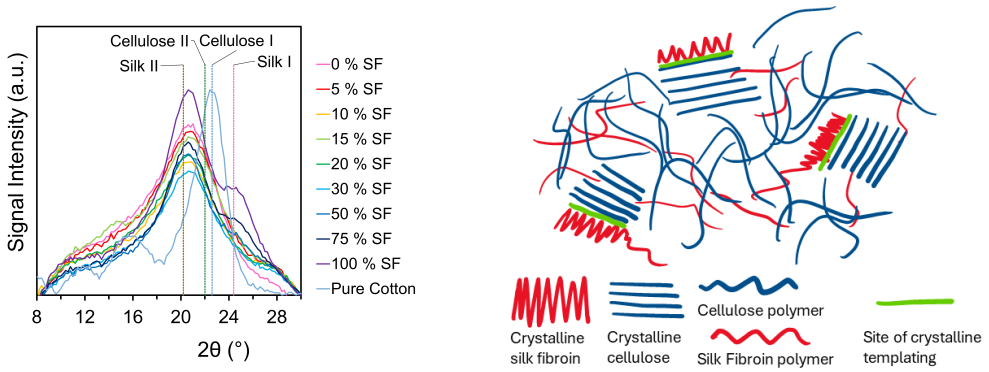

(a) (b)

Figure 4.4: (a) X-ray diffraction 2θ diffractogram for each film composition and an example undissolved cotton sample, and (b) an example diagram indicating the crystalline templating effect of cellulose crystallites on silk fibroin content, as proposed in literature.

XRD confirms the conversion of cellulose content from Cellulose I to Cellulose II polymorphs (see Figure 4.4 (a)), and hence confirms the complete dissolution of the cellulose content [67, 79]. This can be seen as contributions from the Cellulose I peak in Figure 4.4 (a) are not seen in coagulated film samples. However, as discussed in Section 2.6, significant overlap of the crystalline SF and cellulose peaks was seen that negated the accuracy of the fitting solution. Hence, fittings have been dismissed and the evidence must instead be considered with respect to the literature before further testing with alternative analyses.

Literature examples have shown Silk II crystalline structures are promoted in hybrid films, above the formation of Silk I crystals [18, 78, 99]. The increase in silk II crystals could be due to cellulose templating the formation of the hydrogen bonded β-sheets due to strong interactions [18, 78, 99]. This occurs at cellulose-SF interfaces and hence in hybrid films, as shown in Figure 4.4 (b). β-sheet formation is also encouraged by coagulation from high concentration proteins solutions, methanol coagulation conditions, solvent choice, and slow drying [13, 86, 99]. Though the mechanism of formation is not fully understood, the formation of highly interacting regions enables stress transfer between chains in the network and hence increases material toughness [1, 86]. An increase in the amorphous content in hybrid films is seen in literature examples which show

crystalline disruption of cellulose in hybrid samples [1]. This is due to interspersal of the flexible SF chains within the cellulose network interrupting the formation of crystalline structures. This causes an ultimate decrease in total crystalline content.

Molecular Relaxation Mechanisms - DMTA

Temperature ramp tests were performed to understand the effect of composition on the secondary relaxations often correlated with material toughness via the intensity of corresponding tan(δ) peaks [133]. Pure cellulose DMTA studies exhibit a peak between -50 and -80 °C corresponding to γ or β relaxations that have been attributed to a variety of mechanisms [146]. For example, these relaxations have been attributed to hydroxyl side chains in cellulose but could be connected with a hierarchical facilitation of longer scale cooperative relaxations [143, 146]. In SF a similar peak is seen around this temperature which is associated to movements of hydrated peptide side chains [144]. Figure 4.5 shows the trend for both tan(δ), as defined by Eq. 2.15, and the peak position to decrease with addition of SF.

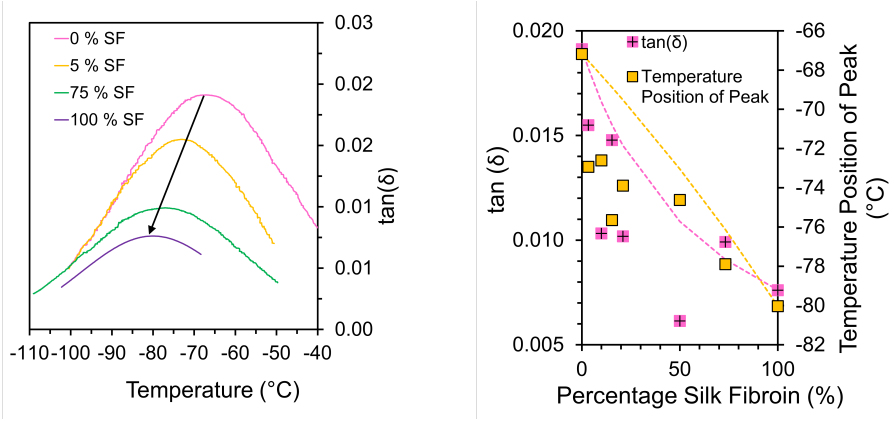

(a) (b)

Figure 4.5: Graphs showing (a) typical secondary relaxation peaks with background removed at various sample compositions; and (b) trends in tan(δ) and peak position with sample composition. A fitting with the Fox rule, as described in Eq. 2.16, has been included to indicate the mixing relationship and deviation from this in the data [151, 219]. T_g values for fitting were taken directly from the graph and molar fractions were calculated from the weight percentages.

In Figure 4.5 (b), the negative trend shown with increasing SF content can be correlated to a reduction in both the total energy of the relaxations occurring, and energetic cost for the associated secondary relaxation event to occur [133]. Guan *et al.* denote this relaxation in pure SF fibres as $T_{\beta 1}$, due to the loss event (molecular motion/energy dissipation) of axial group motion with peptide-water interactions (See Figure 4.6) [144]. As this trend appears monotonic this motion does not correlate with the bulk non-monotonic trends seen in mechanical analyses (see Section 4.3). However, the sharp decrease in tan(δ) and the peak position with addition of SF deviates from the Fox equation or linear rules of mixing as seen in Figure 4.5(b) [151, 219]. This deviation from typical mixing behaviour indicates the blend is not fully miscible and implies the presence of some phase separation, as supported by evidence in Section 2.5 [151].

The negative trend shows the increasing ease of side group mobility (reducing temperature of relaxation), and the reducing total side group mobility (reducing amplitude of peak) with additional SF polymer content [133]. This can be visualised with the increasing ease of short lengthscale motions in the Crankshaft model as discussed in Section 2.2 (see Figure 2.9). Though plasticisation of these motions can be caused by water or solvents in primary or secondary bound positions [147], it is unlikely water content is the direct cause of this trend due to the similar water contents of different compositions shown in Section 4.3. However, it is possible bonding site accessibility may be impacted by SF addition to cellulose networks. Therefore the bound to free/bulk water ratio change with composition and alter the properties [147]. The adsorption process in cellulose is not always sequential. Increases in system hydration can incur increases in any of the following water states [147]: primary bound water; secondary bound water; free water; bulk water.

Thermal Behaviour - TGA

The results from TGA suggest both partial phase separation and content mixing, due to the presence of peaks attributed to decay of pure and mixed polymer phases (see Figure 4.7 (b)). As shown in Figure 2.15, the percentage weights

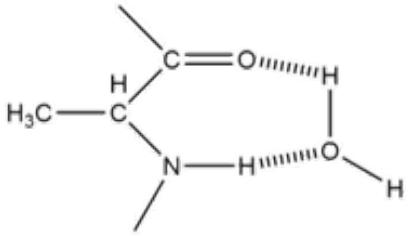

Figure 4.6: Diagram showing SF peptide - water associations for an example alanine amino acid [144].

given in Figure 4.7 (c) were derived from the weight changes of each thermal event in Figure 4.7 (a).

As described by Hadadi *et al.* and Love *et al.*, thermal decomposition is used to infer the stability of each interface by the temperature required to overcome adhesive forces and incur degradation [13, 164]. The mixed polymer phase gives rise to more SF-cellulose interfaces with weaker interactions than those found in pure phases of either polymer [13, 164]. This gives rise to three peaks in our signal which can then be used to ascertain the morphology and content of mixed, pure SF, and pure cellulose phases. Our data agrees with similar evidence from Defrates *et al.* and others who found a distinct peak between 200-300 °C that was attributed to a unique silk-cellulose associated phase [3, 87]. This was in addition to peaks attributed to pure cellulose and silk components [3, 87]. This implies the presence of phase separated regions of each polymer. Further evidence of this is shown by XRD, in Figure 4.4, which indicates the presence of peaks for the presence of pure silk crystallites and pure cellulose II crystallites in hybrid samples. This provides some direct morphological evidence of phase separated regions. Defrates *et al.* further supported this conclusion with scanning electron microscopy of comparable samples. This showed surface aggregation in hybrid samples at 10-30 % SF content due to partial phase separation [87]. Hadadi *et al.* also identify partial phase separation between SF and cellulose (with TGA, scanning electron microscopy, and Fourier-transform infrared spectroscopy) encouraged by free energy minimization during coagulation of the polymer solution [164].

The presence of multiple peaks in the TGA spectra is in contrast to findings by

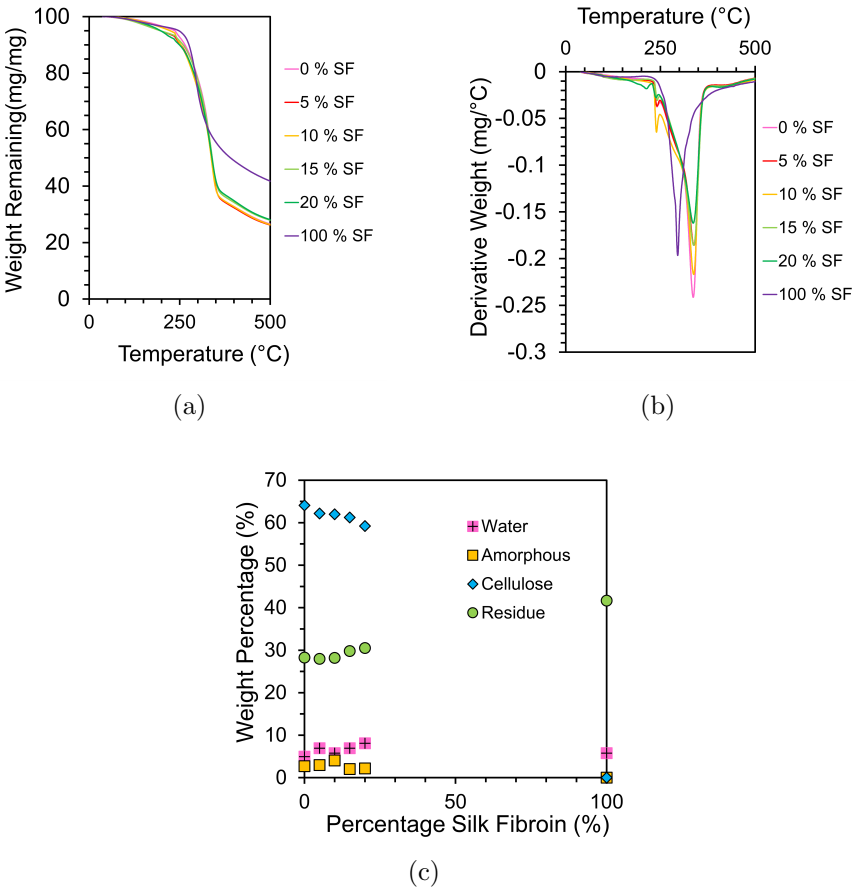

Figure 4.7: Graphs showing (a) normalised data of the TGA temperature ramps, and (b) the derivative plot of the resulting TGA analysis, and (c) the % mass of each peak shown as the percentage of the associated decaying component.

River-Galleti *et al.* and others [56, 82, 99]. These papers showed smooth transitions from the lower SF degradation temperature to the pure cellulose degradation temperature with composition change. This implies a homogeneous behaviour and complete mixing between the polymers, but could also be different due to signal overlap between the SF and cellulose peaks. Chain length, or solvent associations can cause variations in the temperature of degradation to occur [220, 221]. Zhou *et al.* saw no peak from mixed content, and only noted two distinct peaks for pure SF and pure cellulose that varied with size [99]. Interestingly, they also noted no non-monotonic peak in mechanical material properties with mixed com-

positions [99]. This indicates the importance of mixed SF/cellulose associations in hybrid composites, and how they could directly cause the increase in material strength shown in other examples [1].

Figure 4.7 (c) showed a peak in the total percentage of content in the mixed state between 5-20 % SF. This could correlate with other maxima seen in materials properties testing, indicating the impact of the interaction rich mixing occurring at approximately 10% SF composition. This could result in more interactions contributing to higher material strengths. A diagram for this hypothesised interspersal and increased interaction density can be seen in Figure 4.8 [19, 89]. Also noted is an increase in the remaining residue after the test with increasing SF content, this implies SF has a lower content of volatile components within the testing range.

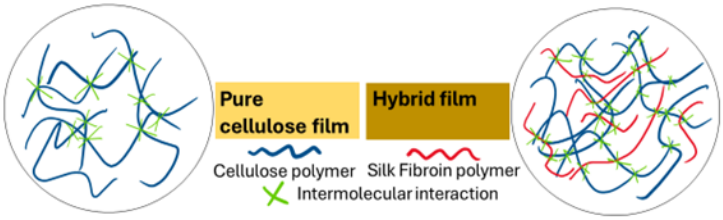

Figure 4.8: Diagram indicating a potential increase in interaction density that occurs as a result of silk interspersal into cellulose network in hybrid composites.

Bulk Mechanical Analysis

To establish the bulk behaviour of films, mechanical testing was performed. Different rates of deformation were tested to understand the impact of time-dependent creep and relaxation on mechanical behaviours. To allow for comparison despite sample dimension variation, typical deflection rates were converted to strain rates in the flexural regime [20, 21]. We therefore compared slow (1.5 % min^{-1}) and fast (25 % min^{-1}) deformation in flexural. These values were selected as extremes of the range of common strain rates seen in literature [21, 119]. Values were converted from mm min^{-1} to strain % min^{-1} to make comparisons possible across different sample dimensions.

Flexural Testing

Mechanical analysis was initially performed in the flexural regime. Example stress-strain curves and extracted data averages are shown in Figure 4.10.

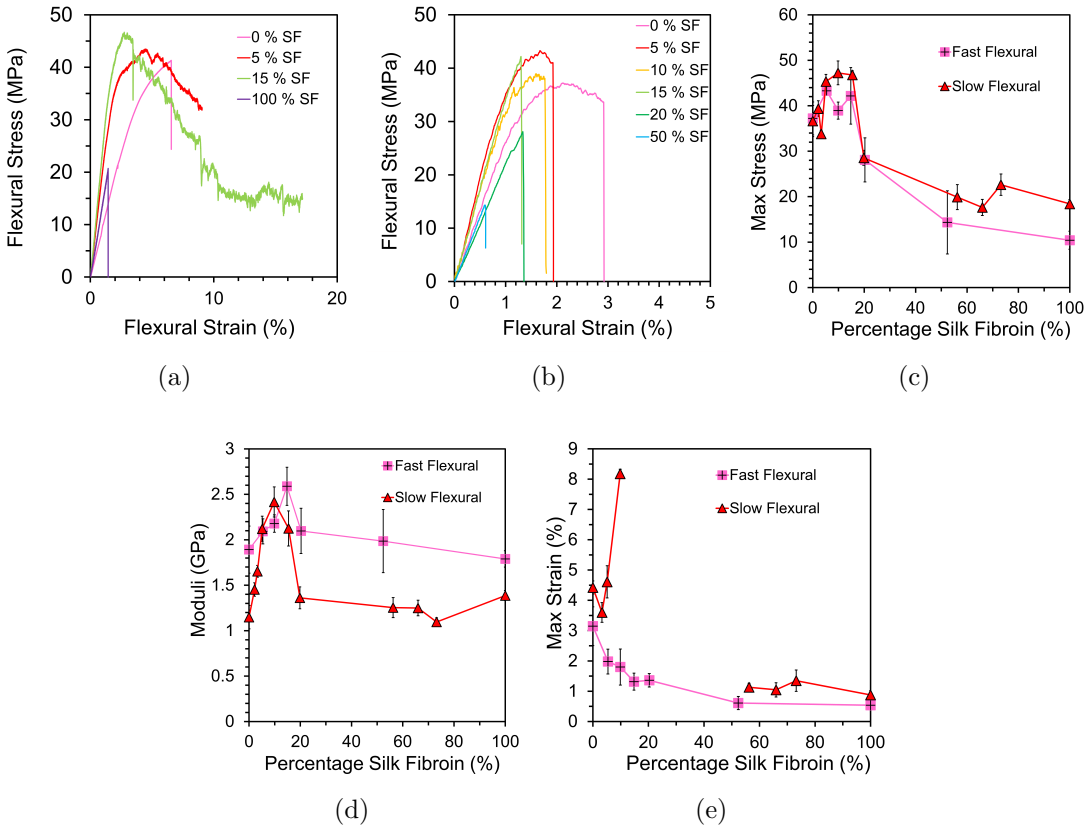

Figure 4.9: Graph showing the stress-strain behaviour of films during (a) 'slow' and (b) 'fast' testing within flexural regimes. This also shows the extracted average data of the Young's moduli (c), the maximum stress (d), and the strain at failure (e) for 'slow' flexural; and 'fast' flexural tests. All data points given are mean averages with SE given as uncertainty ($N > 3$).

Moduli and maximum stress indicate an optimum between 5 - 15 % SF though the maxima differ from those seen in extensional testing modes (see Figure 4.10). This may be because the equation for flexural stress and strain only model the strain of the outer layer of the sample. The extensional testing instead accounts for the entire cross section. Therefore, failure occurs at the weakest point in

the sample [135]. This gives less chance of failure/crack propagation in flexural tests where the surface shows no defects [135]. It could also indicate a deviation from isotropic behaviour as polymer samples may have compressive resistance, increasing the stress values calculated for flexural testing due to contributions from the internal stresses on the internal bending edge [222]. Because of these contributing factors the trend and optimum identified will be considered with respect to further extensional testing.

The strain at failure decreases monotonically at fast rates but deformed and did not fail in hybrid samples with 'slow' deformation. In these case samples were permanently deformed without total failure. This was indicative of interesting rate-dependent relaxations occurring in samples. However, it is important to note that failure via delamination is prevalent in flexural testing which could be contributing to these observations [222]. After the initial deformation, slippage occurred which can be noted by the strain reduction after peaks seen in Figure 4.9 (a). Hence, we repeated measurements in the extensional regime before further conclusions were drawn.

Tensile Testing

Mechanical analysis was then performed in extension. Example stress-strain curves and extracted data averages are shown in Figure 4.10.

For all samples a peak in strength and modulus between 5-15 % SF is seen regardless of strain rate. This can be seen in Figure 4.10 (c) and (d) and is reflected in equivalent flexural testing tests in Figure 4.9 (c) and (d). This peak can be understood with generalised modelling of double networks as described by Nakajima [89]. Using fracture energy, (G, J m^{-2}), robustness can be approximated as the resistance to crack propagation causing material failure [89]. The intrinsic fracture energy can be described with Lake-Thomas theory as:

$$G_0 = NU\nu_{\text{area}} \tag{4.1}$$

where N is the number of chemical bonds in a network strand, U is the dissocation energy of the weakest chemical bond (J), and ν_{area} is the area density of effective network strands (m^{-2}) [89]. Hence, the hypothesised increase in both

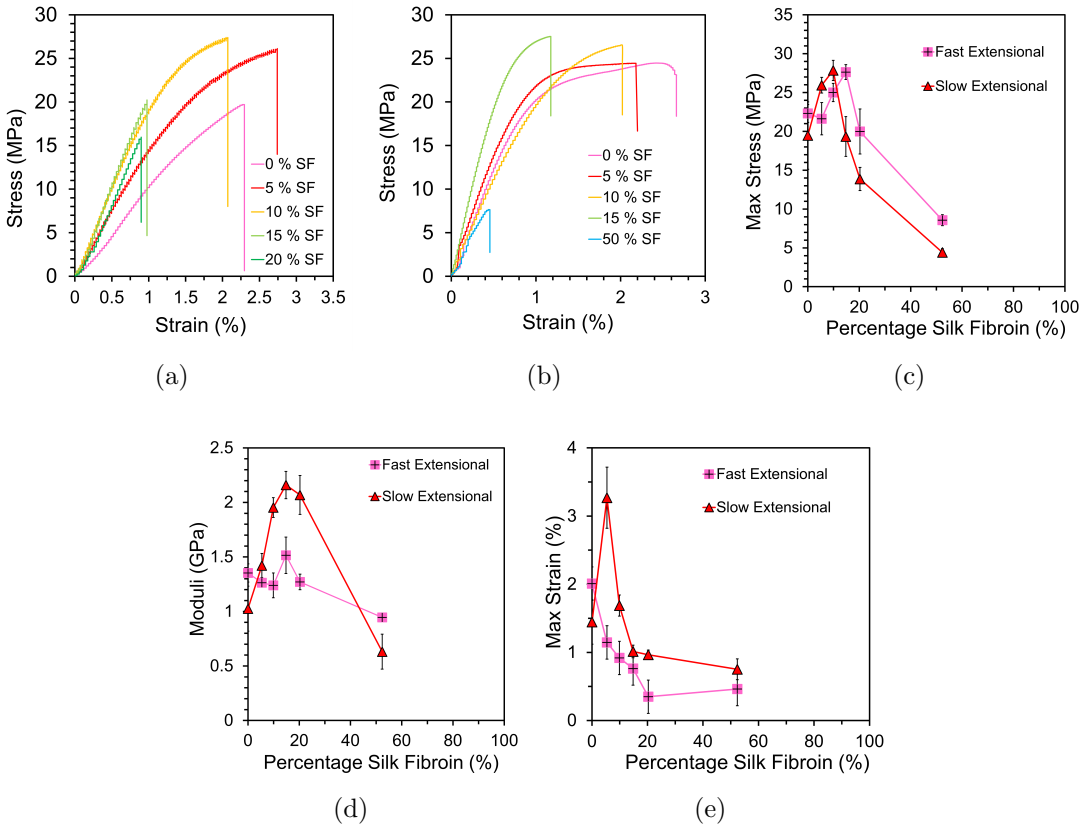

Figure 4.10: Graph showing the stress-strain behaviour of films during (a) 'slow' and (b) 'fast' extensional testing within the extensional regimes. This also shows the extracted average data of the Young's moduli (c), the maximum stress (d), and the strain at failure (e) for 'slow' extensional; and 'fast' extensional tests. All data points given are mean averages with SE given as uncertainty ($N > 3$).

network density and interactions caused by SF interspersal and interactions encourages the increase in material modulus and strength [19]. This is correlated with the presence of a hybrid mixed phase as supported by evidence in Sections 4.3 and 4.3.

Alternatively, Hadadi *et al.* propose a novel theoretical model that accurately correlates bulk properties and microscopic structures. This indicates an increase in modulus with small additions of SF due to entropic contributions [164]. It proposes that composites form sheets of crystalline monocomposition that reduce the number of interfaces seen [164]. Cohesive energies then depend on the ability to

stack and adhere each layer. 'Gelation' of these systems does not originate from chemical crosslinking but from competition between interactions. This triggers phase separation to form the biopolymer hydrogel [164]. Entropy in these systems increases rapidly with small additions of a second component, increasing modulus at low weight percentages of SF composition. Compositions closer to 50:50 then show a greater energetic dependence instead [164]. Hence, it is likely the peak in sample modulus is caused by a combination of entropic and enthalpic contributions.

Notably, in the strain at failure comparisons, monotonic decrease is shown with increasing SF content at fast rates of deformation. At slow rates of deformation a non-monotonic trend is seen, as shown in Figure 4.10 (e) and 4.9 (e). This shows both conflicting trends shown in literature examples: Zhou *et al.* showed a monotonic decrease in properties with added SF; and Tian *et al.* showed a non-monotonic increase in strain at failure [18, 99]. This shows the impact of strain rate on the deformation behaviour of samples. With slow deformation sample relaxation occurs in the hybrid samples between 5-15 % SF allowing greater deformation. This implies the presence of a slow relaxation capable of deforming samples, and imparting rate dependent viscoelastic behaviour. Similar trends in flexural testing data (see Figure 4.9 (e)) support this conclusion. This viscoelastic behaviour is further investigated in Section 4.3. Variation of this peak between comparable studies and samples shows dependence on mixing, testing conditions, polymer compatibility, and component source [1, 85].

Static Mechanical Analysis

Static testing was performed at both a set strain and stress value. This gave stress relaxation and creep test results, both of which were measured in flexural modes.

Stress Relaxation Testing

Stress relaxation tests confirmed the increased moduli of hybrid samples (shown above in Figures 4.9 (d) and 4.10 (d)), as shown by an increase in the stress applied to achieve the given strain. Interestingly, a larger amount of irrecoverable strain

was also seen with these samples after testing. This, as seen in Figure 4.11, shows the presence of viscous relaxation behaviour in hybrid samples. This occurs due to the pronounced secondary creep causing stress relaxation over long periods of time for these samples [223].

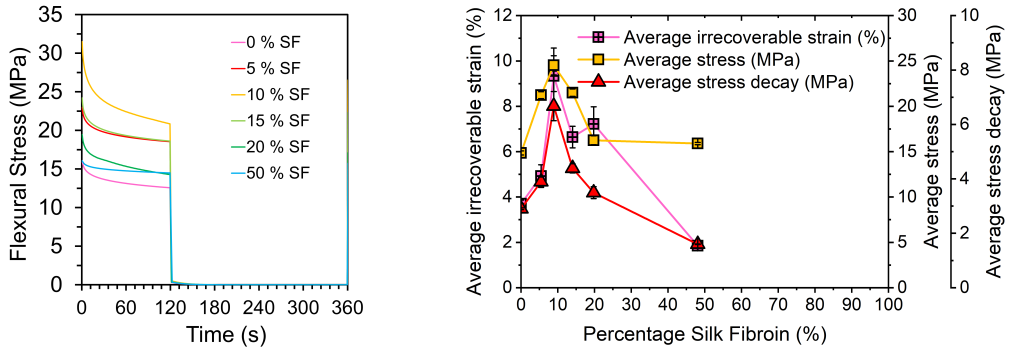

(a) (b)

Figure 4.11: Graphs showing (a) representative stress relaxation at 1 % flexural strain and (b) trends in average irrecoverable strain, average maximum stress, and the average stress decay. All data points given are mean averages with SE given as uncertainty ($N > 3$).

The presence of a slow relaxation mechanism with small addition of SF could point at a molecular slipping mechanism occurring at these hybrid compositions. The presence of hybrid phases, as confirmed in Section 2.5, with weaker interactions could act as regions of 'sacrificial bonds' as described in double network theory [89]. This could give rise to localised failure, allowing slippage and molecular rearrangement in hybrid samples. This mimics the slippage mechanism also proposed by Mohammadi *et al.* for cellulose composites with higher lengthscale reinforcement [86]. A visualisation of this mechanism can be seen in Figure 4.12.

This also mirrors behaviours shown in more complex biological gels. In studies on extracellular matrices and cytoskeletons, as strain is increased gels stiffen and exhibit faster stress relaxation [138, 217, 218]. This dissipates internal stress and elastic energy. This effect is not universal amongst biopolymer networks, but is proposed to occur due to weaker transient bonds, like the hydrogen bonding interactions seen in SF and cellulose hybrids [138, 217, 218]. This non-linear response to strain rates also highlights the presence of multiple relaxation times, as

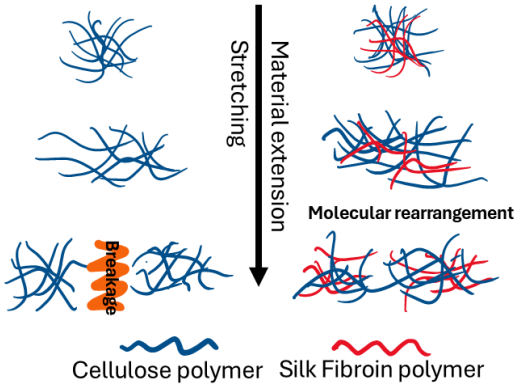

Figure 4.12: Diagram indicating the slippage mechanism for molecular rearrangement in hybrid bioplastics, in comparison to pure cellulose failure and breakage.

indicated by fittings of stretched exponentials with β values between 0.06 - 0.31 in Table 4.1. This is used here as an indicative measure of stress relaxation, showing the quickest macroscopic relaxation time at 10 % SF content [139]. Further understanding of microscopic relaxation processes could be achieved in follow-on studies with X-ray photon correlation spectroscopy [139]. The non-monotonic increase in stress relaxation differs from the monotonic change in side group mobility shown by DMTA. This indicates the sliding mechanism proposed is mediated by higher order cooperative motion allowed by sacrificial bonds at interfaces.

Table 4.1: Stretched exponential fitting values showing the stretched exponent, β, and macroscopic relaxation time, τ_M, for samples of different SF compositions during the stress relaxation testing.

SF / %	Stretching Exponent	Relaxation Time / s
0	0.06	620
5	0.13	650
10	0.15	310
15	0.06	880
20	0.28	710
50	0.15	1250

Creep Testing

To confirm theories about the behaviours shown in Sections 4.3 and 4.3 we analysed the behaviour of samples under constant stress. This also confirmed the pronounced viscous behaviour shown between 5-15% SF. This was shown by an increase in total irrecoverable strain and in the total strain over time during creep tests, as shown in Figure 4.13.

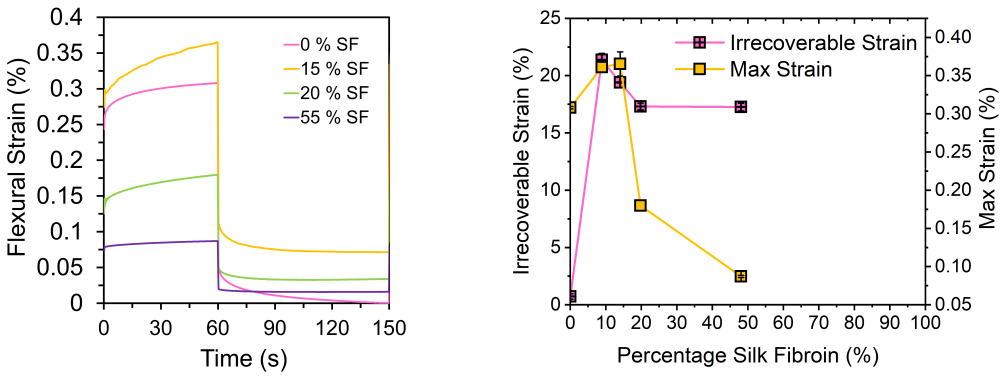

(a) (b)

Figure 4.13: Graphs showing (a) representative creep test strains for 8 MPa stress application and release (b) trends in average irrecoverable strain and the maximum strain achieved on average. All data points given are mean averages with SE given as uncertainty ($N > 3$).

Under 8 MPa of stress, the purely cellulose film showed a largely elastic behaviour, with little irrecoverable strain seen. With added SF, viscous behaviour was shown by the presence of irrecoverable strain. This could indicate that under this given stress the 'slipping' relaxation mechanism occured and incurred a secondary, steady state creep to relax the polymer network [223]. This is also reflected in the gradient difference between 15 % SF samples and 0 % SF samples after 60 seconds of deformation. This strain behaviour indicates prolonged creep in these samples. This could indicate that the reduced strength of mixed biopolymer interactions allows for these 'sacrificial bonds' to fail under applied stress [1, 86]. Higher protein contents caused brittleness as they no longer allow for dissipation of energy by reformation of hydrogen bonds [86]. Hence an optimum SF content gives a cohesive matrix. This value was about 30 % SF

content within the matrix for Mohammadi *et al* but is between 5-15 % SF in our study [86]. This may be as a result of various factors including: solvent choice, polymer source, purity, alignment, and polymer chain length [1, 75, 85, 86, 117].

Water Contact Angles (WCA)

Having established an understanding of the mechanical properties water contact angle (WCA) testing was performed to indicate the hydrophilicity of the samples. This behaviour can impact biological, chemical, and physical processes. The results can be seen in Figure 4.14.

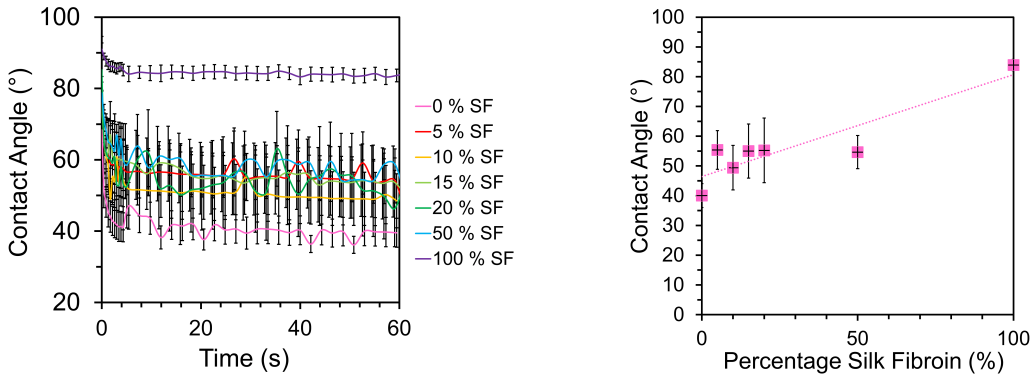

(a) (b)

Figure 4.14: Graphs showing (a) mean average contact angle plotted against time in wetting tests for various hybrid films and (b) average contact angle from 30 – 60 seconds plotted against the percentage silk fibroin showing a positive correlation. Linear trend line included as guide for the eye. All data points given are mean averages with SE given as uncertainty ($N > 3$).

Figure 4.14 (b) indicates a monotonic increase in the WCA with SF addition, though also shows high deviation between samples causing significant overlap. The positive correlation with hydrophobicity and increasing silk fibroin content could explain the antibacterial properties often associated with silk fibroin addition to hybrid biopolymeric materials. The positive correlation indicates this is primarily due to surface energy changes [183], but variations in surface roughness, and pore size cannot be distinguished from these results. These are also dependent on sample composition, so could be the driving factor into differences

in surface wetting behaviour. The correlation could also be a reflection of the loss of available hydrogen bonding sites in SF rich samples inhibiting water adsorption. To further investigate this behaviour surface roughness could be measured with atomic force microscopy, which could elucidate the relationship between chemical composition and surface morphology.

4.4 Conclusions

In this chapter, we indicate an optimum in material strength and stiffness (28 ± 1 MPa and 2.2 ± 0.1 GPa) with tensile testing at approximately 5-15 % SF compositions. We confirm this optimum with further flexural testing. This modulus value is comparable to those found for equivalent materials in literature. Zhou *et al.* reported a modulus of 1.6 ± 0.4 GPa for a 3:1 cellulose:SF film prepared by complete dissolution in BmimCl and coagulation in methanol and water. They also reported an elevated maximum stress of 120 ± 10 due to an increased strain at failure of 18 ± 2 %. This could result from differences in polymer source or processing.

We also demonstrate a dependence of properties on strain rate and confirm, with stress relaxation and creep testing, viscoelastic behaviours characteristic of slow creep and stress relaxation. This material behaviour matches trends shown in complex cytoskeletal examples also possessing transient bonds [138, 217, 218]. Both of these behaviours are attributed to the presence of mixed amorphous phase of SF and cellulose indicated by TGA, and DMTA. This interspersed double network increases interaction density and interfaces, increasing material strength from added enthalpic and entropic contributions. In addition, the failure of 'sacrificial' transient hydrogen bonds under stress within this double network allows network relaxation [86]. This causes a large-scale relaxation which may contribute to conflicting trends previously unexplained in literature.

Increasing the lengthscale of reinforcement and comparing material properties could offer insight into further optimisations possible with this system; as aligned reinforcements showed higher material toughness than isotropic dispersed fibre reinforcements [24, 224]. The fully dissolved film from this study could act as an effective matrix for a self-reinforced composite with high performance to better

implement these materials in numerous applications, such as biomimetic tissue replacements. To this end, the Chapter 5 will explore the creation and testing of reinforced short-fibre composites with a hybrid matrix.

4. PROPERTIES OF HYBRID SILK FIBROIN/CELLULOSE FILMS

Chapter 5

Biocomposites Comprising of Short Cellulose Fibres in a Hybrid Cellulose/Silk Fibroin Matrix.

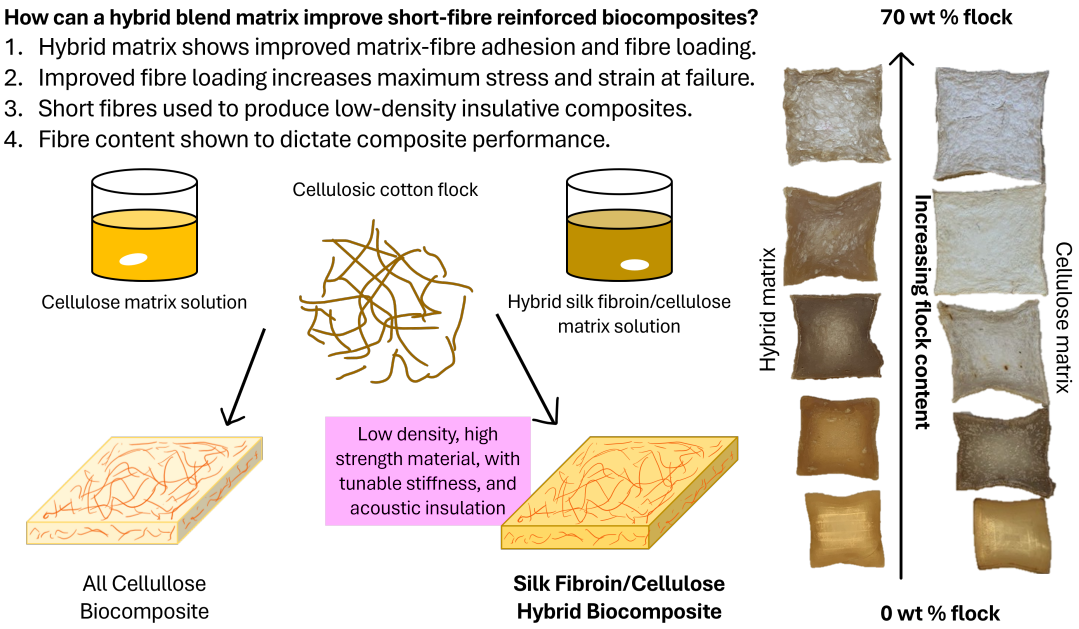

Figure 5.1: Graphical abstract indicating the study and fabrication of short fibre reinforced with matrices of cellulose and a cellulose/SF hybrid blend.

5.1 Introduction

As concerns about environmental damage grow, the need for sustainable and effective replacements for traditional petroleum-based materials has become increasingly evident. Ideal solutions should be sustainably sourced, processable, biodegradable, and high-performance. Although synthetic polymers are widely used due to their low cost and uniformity, they are unsustainable, exhibit poor biocompatibility, and may produce toxic degradation products [1]. Biopolymers, such as cellulose and silk fibroin (SF), address these challenges and are thus of great interest.

Blending these two biopolymers has been shown to enhance material strength, stiffness, and biocompatibility [2, 78, 82, 83, 84]. Tian *et al.* showed with nuclear magnetic resonance studies that SF and cellulose were miscible due to hydrogen bonding encouraging molecular association [18]. This was supported by atomic force microscopy studies which indicated homogenous blending [18, 82, 87]. In the previous chapter, we optimized hybrid films by composition to produce samples with improved modulus, strength, and flexibility due to increased molecular interactions and viscoelastic network relaxation facilitated by molecular slippage [86, 165].

Combining the concept of hybrid biopolymer blends with isotropic short fibre reinforcement offers a novel approach to repurposing waste materials into high-performance, circular materials. Natural fibre materials have good thermal insulation, acoustic insulation, and mechanical properties [193, 194]. Victoria *et al.* demonstrated all-biopolymer composites of woven cotton can improve mechanical properties over the raw material [20, 181]. They achieved a Young's modulus of 3.4 ± 0.2 GPa and an average tensile strength of 72 ± 2 MPa: values comparable with some widely used engineering plastics [181]. Adapting these self-reinforcing composites (and optimising them with hybrid matrices) to utilise short-fibre reinforcement will allow for the direct use of post-consumer waste textiles. Energy use in building can be up to 40 % of the total energy consumption in industrialised countries and improved insulative materials would reduce this environmental impact [225]. Use of natural textile waste avoids incineration of these

materials while promoting carbon sequestering natural fibre industries, which have been adversely affected by synthetic fabric market growth [21, 113, 194].

In this chapter, we compare the performance of isotropically reinforced short fibre biocomposites with cellulose and optimised hybrid matrices (90:10, cellulose:SF). We prepare composite samples by reinforcing hybrid cellulose/SF biopolymer solutions with isotropically oriented cellulosic cotton flock and systematically vary the weight percentage of reinforcing cotton flock. We utilise ionic liquids as our solvent for biopolymer dissolution as a sustainable solvent with effective dissolution, recyclability, and minimal environmental impact [11, 34, 35]. We chose 1-ethyl-3-methylimidazolium acetate (EmimAc) and dimethyl sulfoxide (DMSO) as our solvent mixture based on the optimisation study, performed in Chapter 3, for the dissolution of SF and cellulose [159].

X-ray diffraction (XRD) is used to establish the morphology and hence the fibre volume percentage of the composites. Gravimetric density analysis is then used to indicate the effect of increasing reinforcement content on processing conditions, resulting in decreasing density. The different matrices are compared to show that the hybrid solutions give superior fibre interpenetration and adhesion. Tensile testing was then performed to show superior performance in samples with hybrid matrix due to improved extensibility, fibre loading, and fibre-matrix adhesion at interfaces. The experimental evidence is used to validate a model composite modulus prediction to allow future sample tunability. Characterisation with optical and scanning electron microscopy is used to confirm behaviours seen and discuss failure mechanisms. Lastly, the samples are characterised with acoustic insulation testing to indicate the applicability of these materials. The proposed composites are shown to produce valuable materials and indicate the importance of both biopolymer blends and short-fibre reinforcement for textile waste usage. This promising study provides motivation for future testing of these materials in structural applications with acoustic insulation needs, or in biomedical applications [1, 24, 116].

5.2 Materials and Methods

Sample Preparation

The hybrid solution of cellulose and silk fibroin was prepared with a 10 % SF and 90 % cellulose polymer composition, based on the previous chapter indicating a peak in hybrid matrix performance between 5 - 15 wt % SF content [165]. The solvent ratios were selected based on the previous chapter detailing the effective dissolution of SF and cellulose with EimmAc and DMSO solvent mixtures [1, 64, 159]. A diagram of the production process can be seen in Figure 5.2.

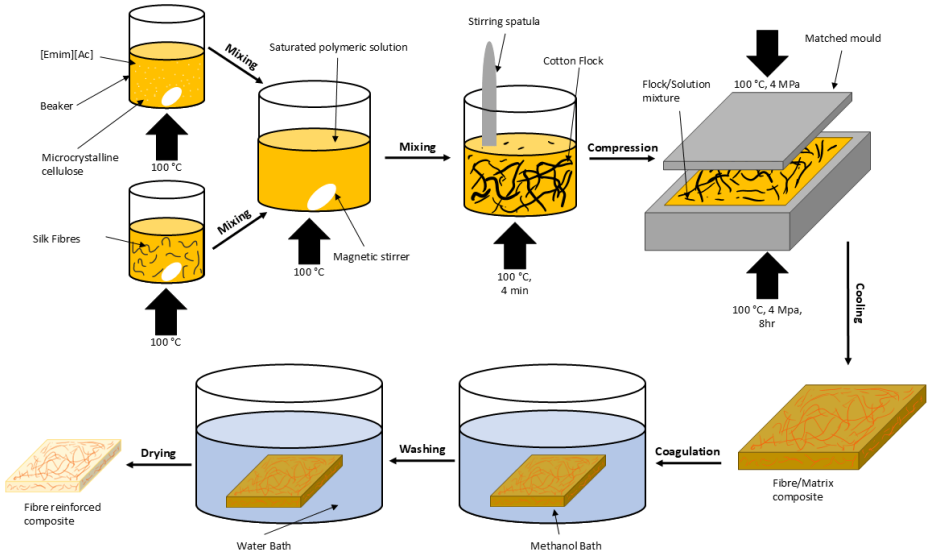

(a)

Figure 5.2: Diagram indicating the production process for the composites with a hybrid matrix.

Cellulose was dissolved at 10 wt% in a 20:80, EmimAc:DMSO mixture of solvents. Silk fibres were dissolved at 10 wt % in an 80:20, EmimAc:DMSO mixture of solvents. Polymeric solids were firstly dispersed in the relevant weight of DMSO, then stirred and preheated to 100 °C for 30 mins. The relevant weight of EmimAc was preheated at 100 °C for 30 mins then mixed with the dispersed solids in DMSO. Solutions were then stirred for 16 hr, at 100 °C, at 200 rpm to produce pale yellow to dark amber transparent solutions. Hybrid solutions were

prepared by mixing the SF and cellulose solutions at the required ratio for 30 minutes, at 100 °C and 200 rpm. Cellulose solutions were prepared by the same cellulose dissolution method without mixing in SF solution. All dissolution was performed in sealed vessels to reduce the effects of humidity on dissolution.

The polymer solution was then mixed with cotton flock for 5 minutes until the mixture was homogenous. Both flock and solution were preheated to 100 °C and stirred while heated at 100 °C. The mixture of undissolved flock and polymeric solution was then dispersed in matched moulds and compressed for 8 hours at 4 MPa and 100 °C. This period and pressure was selected after a short optimisation study described below. Samples were then removed from compression and allowed to cool to room temperature for 12 hours. Samples were coagulated in a methanol bath for 24 hr before washing in deionised water (5 l) for 48 hr. The water was replaced twice in that period. Coagulated and washed samples were dried at room temperature and humidity for 6 hr. Samples were compressed between metal sheets ($\approx$ 10 KPa using bulldog clips), to alleviate deformation due to differential shrinkage during drying and cooling, then dried for 24 hr at 60 °C whilst still under compression. Sample thickness varied from 1.2 - 3.9 mm with increasing reinforcement correlating with reduced shrinkage as discussed in Section 5.3. Images of samples at each stage of production can be seen in Figure 5.3.

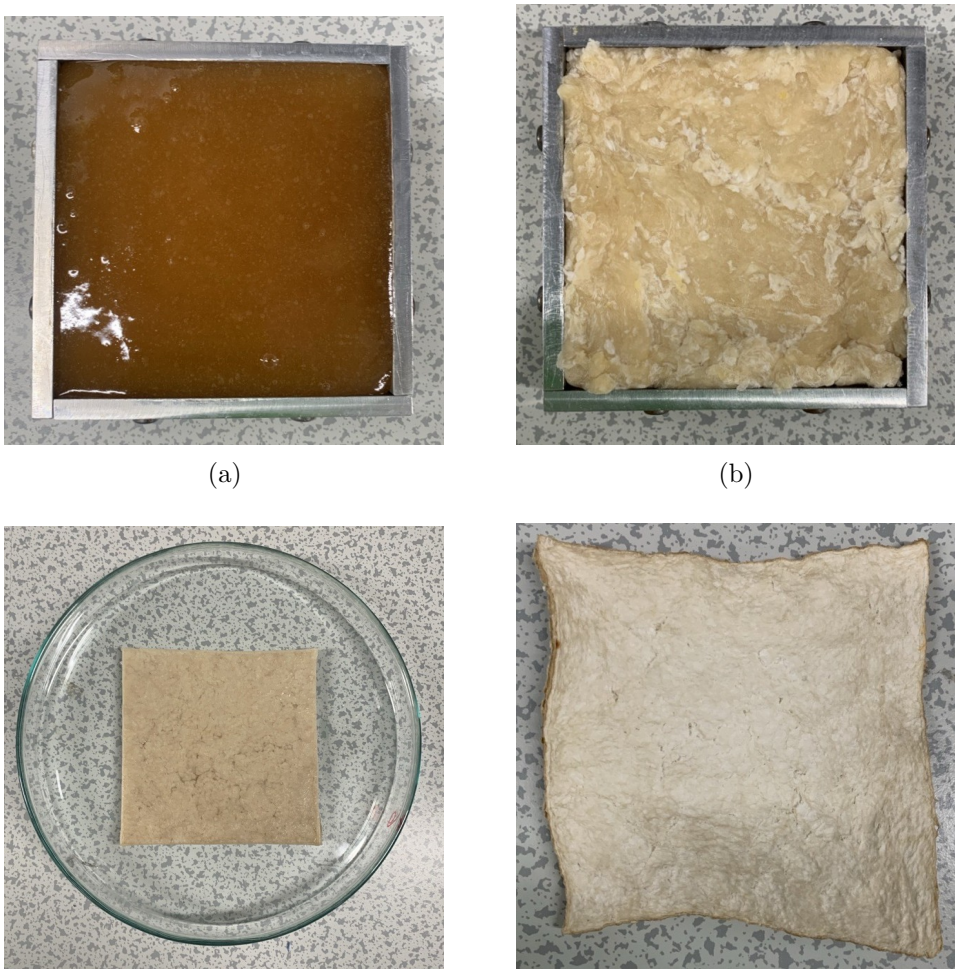

(a) (b)

(c) (d)

Figure 5.3: Images of (a) a hybrid polymer solution of 10:90 silk fibroin: cellulose in EmimAc/DMSO solvent mixture showing bubbles present directly after mixing, (b) an example flock/solution mixture of 66 wt% cotton flock and 34 wt% polymer matrix after dispersion into a matched mould, (c) an example coagulated and washed composite before drying as a hydrogel, and (d) a fully prepared composite after drying.

Before any characterisation, samples were equilibrated under ambient conditions for at least 24 hours. The average room humidity was 50 ± 1 % and the average temperature was 20.6 ± 0.2 °C. Analysis results were averaged over at least three measurements, unless otherwise mentioned, with errors calculated as the standard error. Examples of samples with cellulose and hybrid matrices can

be seen in Figure 5.4. Throughout this chapter the reinforced samples with hybrid or cellulose matrices will be referred to as only hybrid or cellulose samples respectively.

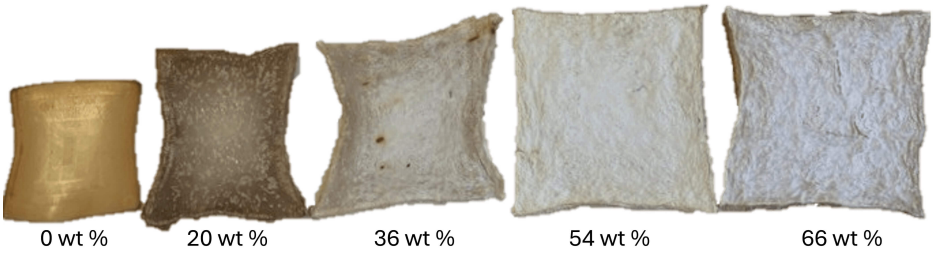

(a)

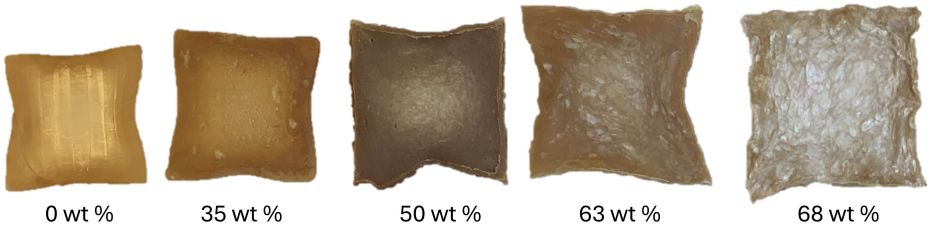

(b)

Figure 5.4: Images of example composites ranging from 0 to approximately 70 wt % fibre content for (a) cellulose matrices reinforced with cotton flock and (b) hybrid matrices reinforced with cotton flock. In the image, reinforcement concentration increases from left to right. It can be noted that with increased fibre content samples experienced less shrinkage.

This methodology was selected after a series of screening stages were performed to improve efficiency and maximise the resulting performance of composites. With a nominal preparation method adapted from literature samples with pure silk, optimal hybrid (9:1 cellulose:SF), and pure cellulose matrices were prepared with 50 wt % reinforcement from cotton flock, silk flock, or a 50:50 flock mixture. Resulting samples can be seen in Figure 5.5. It was found that utilising silk flock as the reinforcing agent resulted in excessive reinforcement dissolution and inferior resulting composites. This may be due to the noted sensitivity on thermal history of silk materials [144].

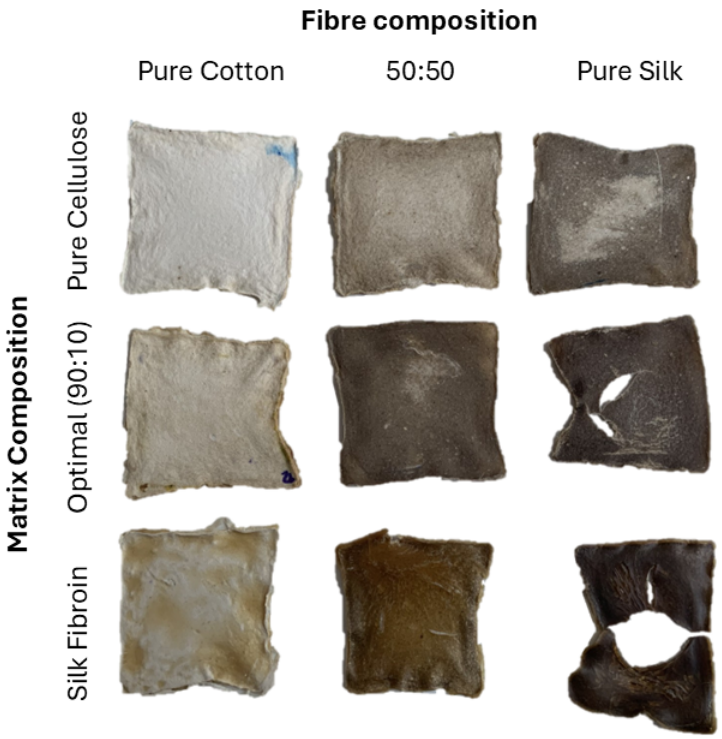

Figure 5.5: Images of sample composites produced cellulose, optimal hybrid, and SF matrices with cotton or silk flock reinforcement indicating the increased solvation and sample failure in silk reinforced samples.

A high viscosity sample of 50 wt % cotton flock with cellulose matrix was then selected and the compressive stage of preparation was optimised by varying the vessel for compression, the temperature, and the pressure. Matched moulds were seen to effectively compress the composites during mixing, to reduce wastage due to flash, and to allow the formation of cohesive composite samples [20]. These were selected after comparison with uncompressed samples, and samples compressed in a picture frame. Lastly, compression time and pressure were varied to investigate the optimal preparation procedure using simple experimental design concepts to effectively probe the parameter space [181]. Samples were tested with compression times from 0 to 24 hours and compression pressures from 0-6 MPa. The resulting moduli and bulk densities of samples resulting from this testing can be seen in Figure 5.6.

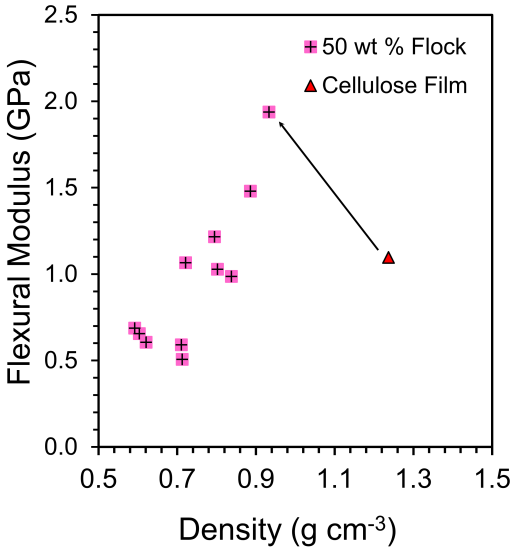

Figure 5.6: Ashby plot of flexural modulus against density for cellulose film and a series of cellulose matrix composites with 50 wt% cotton flock reinforcement. The density and modulus of reinforced samples varies as a result of altered compression parameters during manufacture. The arrow is included as a guide for the eye to indicate the optimal sample's increased modulus with reduced density in comparison to a non-reinforced film sample.

The optimal sample was elected as one with the maximum flexural modulus and was produced with a pressure of 4 MPa for 8 hours. Interestingly, at a single flock composition, the modulus is seen to increase linearly with density increase. Hence, the densest sample also produced the sample with the highest modulus.

Sample Testing

Dumbbells of each sample were tensile tested as described in Section 2.2. The bulk density and the true density of all samples were tested as described in Section 2.8. The acoustic insulation performance of samples was tested as indicated in Section 2.8. After fabrication, cross-sections of each sample were cut and optically imaging as shown in Section 2.7.Secondary imaging was performed with SEM as described in Section 2.7. The morphology of each sample was tested with XRD 2θ scans as detailed in Section 2.6. To investigate crystallite orientation, scans

from $\alpha = 0$ to 90° were also performed. The 2θ angle was set to 22.4° to probe the orientation behaviour of cellulose I crystals and hence of reinforcing fibres.

Reinforcement Volume Fraction Analysis

The volume fraction of internal reinforcing fibres (cotton flock) was estimated using analysis of crystalline polymorphs from XRD. This was done to overcome difficulties in distinguishing the fibres from the chemically indistinct and interdiffused matrix. Firstly, the ratio of Cellulose I to Cellulose II crystalline polymorphs in cotton flock (R_{CF}) was derived by the following equation:

$$R_{\mathrm{CF}} = \frac{CI_{\mathrm{CelluloseI}}}{CI_{\mathrm{CelluloseII}}} \tag{5.1}$$

where $CI_{\mathrm{CelluloseI}}$ is the crystallinity index of Cellulose I determined as described in Section 2.6. The ratio of Cellulose I to Cellulose II crystalline polymorphs in each composite, $R_{\mathrm{Composite}}$, is then found for all samples. As Cellulose I is only present in raw/undissolved cellulose samples it can then be assumed all Cellulose I content is present only in the undissolved reinforcing fibres [67, 79]. By assuming that diffraction intensity correlates with the volume fraction of the diffracting polymorph the volume percentage of cotton flock content ($Vol\%_{\mathrm{CF}}$) can be estimated by:

$$Vol\%_{\mathrm{CF}} = \frac{R_{\mathrm{Composite}}}{R_{\mathrm{CF}}} \times 100\% \tag{5.2}$$

Flock Analysis

To aid with theoretical modelling of the composite behaviours, representative samples of the reinforcing cotton flock were dispersed on glass slides, imaged, and analysed to indicate the distribution of fibre lengths, widths, and aspect ratios. Images were taken in transmission mode at 10 × magnification using a Leica non-polarised light microscope (London, United Kingdom) with a Nikon D7200 digital camera (Tokyo, Japan). Multiple images were taken across five different samples and a total of more than 1000 individual fibres were counted. Fibre lengths and widths were analysed in ImageJ as shown in Figure 5.7. In

addition to the cotton flock used, the reinforcing silk flock used for comparative testing in Section 5.2 has also been imaged.

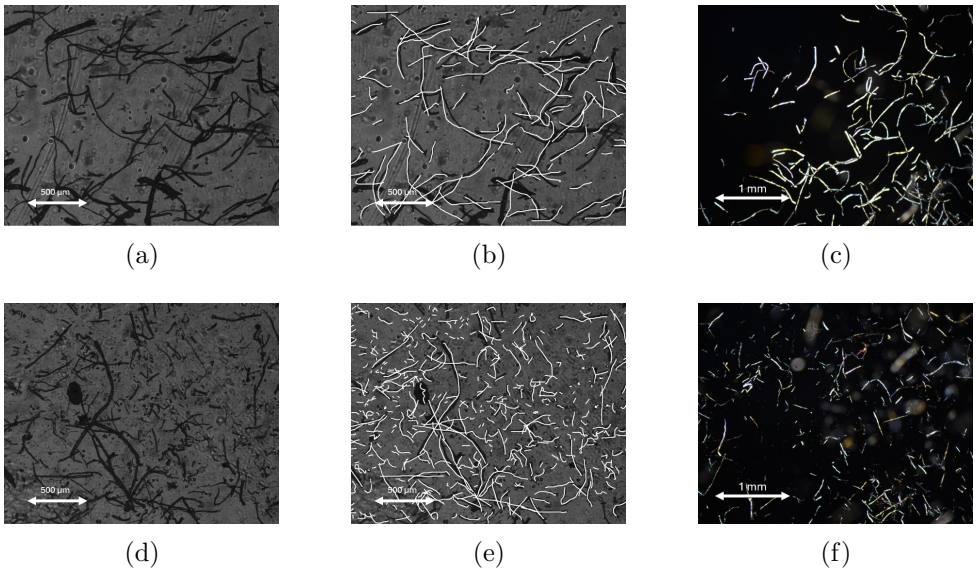

(a) (b) (c)

(d) (e) (f)

Figure 5.7: Optical microscopy images of dispersed cotton (a,b,c) and silk (d,e,f) flock across a glass slides before and after marking of all fibres with ImageJ with which individual fibre widths and lengths were measured. (c) and (f) show the polarised optical microscopy images. The width and length were taken to calculate the aspect ratio of each fibre.

It can be clearly noted that the silk flock demonstrates a higher content of impurities as indicated by the qualitative differences between Figures 5.7 (d) and (f). While the polarised image only captures polymeric silk content the non-polarized image captures instead all of the flock content which can be compared to indicate impurities. The difference shown highlights the non-silk content in this flock which could contribute to increased impurity in the silk reinforced composites causing increased ease of fracture. The lengths and widths of each fibre from Figure 5.7 (a) and (d) were used to calculate the aspect ratio and distributions were used to generate mean, median, and modal average values as shown in Figure 5.8. As shown to be suitable by Virk *et al.*, the median was used for theoretical modelling though the mean average has been used in other studies [226, 227].

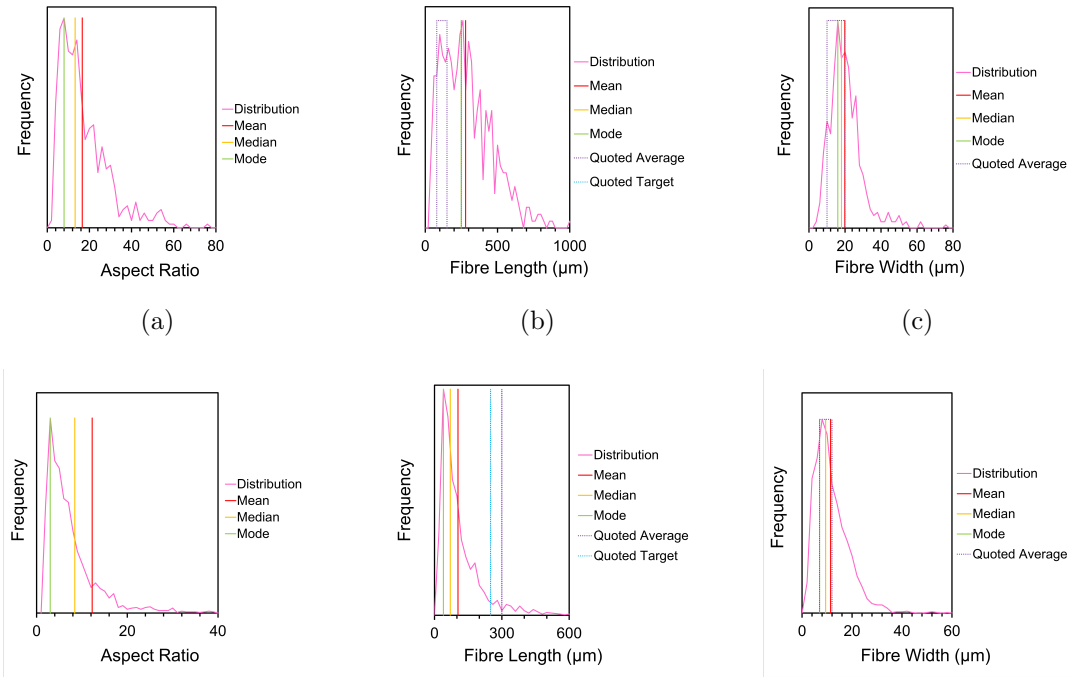

Figure 5.8: The distribution of aspect ratio, length, and width for cotton (a,b,c) and silk (d,e,f) flock samples with statistical data marked. The quoted average and quoted target refer to target and measured values provided by the distributor, Goonvean.

Figure 5.8 shows the resulting statistical analysis from the flock sizing of both cotton and silk flocks. It can be seen that silk fibres have a smaller mean length and width compared to the cotton fibres. The silk flock was reduced in length compared to the average quoted by the distributor. The aspect ratio of the flock was of key importance, as discussed later in Section 5.3, with a larger aspect ratio increasing the reinforcing efficiency of the fibre. The silk flock showed a reduced median aspect ratio (8.4) compared with that of the cotton flock (13.2) so the cotton flock was used going forward.

5.3 Results and Discussion

Morphology Analysis

Morphological analysis was performed using XRD to indicate the crystalline and amorphous morphology of samples. This indicated an increasing presence of Cellulose I with increased content of undissolved fibres as shown in Figure 5.9 (a). The crystallinity of samples was estimated with Gaussian fittings then used to calculate the fibre volume percentages shown in Figure 5.9 (b). Only analysis for samples with cellulose matrices have been included as SF and cellulose crystals produce overlapping peaks in the 2θ scans and hence cannot be fitted using the same gaussian method in XRD. Discussion of this behaviour can be seen in Section 5.3.

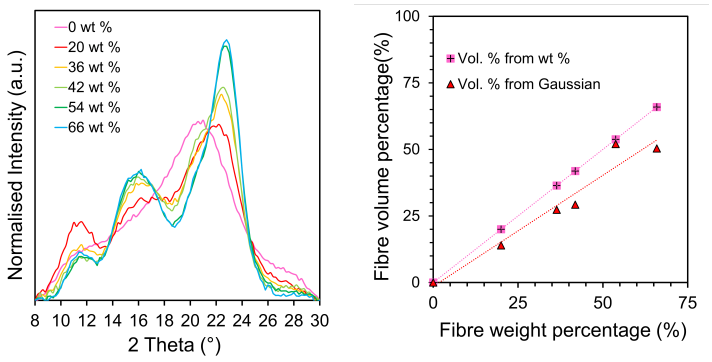

(a) (b)

Figure 5.9: Graphs showing (a) normalised XRD diffractograms for composite samples with cellulose matrix and cotton flock reinforcement with fibre weight percentage indicated, and (b) calculated fibre volume percentages against the fibre weight percentage. The fibre volume percentages have been calculated from Eq. 5.2 with Gaussian peak fitting of XRD, or by assuming the fibre weight percentage is equal to its fibre volume percentage.

On addition of undissolved fibres, the relative size of the cellulose I peaks can be seen to increase. This can be seen in particularly in the main diffraction peak at 22.4° in Figure 5.9 (a). Simultaneously, Cellulose II peaks and the central amorphous peak at ≈19° are seen to decrease relatively. This is reflected in

the estimated volume fraction of cotton fibre increasing with added cotton fibre content in Figure 5.9 (b).

Notably, the calculated volume fraction of cotton fibres is lower than that estimated by assuming the fibre weight percentage is equal to its fibre volume percentage. Assuming the density of the cellulose fibres and matrix are equivalent as shown in Figure 5.11, this indicates that partial dissolution is occurring. This is supported by previous studies showing the concentration of the matrix solution is slightly below that of the maximum saturation concentration of the chosen solvent mixture [159]. This is also supported by the cohesive matrix-fibre interface shown in Section 5.3, indicating polymer penetration from matrix to fibre, as shown in other studies including partial dissolution [22, 53, 181]. As hybrid samples couldn't be characterised using this method, the average percentage of undissolved cotton flock was calculated as $\%_{\mathrm{UCF}} = \frac{Vol\%_{\mathrm{CF}}}{Vol\%_{\mathrm{Weight}}} \times 100\%$ where $Vol\%$ is the volume percentage calculated from gaussian fitting or estimated as equal to the weight percentage. From this $\%_{\mathrm{UCF}} = 78 \pm 5\%$ which was used to estimate the $Vol\%_{\mathrm{CF}}$ for hybrid samples. Volume percentage is used to indicate fibre content in samples for subsequent mechanical analyses in this chapter unless otherwise mentioned.

Density Analysis

Inclusion of reinforcing fibres was observed to effect sample processing and the resulting sample structure. Densities of samples were measured using bulk gravimetric techniques and results can be seen in Figure 5.10.

It can be seen that addition of reinforcing flock causes a reduction in sample density with both hybrid and cellulose matrices. As the cellulosic fibres have an approximately equal density to the matrices (1.3 - 1.5 g cm^{-3}) [180, 181], it can be assumed that the large density decrease is correlated with the presence of internal pores. This is also confirmed by the true density analysis using gas pycnometry. In Figure 5.11 no change in sample true density was seen with changes in content of fibres at values of 1.512 $\pm$ 0.004 g cm^{-3} and 1.498 $\pm$ 0.002 g cm^{-3} for samples with pure cellulose or hybrid matrices respectively. This assumption is supported by work by Yong *et al.* showing density reductions to be caused by internal

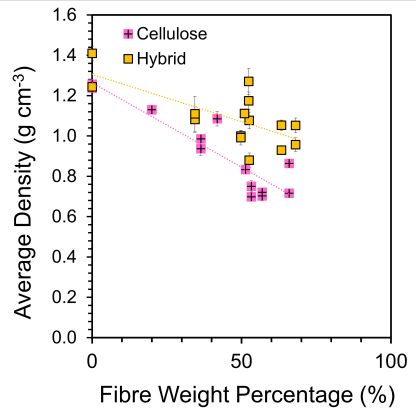

(a)

Figure 5.10: Graph showing the density values of samples with linear fittings for composite samples with hybrid and cellulose matrices. The gradient of these linear fittings, as shown in Table 5.1, is taken to aid in later fittings of modulus theory. All data points given are mean averages with SE given as uncertainty ($N > 3$).

voiding [179]. The presence of pores is indicated by visual evidence in Section 5.3. It was found, during process optimisation, that compressing samples less during manufacture also produced lower density samples. This further indicates the density behaviour is dictated by the presence of voids. This trend is caused by the increasing viscosity of samples during mixing, as undissolved fibres are added, avoiding the collapse of voids during processing. Victoria *et al.* also noted reduced density due to void formation in equivalent samples where solvent or solution penetration was inhibited between reinforcing fibres [20].

The true density of most samples does not vary significantly with fibre addition though a very slight increase in true density can be seen in fibres over amorphous samples. This agrees with studies showing crystalline samples to be of increased density over amorphous polymer content. This confirms the calculations based on the assumption that the bulk density difference is caused by the presence of pores and cavities in composite samples.

The cellulose samples show a larger decrease in density than the hybrid samples with addition of flock. This may be due to the reduced viscosity of SF solutions in comparison to cellulose solution (due to greater chain flexibility and/or

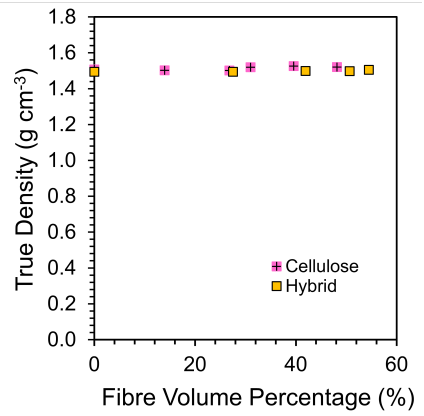

(a)

Figure 5.11: Graph showing the true density values of samples with linear fittings for composite samples with hybrid and cellulose matrices. These values indicate the lack of change in the true density of samples, without considering the presence of pores in the composite. All data points given are mean averages with SE given as uncertainty ($N > 3$). Uncertainties in this graph are too small to be seen.

lower molecular weights) increasing fibre penetration and reducing total void content [1, 21, 159]. Alternatively, the improved solvation ability of the hybrid solution utilised could dissolve more fibre content and hence cause increased void collapse [1, 21, 113, 159]. Linear fits of the data for cellulose and hybrid samples were perfomed and the parameters this are shown in Table 5.1. These fits of sample density behaviours are utilised to estimate trends with respect to density changes in Section 5.3. It may be of future interest to replace the reinforcement with air-laid nonwoven textile waste mats as lower density reinforcement examples to reduce density further for specialised applications [80].

Matrix	c	m
Cellulose	1.26 ± 0.05	-0.8 ± 0.1
Hybrid	1.31 ± 0.07	-0.5 ± 0.1

Table 5.1: Fit parameters for a generalised linear equation, $y = \mathrm{m}x + \mathrm{c}$, for hybrid and cellulose bulk density data as shown in Figure 5.10. The larger magnitude of the negative gradient, c, for cellulose samples indicates the greater dependence of cellulose sample density on flock content

Bulk Mechanical Analysis

To test mechanical performance of samples tensile testing was performed as shown in Figure 5.12. This was done to indicate the bulk behaviours of the composites and compare performance between hybrid and cellulose samples.

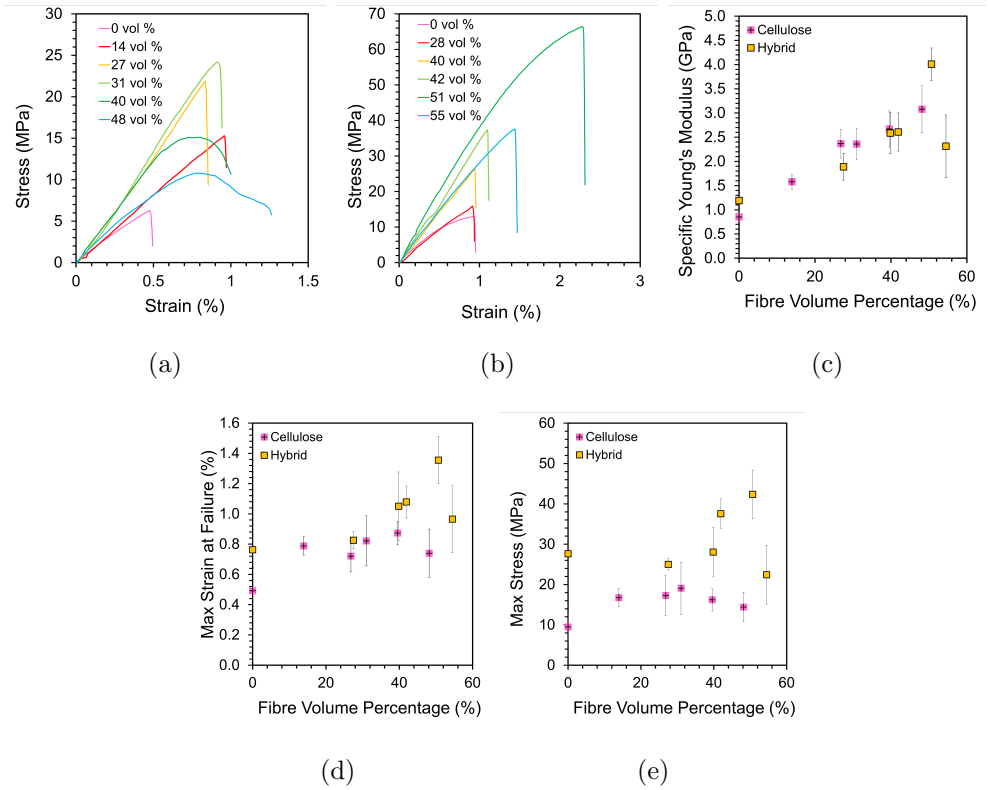

Figure 5.12: Graphs showing example stress-strain curves for tensile testing of (a) cellulose samples, and (b) hybrid samples with extracted average data showing (c) the specific Young's Modulus, (d) max strain at failure, and (e) max stress. The numbers included in the legend of the example stess-strain curves indicate the volume percentage of included flock reinforcement for each sample. All data points given are mean averages with SE given as uncertainty ($N > 3$).

Figure 5.12 (a) and (b) show the stress-strain curves for cellulose samples. It can be seen that samples with higher fibre content did not show brittle failure, as indicated by steep drop in stress after failure. This is caused by the fibre-pullout failure mechanism causing a more gradual reduction in stress upon failure. Variation in this mechanism leads to larger standard error in these samples, though

uncertainty was already pronounced due to sample warp and variation in lab-scale fabrication potentially impacting local fibre alignment. It is also notable that the maximum stress achieved with cellulose samples was lower than that of the hybrid samples. This is primarily due to the presence of significant void content discussed in Section 2.8, and the inferior fibre-matrix bonding seen in cellulose samples with insufficient matrix causing fibre pullout. Secondarily, additional processing time could impact fibre quality due to heat or solvent induced degradation and reduce this value.

As shown in Figure 5.12 (c), both sets of composite samples showed comparable increase in the specific Young's modulus with increases in the fibre volume percentage once voiding was taken into account. As trends in specific modulus agree, within uncertainty, for both hybrid and cellulose matrices it is indicated that the modulus of samples is primarily controlled by the volume percentage of the reinforcing fibres. In support of this, it was shown by Mohammadi *et al.* that aligned SF or cellulose fibres can improve modulus beyond those seen in unaligned examples [1, 86]. This holds true as long as the supporting matrix is of sufficient volume and interfacial adhesion to transfer composite stress to the internal fibres. Deviation from the trend can be seen at maximum content of fibre volume percentage as insufficient matrix is seen in this sample to provide a cohesive composite [76]. The maximum volume percentage achieved was higher than that of typical randomly reinforced composite samples ($V_f = 0.1-0.3$) [228]. This may be due to reinforcing fibre flexibility, or dissolution which is not considered in the optimal cases [159, 228].

It can also be noted for these samples that a negative correlation is broadly observed between sample density and Young's modulus. This breaks from typical convention, as shown in Figure 5.6, and arises due to the reinforcing fibre both encouraging reduced sample density and increasing sample modulus [20, 76]. This simultaneous effect improves samples stiffness while reducing density. This arises due to the described reinforcing behaviour of fibre inclusion occuring alongside cavity formation described in Section 5.3. This could indicate a use for these composites in low density applications.

The hybrid composites are able to form composites with higher volume percentages of fibres due to reduced viscosity and increased saturation concentration

of the hybrid solution. This allows for effective inclusion of higher quantities of fibres and hence a greater maximum modulus. Secondly, the hybrid matrix exhibits a greatly improved maximum strain at failure performance at optimal fibre loading, as shown in Figure 5.12 (d). This may be due to improved matrix extensibility as a result of time-dependent relaxations incurring viscoelastic behaviour in the polymer blend [86, 165]. In these samples sacrificial bonds allow for localised failure and total network relaxation which mimics behaviours seen in high performance natural double networks [89, 138, 165, 217, 218]. This allows fibres to be loaded more effectively and could lead to the dramatic increase in failure stress shown in these samples. The distinct peak in max stress and strain occurs between $42 - 55$ vol % fibre in hybrid samples.

To establish if the modulus results are in line with expectations, the experimental results can be compared to theoretical predictions using standard rule of mixtures for composite models. The modified rule of mixing was altered to model the modulus of the composite (E_{C_i}) while considering the void content with the following derivation.

Considering a section of a material normal to the loading direction the applied load of a composite can be expressed as the contributions from its components [76]:

$$\sigma_c = f\bar{\sigma}_f + (1-f)\bar{\sigma}_m \tag{5.3}$$

Where σ_c is the composite stress, f is the fibre volume fraction, and $\bar{\sigma}_f$ and $\bar{\sigma}_m$ are the volume average stress of the fibre and matrix respectively. It is assumed that sum of the fibre and matrix volume fraction equals one for the loaded cross-section. Therefore, if strains remain equal for all components it can be modelled that [76]:

$$E_c = fE_f + (1-f)E_m \tag{5.4}$$

Where E_c, E_f, and E_m are the moduli of the composite, fibre, and matrix respectively. This is also known as the Voigt rule of mixing, as shown in Figure 5.14 (a), and (b) [229]. This assumes perfect interface adhesion and continuous fibres so models the composite under equal strain. If one instead models the

composite with imperfect adhesion, as particles in a matrix, the stress is instead equilibrated between components as in the Reuss model, $E_c = (\frac{f}{E_f} + \frac{(1-f)}{E_m})^{-1}$. This was noted to significantly undershoot data given in Figure 5.14 which provides support for our theory of good interfacial adhesion.

To develop the Voigt model (Eq. 5.4), it must also be considered that the tensile loading of the fibres from the matrix is dependent on interfacial shear stresses. If one assumes that the matrix and fibre remain elastic and the interface bond is perfect, and the shear stress at the fibre ends is maximum and falls to zero after half the 'critical length'. The tensile stress at the fibre ends is then assumed to be zero rising to a maximum after half the 'critical length'. By modelling the strain of the matrix and fibre as both equal to the composite strain, and that the fibres can be modelled as a hexagonal array the composite modulus of a sample reinforced with fibres aligned along the loaded axis is given by [76]:

$$E_c = (1 - \frac{\tanh{(ns)}}{ns})fE_f + (1-f)E_m = \eta_l f E_f + (1-f)E_m \tag{5.5}$$

where s is the fibre aspect ratio, and n is a dimensionless constant given by:

$$n = [\frac{2E_m}{E_f(1+\nu_m)\ln{(1/f)}}]^{1/2} \tag{5.6}$$

Where ν_m is the Poisson's ratio of the matrix. More detailed derivations can be found in works by Hull and Clyne, based on the original works by Cox [76, 230]. It must also be considered that the fibres may not be oriented in the loading direction which impacts fibre loading and total composite performance. This was modelled by Krenchel's orientation factor to give the modified rule of mixing [226, 227, 229]:

$$E_c = (\Sigma_n a_n \cos^4{\theta_n})\eta_l f E_f + (1-f)E_m = \eta_o \eta_l f E_f + (1-f)E_m \tag{5.7}$$

Where a_n is the proportion of fibres oriented at a fibre angle θ_n relative to the applied load direction. Lastly, for our composites it was noted that significant pores contributed to a reduced sample density. This could be modelled as regions of the cross section which contributed nothing when the sample was loaded. We

modelled this by assuming all density change arose from pore formation, which gave [76, 226, 227]:

$$E_{C_i} = (\eta_o \eta_L E_f f_i + (1 - f_i) E_m) \times \frac{\rho_i}{\rho_{\text{matrix}}} \tag{5.8}$$

where E is the modulus of the composite, fibre, or matrix respectively (GPa); η_o is the Krenchel orientation factor; η_L is the Cox shear lag factor; f_i is the fibre volume fraction corresponding to sample i; and ρ is the density of the pure matrix or the composite respectively. The density term is taken to represent the presence of voids not contributing to stress loading in extension. The reinforcement was modelled as randomly oriented in plane ($\eta_O = 3/8$). The modulus of each matrix, E_m, was taken from the modulus of the given equivalent film and the modulus of the fibre was taken from literature example of cotton fibres, $E_f = 20$ GPa. The aspect ratio of fibres was found, in Section 5.2, to be 13.2. The effect of the fibre aspect ratio on the reinforcing efficiency of the fibre can be estimated by varying the aspect ratio and comparing it with a sample with infinitely long fibres according to Eq. 5.8. Hence, the reinforcing efficiency defines the ability of a fibre to be effectively loading as controlled by shear variation with variation in aspect ratio. This is given as $\text{RE} = \text{E}_\text{c}/\text{E}_\text{Inf}$, where E_c and E_{Inf} are modulus of composites reinforced with short fibres and infinitely long fibres respectively.The results of the aspect ratio variation can be seen in Figure 5.13.

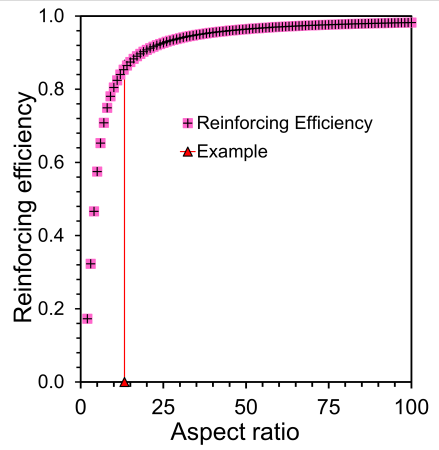

Figure 5.13: The reinforcing efficiency, calculated as the modulus of sample with aspect ratio x divided by a sample reinforced with infinitely long samples (negating the effect of shear lag). This indicates the percentage of effective reinforcement provided by reinforcement of a given length, with aspect ratio of the common flock used marked.

Using the cotton flock's median aspect ratio provides a reinforcing efficiency of 87 % based on the Cox Shear lag factor as shown in Figure 5.13. All data and fittings for cellulose and hybrid samples can be seen in Figure 5.14 [76, 226, 227, 229, 230, 231]. The moduli of experimental samples is fitted against Eq. 5.8 in Figure 5.14 (c) and (d).

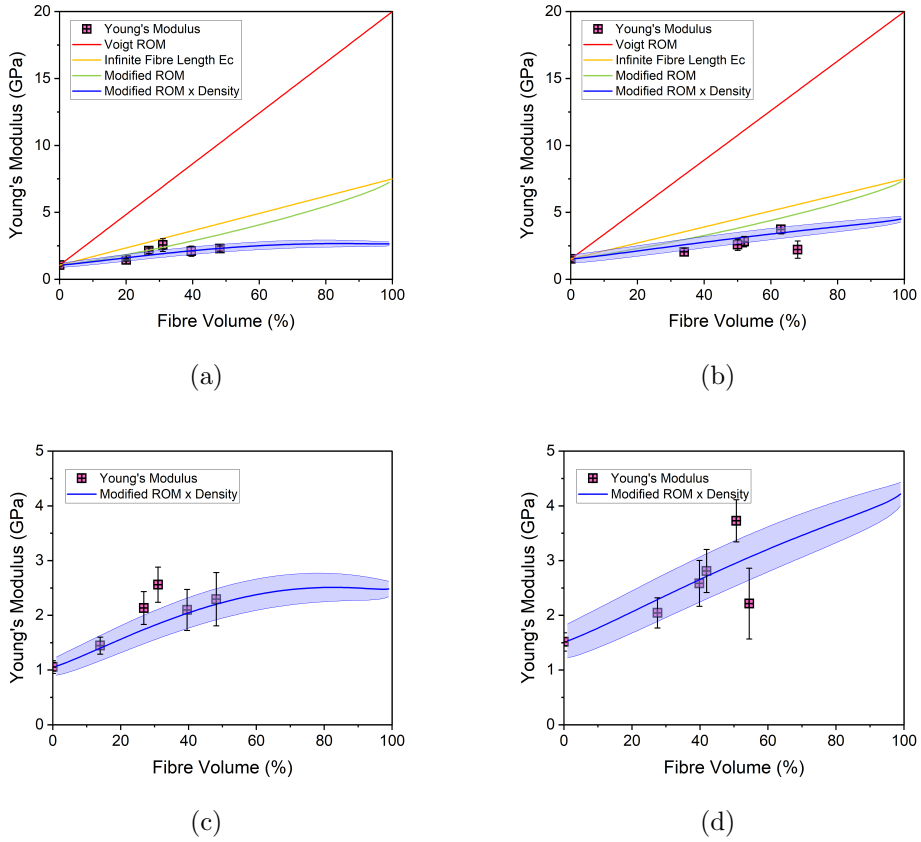

Figure 5.14: Graphs showing the tensile modulus against the fibre volume percentage for all experimentally measured (a) cellulose samples with all different iterations of theoretical modelling applied, (b) hybrid samples with all different iterations of theoretical modelling applied, (c) cellulose samples compared with the final theoretical modelling, (d) hybrid samples compared with the final theoretical modelling. The infinite fibre length, Ec, refers to modelling with only the Krenchel orientation factor applied. The modified rule of mixing (ROM) refers to the modelling with both the Krenchel orientation factor and the Cox shear lag factor applied (Eq. 5.7). In figures (c) and (d) the solid line shows the modified rule of mixtures included Cox, Krenchel, and density fitting parameters (Eq. 5.8). Errors shown with the shaded region are calculated using error propagation. All data points given are mean averages with SE given as uncertainty ($N > 3$).

It can be seen from Figure 5.14 that experimental results largely agree with theoretical fittings, within uncertainties, until composite failure is seen due to insufficient matrix content. At this point sample modulus is seen to decrease, which

can be correlated with insufficient matrix content causing interfacial failure between fibres and reduced stress transfer. The agreement confirms the validity of the model described in Eq. 5.8 and implies the tunability of the field of composites for multiple applications requiring varied moduli. In cellulose samples the optimally reinforced samples fall outside of uncertainties of theoretical predictions. This could be due to alignment of fibres incurred during preparation causing failure of the assumptions used for the orientation modelling. This would cause the modelling to underestimate the modulus of these samples. Though sufficient, the model may be further improved by additional factors to account for the following assumptions which may not always hold true for the composites in question:

1. Fibres are linear and unbent
2. Fibre-matrix interfacial adhesion is perfect
3. The fibres and matrix are under uniform tensile strain

To confirm the system optimum with fibre volume percentage for samples with hybrid matrices several samples were prepared with an optimal fibre content of 48 vol % and tensile tested. This confirmed the maximum in sample modulus at 3.3 ± 0.3 GPa, and indicated bulk anistropy in samples by testing samples at 0, 45, and 90° directions. This can be seen in Figure 5.15.

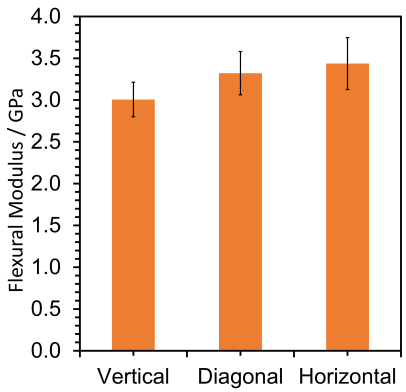

Figure 5.15: Bar chart showing the Young's moduli of an optimised sample tested in strips taken vertically, diagonally, and horizontally to an arbitrary axis in the plane of the flat sample.

Agreement of each sample's modulus within uncertainty regardless of the sample testing direction confirms the bulk anisotropy of samples. Local isotropy was also tested using XRD and confirmed that samples showed local directionality on the sub-mm lengthscale, as shown in Figure 5.16. This was indicated by orientation in an alpha scan, which tests on the mm length scale of the beam thickness, and so shows that fibres remain locally oriented in the composite.

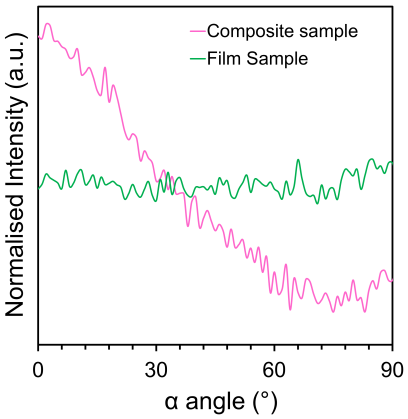

Figure 5.16: Diffractogram showing the normalised alpha scans for the optimised reinforced sample relative to a comparative unaligned film sample. This shows evidence of local directionality of cellulose I crystals below the mm length scale of the XRD beam. This indicates directionality of fibres at this lengthscale.

Figure 5.16 shows the local orientation of Cellulose I crystals in a composite sample and an unreinforced film sample. This confirms the local anisotropy of the composite fibres on the mm lengthscale and the isotropy of the fully dissolved and coagulated film samples. Hence, the fibre reinforced samples present local anisotropy and macroscopic isotropy.

The mechanical performance of these materials indicates a host of promising applications. For example, the sample modulus is within the range seen for cancelous bone (0.05 - 5 GPa) [113, 118]. This, alongside literature evidence of biocompatability, shows that these materials could be used to create biomimetic materials for wound healing applications [85].

Failure Analysis - Sample Imaging

After testing, sample failure mechanisms and structures were analysed by imaging with both polarised optical microscopy and SEM. Polarised optical microscopy was performed on thin cross sections cut from samples while SEM was performed directly on the failure cross sections of tensile tested samples. Images of the cellulose samples can be seen in Table 5.2.

Table 5.2: Images of composite cross sections for cellulose and hybrid samples in polarised optical microscopy and SEM. Samples of various fibre volume percentages shown at different magnifications.

Cellulose Matrix		
25 %	**40 %**	**50 %**
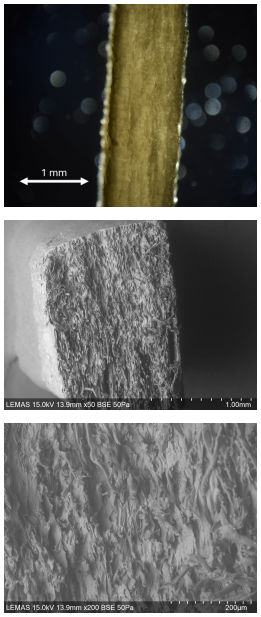		
Hybrid Matrix		
30 %	**40 %**	**55 %**
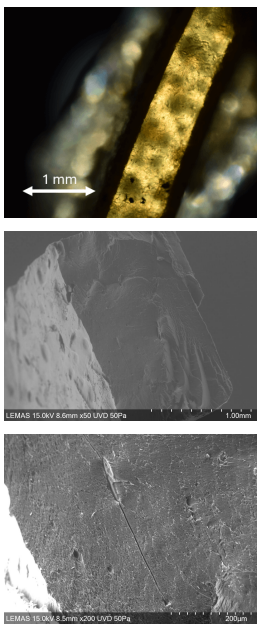		

Light microscopy in Table 5.2 shows increasing evidence of voids and laminar gaps forming as fibre content increases. This is supported by the increased laminar separation in SEM images of 50 % fibre volume cellulose samples. This coincides also with increased fibre pullout in these samples, causing the distinct stress-strain curves shown in Figure 5.12 (a). It appears that fibre matrix interfaces are more smoothly integrated at 40 % fibre volume in both matrices than in the upper extremes, though superior interfacial adhesion is seen in the hybrid matrix. This confirms discussion of the hybrid matrix's superior processing power at higher fibre concentrations as discussed in Section 5.3.

In hybrid samples, the increased dissolving ability is clearly demonstrated by the lack of fibres at the surface of 30 % fibre volume sample. This instead demonstrates a brittle fracture surface with a chevroned fracture surface and smooth surfaces along crystallographic planes [232]. This indicates that further research into the fibre volume analysis could be of interest for these complex novel materials to improve the estimations used in this study. 40 and 50 % fibre volume samples show similar trends to cellulose samples with increasing fibre pull out and interlaminar failure in highly reinforced samples. It can be seen that at 40 % fibre volume good matrix-fibre adhesion is seen and fibres pull-out appears to be limited, which indicates proper fibre loading [76, 233].

Acoustic Insulation Analysis

To indicate the potential application of these materials in non-load bearing acoustic insulation capacities the acoustic insulation performance was tested with respect to matrix and reinforcing flock. The sound transmission loss performance can be seen in Figure 5.17 with the average transmission loss across the tested frequencies given in Table 5.3. Though not measured here, sample noise-reduction coefficient (see Section 2.8) would be of great interest for acoustic applications in the future.

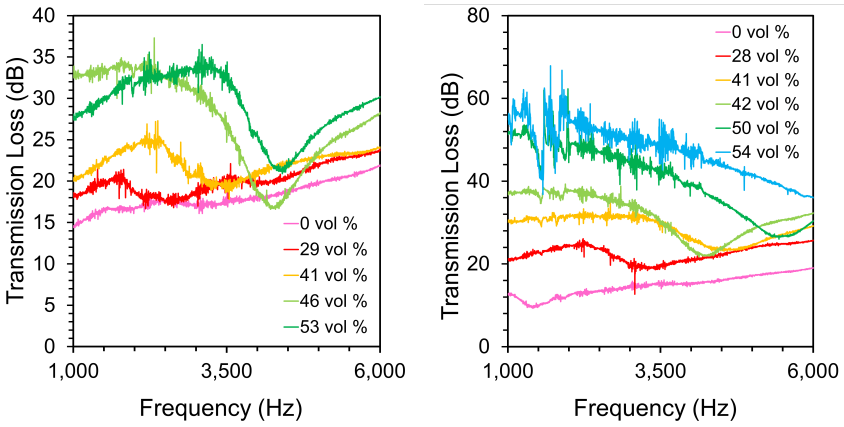

(a) (b)

Figure 5.17: Acoustic transmission loss plotted against frequency for both (a) cellulose matrix, and (b) hybrid matrix samples. The numbers included in the legend indicate the volume percentage of included flock reinforcement for each sample.

Figure 5.17 and Table 5.3 show that hybrid samples achieved a greater average acoustic transmission loss (47 ± 7 dB) compared to that of cellulose samples (29 ± 4 dB), again indicating their improved performance. An increase in average transmission loss was seen with increasing fibre content for samples with both cellulose and hybrid matrices. This indicates an improved acoustic insulation performance. This behaviour is mediated by sound wave interactions with material micropores and macrostructure [194]. Acoustic insulation can be aided (in porous materials) by air molecules vibrating to transform acoustic vibrations into viscous and thermal energy, or (in fibrous materials) energy being transformed into fibre vibrations [194]. In these composites, closed-cell cavities may be formed by interstices of fibres where matrix was unable to enter during preparation [194]. The increasing addition of fibres may greatly improve scattering by introducing interfaces between fibres, matrix, and cavities and hence to improve acoustic insulation. The improved performance at low frequencies is comparable to work by Sui *et al.* on honeycomb acoustic metamaterials [192]. Multiple reflections between interfaces was proposed to encourage standing waves which greatly improved the transmission loss [192]. Sample acoustic performance was superior to

standard single layer building materials (plywood, aerated concrete, laminated glass, and rock wool) which largely showed transmission loss below 25 dB when below 1000 Hz [234, 235].

Notably, the performance of samples with hybrid matrices was superior to samples with cellulose matrices. This may be related to increased sample density, as seen in Figure 5.10, which is shown to increase acoustic insulation in accordance with the mass law [189]. Though promising, these results should be considered as only preliminary evidence of performance as it is likely surface behaviours affected the acoustic performance which would be magnified by the use of relatively thin samples in this case [236]. The effect of fibre content on pore size and surface roughness should be considered in future studies more primarily focused on acoustic performance.

Dips in the transmission loss can be seen in Figure 5.17 (a) and (b) which occur at higher frequencies as the fibre content is increased. This is likely the samples critical valley, at which the bending wavelength matches the acoustic wavelength [189]. This allows more efficient transfer of sound wave energy across the sample. The frequency of the critical valley increases with flock content and likely corresponds to the bending wavelength of the material decreasing with its modulus change, as shown in Figure 5.12 (c). This indicates the tunability of this material for selective insulation over certain frequencies.

Table 5.3: Average values and standard deviation derived from acoustic transmission loss graphs for both cellulose matrix (top rows), and hybrid matrix (bottom rows) samples. For clarity, transmission loss has been abbreviated to TL in the table below.

Fibre vol (%)	0 %	29 %	41 %	46 %	53 %	
Average TL (dB)	18 ± 2	20 ± 2	22 ± 2	28 ± 5	29 ± 4	
Fibre vol (%)	0 %	28 %	41 %	42 %	50 %	54 %
Average TL (dB)	15 ± 3	23 ± 2	29 ± 3	32 ± 5	40 ± 8	47 ± 7

Figure 5.17 offers an initial look at the acoustic performance of these materials and indicates the fruitful application of these materials. It can be observed

that the maximum transmission loss performance (≈60 dB) exceeds the typical standard for internal interior soundproofing between rooms (45 dB) though the performance must be compared over relevant frequencies [191]. This is achieved without significant mass increase, contrary to the typical mass law, and so offers the potential for application as a lightweight, sustainable, insulative material [189, 191, 193].

5.4 Conclusions

This chapter has demonstrated the feasibility of a novel isotropically reinforced short-fibre biopolymer composite and confirmed the effectiveness of an optimized hybrid cellulose/silk fibroin matrix in reinforced composites. The results highlight the importance of innovative biopolymer hybrid blends in developing high-performance, tunable materials for diverse applications.

Solutions of pure cellulose and a 10 % SF SF/cellulose hybrid blend were isotropically reinforced with cotton flock through mixing, coagulation, washing, and drying, yielding composite samples with an optimal balance of low density and mechanical properties. The modulus increased with fibre content (to 3.3 ± 0.3 GPa), while density decreased and a peak in max stress and strain (1.4 ± 0.2% and 42 ± 6 MPa) occurs between 42 - 55 vol % fibre in hybrid samples. Notably, the modulus trends overlapped for cellulose and silk fibroin samples, indicating that tensile modulus was governed primarily by flock content rather than the matrix. However, the hybrid matrix allowed processing with higher flock content and exhibited optima in maximum stress and strain at failure. Additionally, the hybrid matrix demonstrated improved extensibility and interfacial adhesion, enhancing stress transfer to fibres and overall sample strength. Experimental results aligned well with a theoretical rule of mixtures incorporating Cox shear lag, Krenchel orientation, and density factors, suggesting the model's potential for predicting tunable composites for acoustic or biomedical applications.

Finally, the acoustic insulation performance of samples was tested. Hybrid samples achieved a greater average acoustic transmission loss (47 ± 7 dB) compared to that of cellulose samples (29 ± 4 dB) indicating the applicability of this material for insulative materials.

Chapter 6

Conclusions

6.1 Overall Findings

This thesis has set out to explore the behaviour of silk fibroin (SF) and cellulose blends in dissolution, coagulated materials, and reinforced composites. In particular, we aimed to valorise potential waste textile streams and outline a potential processing pathway with fruitful applications. We indicated optimisations at each step of the process and discussed potential applications in biomedical and acoustic insulation applications. The overall findings of each chapter are summarised below.

Chapter 3: Dissolution of Biopolymers

This chapter investigates the dissolution of cellulose and silk fibroin (SF) in a mixture of 1-ethyl-3-methylimidazolium acetate (EmimAc) and dimethyl sulphoxide (DMSO). EmimAc is a promising environmentally friendly solvent currently in wide use but can be limited by its high viscosity, which inhibits the speed of dissolution. To mediate this, DMSO has been used as a cosolvent and has been shown to significantly lower the solution viscosity and aid mass transport. Dissolution experiments were carried out separately for both cellulose and SF with a range of EmimAc:DMSO ratios from 100 wt% EmimAc to 100 wt% DMSO. Interestingly, the optimal EmimAc:DMSO ratio (in terms of dissolution speed) is found to be very different for the two biopolymers. For cellulose, a mixture of 20

wt% EmimAc with 80 wt% DMSO is found to have the fastest dissolution speed, while for SF, a ratio of 80 wt% EmimAc with 20 wt% DMSO proves the fastest. These dissolution trials are complemented by rheological and nuclear magnetic resonance experiments to provide further insight into the underlying mechanisms. This indicated that hierarchically aligned biopolymer sources were impacted by bulk viscosity before molecular saturation was achieved so rigorous agitation was essential to effectively dissolve these sources. It was also noted that larger structures required more active solvent molecules to effectively be dissolved. This could be used to guide future optimisation between different biopolymer sources. Finally, we produce homogenous hybrid biopolymer solutions to show how this work provides a foundation for effective dissolution during the preparation of hybrid biopolymer films and hybrid biocomposites.

Chapter 4: Hybrid Films of Mixed Cellulose and Silk Fibroin

This chapter investigates hybrid biopolymeric films of SF and cellulose showing superior strength, biocompatibility, and flexibility. We investigate the behaviours of fully dissolved and coagulated hybrid films ait various compositions and characterise the system with X-ray diffraction, dynamic mechanical thermal, thermogravimetric, and mechanical analyses. We confirm a system optimum in modulus, maximum strength, and maximum strain at failure (2.2 ± 0.1 GPa, 28 ± 1 MPa, and 3.3 ± 0.4 % respectively) at 85 % – 95 % cellulose and 5 % – 15 % silk fibroin hybrid composition. Thermogravimetric analysis indicates this is due to increasing interaction density in hybrid compositions correlated with the formation of a hybrid mixed phase up to 4 wt %. We recreate conflicting trends in literature showing sample flexibility improving and reducing with addition of silk fibroin and indicate this is due to variations in sample creep and strain rate. We report a slow stress relaxation and time-dependent viscoelasticity causing this, using comparative mechanical tests at different rates of deformation. We propose a slipping mechanism for stress relaxation similar to those seen in other biopolymer-based biological systems, for example actin filaments in cytoskeletons. We explain this behaviour by comparison with double network theory in which the increase in

total interactions increases material modulus. The presence of transient 'sacrificial' bonds in hybrid phases allow local failure and network reorganization prior to total failure and so introduce viscous behaviours.

Chapter 5: Isotropically Reinforced Short Fibre Composites

This chapter investigates biocomposites produced by reinforcing a hybrid biopolymer matrix (90:10 cellulose:silk fibroin) with randomly oriented short cotton fibres and varying the reinforcement weight percentage. A pure cellulose matrix was tested for comparison. The composites were characterized using X-ray diffraction (XRD), density analysis, tensile testing, optical microscopy, scanning electron microscopy (SEM), and acoustic insulation analysis. Optimal hybrid composites with 50 vol% reinforcement exhibited superior performance to pure cellulose, achieving a Young's modulus of 3.3 ± 0.3 GPa, strain at failure of 1.4 ± 0.2%, and maximum stress of 42 ± 6 MPa. These enhancements were attributed to the hybrid matrix's reduced viscosity and improved solvation capacity allowing higher fibre loading and stronger interfacial adhesion. In addition, the hybrid matrix's greater extensibility enabled more efficient stress transfer to the fibres, maximizing mechanical performance. Fibre content was identified as the primary driver of sample modulus, underscoring the critical role of reinforcement. Flock content was then shown to correlate with improved acoustic insulation performance. This work demonstrates the viability of hybrid biopolymer blends for creating low-density, high-performance materials from short-fibre textile waste with sustainable applications in insulative structural engineering.

6.2 Future Research

In each chapter choices were made to best research the topic in question within the scope of the project and research facilities available. Our work has highlighted potential avenues of future research which could provide elucidating evidence to behaviours noted or expand research topics covered in this work.

Chapter 3: Dissolution of Biopolymers

In future studies, computational coarse-grained modelling may be able to bridge the understanding between macroscopic, mesoscopic, and microscopic dissolution behaviour in hybrids systems [79, 237]. This could help elucidate further the effect of macroscopic arrangement, hierarchical structure, biopolymer sources, and DP on complex solution behaviours [22]. In particular, SF specific studies on this topic would add to the current understanding greatly due to the current lack. If too computationally expensive further use of analytical theories could correlate our observations with traditional theories relating to swelling, entanglement, and DOP.

More detailed investigation can also be performed with more advanced techniques like fast-field cycling NMR [72]. Though not within the scope of this investigation, these could be used in future to better understand entanglement states and diffusion mechanics in hybrid solutions.

It is important to note that this study lacks the direct observation of dissolution mechanisms occurring in the solvent system. This could be improved by the use of cryogenic transmission electron microscopy imaging in future studies [210]. A more precise optimum could also be derived for this system with more solvent/cosolvent ratio variations, through a design of experiments approach.

Chapter 4: Hybrid Films of Mixed Cellulose and Silk Fibroin

Further studies should be performed to statistically analyse and model the relaxation behaviour outlined in this work, to provide insight into the molecular relaxation mechanisms involved. Materials could also be explored with Fourier-transform infrared (FTIR) spectroscopy, Raman spectroscopy, and differential scanning calorimetry (DSC). Alongside direct morphological characterisation with scanning electron microscopy, these techniques could be used to further confirm observations about the bulk relaxations from this work. FTIR may indicate individual intermolecular bond behaviours, while DSC could indicate if any associated changes have thermally impactful phase changes.

Detailed information can be gained about the chemical bonds present in the sample using FTIR spectrometry. FTIR can be used to track crystallinity of SF by tracking amide I and II peaks (1576 - 1646 cm^{-1}). Increasing amide I peaks are seen to indicate SF β-sheet formation which can be used to calculate total secondary structure percentages. In some cases increasing silk percentage is seen to increase total crystallinity [164] and in other articles the inverse is seen [19]. Insights from this technique could help further understand material behaviours seen.

More complex cycling creep and stress experiments could be used to indicate behaviours in different thermal environments [238]. This could be used to better test applied examples of the material and also to understand variation of observed behaviours under different humidities and temperatures.

Chapter 5: Isotropically Reinforced Short Fibre Composites

Further sound absorption studies would allow an improved understanding of this performance in more varied applications [195]. To further optimize these materials, future studies could seek to combine these novel materials with other techniques to maximize performance. Liu *et al.* showed effective sound absorption in honeycomb sandwich composites with woven skin structures [236]. A noise reduction coefficient of 0.670 was achieved with a double layered structure to optimise sound absorption induced by thermofriction between the air and fabric, and cavity resonance [236]. The noise reduction coefficient indicates the ability of the partition, at specific mid-range frequencies to reflect noise. It ranges from 0 (complete reflection) to 1 (no reflection). Combining structural design techniques with our new material could improve sound absorption and transmission loss over a broad range of frequencies with promising applications [193, 239].

The mechanical and acoustic properties could enable uses as a sustainable building material for interior decoration [24, 193]. Due to sample flammability, to achieve these applications flame retardency treatments should be a priority of focus for future study [240]. Surface treatments could improve sample fire retardency for wider application [241].

Lastly, further investigation into their practical performance and end-of-life behaviour such as degradation studies and life cycle analysis could better assess their environmental sustainability and broaden their applicability. This thesis indicates the potential benefits of using hybrid biopolymer blends in biocomposite creation and provides scope for further study into differing blends, reinforcement types, and applications of this novel set of materials. Future study should test the scalability of the sample production and directly test sample performance in non-load bearing acoustic building applications.

6.3 Future Directions and Applications

To maximise the impact of this study, the work in this thesis is intended to aid both future research and applied efforts. With this in mind we specify here some examples of how this manuscript can be utilised:

- Composites manufactured with the understanding developed in Chapters 4 and 5 could help in both biomedical and structural material application [25, 85, 115, 116]. The material produced has comparable moduli some with biological systems and hence could act as a promising tissue substitute[85, 114, 217, 218]. Hybrid biopolymeric blend materials offer a low rejection rate when applied as a biomimetic scaffold for cell or tissue growth and proliferation[85, 113, 115]. The findings here could be used to develop work by Lee *et al.* who showed the effective application of SF and bacterial cellulose composites as bioresorbable fixation plates in zygomatic arches of rats[85]. For example, the more effective solvent system and blending presented in this study could be utilised to better control blend properties of the resulting material. This could be confirmed by biological analysis of cytocompatibility, biodegradation, or sterilization behaviours in future studies.

- Further research of ionogel devices created with the solutions studied in Chapter 3 could aid the development of next-generation sustainable electrochemical devices [67, 242]. For example, ionic liquids can act as high-performance electrolytes in cellulose-based flexible super-capacitors [242].

This could enable applications in biological electrical systems with interesting applications in medicine or textiles.

- Lastly, the evidence from Chapter 5 indicates that short fibre reinforced hybrid composites offer a viable material for acoustically insulating structural materials. Our promising evidence of acoustic transmission loss indicates the potential of these materials as a natural fibre insulator to reduce the noted environmental impact of construction materials [193, 194].

References

[1] Marc Kostag, Kerstin Jedvert, and Omar A. El Seoud. Engineering of sustainable biomaterial composites from cellulose and silk fibroin: Fundamentals and applications. *International Journal of Biological Macromolecules*, 167:687–718, 2021. ISSN 18790003. doi: 10.1016/j.ijbiomac.2020.11.151. URL https://doi.org/10.1016/j.ijbiomac.2020.11.151. xi, 1, 2, 3, 5, 9, 10, 11, 12, 20, 25, 28, 50, 51, 63, 77, 81, 89, 95, 98, 106, 110, 111, 115, 119, 122, 123, 129, 130, 131, 143, 145

[2] Omar A. El Seoud, Kerstin Jedvert, Marc Kostag, and Shirley Possidonio. Cellulose, chitin and silk: the cornerstones of green composites. *Emergent Materials*, 5:785–810, 2021. ISSN 2522574X. doi: 10.1007/s42247-021-00308-0. URL https://doi.org/10.1007/s42247-021-00308-0. 1, 2, 20, 28, 129

[3] John Stanton, Ye Xue, Joshua C Waters, Ashley Lewis, Darrel Cowan, Xiao Hu, and David Salas de la Cruz. Structure–property relationships of blended polysaccharide and protein biomaterials in ionic liquid. *Cellulose*, 24(4):1775–1789, 2017. ISSN 1572882X. doi: 10.1007/s10570-017-1208-y. 1, 13, 20, 49, 63, 109, 113

[4] Elizabeth Mora. Plant and Animal Fibres. *Diversity*, pages 244–254, 2020. doi: 10.2307/j.ctv10kmcd6.49. 1, 19

[5] Ryo Nagamine, Kayoko Kobayashi, Ryosuke Kusumi, and Masahisa Wada. Cellulose fiber biodegradation in natural waters: river water, brackish water, and seawater. *Cellulose*, 29(5):2917–2926, 2022. ISSN 1572882X.

doi: 10.1007/s10570-021-04349-w. URL https://doi.org/10.1007/s10570-021-04349-w. 1

[6] Roozbeh Abidnejad, Hossein Baniasadi, Mahyar Fazeli, Sami Lipponen, Eero Kontturi, Orlando J. Rojas, and Bruno D. Mattos. High-fiber content composites produced from mixed textile waste: Balancing cotton and polyester fibers for improved composite performance. *International Journal of Biological Macromolecules*, 292:139227, 2025. ISSN 18790003. doi: 10.1016/j.ijbiomac.2024.139227. URL https://doi.org/10.1016/j.ijbiomac.2024.139227. 1, 106

[7] Elena S. Sashina and Olga I. Yakovleva. The current state and prospects of recycling silk industry waste into nonwoven materials. *Fibers*, 11(6), 2023. ISSN 2079-6439. doi: 10.3390/fib11060056. URL https://www.mdpi.com/2079-6439/11/6/56. 1

[8] Alfred D French. Glucose, not cellobiose, is the repeating unit of cellulose and why that is important. *Cellulose*, 24(11):4605–4609, 2017. ISSN 0969-0239. doi: 10.1007/s10570-017-1450-3. xi, 1, 2

[9] Mohammed Nasir, Rokiah Hashim, Othman Sulaiman, and Mohd Asim. Nanocellulose: Preparation methods and applications. *Cellulose-Reinforced Nanofibre Composites: Production, Properties and Applications*, 11:261–276, 2017. doi: 10.1016/B978-0-08-100957-4.00011-5. xi, xii, 2, 4, 6, 7

[10] Eero Kontturi, Tekla Tammelin, and Monika Österberg. Cellulose—model films and the fundamental approach. *Chemical Society Reviews*, 35(12): 1287–1304, 2006. ISSN 14604744. doi: 10.1039/b601872f. 2, 14

[11] Bahareh Azimi, Homa Maleki, Vito Gigante, Roohollah Bagherzadeh, Andrea Mezzetta, Mario Milazzo, Lorenzo Guazzelli, Patrizia Cinelli, Andrea Lazzeri, and Serena Danti. *Cellulose-based fiber spinning processes using ionic liquids*, volume 29. Springer Netherlands, 2022. ISBN 0123456789. doi: 10.1007/s10570-022-04473-1. URL https://doi.org/10.1007/s10570-022-04473-1. 2, 7, 8, 15, 22, 106, 130

[12] Michael Edward Ries, Peter John Hine, and Luke Mancell. Circular is the new black. *Materials World*, pages 27–29, 2020. 2, 23

[13] Stacy A Love, Xiao Hu, and David Salas-de la Cruz. Controlling the structure and properties of semi-crystalline cellulose/silk-fibroin biocomposites by ionic liquid type and hydrogen peroxide concentration. *Carbohydrate Polymer Technologies and Applications*, 3:100193, 2022. ISSN 26668939. doi: 10.1016/j.carpta.2022.100193. URL https://doi.org/10.1016/j.carpta.2022.100193. 2, 11, 17, 18, 25, 26, 27, 28, 58, 59, 63, 110, 113

[14] Mark J. Bonino. Material Properties of Spider Silk. *Modeling and Numerical Simulation of Material Science*, page 115, 2003. 2

[15] Ingi Agnarsson, Matjaž Kuntner, and Todd A. Blackledge. Bioprospecting finds the toughest biological material: Extraordinary silk from a giant riverine orb spider. *PLOS ONE*, 5(9):1–8, 09 2010. doi: 10.1371/journal.pone.0011234. URL https://doi.org/10.1371/journal.pone.0011234. 2

[16] Roberto Nisticò, Philippe Evon, Laurent Labonne, Guadalupe Vaca-Medina, Enzo Montoneri, Carlos Vaca-Garcia, and Michèle Negre. Post-harvest tomato plants and urban food wastes for manufacturing plastic films. *Journal of Cleaner Production*, 167:68–74, 2017. ISSN 09596526. doi: 10.1016/j.jclepro.2017.08.160. 3

[17] Bruno Medronho, Anabela Romano, Maria Graça Miguel, Lars Stigsson, and Björn Lindman. Rationalizing cellulose (in)solubility: Reviewing basic physicochemical aspects and role of hydrophobic interactions. *Cellulose*, 19 (3):581–587, 2012. ISSN 09690239. doi: 10.1007/s10570-011-9644-6. 3, 8

[18] Donglin Tian, Tao Li, Rongchun Zhang, Qiang Wu, Tiehong Chen, Pingchuan Sun, and Ayyalusamy Ramamoorthy. Conformations and Intermolecular Interactions in Cellulose/Silk Fibroin Blend Films: A Solid-State NMR Perspective. *Journal of Physical Chemistry B*, 121(25):6108–6116, 2017. ISSN 1520-6106. doi: 10.1021/acs.jpcb.7b02838. xii, 3, 14, 20, 21, 27, 49, 56, 106, 109, 110, 119, 129

[19] Songmin Shang, Lei Zhu, and Jintu Fan. Physical properties of silk fibroin/cellulose blend films regenerated from the hydrophilic ionic liquid. *Carbohydrate Polymers*, 86(2):462–468, 2011. ISSN 0144-8617. doi: 10.1016/j.carbpol.2011.04.064. 3, 14, 20, 21, 81, 106, 115, 118, 163

[20] Ashley Victoria, Michael Edward Ries, and Peter John Hine. Use of interleaved films to enhance the properties of all-cellulose composites. *Composites Part A: Applied Science and Manufacturing*, 160:107062, 2022. ISSN 1359835X. doi: 10.1016/j.compositesa.2022.107062. URL https://doi.org/10.1016/j.compositesa.2022.107062. 3, 19, 24, 77, 78, 84, 89, 90, 106, 107, 115, 129, 135, 142, 145

[21] Xin Zhang, Michael E. Ries, and Peter J. Hine. Time-Temperature Superposition of the Dissolution of Silk Fibers in the Ionic Liquid 1-Ethyl-3-methylimidazolium Acetate. *Biomacromolecules*, 22(3):1091–1101, 2021. ISSN 15264602. doi: 10.1021/acs.biomac.0c01467. 3, 13, 16, 68, 84, 95, 115, 130, 143

[22] Yunhao Liang, James E. Hawkins, Michael E. Ries, and Peter J. Hine. Dissolution of cotton by 1-ethyl-3-methylimidazolium acetate studied with time–temperature superposition for three different fibre arrangements. *Cellulose*, 28(2):715–727, 2021. ISSN 1572882X. doi: 10.1007/s10570-020-03576-x. URL https://doi.org/10.1007/s10570-020-03576-x. 3, 8, 9, 22, 24, 25, 83, 89, 90, 98, 102, 141, 162

[23] James E Hawkins, Yunhao Liang, Michael E Ries, and Peter J Hine. Time temperature superposition of the dissolution of cellulose fibres by the ionic liquid 1-ethyl-3-methylimidazolium acetate with cosolvent dimethyl sulfoxide. *Carbohydrate Polymer Technologies and Applications*, 2:100021, 2021. ISSN 26668939. doi: 10.1016/j.carpta.2020.100021. URL https://doi.org/10.1016/j.carpta.2020.100021. 3, 16, 77, 83, 89, 90, 102

[24] Chiara Cianci, David Chelazzi, Giovanna Poggi, Francesco Modi, Rodorico Giorgi, and Marco Laurati. Hybrid fibroin-nanocellulose composites for the consolidation of aged and historical silk. *Colloids and Surfaces A:*

Physicochemical and Engineering Aspects, 634(November 2021):127944, 2022. ISSN 18734359. doi: 10.1016/j.colsurfa.2021.127944. URL https://doi.org/10.1016/j.colsurfa.2021.127944. 3, 4, 10, 31, 106, 124, 130, 163

[25] Pimnattha Ang-atikarnkul, Anyarat Watthanaphanit, and Ratana Rujiravanit. Fabrication of cellulose nanofiber/chitin whisker/silk sericin bionanocomposite sponges and characterizations of their physical and biological properties. *Composites Science and Technology*, 96:88–96, 2014. ISSN 02663538. doi: 10.1016/j.compscitech.2014.03.006. URL http://dx.doi.org/10.1016/j.compscitech.2014.03.006. 4, 28, 30, 164

[26] H. P.S. Abdul Khalil, A. H. Bhat, and A. F. Ireana Yusra. Green composites from sustainable cellulose nanofibrils: A review. *Carbohydrate Polymers*, 87(2):963–979, 2012. ISSN 01448617. doi: 10.1016/j.carbpol.2011.08.078. URL http://dx.doi.org/10.1016/j.carbpol.2011.08.078. 4, 5, 23

[27] Lennart Salmén. On the organization of hemicelluloses in the wood cell wall. *Cellulose*, 29(3):1349–1355, 2022. ISSN 1572882X. doi: 10.1007/s10570-022-04425-9. 4

[28] Prodyut Dhar, Kazuki Sugimura, Mariko Yoshioka, Arata Yoshinaga, and Hiroshi Kamitakahara. Fabrication of wood-inspired high-performance composites through fermentation routes. *Cellulose*, 29(5):2927–2947, 2022. ISSN 1572882X. doi: 10.1007/s10570-021-04354-z. URL https://doi.org/10.1007/s10570-021-04354-z. 4

[29] Alain Dufresne and Michel R. Vignon. Improvement of starch film performances using cellulose microfibrils. *Macromolecules*, 31(8):2693–2696, 1998. ISSN 00249297. doi: 10.1021/ma971532b. 5

[30] L. M.J. Kroon-Batenburg and J. Kroon. The crystal and molecular structures of cellulose I and II. *Glycoconjugate Journal*, 14(5):677–690, 1997. ISSN 02820080. doi: 10.1023/A:1018509231331. 6, 8, 64

[31] Masahisa Wada, Henri Chanzy, Yoshiharu Nishiyama, and Paul Langan. Cellulose III I crystal structure and hydrogen bonding by synchrotron X-ray and neutron fiber diffraction. *Macromolecules*, 37(23):8548–8555, 2004. ISSN 00249297. doi: 10.1021/ma0485585. 6

[32] P. H. Hermans and A. Weidinger. On the transformation of cellulose II into cellulose IV. *Journal of Colloid Science*, 1(6):495–504, 1946. ISSN 00958522. doi: 10.1016/0095-8522(46)90057-8. 6

[33] Sachin C. Gondhalekar, Pravin J. Pawar, Sunil S. Dhumal, and Shirish Thakre. Fate of CS2 in viscose process: a chemistry perspective. *Cellulose*, 29(3):1451–1461, 2022. ISSN 1572882X. doi: 10.1007/s10570-021-04398-1. URL https://doi.org/10.1007/s10570-021-04398-1. 7

[34] Yue Xi, Lili Zhang, Yahui Tian, Junlong Song, Jinxia Ma, and Zhiguo Wang. Rapid dissolution of cellulose in an AlCl3/ZnCl2aqueous system at room temperature and its versatile adaptability in functional materials. *Green Chemistry*, 24(2):885–897, 2022. ISSN 14639270. doi: 10.1039/d1gc03918k. 7, 15, 89, 106, 130

[35] Xin Li, Haichao Li, Tingting You, Xiaomei Chen, Shri Ramaswamy, Yu Ying Wu, and Feng Xu. Enhanced Dissolution of Cotton Cellulose in 1-Allyl-3-methylimidazolium Chloride by the Addition of Metal Chlorides. *ACS Sustainable Chemistry and Engineering*, 7(23):19176–19184, 2019. ISSN 21680485. doi: 10.1021/acssuschemeng.9b05159. 7, 16, 106, 130

[36] Natalia V. Plechkova and Kenneth R. Seddon. Applications of ionic liquids in the chemical industry. *Chemical Society Reviews*, 37(1):123–150, 2008. ISSN 03060012. doi: 10.1039/b006677j. 7, 15

[37] Junji Nemoto and Keiichi Nakamata. All-cellulose material prepared using aqueous zinc chloride solution. *Cellulose*, 29(5):2795–2803, 2022. ISSN 1572882X. doi: 10.1007/s10570-021-04344-1. URL https://doi.org/10.1007/s10570-021-04344-1. 8

[38] Gyanendra Sharma, Yui Kato, Ayumi Hachisu, Kojiro Ishibashi, Kazuaki Ninomiya, Kenji Takahashi, Eishu Hirata, and Kosuke Kuroda. Synthesis of a cellulose dissolving liquid zwitterion from general and low-cost reagents. *Cellulose*, 29(5):3017–3024, 2022. ISSN 1572882X. doi: 10.1007/s10570-021-04185-y. URL https://doi.org/10.1007/s10570-021-04185-y. 8, 15, 16

[39] Katherine S. Lefroy, Brent S. Murray, and Michael E. Ries. Advances in the use of microgels as emulsion stabilisers and as a strategy for cellulose functionalisation. *Cellulose*, 28(2):647–670, 2021. ISSN 1572882X. doi: 10.1007/s10570-020-03595-8. URL https://doi.org/10.1007/s10570-020-03595-8. xii, 8

[40] Yunhao Liang, Michael E Ries, and Peter J Hine. Three methods to measure the dissolution activation energy of cellulosic fibres using time-temperature superposition. *Carbohydrate Polymers*, 291:119541, 2022. ISSN 01448617. doi: 10.1016/j.carbpol.2022.119541. URL https://doi.org/10.1016/j.carbpol.2022.119541. 8

[41] Eivind Bering, Jonathan Torstensen, Anders Lervik, and Astrid S. de Wijn. Computational study of the dissolution of cellulose into single chains: the role of the solvent and agitation. *Cellulose*, 29(3):1365–1380, 2022. ISSN 1572882X. doi: 10.1007/s10570-021-04382-9. URL https://doi.org/10.1007/s10570-021-04382-9. 8, 15, 21, 98

[42] Stacy A Love, Elizabeth Popov, Karleena Rybacki, Xiao Hu, and David Salas-de la Cruz. Facile treatment to fine-tune cellulose crystals in cellulose-silk biocomposites through hydrogen peroxide. *International Journal of Biological Macromolecules*, 147:569–575, 2020. ISSN 18790003. doi: 10.1016/j.ijbiomac.2020.01.100. URL https://doi.org/10.1016/j.ijbiomac.2020.01.100. 8, 26, 27

[43] Ying Wang and Yulin Deng. The kinetics of cellulose dissolution in sodium hydroxide solution at low temperatures. *Biotechnology and Bioengineering*,

102(5):1398–1405, 2009. ISSN 00063592. doi: 10.1002/bit.22160. 8, 9, 63, 64

[44] María Evangelina Vallejos, Graciela Viviana Olmos, María Claudia Taleb, Fernando Esteban Felissia, Nanci Vanesa Ehman, Maria Soledad Peresin, María Cristina Area, and Mirtha Graciela Maximino. Dissolving pulp from eucalyptus sawdust for regenerated cellulose products. *Cellulose*, 29(8): 4645–4659, 2022. ISSN 1572882X. doi: 10.1007/s10570-022-04581-y. URL https://doi.org/10.1007/s10570-022-04581-y. 9

[45] Benoît J.C. Duchemin, Roger H. Newman, and Mark P. Staiger. Structure-property relationship of all-cellulose composites. *Composites Science and Technology*, 69(7-8):1225–1230, 2009. ISSN 02663538. doi: 10.1016/j.compscitech.2009.02.027. URL http://dx.doi.org/10.1016/j.compscitech.2009.02.027. 9, 23, 24

[46] Luke M. Haverhals, W. Matthew Reichert, Hugh C. De Long, and Paul C. Trulove. Natural fiber welding. *Macromolecular Materials and Engineering*, 295(5):425–430, 2010. ISSN 14387492. doi: 10.1002/mame.201000005. 9

[47] Céline Cuissinat and Patrick Navard. Swelling and dissolution of cellulose, Part III: Plant fibres in aqueous systems. *Cellulose*, 15(1):67–74, 2008. ISSN 09690239. doi: 10.1007/s10570-007-9158-4. 9, 15, 90

[48] E. S. Sashina, A. M. Bochek, N. P. Novoselov, and D. A. Kirichenko. Structure and solubility of natural silk fibroin. *Russian Journal of Applied Chemistry*, 79(6):869–876, 2006. ISSN 10704272. doi: 10.1134/S1070427206060012. 10, 12, 13, 14, 25

[49] A. I. Susanin, E. S. Sashina, N. P. Novoselov, and V. V. Zakharov. Change of Silk Fibroin Molecular Mass During Dissolution in Ionic Liquids. *Fibre Chemistry*, 52(3):208–213, 2020. ISSN 15738493. doi: 10.1007/s10692-020-10182-x. 10, 12, 13

[50] Sigal Meirovitch, Zvi Shtein, Tal Ben-Shalom, Shaul Lapidot, Carmen Tamburu, Xiao Hu, Jonathan A. Kluge, Uri Raviv, David L. Kaplan, and Oded

Shoseyov. Spider silk-CBD-cellulose nanocrystal composites: Mechanism of assembly. *International Journal of Molecular Sciences*, 17(9), 2016. ISSN 14220067. doi: 10.3390/ijms17091573. 10

[51] Weitao Zhou, Jianxin He, Shan Du, Shizhong Cui, and Weidong Gao. Electrospun Silk Fibroin/Cellulose Acetate Blend Nanofibres: Structure and Properties. *Iranian Polymer Journal*, 20(5):389–397, 2011. 11, 14

[52] E. S. Sashina, Yu A. Golubikhin, and N. P. Novoselov. Thermochemical study on the dissolution and regeneration of fibroin from solutions in imidazole-based ionic liquids. *Russian Journal of General Chemistry*, 82 (8):1440–1443, 2012. ISSN 10703632. doi: 10.1134/S107036321208018X. 11, 12, 78

[53] Tim Huber, Shusheng Pang, and Mark P. Staiger. All-cellulose composite laminates. *Composites Part A: Applied Science and Manufacturing*, 43(10): 1738–1745, 2012. ISSN 1359835X. doi: 10.1016/j.compositesa.2012.04.017. URL http://dx.doi.org/10.1016/j.compositesa.2012.04.017. 13, 22, 23, 106, 141

[54] Ke Wang, Raj Shankar Hazra, Qian Ma, Long Jiang, Zhaohui Liu, Yuanming Zhang, Shudong Wang, and Guangting Han. Multifunctional silk fibroin/PVA bio-nanocomposite films containing TEMPO-oxidized bacterial cellulose nanofibers and silver nanoparticles. *Cellulose*, 29(3):1647–1666, 2022. ISSN 1572882X. doi: 10.1007/s10570-021-04369-6. URL https://doi.org/10.1007/s10570-021-04369-6. 13, 109

[55] Wang Yue, Lihua Zhang, Lulu Deng, Yuanlong Guo, Qinqin Xu, Wei Peng, Peng Chen, Haibo Xie, Guanglong Zou, and Songmiao Liang. Co-dissolution of cellulose and silk fibroin in levulinic acid-derived protic ionic liquids for composited membrane and fiber preparation. *Green Chemistry*, 23(23):9669–9682, 2021. ISSN 14639270. doi: 10.1039/d1gc02837e. 13, 25

[56] Ashley Rivera-Galletti, Christopher R Gough, Farhan Kaleem, Michael Burch, Chris Ratcliffe, Ping Lu, David Salas-De la Cruz, and Xiao Hu. Silk-cellulose acetate biocomposite materials regenerated from ionic liquid.

Polymers, 13(17), 2021. ISSN 20734360. doi: 10.3390/polym13172911. 13, 24, 26, 109, 114

[57] Chieko Narita, Yoko Okahisa, and Kazushi Yamada. A novel technique in the preparation of environmentally friendly cellulose nanofiber/silk fibroin fiber composite films with improved thermal and mechanical properties. *Journal of Cleaner Production*, 234:200–207, 2019. ISSN 09596526. doi: 10.1016/j.jclepro.2019.06.215. URL https://doi.org/10.1016/j.jclepro.2019.06.215. 14, 15, 24

[58] Jungju Eom, Subong Park, Hyoung Joon Jin, and Hyo Won Kwak. Multi-scale Hybridization of Natural Silk–Nanocellulose Fibrous Composites With Exceptional Mechanical Properties. *Frontiers in Materials*, 7:1–12, 2020. ISSN 22968016. doi: 10.3389/fmats.2020.00098. 14, 106

[59] Romain Sescousse, Kim Anh Le, Michael E. Ries, and Tatiana Budtova. Viscosity of cellulose-imidazolium-based ionic liquid solutions. *Journal of Physical Chemistry B*, 114(21):7222–7228, 2010. ISSN 15205207. doi: 10.1021/jp1024203. 15, 17, 18, 83, 96

[60] Martin Brehm, Julian Radicke, Martin Pulst, Farzaneh Shaabani, Daniel Sebastiani, and Jörg Kressler. Dissolving cellulose in 1,2,3-triazolium-and imidazolium-based ionic liquids with aromatic anions. *Molecules*, 25(15): 1–20, 2020. ISSN 14203049. doi: 10.3390/molecules25153539. 15

[61] Miguel Angel Vera-Baceta, Michael Thelwall, and Kayvan Kousha. Web of Science and Scopus language coverage, 2019. ISSN 15882861. URL https://link.springer.com/article/10.1007/s11192-019-03264-z. 15

[62] Crystal E. Owens, Jianyi Du, and Pablo B. Sánchez. Understanding the Dynamics of Cellulose Dissolved in an Ionic Liquid Solvent Under Shear and Extensional Flows. *Biomacromolecules*, 2022. ISSN 1525-7797. doi: 10.1021/acs.biomac.1c01623. 16, 83, 86, 92, 95

[63] Fei Ren, Jinwei Wang, Jinglin Yu, Cheng Zhong, Fengwei Xie, and Shujun Wang. Dissolution of Cellulose in Ionic Liquid-DMSO Mixtures: Roles of

DMSO/IL Ratio and the Cation Alkyl Chain Length. *ACS Omega*, 6(41): 27225–27232, oct 2021. ISSN 24701343. doi: 10.1021/acsomega.1c03954. 16, 82, 83, 89, 90, 92, 102

[64] Yuta Tomimatsu, Hiroki Suetsugu, Yukihiro Yoshimura, and Akio Shimizu. The solubility of cellulose in binary mixtures of ionic liquids and dimethyl sulfoxide: Influence of the anion. *Journal of Molecular Liquids*, 279:120–126, 2019. ISSN 01677322. doi: 10.1016/j.molliq.2019.01.093. URL https://doi.org/10.1016/j.molliq.2019.01.093. 16, 77, 82, 83, 89, 96, 102, 131

[65] Anett Zajáros, Klára Szita, Károly Matolcsy, and Dániel Horváth. Life cycle sustainability assessment of DMSO solvent recovery from hazardous waste water. *Periodica Polytechnica Chemical Engineering*, 62(3):305–309, 2018. ISSN 15873765. doi: 10.3311/PPch.11097. 16

[66] Sadiye Velioglu, Xun Yao, Julien Devémy, M. Goktug Ahunbay, S. Birgul Tantekin-Ersolmaz, Alain Dequidt, Margarida F. Costa Gomes, and Agílio A.H. Pádua. Solvation of a cellulose microfibril in imidazolium acetate ionic liquids: Effect of a cosolvent. *Journal of Physical Chemistry B*, 118(51):14860–14869, 2014. ISSN 15205207. doi: 10.1021/jp508113a. 16, 83

[67] Chandrabhan Verma, Ankush Mishra, S. Chauhan, Pratibha Verma, Vandana Srivastava, M. A. Quraishi, and E. E. Ebenso. Dissolution of cellulose in ionic liquids and their mixed cosolvents: A review. *Sustainable Chemistry and Pharmacy*, 13:100162, 2019. ISSN 23525541. doi: 10.1016/j.scp.2019.100162. URL https://doi.org/10.1016/j.scp.2019.100162. 16, 21, 24, 61, 65, 77, 83, 110, 137, 164

[68] Asanah Radhi, Kim Anh Le, Michael E. Ries, and Tatiana Budtova. Macroscopic and microscopic study of 1-ethyl-3-methyl-imidazolium acetate-DMSO mixtures. *Journal of Physical Chemistry B*, 119(4):1633–1640, jan 2015. ISSN 15205207. doi: 10.1021/jp5112108. 16, 83, 87, 88, 89

[69] Eliane Roos, Cora Gradaus, Daniel Sebastiani, and Martin Brehm. A force field for the solubility of cellulose in DMSO/Ionic liquids. *Cellulose*, 31(8): 4793–4815, 2024. ISSN 1572882X. doi: 10.1007/s10570-024-05854-4. 16, 83, 89

[70] Yuxia Lv, Jin Wu, Jinming Zhang, Yanhua Niu, Chen Yang Liu, Jiasong He, and Jun Zhang. Rheological properties of cellulose/ionic liquid/dimethylsulfoxide (DMSO) solutions. *Polymer*, 53(12):2524–2531, 2012. ISSN 00323861. doi: 10.1016/j.polymer.2012.03.037. URL http://dx.doi.org/10.1016/j.polymer.2012.03.037. 16, 83, 86, 87, 88, 95, 96

[71] Yuling Zhao, Xiaomin Liu, Jianji Wang, and Suojiang Zhang. Insight into the cosolvent effect of cellulose dissolution in imidazolium-based ionic liquid systems. *Journal of Physical Chemistry B*, 117(30):9042–9049, 2013. ISSN 15206106. doi: 10.1021/jp4038039. 16, 89

[72] Katherine S. Lefroy, Brent S. Murray, and Michael E. Ries. Rheological and NMR Studies of Cellulose Dissolution in the Ionic Liquid BmimAc. *Journal of Physical Chemistry B*, 125(29):8205–8218, 2021. ISSN 15205207. doi: 10.1021/acs.jpcb.1c02848. 17, 18, 25, 56, 77, 83, 86, 88, 89, 93, 94, 95, 98, 162

[73] John Stanton, Ye Xue, Prabhdeep Pandher, Laura Malek, Tyler Brown, Xiao Hu, and David Salas-de la Cruz. Impact of ionic liquid type on the structure, morphology and properties of silk-cellulose biocomposite materials. *International Journal of Biological Macromolecules*, 108:333–341, 2018. ISSN 18790003. doi: 10.1016/j.ijbiomac.2017.11.137. URL http://dx.doi.org/10.1016/j.ijbiomac.2017.11.137. 17, 18, 26, 49, 64

[74] Kamrun N. Keya, Nasrin A. Kona, Farjana A. Koly, Kazi Madina Maraz, Md. Naimul Islam, and Ruhul A. Khan. Natural fiber reinforced polymer composites: history, types, advantages, and applications. *Materials Engineering Research*, 1(2):69–87, 2019. doi: 10.25082/mer.2019.02.006. 18

[75] Luminita Ciobanu. Development of 3D Knitted Fabrics for Advanced Composite Materials. In *Advances in Composite Materials - Ecodesign and Analysis*, pages 161–190. InTech, 2011. doi: 10.5772/14876. URL https://api.semanticscholar.org/CorpusID:136557679. xii, 18, 19, 106, 107, 123

[76] D Hull and W Clyne, T. *An Introduction to Composite Materials*. Cambridge University Press, Cambridge, 2 edition, 1996. xii, 19, 145, 146, 147, 148, 149, 155

[77] Mohd Pahmi Bin Saiman, Md Saidin Bin Wahab, and Mat Uzir Bin Wahit. The effect of alkali treatment on impact strength of woven kenaf reinforced unsaturated polyester composite using vacuum infusion process. *Applied Mechanics and Materials*, 564:422–427, 2014. ISSN 16627482. doi: 10.4028/www.scientific.net/AMM.564.422. 19

[78] Y Noishiki, Y Nishiyama, M Wada, S Kuga, and J Magoshi. Mechanical properties of silk fibroin-microcrystalline cellulose composite films. *Journal of Applied Polymer Science*, 86(13):3425–3429, dec 2002. ISSN 0021-8995. doi: 10.1002/app.11370. 19, 20, 106, 110, 129

[79] Krishna M. Gupta and Jianwen Jiang. Cellulose dissolution and regeneration in ionic liquids: A computational perspective. *Chemical Engineering Science*, 121:180–189, 2015. ISSN 00092509. doi: 10.1016/j.ces.2014.07.025. URL http://dx.doi.org/10.1016/j.ces.2014.07.025. 19, 61, 65, 83, 110, 137, 162

[80] Alva Hjelm, Mikael Skrifvars, and Pooria Khalili. Short fiber composites from postconsumer textile waste and their suitability in packaging applications. *Heliyon*, 11(3):e42335, 2025. ISSN 24058440. doi: 10.1016/j.heliyon.2025.e42335. URL https://doi.org/10.1016/j.heliyon.2025.e42335. 19, 20, 143

[81] Song Ruoyuan and Kimura Teruo. Mechanical properties of silk/bamboo hybrid paper reinforced pbs green composite. *Journal of Textile Engineering*, 57(1):1–7, 2011. ISSN 13468235. doi: 10.4188/jte.57.1. 20, 24

[82] Bailey Blessing, Cory Trout, Abneris Morales, Karleena Rybacki, Stacy A Love, Guillaume Lamoureux, Sean M. O'malley, Xiao Hu, and David Salas-De la Cruz. The impact of composition and morphology on ionic conductivity of silk/cellulose bio-composites fabricated from ionic liquid and varying percentages of coagulation agents. *International Journal of Molecular Sciences*, 21(13):1–23, 2020. ISSN 14220067. doi: 10.3390/ijms21134695. 20, 26, 27, 114, 129

[83] Ke Wang, Qian Ma, Yuan Ming Zhang, Guang Ting Han, Cai Xin Qu, and Shu Dong Wang. Preparation of bacterial cellulose/silk fibroin double-network hydrogel with high mechanical strength and biocompatibility for artificial cartilage. *Cellulose*, 27(4):1845–1852, 2020. ISSN 1572882X. doi: 10.1007/s10570-019-02869-0. URL https://doi.org/10.1007/s10570-019-02869-0. 20, 129

[84] Susana Guzman-Puyol, José A. Heredia-Guerrero, Luca Ceseracciu, Hadi Hajiali, Claudio Canale, Alice Scarpellini, Roberto Cingolani, Ilker S Bayer, Athanassia Athanassiou, and Elisa Mele. Low-Cost and Effective Fabrication of Biocompatible Nanofibers from Silk and Cellulose-Rich Materials. *ACS Biomaterials Science and Engineering*, 2(4):526–534, 2016. ISSN 23739878. doi: 10.1021/acsbiomaterials.5b00500. 20, 129

[85] Jung Min Lee. The Fixation Effect of a Silk Fibroin–Bacterial Cellulose Composite Plate in Segmental Defects of the Zygomatic Arch: An Experimental Study. *JAMA Otolaryngology–Head & Neck Surgery*, 139(6):629, 2013. ISSN 2168-6181. doi: 10.1001/jamaoto.2013.3044. URL http://archotol.jamanetwork.com/article.aspx?doi=10.1001/jamaoto.2013.3044. 20, 28, 29, 107, 119, 123, 152, 164

[86] Pezhman Mohammadi, A Sesilja Aranko, Christopher P Landowski, Olli Ikkala, Kristaps Jaudzems, Wolfgang Wagermaier, and Markus B Linder. Biomimetic composites with enhanced toughening using silk-inspired triblock proteins and aligned nanocellulose reinforcements. *Science Advances*, 5(9), 2019. ISSN 2375-2548. doi: 10.1126/sciadv.aaw2541. 20, 24, 106, 107, 110, 120, 122, 123, 124, 129, 145, 146

[87] Kelsey DeFrates, Theodore Markiewicz, Kayla Callaway, Ye Xue, John Stanton, David Salas-de la Cruz, and Xiao Hu. Structure–property relationships of Thai silk–microcrystalline cellulose biocomposite materials fabricated from ionic liquid. *International Journal of Biological Macromolecules*, 104:919–928, 2017. ISSN 18790003. doi: 10.1016/j.ijbiomac.2017.06.103. URL http://dx.doi.org/10.1016/j.ijbiomac.2017.06.103. 20, 28, 77, 113, 129

[88] Md Anamul Haque, Takayuki Kurokawa, and Jian Ping Gong. Super tough double network hydrogels and their application as biomaterials, 2012. ISSN 00323861. 21

[89] Tasuku Nakajima. Generalization of the sacrificial bond principle for gel and elastomer toughening. *Polymer Journal*, 49(6):477–485, 2017. ISSN 13490540. doi: 10.1038/pj.2017.12. URL http://dx.doi.org/10.1038/pj.2017.12. 21, 115, 117, 120, 146

[90] Dariusz Wawro, Michael Hummel, Anne Michud, and Herbert Sixta. Strong cellulosic film cast from ionic liquid solutions. *Fibres and Textiles in Eastern Europe*, 105(3):35–42, 2014. ISSN 23007354. 21

[91] Cho Hee Park, Lim Jeong, Donghwan Cho, Oh Hyeong Kwon, and Won Ho Park. Effect of methylcellulose on the formation and drug release behavior of silk fibroin hydrogel. *Carbohydrate Polymers*, 98(1):1179–1185, 2013. ISSN 01448617. doi: 10.1016/j.carbpol.2013.07.028. URL http://dx.doi.org/10.1016/j.carbpol.2013.07.028. 22, 28

[92] Noriyuki Isobe, Satoshi Kimura, Masahisa Wada, and Shigenori Kuga. Mechanism of cellulose gelation from aqueous alkali-urea solution. *Carbohydrate Polymers*, 89(4):1298–1300, 2012. ISSN 01448617. doi: 10.1016/j.carbpol.2012.03.023. URL http://dx.doi.org/10.1016/j.carbpol.2012.03.023. xii, 22

[93] Qiang Zhao, Richard C.M. Yam, Baoqing Zhang, Yingkui Yang, Xinjian Cheng, and Robert K.Y. Li. Novel all-cellulose ecocomposites prepared in

ionic liquids. *Cellulose*, 16(2):217–226, 2009. ISSN 09690239. doi: 10.1007/s10570-008-9251-3. 22, 23, 90, 91

[94] Ting Shu, Ke Zheng, Zhizhou Zhang, Jing Ren, Zhengjun Wang, Ying Pei, Jingjie Yeo, Grace X. Gu, and Shengjie Ling. Birefringent silk fibroin hydrogel constructed via binary solvent-exchange-induced self-assembly. *Biomacromolecules*, 22(5):1955–1965, 2021. ISSN 15264602. doi: 10.1021/acs.biomac.1c00065. 22, 25

[95] Lalit Ranakoti and Pawan Kumar Rakesh. Physio-mechanical characterization of tasar silk waste/jute fiber hybrid composite. *Composites Communications*, 22:100526, 2020. ISSN 24522139. doi: 10.1016/j.coco.2020.100526. URL https://doi.org/10.1016/j.coco.2020.100526. 23

[96] Behnaz Baghaei and Mikael Skrifvars. All-Cellulose Composites: A Review of Recent Studies on Structure, Properties and Applications. *Molecules*, 25 (12), 2020. ISSN 14203049. doi: 10.3390/molecules25122836. 23, 77, 106, 107

[97] Megan B. Turner, Scott K. Spear, John D. Holbrey, and Robin D. Rogers. Production of bioactive cellulose films reconstituted from ionic liquids. *Biomacromolecules*, 5(4):1379–1384, 2004. ISSN 15257797. doi: 10.1021/bm049748q. 24

[98] Zhuojun Meng, Xuejing Zheng, Keyong Tang, Jie Liu, and Shufa Qin. Dissolution of natural polymers in ionic liquids: A review. *E-Polymers*, 2012. ISSN 1618-7229. 24

[99] Liang Zhou, Qin Wang, Jianchuan Wen, Xin Chen, and Zhengzhong Shao. Preparation and characterization of transparent silk fibroin/cellulose blend films. *Polymer*, 54(18):5035–5042, 2013. ISSN 00323861. doi: 10.1016/j.polymer.2013.07.002. 24, 26, 77, 84, 106, 109, 110, 114, 115, 119

[100] Zuwei Luo, Mingzhong Li, Qiang Zhang, Renchuan You, Shuqin Yan, Xiufang Li, Li Ai, and Pibo Ma. Green preparation of silk fibroin/bamboo-derived cellulose nanofibril nanocomposite films with high mechanical

strength. *Journal of Materials Science*, 57(20):9265–9276, 2022. ISSN 15734803. doi: 10.1007/s10853-022-07252-2. 24

[101] Reza Eivazzadeh-Keihan, Farnoush Ahmadpour, Hooman Aghamirza Moghim Aliabadi, Fateme Radinekiyan, Ali Maleki, Hamid Madanchi, Mohammad Mahdavi, Ahmed Esmail Shalan, and Senentxu Lanceros-Méndez. Pectin-cellulose hydrogel, silk fibroin and magnesium hydroxide nanoparticles hybrid nanocomposites for biomedical applications. *International Journal of Biological Macromolecules*, 192:7–15, 2021. ISSN 18790003. doi: 10.1016/j.ijbiomac.2021.09.099. 24, 28, 29

[102] Lin Liu, Xiaogang Yang, Houyong Yu, Chao Ma, and Juming Yao. Biomimicking the structure of silk fibers via cellulose nanocrystal as β-sheet crystallite. *RSC Advances*, 4(27):14304–14313, 2014. ISSN 20462069. doi: 10.1039/c4ra01284d. 24, 25

[103] Mayakrishnan Arumugam, Balaji Murugesan, Nithya Pandiyan, Dhilip Kumar Chinnalagu, Gowri Rangasamy, and Sundrarajan Mahalingam. Electrospinning cellulose acetate/silk fibroin/Au-Ag hybrid composite nanofiber for enhanced biocidal activity against MCF-7 breast cancer cell. *Materials Science and Engineering C*, 123:112019, 2021. ISSN 18730191. doi: 10.1016/j.msec.2021.112019. URL https://doi.org/10.1016/j.msec.2021.112019. 25

[104] Yongbo Yao, Kanukai Susan Mukuze, Yumei Zhang, and Huaping Wang. Rheological behavior of cellulose/silk fibroin blend solutions with ionic liquid as solvent. *Cellulose*, 21(1):675–684, 2014. ISSN 09690239. doi: 10.1007/s10570-013-0117-y. 25, 77, 86, 93, 95

[105] G Yang, L N Zhang, X D Cao, and Y G Liu. Structure and microporous formation of cellulose/silk fibroin blend membranes Part II. Effect of post-treatment by alkali. *Journal of Membrane Science*, 210(2):379–387, 2002. ISSN 0376-7388. doi: 10.1016/S0376-7388(02)00419-2. 25

[106] Yanfei Feng, Xiufang Li, Qiang Zhang, Dezhan Ye, Mingzhong Li, Renchuan You, and Weilin Xu. Fabrication of porous silk fibroin/cellulose

nanofibril sponges with hierarchical structure using a lithium bromide solvent system. *Cellulose*, 26(2):1013–1023, 2019. ISSN 0969-0239. doi: 10.1007/s10570-018-2149-9. 26

[107] Yanfei Feng, Xiufang Li, Mingzhong Li, Dezhan Ye, Qiang Zhang, Renchuan You, and Weilin Xu. Facile Preparation of Biocompatible Silk Fibroin/Cellulose Nanocomposite Films with High Mechanical Performance. *ACS Sustainable Chemistry and Engineering*, 5(7):6227–6236, 2017. ISSN 2168-0485. doi: 10.1021/acssuschemeng.7b01161. 26, 28

[108] Giulia Guidetti, Hui Sun, Alesja Ivanova, Benedetto Marelli, and Bruno Frka-Petesic. Co-Assembly of Cellulose Nanocrystals and Silk Fibroin into Photonic Cholesteric Films. *Advanced Sustainable Systems*, 5(6), 2021. ISSN 23667486. doi: 10.1002/adsu.202000272. 27, 30

[109] Kim Anh Le, Romain Sescousse, and Tatiana Budtova. Influence of water on cellulose-EMIMAc solution properties: A viscometric study. *Cellulose*, 19(1):45–54, 2012. ISSN 09690239. doi: 10.1007/s10570-011-9610-3. 27, 54

[110] Heshan Qi, Tianqi Wei, Wei Zhao, Bin Zhu, Guoliang Liu, Pingping Wang, Zhenhui Lin, Xueyang Wang, Xiuqiang Li, Xiaowei Zhang, and Jia Zhu. An Interfacial Solar-Driven Atmospheric Water Generator Based on a Liquid Sorbent with Simultaneous Adsorption–Desorption. *Advanced Materials*, 31(43), 2019. ISSN 15214095. doi: 10.1002/adma.201903378. 27

[111] R. Pramanik and A. Arockiarajan. Mechanical and morphological characterization of a novel silk/cellulose-based soft composite. *Materials Letters*, 314:131871, 2022. ISSN 18734979. doi: 10.1016/j.matlet.2022.131871. URL https://doi.org/10.1016/j.matlet.2022.131871. 28, 29

[112] Valarmathi Narayanan and Shanmugam Sumathi. Preparation, characterization and in vitro biological study of silk fiber/methylcellulose composite for bone tissue engineering applications. *Polymer Bulletin*, 76(6): 2777–2800, 2019. ISSN 01700839. doi: 10.1007/s00289-018-2518-4. URL https://doi.org/10.1007/s00289-018-2518-4. 28, 30

[113] James A. King, Xin Zhang, and Michael E. Ries. The Formation of All-Silk Composites and Time–Temperature Superposition. *Materials*, 16(10), 2023. ISSN 19961944. doi: 10.3390/ma16103804. 28, 51, 95, 106, 130, 143, 152, 164

[114] Chris Holland, Keiji Numata, Jelena Rnjak-Kovacina, and F. Philipp Seib. The Biomedical Use of Silk: Past, Present, Future. *Advanced Healthcare Materials*, 8(1), 2019. ISSN 21922659. doi: 10.1002/adhm.201800465. 28, 78, 164

[115] Saloni Tandon, Balasubramanian Kandasubramanian, and Sobhy M Ibrahim. Silk-Based Composite Scaffolds for Tissue Engineering Applications. *Industrial and Engineering Chemistry Research*, 59(40):17593–17611, 2020. ISSN 15205045. doi: 10.1021/acs.iecr.0c02195. 28, 164

[116] Zong Ju Chen, Yi Zhang, Liang Zheng, Hua Zhang, Hui Hong Shi, Xiu Cheng Zhang, and Bing Liu. Mineralized self-assembled silk fibroin/cellulose interpenetrating network aerogel for bone tissue engineering. *Materials Science and Engineering C*, 134:112549, 2021. ISSN 18730191. doi: 10.1016/j.msec.2021.112549. URL https://doi.org/10.1016/j.msec.2021.112549. 28, 30, 130, 164

[117] B N Singh and K Pramanik. Generation of bioactive nano-composite scaffold of nanobioglass/silk fibroin/carboxymethyl cellulose for bone tissue engineering. *Journal of Biomaterials Science, Polymer Edition*, 29(16): 2011–2034, 2018. ISSN 0920-5063. doi: 10.1080/09205063.2018.1523525. 28, 30, 107, 123

[118] Jian Chen, Ao Zhuang, Huili Shao, Xuechao Hu, and Yaopeng Zhang. Robust silk fibroin/bacterial cellulose nanoribbon composite scaffolds with radial lamellae and intercalation structure for bone regeneration. *Journal of Materials Chemistry B*, 5(20):3640–3650, 2017. ISSN 2050-750X. doi: 10.1039/c7tb00485k. 28, 29, 30, 152

[119] Pramod Dorishetty, Rajkamal Balu, Sandya S. Athukoralalage, Tamar L. Greaves, Jitendra Mata, Liliana De Campo, Nabanita Saha, Andrew C.W.

Zannettino, Naba K. Dutta, and Namita Roy Choudhury. Tunable Biomimetic Hydrogels from Silk Fibroin and Nanocellulose. *ACS Sustainable Chemistry and Engineering*, 8(6):2375–2389, 2020. ISSN 21680485. doi: 10.1021/acssuschemeng.9b05317. 28, 115

[120] Xin Cao, Jinghua Li, Weijie Zhai, Bowen Zhou, Hao Lin, and Yi Wang. Inhibiting Friction-Induced Exogenous Adhesion via Robust Lubricative Core-Shell Nanofibers for High-Quality Tendon Repair. *Biomacromolecules*, 2025. ISSN 15264602. doi: 10.1021/acs.biomac.4c01729. 28

[121] Shujie Cheng, Jihong Yang, Jianguo Song, Xin Cao, Bowen Zhou, Lan Yang, Chong Li, and Yi Wang. A motion-responsive injectable lubricative hydrogel for efficient Achilles tendon adhesion prevention, 2025. ISSN 25900064. 28

[122] Gabriela Carrasco-Torres, Manuel A. Valdés-Madrigal, Verónica R. Vásquez-Garzón, Rafael Baltiérrez-Hoyos, Eduard D. De la Cruz-Burelo, Ramón Román-Doval, and Anaí A. Valencia-Lazcano. Effect of Silk Fibroin on cell viability in electrospun scaffolds of polyethylene oxide. *Polymers*, 11(3), 2019. ISSN 20734360. doi: 10.3390/polym11030451. 28

[123] Keya Ganguly, Hexiu Jin, Sayan Deb Dutta, Dinesh K Patel, Tejal V Patil, and Ki Taek Lim. Magnetic field-assisted aligned patterning in an alginate-silk fibroin/nanocellulose composite for guided wound healing. *Carbohydrate Polymers*, 287:119321, 2022. ISSN 01448617. doi: 10.1016/j.carbpol.2022.119321. URL https://doi.org/10.1016/j.carbpol.2022.119321. 29

[124] Zong Ju Chen, Hui Hong Shi, Liang Zheng, Hua Zhang, Yu Ying Cha, Hui Xian Ruan, Yi Zhang, and Xiu Cheng Zhang. A new cancellous bone material of silk fibroin/cellulose dual network composite aerogel reinforced by nano-hydroxyapatite filler. *International Journal of Biological Macromolecules*, 182:286–297, 2021. ISSN 18790003. doi: 10.1016/j.ijbiomac.2021.03.204. 29, 30, 107

[125] Zuguang Gong, Yuhong Yang, Qingguang Ren, Xin Chen, and Zhengzhong Shao. Injectable thixotropic hydrogel comprising regenerated silk fibroin and hydroxypropylcellulose. *Soft Matter*, 8(10):2875–2883, 2012. ISSN 1744683X. doi: 10.1039/c2sm06984a. 30

[126] Dan Yan, Lili Qiu, Kenneth J Shea, Zihui Meng, and Min Xue. Dyeing and Functionalization of Wearable Silk Fibroin/Cellulose Composite by Nanocolloidal Array. *ACS Applied Materials & Interfaces*, 11(42):39163–39170, 2019. ISSN 1944-8244. doi: 10.1021/acsami.9b11576. 30, 31

[127] Hannah Richie, Veronika Samborska, and Max Roser. Plastic Pollution. *Our World in Data*, 2023. URL https://ourworldindata.org/plastic-pollution. 32

[128] UK Statistics on Waste. Technical report, Department for Environment, Food, and Rural Affairs, 2025. URL https://www.gov.uk/government/statistics/uk-waste-data/uk-statistics-on-waste. 32

[129] Plastic Leakage in 2019. Technical report, OECD, 2019. 32

[130] Manikant Tripathi, Minaxi Sharma, Saroj Bala, Vijay Kumar Thakur, Anoop Singh, Kavya Dashora, Phil Hart, and Vijai Kumar Gupta. Recent technologies for transforming textile waste into value-added products: A review. *Current Research in Biotechnology*, 7:100225, 2024. ISSN 25902628. doi: 10.1016/j.crbiot.2024.100225. URL https://doi.org/10.1016/j.crbiot.2024.100225. 32

[131] Linlin Huang, Jifeng Shi, Wei Zhou, and Qing Zhang. Advances in Preparation and Properties of Regenerated Silk Fibroin. *International Journal of Molecular Sciences*, 24(17), 2023. ISSN 14220067. doi: 10.3390/ijms241713153. 32

[132] Carina Olsson, Alexander Idström, Lars Nordstierna, and Gunnar Westman. Influence of water on swelling and dissolution of cellulose in 1-ethyl-3-methylimidazolium acetate. *Carbohydrate Polymers*, 99:438–446, 2014. ISSN 01448617. doi: 10.1016/j.carbpol.2013.08.042. URL http://dx.doi.org/10.1016/j.carbpol.2013.08.042. 32, 54

[133] Kevin Menard. *Dynamic Mechanical Analysis: A Practical Introduction*. CRC Press, Boca Raton, 2 edition, 2008. xiii, 37, 41, 42, 43, 46, 48, 49, 50, 51, 111, 112

[134] TA Instruments. Dynamic Mechanical Analysis Course, 2023. 40, 48, 49

[135] Stephen Timoshenko. *Strength of Materials*. Van Nostrand, Princeton, 3 edition, 1956. 41, 42, 52, 117

[136] Turner S. *Mechanical Testing of Plastics*. The Plastics Institute, London, members edition, 1973. ISBN 0592000761. 42

[137] O. Lieleg, J. Kayser, G. Brambilla, L. Cipelletti, and A. R. Bausch. Slow dynamics and internal stress relaxation in bundled cytoskeletal networks. *Nature Materials*, 10(3):236–242, 2011. ISSN 14764660. doi: 10.1038/nmat2939. 43, 44, 45

[138] Yuval Mulla, F. C. Mackintosh, and Gijsje H. Koenderink. Origin of Slow Stress Relaxation in the Cytoskeleton. *Physical Review Letters*, 122(21):218102, 2019. ISSN 10797114. doi: 10.1103/PhysRevLett.122.218102. URL https://doi.org/10.1103/PhysRevLett.122.218102. 43, 45, 107, 120, 124, 146

[139] Jake Song, Qingteng Zhang, Felipe De Quesada, Mehedi H. Rizvi, Joseph B. Tracy, Jan Ilavsky, Suresh Narayanan, Emanuela Del Gado, Robert L. Leheny, Niels Holten-Anderse, and Gareth H. McKinley. Microscopic dynamics underlying the stress relaxation of arrested soft materials. *Proceedings of the National Academy of Sciences of the United States of America*, 119(30):1–8, 2022. ISSN 10916490. doi: 10.1073/pnas.2201566119. 43, 45, 121

[140] Donald D. Joye. Stress–relaxation in three-element and four-element mechanical models of viscoelastic materials. *Journal of Applied Polymer Science*, 47(2):345–350, 1993. ISSN 10974628. doi: 10.1002/app.1993.070470214. xiii, 43, 44

[141] Scott Mackenzie. The Mechanism of Creep and its Stages, 2024. URL https://thermalprocessing.com/the-mechanism-of-creep-and-its-stages/. 44

[142] M. E. Kassner and M. T. Pérez-Prado. *Fundamentals of Creep in Metals and Alloys*. Elsevier, 3 edition, 2004. ISBN 9780080436371. doi: 10.1016/B978-0-08-043637-1.X5000-5. 44

[143] Daniel L. Baker, Matthew Reynolds, Robin Masurel, Peter D. Olmsted, and Johan Mattsson. Cooperative Intramolecular Dynamics Control the Chain-Length-Dependent Glass Transition in Polymers. *Physical Review X*, 12(2), 2022. ISSN 21603308. doi: 10.1103/PhysRevX.12.021047. 45, 48, 111

[144] Juan Guan, David Porter, and Fritz Vollrath. Thermally induced changes in dynamic mechanical properties of native silks. *Biomacromolecules*, 14 (3):930–937, 2013. ISSN 15257797. doi: 10.1021/bm400012k. xviii, 48, 52, 111, 112, 113, 134

[145] Juan Guan, Fritz Vollrath, and David Porter. Silk "Quality" Revealed Using Dynamic Mechanical Thermal Analysis (DMTA). In *BACSA International Conference: Building value Chains in Sericulture Silk*, 2013. URL www.oxfordsilkgroup.com/DMTA. 48

[146] S. A. Bradley and S. H. Carr. Mechanical Loss Processes in Polysaccharides. *Journal of Polymer Science, Polymer Physics Edition*, 14(1):111–124, 1976. ISSN 00981273. doi: 10.1002/pol.1976.180140109. 48, 49, 111

[147] M. F. Froix and R. Nelson. Interaction of water with cellulose from nuclear magnetic resonance relaxation times. *Macromolecules*, 8(6):726–730, 1975. 49, 70, 112

[148] Johan Sundberg, Guillermo Toriz, and Paul Gatenholm. Moisture induced plasticity of amorphous cellulose films from ionic liquid. *Polymer*, 54(24): 6555–6560, 2013. ISSN 00323861. doi: 10.1016/j.polymer.2013.10.012. URL http://dx.doi.org/10.1016/j.polymer.2013.10.012. 49

[149] Perkin Elmer. Dynamic Mechanical Analysis (DMA) A Beginner's Guide, 2013. 49

[150] V.A. Bershtein, V. M. Egorov, and G. V. Leib. *Differential Scanning Calorimetry of Polymers: Physics, Chemistry, Analysis, Technology*. Ellis Horwood, 1994. 49

[151] Witold Brostow, Rachel Chiu, Ioannis M. Kalogeras, and Aglaia Vassilikou-Dova. Prediction of glass transition temperatures: Binary blends and copolymers. *Materials Letters*, 62(17-18):3152–3155, 2008. ISSN 0167577X. doi: 10.1016/j.matlet.2008.02.008. xviii, 50, 111, 112

[152] PerkinElmer. Relaxation of PMMA and Calculation of the Activation Energy, 2011. 51

[153] Daniel Herschlag and Margaux M. Pinney. Hydrogen Bonds: Simple after All?, jun 2018. ISSN 15204995. 51

[154] Thomas G Mezger. *The Rheology Handbook*. Coatings Compendia, Hannover, 2 edition, 2006. ISBN 3-87870-174-8. xiv, 53

[155] Donald L. Pavia, Gary M. Lampman, and George S. Kriz. *Introduction to Spectroscopy*. Thomson Learning, 3 edition, 2001. ISBN 0-03-031961-7. xiv, 55, 56

[156] Simon Duckett and Bruce Gilbert. *Foundations of Spectroscopy*. Oxford University Press, 1 edition, 2001. ISBN 0-19-850335. xiv, 56

[157] Melinda J. Duer. *Introduction to Solid-State NMR Spectroscopy*. Blackwell Publishing, 1 edition, 2004. ISBN 1-4051-0914-9. xiv, 56

[158] H. W. Spiess. Nuclear Magnetic Resonance. In I. M. Ward, editor, *Structure and Properties of Oriented Polymers*, chapter 5, pages 234–269. Chapman and Hall, 2 edition, 1997. ISBN 0412 60880 4. xiv, 55, 56, 57

[159] James A King, Peter J Hine, Daniel L Baker, and Michael E Ries. Understanding the Dissolution of Cellulose and Silk Fibroin in 1-ethyl-3-methylimidazolium Acetate and Dimethyl Sulphoxide for Application in

Hybrid Films. *Materials*, 17(21):5262, 2024. ISSN 1996-1944. doi: 10.3390/ma17215262. URL https://www.mdpi.com/1996-1944/17/21/5262. 56, 107, 130, 131, 141, 143, 145

[160] Christopher S. Lovell, Adam Walker, Robin A. Damion, Asanah Radhi, Steven F. Tanner, Tatiana Budtova, and Michael E. Ries. Influence of cellulose on ion diffusivity in 1-ethyl-3-methyl-imidazolium acetate cellulose solutions. *Biomacromolecules*, 11(11):2927–2935, 2010. ISSN 15264602. doi: 10.1021/bm1006807. 56, 57, 81, 83, 90, 92, 96, 97, 98

[161] Jinming Zhang, Hao Zhang, Jin Wu, Jun Zhang, Jiasong He, and Junfeng Xiang. NMR spectroscopic studies of cellobiose solvation in EmimAc aimed to understand the dissolution mechanism of cellulose in ionic liquids. *Physical Chemistry Chemical Physics*, 12(8):1648–1648, 2010. ISSN 14639076. doi: 10.1039/c001176m. 56, 57, 98

[162] Yang Zhao, Shanjiao Gao, Jianji Wang, and Junming Tang. Aggregation of ionic liquids [Cnmim]Br (n = 4, 6, 8, 10, 12) in D2O: A NMR study. *Journal of Physical Chemistry B*, 112(7):2031–2039, 2008. ISSN 15206106. doi: 10.1021/jp076467e. 57

[163] Syed Muhammad Alay-e Abbas, Khalid Mahmood, Adnan Ali, Muhammad Imran Arshad, Nasir Amin, and Muhammad Sajjad Hasan. Characterisation Techniques for Bionanocomposites. In *Bionanocomposites*, chapter 5, pages 105–144. Elsevier, 2020. 58

[164] Amnah Hadadi, John W Whittaker, David E Verrill, Xiao Hu, Luca Larini, and David Salas-De La Cruz. A Hierarchical Model to Understand the Processing of Polysaccharides/Protein-Based Films in Ionic Liquids. *Biomacromolecules*, 19(10):3970–3982, 2018. ISSN 15264602. doi: 10.1021/acs.biomac.8b00903. xiv, 58, 59, 106, 113, 118, 119, 163

[165] James A King, Peter J Hine, Daniel L Baker, Matthew Creswick, and Michael E Ries. Hybrid biocomposites: From molecular behaviour to material properties in silk fibroin/cellulose films. *International Journal of Biological Macromolecules*, page 145931, 2025. ISSN 0141-8130. doi: https://doi.

org/10.1016/j.ijbiomac.2025.145931. URL https://www.sciencedirect.com/science/article/pii/S0141813025064864. 59, 129, 131, 146

[166] B. D. Cullity and S. R. Stock. *Elements of X-Ray Diffraction*. Prentice Hall, 3 edition, 2001. xiv, 60, 63

[167] L. Segal, J. J. Creely, A. E. Martin, and C. M. Conrad. An Empirical Method for Estimating the Degree of Crystallinity of Native Cellulose Using the X-Ray Diffractometer. *Textile Research Journal*, 29(10):786–794, 1959. ISSN 00405175. doi: 10.1177/004051755902901003. 61

[168] Sunkyu Park, John O Baker, Michael E Himmel, Philip A Parilla, and David K Johnson. Cellulose crystallinity index: measurement techniques and their impact on interpreting cellulase performance. *Biotechnology for Biofuels*, 3, 2010. ISSN 1754-6834. doi: 10.1186/1754-6834-3-10. 61, 63

[169] Alfred D. French. Increment in evolution of cellulose crystallinity analysis, 2020. ISSN 1572882X. 61, 63

[170] Alfred D. French. Idealized powder diffraction patterns for cellulose polymorphs. *Cellulose*, 21(2):885–896, 2014. ISSN 09690239. doi: 10.1007/s10570-013-0030-4. 61

[171] James E Hawkins. *Analysis of the Dissolution Behaviour of Flax Based Yarn in an Ionic Liquid*. PhD thesis, University of Leeds, 2021. 61

[172] Erik Kissa. Characterization, Testing, and Measurement. In *Dispersions*, page 708. Routledge, New York, 1 edition, 1999. ISBN 9781315141381. 65

[173] Muhammad Noman Khan, Zain ul Abidin, Shamim Khan, Almas, Sonia Mustafa, and Iftikhar Ahmad. Birefringence of cellulose: review, measurement techniques, dispersion models, biomedical applications and future perspectives. *Wood Science and Technology*, 58(1):5–22, 2024. ISSN 14325225. doi: 10.1007/s00226-023-01512-3. URL https://doi.org/10.1007/s00226-023-01512-3. 65, 66

[174] Patcharida Chaosri, Patthraporn Siripipatthana, and P. Srihanam. Water hyacinth cellulose/silk fibroin composite films: Preparation and characterization. *Asian Journal of Chemistry*, 33(1):132–136, 2021. ISSN 09707077. doi: 10.14233/ajchem.2021.22973. 68

[175] Takashi Nishino, Ikuyo Matsuda, and Koichi Hirao. All-cellulose composite. *Macromolecules*, 37(20):7683–7687, 2004. ISSN 00249297. doi: 10.1021/ma049300h. 68

[176] Chunhong Wang, Ni Wang, Shuhan Liu, Lin P'ing Choo-Simth, Hongxia Zhang, and Zhongxiang Zhi. Investigation of Microfibril Angle of Flax Fibers Using X-Ray Diffraction and Scanning Electron Microscopy. *Journal of Natural Fibers*, 17(7):1001–1010, 2020. ISSN 1544046X. doi: 10.1080/15440478.2018.1546639. URL https://doi.org/10.1080/15440478.2018.1546639. 68

[177] Ke Chen, Weixin Xu, Yun Ding, Ping Xue, Pinghou Sheng, Hui Qiao, and Jimin He. Hemp-based all-cellulose composites through ionic liquid promoted controllable dissolution and structural control. *Carbohydrate Polymers*, 235(February):116027, 2020. ISSN 01448617. doi: 10.1016/j.carbpol.2020.116027. URL https://doi.org/10.1016/j.carbpol.2020.116027. 68

[178] Joseph Goldstein, Dale E. Newbury, Joseph R. Michael, W. M. Ritchie, Nicholas, John Henry J. Scott, and David C. Joy. *Scanning Electron Microscopy and X-Ray Microanalysis*. Springer, 2018. 68

[179] Li Yong, Li Jian, Liu Xian, and Wu Bei. Test and analysis of the porosity of cotton fiber assembly. *Journal of Engineered Fibers and Fabrics*, 16, 2021. ISSN 15589250. doi: 10.1177/15589250211024225. 68, 142

[180] Yasemin Seki, Figen Selli, Umit Halis Erdogan, Metehan Atagur, and M. Ozgur Seydibeyoglu. A review on alternative raw materials for sustainable production: novel plant fibers. *Cellulose*, 29(9):4877–4918, 2022. ISSN 1572882X. doi: 10.1007/s10570-022-04597-4. URL https://doi.org/10.1007/s10570-022-04597-4. 68, 141

[181] Ashley Victoria, Peter John Hine, Keeran Ward, and Michael Edward Ries. Design of experiments in the optimization of all-cellulose composites. *Cellulose*, 30(17):11013–11039, 2023. ISSN 1572882X. doi: 10.1007/s10570-023-05535-8. 68, 107, 129, 135, 141

[182] Martin A. Hubbe, Douglas J. Gardner, and Wei Shen. Contact angles and wettability of cellulosic surfaces: A review of proposed mechanisms and test strategies. *BioResources*, 10(4):8657–8749, 2015. ISSN 19302126. doi: 10.15376/biores.10.4.Hubbe_Gardner_Shen. 69, 70

[183] Tommi Huhtamäki, Xuelin Tian, Juuso T. Korhonen, and Robin H.A. Ras. Surface-wetting characterization using contact-angle measurements. *Nature Protocols*, 13(7):1521–1538, 2018. ISSN 17502799. doi: 10.1038/s41596-018-0003-z. URL http://dx.doi.org/10.1038/s41596-018-0003-z. 69, 70, 123

[184] Xiaoyan Liu, Zhao Qin, Yuxiang Ma, Huamin Liu, and Xuede Wang. Cellulose-Based Films for Food Packaging Applications: Review of Preparation, Properties, and Prospects. *Journal of Renewable Materials*, 11(8): 3203–3225, 2023. ISSN 21646341. doi: 10.32604/jrm.2023.027613. 69, 70

[185] Sara Rbihi, Abdelkhalk Aboulouard, Latifa Laallam, and Ahmed Jouaiti. Contact Angle Measurements of Cellulose based Thin Film composites: wettability, surface free energy and surface hardness, 2020. ISSN 24680230. 69

[186] Shuaiyan Wang, Tao Huang, Chen Lai, Tingfei Xi, Shibo Liao, and Fang Nan. Oxidized Nano-Bacterial Cellulose/Silk Fibroin Composite Films. *Cellulose Chemistry and Technology*, 50(7-8):853–862, 2016. ISSN 05769787. 70

[187] Supranee Kaewpirom, Sarayoot Piboonnithikasem, Pongsathorn Sroisroemsap, Sittichai Uttoom, and Siridech Boonsang. Tailoring silk fibroin hydrophilicity and physicochemical properties using sugar alcohols for medical device coatings. *Scientific Reports*, 14(1):1–14, 2024. ISSN

20452322. doi: 10.1038/s41598-024-64450-5. URL https://doi.org/10.1038/s41598-024-64450-5. 70

[188] Albert Yan. Sound Transmission. URL https://www.sekon.cc/acoustics/SoundTransmission/index.htm. xvi, 72

[189] A. C. C. Warnock. *Fundamentals of building acoustics*. National Research Council of Canada. Institute for Research in Construction, 1985. 72, 157, 158

[190] Muhammad Tuhin. What Is Resonance in Physics? Vibrating at Natural Frequencies, 2025. URL https://www.sciencenewstoday.org/what-is-resonance-in-physics-vibrating-at-natural-frequencies. 72

[191] Arun Arjunan, Ahmad Baroutaji, John Robinson, Aaron Vance, and Abul Arafat. Acoustic metamaterials for sound absorption and insulation in buildings. *Building and Environment*, 251:111250, 2024. ISSN 03601323. doi: 10.1016/j.buildenv.2024.111250. URL https://doi.org/10.1016/j.buildenv.2024.111250. 73, 158

[192] Ni Sui, Xiang Yan, Tai Yun Huang, Jun Xu, Fuh Gwo Yuan, and Yun Jing. A lightweight yet sound-proof honeycomb acoustic metamaterial. *Applied Physics Letters*, 106(17), 2015. ISSN 00036951. doi: 10.1063/1.4919235. URL http://dx.doi.org/10.1063/1.4919235. 73, 156

[193] Francesco Asdrubali, Francesco D'Alessandro, and Samuele Schiavoni. A review of unconventional sustainable building insulation materials. *Sustainable Materials and Technologies*, 4(2015):1–17, 2015. ISSN 22149937. doi: 10.1016/j.susmat.2015.05.002. URL http://dx.doi.org/10.1016/j.susmat.2015.05.002. 73, 129, 158, 163, 165

[194] Umberto Berardi and Gino Iannace. Acoustic characterization of natural fibers for sound absorption applications. *Building and Environment*, 94:840–852, 2015. ISSN 03601323. doi: 10.1016/j.buildenv.2015.05.029. URL http://dx.doi.org/10.1016/j.buildenv.2015.05.029. 73, 129, 130, 156, 165

[195] Olivier Doutres, Yacoubou Salissou, Noureddine Atalla, and Raymond Panneton. Evaluation of the acoustic and non-acoustic properties of sound absorbing materials using a three-microphone impedance tube, 2010. ISSN 0003682X. 73, 163

[196] Ronalds Gonzalez, Hasan Jameel, Hou Min Chang, Trevor Treasure, Adrian Pirraglia, and Daniel Saloni. Thermo-mechanical pulping as a pretreatment for agricultural biomass for biochemical conversion. *BioResources*, 6(2): 1599–1614, 2011. ISSN 19302126. doi: 10.15376/biores.6.2.1599-1614. 77

[197] S Wolf, J Lambauer, U Fahl, M Blesl, and A Voss. Industrial heat pumps in Germany - potentials , technological development and application examples. *ECEEE 2012 Summer Study - Energy Efficiency in Industry*, (September): 543–550, 2012. URL http://web.ornl.gov/sci/ees/etsd/btric/usnt/03InHPsAchmaIERWolf.pdf. 77

[198] Yongbo Yao, Zhiyong Yan, Zhe Li, Yumei Zhang, and Huaping Wang. Viscoelastic behavior and sol-gel transition of cellulose/silk fibroin/1-butyl-3-methylimidazolium chloride extended from dilute to concentrated solutions. *Polymer Engineering and Science*, 58(11):1931–1936, 2018. ISSN 15482634. doi: 10.1002/pen.24802. 77, 86, 93

[199] Omar A.El Seoud, Marc Kostag, Shirley Possidonio, Marcella T. Dignani, Paulo A.R. Pires, and Matheus C. Lourenço. Dissolution of silk fibroin in mixtures of ionic liquids and dimethyl sulfoxide: On the relative importance of temperature and binary solvent composition. *Polymers*, 14(1), 2022. ISSN 20734360. doi: 10.3390/polym14010013. 77, 81, 89, 93

[200] Yan Zhou, Xiaocheng Zhang, Jinming Zhang, Yaohui Cheng, Jin Wu, Jian Yu, and Jun Zhang. Molecular weight characterization of cellulose using ionic liquids. *Polymer Testing*, 93:106985, 2021. ISSN 01429418. doi: 10.1016/j.polymertesting.2020.106985. URL https://doi.org/10.1016/j.polymertesting.2020.106985. 78

[201] Cheng Zhang, Xin Chen, and Zhengzhong Shao. Sol-Gel Transition of Regenerated Silk Fibroins in Ionic Liquid/Water Mixtures. *ACS Biomaterials Science and Engineering*, 2(1):12–18, 2016. ISSN 2373-9878. doi: 10.1021/acsbiomaterials.5b00149. 81, 84, 93, 102

[202] Nicolas Keppeler, Paulo Augusto R. Pires, José Leandro S. Freitas, and Omar A. El Seoud. Cellulose dissolution in mixtures of ionic liquids and molecular solvents: The fruitful synergism of experiment and theory. *Journal of Molecular Liquids*, 386, 2023. ISSN 01677322. doi: 10.1016/j.molliq.2023.122490. 81

[203] Martin Gericke, Kerstin Schlufter, Tim Liebert, Thomas Heinze, and Tatiana Budtova. Rheological properties of cellulose/ionic liquid solutions: From dilute to concentrated states. *Biomacromolecules*, 10(5):1188–1194, 2009. ISSN 15257797. doi: 10.1021/bm801430x. 86, 92, 95, 96, 102

[204] Daniel C. Harris. Nonlinear least-squares curve fitting with microsoft excel solver. *Journal of Chemical Education*, 75(1):119–121, 1998. ISSN 00219584. doi: 10.1021/ed075p119. 88

[205] Lihua Zhang, Cong Huang, Chenrui Zhang, and Hui Pan. Swelling and dissolution of cellulose in binary systems of three ionic liquids and three co-solvents. *Cellulose*, 28(8):4643–4653, 2021. ISSN 1572882X. doi: 10.1007/s10570-021-03844-4. URL https://doi.org/10.1007/s10570-021-03844-4. 89

[206] Bjorn Lindman, Gunnar Karlstrom, and Lars Stigsson. On the mechanism of dissolution of cellulose. *Journal of Molecular Liquids*, 156(1, SI):76–81, 2010. ISSN 0167-7322. doi: 10.1016/j.molliq.2010.04.016. 89

[207] David M. Phillips, Lawrence F. Drummy, Deborah G. Conrady, Douglas M. Fox, Rajesh R. Naik, Morley O. Stone, Paul C. Trulove, Hugh C. De Long, and Robert A. Mantz. Dissolution and regeneration of Bombyx mori silk fibroin using ionic liquids. *Journal of the American Chemical Society*, 126 (44):14350–14351, 2004. ISSN 00027863. doi: 10.1021/ja046079f. 90, 98

[208] Mitsuharu Koide, Isao Wataoka, Hiroshi Urakawa, Kanji Kajiwara, Ute Henniges, and Thomas Rosenau. Intrinsic characteristics of cellulose dissolved in an ionic liquid: the shape of a single cellulose molecule in solution. *Cellulose*, 26(4):2233–2242, 2019. ISSN 1572882X. doi: 10.1007/s10570-018-02238-3. 90

[209] Takatsugu Endo, Shota Hosomi, Shunsuke Fujii, Kazuaki Ninomiya, and Kenji Takahashi. Nano-structural investigation on cellulose highly dissolved in ionic liquid: A small angle X-ray scattering study. *Molecules*, 22(1), 2017. ISSN 14203049. doi: 10.3390/molecules22010178. 90

[210] Sofia Napso, Dmitry M. Rein, Rafail Khalfin, and Yachin Cohen. Semidilute solution structure of cellulose in an ionic liquid and its mixture with a polar organic co-solvent studied by small-angle X-ray scattering. *Journal of Polymer Science, Part B: Polymer Physics*, 55(11):888–894, 2017. ISSN 10990488. doi: 10.1002/polb.24337. 90, 162

[211] Gamal Abdalla Suliman Haron, Hamayoun Mahmood, Hilmi Bin Noh, Masahiro Goto, and Muhammad Moniruzzaman. Cellulose nanocrystals preparation from microcrystalline cellulose using ionic liquid-DMSO binary mixture as a processing medium. *Journal of Molecular Liquids*, 346, 2022. ISSN 01677322. doi: 10.1016/j.molliq.2021.118208. 91

[212] Fei Lu, Lejun Wang, Chao Zhang, Bowen Cheng, Ruigang Liu, and Yong Huang. Influence of temperature on the solution rheology of cellulose in 1-ethyl-3-methylimidazolium chloride/dimethyl sulfoxide. *Cellulose*, 22(5): 3077–3087, 2015. ISSN 1572882X. doi: 10.1007/s10570-015-0740-x. 95, 96

[213] Hossein Baniasadi, Ziba Fathi, Cristina D. Cruz, Roozbeh Abidnejad, Päivi Tammela, Jukka Niskanen, and Erlantz Lizundia. Structure-property correlations and environmental impact assessment of sustainable antibacterial food packaging films reinforced with fungal chitin nanofibrils. *Food Hydrocolloids*, 162, 2025. ISSN 0268005X. doi: 10.1016/j.foodhyd.2024.110987. 106

[214] Hossein Baniasadi, Ziba Fathi, Erlantz Lizundia, Cristina D. Cruz, Roozbeh Abidnejad, Mahyar Fazeli, Päivi Tammela, Eero Kontturi, Juha Lipponen, and Jukka Niskanen. Development and characterization of pomegranate peel extract-infused carboxymethyl cellulose composite films for functional, sustainable food packaging. *Food Hydrocolloids*, 158, 2025. ISSN 0268005X. doi: 10.1016/j.foodhyd.2024.110525. 106

[215] Mayank, Andreas Bardenhagen, Vishal Sethi, and Heena Gudwani. Spider-silk composite material for aerospace application. *Acta Astronautica*, 193: 704–709, 2022. ISSN 00945765. doi: 10.1016/j.actaastro.2021.08.013. URL https://doi.org/10.1016/j.actaastro.2021.08.013. 106

[216] Nattakan Soykeabkaew, Noriko Arimoto, Takashi Nishino, and Ton Peijs. All-cellulose composites by surface selective dissolution of aligned lignocellulosic fibres. *Composites Science and Technology*, 68(10-11):2201–2207, 2008. ISSN 02663538. doi: 10.1016/j.compscitech.2008.03.023. 107

[217] Sihan Chen, Chase P. Broedersz, Tomer Markovich, and Fred C. MacKintosh. Nonlinear stress relaxation of transiently crosslinked biopolymer networks. *Physical Review E*, 104(3):1–14, 2021. ISSN 24700053. doi: 10.1103/PhysRevE.104.034418. 107, 120, 124, 146, 164

[218] Sungmin Nam, Kenneth H. Hu, Manish J. Butte, and Ovijit Chaudhuri. Strain-enhanced stress relaxation impacts nonlinear elasticity in collagen gels. *Proceedings of the National Academy of Sciences of the United States of America*, 113(20):5492–5497, 2016. ISSN 10916490. doi: 10.1073/pnas.1523906113. 107, 120, 124, 146, 164

[219] Paul C. Hiemenz and Timothy. Lodge. *Polymer chemistry*. 2 edition, 2007. ISBN 1574447793. URL https://www.eng.uc.edu/{~}beaucag/Classes/Properties/Books/PaulC.Hiemenz,TimothyP.Lodge-PolymerChemistry-CRCPress(2007).pdf. xviii, 111, 112

[220] Eduardo Fischer Kerche, Roberta Neves, Heitor Ornaghi Jr., Ademir José Zattera, and Henri Stephan Schrekker. The Influence of Ionic Liquid Con-

centration on Microcrystalline Cellulose Surface Modification. *SSRN Electronic Journal*, 3:0–9, 2022. doi: 10.2139/ssrn.4063476. 114

[221] Ali Abdulkhani, Maryam Daliri Sousefi, Alireza Ashori, and Ghanbar Ebrahimi. Preparation and characterization of sodium carboxymethyl cellulose/silk fibroin/graphene oxide nanocomposite films. *Polymer Testing*, 52: 218–224, 2016. ISSN 01429418. doi: 10.1016/j.polymertesting.2016.03.020. 114

[222] Jovan Mijovic. *Prediction of the deformation properties of polymeric and composite materials*. ACS, Washington, 1995. 117

[223] Norman E. Dowling. *Mechanical Behaviour of Materials: Engineering Methods for Deformation, Fracture, and Fatigue*. Pearson, 4 edition, 2013. 120, 122

[224] A Venu Nadhan, A Varada Rajulu, R Li, J Cai, and L. Zhang. Properties of waste silk short fiber/cellulose green composite films. *Journal of Composite Materials*, 46(1):123–127, 2012. ISSN 00219983. doi: 10.1177/0021998311410507. 124

[225] Francesco Asdrubali. The role of Life Cycle Assessment (LCA) in the design of sustainable buildings: Thermal and sound insulating materials. *8th European Conference on Noise Control 2009, Euronoise 2009 - Proceedings of the Institute of Acoustics*, 31(3), 2009. 129

[226] A. S. Virk, W. Hall, and J. Summerscales. Modulus and strength prediction for natural fibre composites. In *Materials Science and Technology (United Kingdom)*, volume 28, pages 864–871. Maney Publishing, 2012. doi: 10.1179/1743284712Y.0000000022. 138, 147, 148, 149

[227] Peter Hine, Bushra Parveen, Dave Brands, and Fin Caton-Rose. Validation of the modified rule of mixtures using a combination of fibre orientation and fibre length measurements. *Composites Part A: Applied Science and Manufacturing*, 64:70–78, 2014. ISSN 1359835X. doi: 10.1016/j.compositesa.2014.04.017. 138, 147, 148, 149

[228] John Summerscales. Composites Design and Manufacture Module, 2025. URL http://lists.lib.plymouth.ac.uk/lists/15D82EF9-06E6-A71D-1544-EE8162EE9D0A.html{#}section-17E16A67-C278-4486-9284-4440D67327B0. 145

[229] Herbert Krenchel. *Fibre reinforcement : theoretical and practical investigations of the elasticity and strength of fibre-reinforced materials.* Akademisk Forlag, Copenhagen, 1964. URL https://lib.ugent.be/catalog/rug01:001280222. 146, 147, 149

[230] H. L. Cox. The elasticity and strength of paper and other fibrous materials. *British Journal of Applied Physics*, 3(3):72–79, 1952. ISSN 05083443. doi: 10.1088/0508-3443/3/3/302. 147, 149

[231] Assia Chichane, Radouane Boujmal, and Abdellah El Barkany. Towards a green & ecological revolution: Review of natural reinforcing bio-composites and bio-hybrid composites, 2024. ISSN 14782391. 149

[232] D. Scott MacKenzie. Four basic types of fracture mechanisms — Gear Solutions Magazine Your Resource to the Gear Industry, 2020. URL https://gearsolutions.com/departments/hot-seat/four-basic-types-of-fracture-mechanisms/. 155

[233] Abdulrahman Alshabib, Carlos A. Jurado, and Akimasa Tsujimoto. Short fiber-reinforced resin-based composites (SFRCs); Current status anfuture perspectives. *Dental Materials Journal*, 41(5):647–654, 2022. ISSN 18811361. doi: 10.4012/dmj.2022-080. 155

[234] Robin R. Wareing, John L. Davy, and John R. Pearse. Variations in measured sound transmission loss due to sample size and construction parameters. *Applied Acoustics*, 89:166–177, 2015. ISSN 1872910X. doi: 10.1016/j.apacoust.2014.10.001. URL http://dx.doi.org/10.1016/j.apacoust.2014.10.001. 157

[235] W. H. Tan and C. F. Sin. Sound Transmission Loss Analysis on Building Materials. *International Journal of Automotive and Mechanical Engineering*, 15(4):6001–6011, 2018. 157

[236] Zhao Liu, Chenhao Dong, Saihua Li, Xiaoye Cong, Xin Wang, Chris Rudd, Xiaosu Yi, and Xiaoling Liu. Novel design of skin construction on the sound absorption of honeycomb sandwich panels. *Composite Structures*, 356:118870, 2025. ISSN 02638223. doi: 10.1016/j.compstruct.2025.118870. URL https://doi.org/10.1016/j.compstruct.2025.118870. 157, 163

[237] Florian Müller-Plathe. Coarse-graining in polymer simulation: From the atomistic to the mesoscopic scale and back. *ChemPhysChem*, 3(9):754–769, 2002. ISSN 14394235. doi: 10.1002/1439-7641(20020916)3:9⟨754::AID-CPHC754⟩3.0.CO;2-U. 162

[238] Roberta Motta Neves, Heitor Luiz Ornaghi, Fillip Cortat Alves, Ademir José Zattera, Milanta Tom, Hiran Mayookh Lal, Arya Uthaman, and Sabu Thomas. Creep and stress relaxation behavior of functionalized microcrystalline cellulose/epoxy composites. *Cellulose*, 30(4):2197–2216, 2023. ISSN 1572882X. doi: 10.1007/s10570-022-05020-8. URL https://doi.org/10.1007/s10570-022-05020-8. 163

[239] Zhao Liu, Chenhao Dong, Lu Tong, Chris Rudd, Xiaosu Yi, and Xiaoling Liu. Sound Absorption Performance of Ultralight Honeycomb Sandwich Panels Filled with "Network" Fibers—Juncus effusus. *Polymers*, 16(13), 2024. ISSN 20734360. doi: 10.3390/polym16131953. 163

[240] Mohsen Bahrami, Juana Abenojar, and Miguel Angel Martinez. Recent progress in hybrid biocomposites: Mechanical properties, water absorption, and flame retardancy, 2020. ISSN 19961944. 163

[241] S. Fatima and A. R. Mohanty. Acoustical and fire-retardant properties of jute composite materials. *Applied Acoustics*, 72(2-3):108–114, 2011. ISSN 0003682X. doi: 10.1016/j.apacoust.2010.10.005. URL http://dx.doi.org/10.1016/j.apacoust.2010.10.005. 163

[242] Zihao Wang, Jiahang Liu, Jianxin Zhang, Shuai Hao, Xiaoli Duan, Hongzan Song, and Jun Zhang. Novel chemically cross-linked chitosan-cellulose based ionogel with self-healability, high ionic conductivity, and high thermo-mechanical stability. *Cellulose*, 27(9):5121–5133, 2020. ISSN

1572882X. doi: 10.1007/s10570-020-03144-3. URL https://doi.org/10.1007/s10570-020-03144-3. 164